

IAEA-TECDOC-1704

# ***Pathways to Energy from Inertial Fusion: An Integrated Approach***

*Report of a Coordinated Research Project 2006–2010*



**IAEA**

International Atomic Energy Agency

PATHWAYS TO ENERGY FROM  
INERTIAL FUSION:  
AN INTEGRATED APPROACH

The following States are Members of the International Atomic Energy Agency:

AFGHANISTAN	GUATEMALA	PANAMA
ALBANIA	HAITI	PAPUA NEW GUINEA
ALGERIA	HOLY SEE	PARAGUAY
ANGOLA	HONDURAS	PERU
ARGENTINA	HUNGARY	PHILIPPINES
ARMENIA	ICELAND	POLAND
AUSTRALIA	INDIA	PORTUGAL
AUSTRIA	INDONESIA	QATAR
AZERBAIJAN	IRAN, ISLAMIC REPUBLIC OF	REPUBLIC OF MOLDOVA
BAHRAIN	IRAQ	ROMANIA
BANGLADESH	IRELAND	RUSSIAN FEDERATION
BELARUS	ISRAEL	RWANDA
BELGIUM	ITALY	SAUDI ARABIA
BELIZE	JAMAICA	SENEGAL
BENIN	JAPAN	SERBIA
BOLIVIA	JORDAN	SEYCHELLES
BOSNIA AND HERZEGOVINA	KAZAKHSTAN	SIERRA LEONE
BOTSWANA	KENYA	SINGAPORE
BRAZIL	KOREA, REPUBLIC OF	SLOVAKIA
BULGARIA	KUWAIT	SLOVENIA
BURKINA FASO	KYRGYZSTAN	SOUTH AFRICA
BURUNDI	LAO PEOPLE'S DEMOCRATIC REPUBLIC	SPAIN
CAMBODIA	LATVIA	SRI LANKA
CAMEROON	LEBANON	SUDAN
CANADA	LESOTHO	SWAZILAND
CENTRAL AFRICAN REPUBLIC	LIBERIA	SWEDEN
CHAD	LIBYA	SWITZERLAND
CHILE	LIECHTENSTEIN	SYRIAN ARAB REPUBLIC
CHINA	LITHUANIA	TAJIKISTAN
COLOMBIA	LUXEMBOURG	THAILAND
CONGO	MADAGASCAR	THE FORMER YUGOSLAV REPUBLIC OF MACEDONIA
COSTA RICA	MALAWI	TOGO
CÔTE D'IVOIRE	MALAYSIA	TRINIDAD AND TOBAGO
CROATIA	MALI	TUNISIA
CUBA	MALTA	TURKEY
CYPRUS	MARSHALL ISLANDS	UGANDA
CZECH REPUBLIC	MAURITANIA	UKRAINE
DEMOCRATIC REPUBLIC OF THE CONGO	MAURITIUS	UNITED ARAB EMIRATES
DENMARK	MEXICO	UNITED KINGDOM OF GREAT BRITAIN AND NORTHERN IRELAND
DOMINICA	MONACO	UNITED REPUBLIC OF TANZANIA
DOMINICAN REPUBLIC	MONGOLIA	UNITED STATES OF AMERICA
ECUADOR	MONTENEGRO	URUGUAY
EGYPT	MOROCCO	UZBEKISTAN
EL SALVADOR	MOZAMBIQUE	VENEZUELA
ERITREA	MYANMAR	VIETNAM
ESTONIA	NAMIBIA	YEMEN
ETHIOPIA	NEPAL	ZAMBIA
FIJI	NETHERLANDS	ZIMBABWE
FINLAND	NEW ZEALAND	
FRANCE	NICARAGUA	
GABON	NIGER	
GEORGIA	NIGERIA	
GERMANY	NORWAY	
GHANA	OMAN	
GREECE	PAKISTAN	
	PALAU	

The Agency's Statute was approved on 23 October 1956 by the Conference on the Statute of the IAEA held at United Nations Headquarters, New York; it entered into force on 29 July 1957. The Headquarters of the Agency are situated in Vienna. Its principal objective is "to accelerate and enlarge the contribution of atomic energy to peace, health and prosperity throughout the world".

IAEA-TECDOC-1704

PATHWAYS TO ENERGY FROM  
INERTIAL FUSION:  
AN INTEGRATED APPROACH

REPORT OF A COORDINATED RESEARCH PROJECT 2006–2010

INTERNATIONAL ATOMIC ENERGY AGENCY  
VIENNA, 2013

## COPYRIGHT NOTICE

All IAEA scientific and technical publications are protected by the terms of the Universal Copyright Convention as adopted in 1952 (Berne) and as revised in 1972 (Paris). The copyright has since been extended by the World Intellectual Property Organization (Geneva) to include electronic and virtual intellectual property. Permission to use whole or parts of texts contained in IAEA publications in printed or electronic form must be obtained and is usually subject to royalty agreements. Proposals for non-commercial reproductions and translations are welcomed and considered on a case-by-case basis. Enquiries should be addressed to the IAEA Publishing Section at:

Marketing and Sales Unit, Publishing Section  
International Atomic Energy Agency  
Vienna International Centre  
PO Box 100  
1400 Vienna, Austria  
fax: +43 1 2600 29302  
tel.: +43 1 2600 22417  
email: [sales.publications@iaea.org](mailto:sales.publications@iaea.org)  
<http://www.iaea.org/books>

For further information on this publication, please contact:

Physics Section  
International Atomic Energy Agency  
Vienna International Centre  
PO Box 100  
1400 Vienna, Austria  
Email: [Official.Mail@iaea.org](mailto:Official.Mail@iaea.org)

© IAEA, 2013  
Printed by the IAEA in Austria  
APRIL 2013

### IAEA Library Cataloguing in Publication Data

Pathways to energy from inertial fusion: an integrated approach. – Vienna : International Atomic Energy Agency, 2013.  
p. ; 30 cm. – (IAEA-TECDOC series, ISSN 1011-4289; no. 1704)  
ISBN 978-92-0-139710-2  
Includes bibliographical references.

1. Nuclear fusion – Research. 2. Inertial confinement fusion.  
I. International Atomic Energy Agency. II. Series.

IAEAL

13-00809

## FOREWORD

The IAEA has continuously demonstrated its commitment to supporting the development of safe and environmentally clean nuclear fusion energy. Statistics show that at the current rate of energy consumption, fusion energy would remain an inexhaustible energy source for humankind for millions of years. Furthermore, some of the existing and foreseen risks — such as nuclear waste disposal and rising greenhouse gas emissions from the use of fossil fuels — can also be reduced. In the quest for fusion energy, two main lines of research and development are currently being pursued worldwide, namely the inertial and the magnetic confinement fusion concepts. For both approaches, the IAEA has conducted coordinated research activities focusing on specific physics and technological issues relevant to the establishment of the knowledge base and foundation for the design and construction of fusion power plants. This report describes the recent research and technological developments and challenges in inertial fusion energy within the framework of such a coordinated research effort.

The coordinated research project on Pathways to Energy from Inertial Fusion: An Integrated Approach was initiated in 2006 and concluded in 2010. The project involved experts and institutions from 16 Member States, addressing issues relevant to advancing inertial fusion energy research and development in its practical applications. The key topics addressed include: (i) high repetition rate, low cost, high efficiency ignition drivers; (ii) beam–matter/beam–plasma interaction related to inertial fusion target physics; (iii) target fusion chamber coupling and interface; and (iv) integrated inertial fusion power plant design.

Participants in this coordinated research project have contributed 17 detailed research and technology progress reports of work performed at national and international levels. This report compiles all these reports while highlighting the various achievements. The IAEA officers responsible for this publication were R. Kamendje and T. Desai of the Division of Physical and Chemical Sciences.

#### *EDITORIAL NOTE*

*This publication has been prepared from the original material as submitted by the authors. The views expressed do not necessarily reflect those of the IAEA, the governments of the nominating Member States or the nominating organizations.*

*This publication has not been edited by the editorial staff of the IAEA. It does not address questions of responsibility, legal or otherwise, for acts or omissions on the part of any person.*

*The use of particular designations of countries or territories does not imply any judgement by the publisher, the IAEA, as to the legal status of such countries or territories, of their authorities and institutions or of the delimitation of their boundaries.*

*The mention of names of specific companies or products (whether or not indicated as registered) does not imply any intention to infringe proprietary rights, nor should it be construed as an endorsement or recommendation on the part of the IAEA.*

*The authors are responsible for having obtained the necessary permission for the IAEA to reproduce, translate or use material from sources already protected by copyrights.*

## CONTENTS

SUMMARY .....	1
COUNTRY REPORTS	
Experimental progress on fast electron propagation in cylindrically compressed matter.....	11
<i>R. Jafer, D. Batani, L. Volpe, M. Koenig, S. Baton, E. Brambrink, F. Perez, F. Dorchies, J.J. Santos, C. Fourment, S. Hulin, P. Nicolai, B. Vauzour, K. Lancaster, M. Galimberti, R. Heathcote, M. Tolley, Ch. Spindloe, P. Koester, L. Labate, L. Gizzi, C. Benedetti, A. Sgattoni, M. Richetta, J. Pasley, F. Beg, S. Chawla, D. Higginson, A. MacKinnon, A. McPhee, Duck-Hee Kwon, Y. Ree</i>	
Experimental study on laser non-uniformity mitigation .....	21
<i>T. Desai</i>	
Short pulse KrF lasers for inertial fusion .....	27
<i>I.B. Földes</i>	
Transverse diagnostics of intense, focused heavy ion beams .....	37
<i>D.H.H. Hoffmann, F. Becker, P. Forck</i>	
High power laser based inertial fusion energy research coordinated in associated laboratories .....	43
<i>M. Kalal, S. Yu.Gus'kov, A. Kasperczuk, D. Klir, E. Krouskey, J. Limpouch, M. Martinkova, M. Pfeifer, T. Pisarczyk, Y.J. Rhee, K. Rohlena, N. Rudraiah, J. Skala, O. Slezak, J. Ullschmied</i>	
Investigations of interaction of laser radiation and plasma beams with materials of reactor chamber for inertial confinement fusion .....	53
<i>R.T. Khaydarov, H.B. Beisinbaeva, M.M. Sabitov, V.B. Terentev, G.R. Berdiyborov, T. Akramov</i>	
The study of the beam combination laser system with high power/energy and high repetition rate using stimulated Brillouin scattering phase conjugate mirrors (SBS-PCMs) for laser fusion driver .....	67
<i>H.J. Kong, J.S. Shin, S. Park, K.S. Shim, S. Cha</i>	
Optimizing cryogenic layering for Inertial Fusion Energy (IFE) targets for providing target survival during the injection process.....	77
<i>I.V. Aleksandrova, A.A. Belolipetskiy, E.R. Koresheva, A.M. Oparin, I.E. Osipov, A.A. Tonshin</i>	
Pathway to energy from inertial fusion — an integrated approach.....	97
<i>S. Nakai, K. Mima, H. Azechi, N. Miyanaga, M. Nakai, K. Tanaka</i>	
The role of the spatial and temporal radiation deposition in inertial fusion chambers. ....	105
<i>J.M. Perlado</i>	
Chamber responses and safety and fusion technology in inertial fusion energy (IFE) reactor related to HiPER: A reference study .....	113
<i>J.M. Perlado</i>	

Hydrodynamic instabilities in inertial fusion systems and high energy density physics .....	123
<i>A.R. Piriz, J.J. López Cela, S.A. Piriz, N.A. Tahir</i>	
Optimization of some scenarios of ignitions of micro-explosions in inertial fusion energy (IFE) power plants .....	127
<i>M.L. Shmatov</i>	
Laser–atom, laser–plasma interactions related to target physics and fast ignition .....	145
<i>V. Stancalie</i>	
Direct drive ignition studies for large scale laser facilities .....	161
<i>V. Tikhonchuk</i>	
Target and chamber technologies for direct drive laser inertial fusion energy (IFE) .....	169
<i>M.S. Tillack, A.R. Raffray, F. Najmabadi, L.C. Carlson</i>	
Progress report — pathways to energy from inertial fusion — an integrated approach .....	177
<i>J. Wołowski, J. Badziak, T. Pisarczyk</i>	
List of Publications during CRP.....	187
List of Participants .....	193

## SUMMARY

Inertial Fusion Energy (IFE) research is approaching a critical juncture in its history with high expectations that ignition and physics feasibility will be demonstrated soon in the National Ignition Facility (NIF), USA and related facilities around the world. In order to exploit the growing science basis on fusion ignition, burn and energy gain for practical applications, the technology challenges associated with high repetition rate, affordable and highly reliable energy systems must be overcome through expanded technology R&D programmes.

The IAEA Coordinated Research Project on Pathways to Energy from Inertial Fusion – an Integrated Approach commenced in 2006 with the goal of fostering a worldwide collaborative network and stimulating progress toward a practical inertial fusion energy source. The final Research Coordination Meeting was held in March 2010.

This report summarizes the progress and substantial achievements of this CRP. Technical activities are divided into three areas, each of which offered opportunities for strong international collaboration:

- (1) Beam/Plasma – Matter Interactions. This topic includes both theoretical and experimental activities related to the physics of inertial fusion, including hydrodynamics, fluid instabilities, radiation transport, atomic physics and relativistic electron transport.
- (2) Building blocks for IFE.
  - Drivers: Various energy sources can be used to create implosion conditions and ignite fuel. These include solid state lasers and Excimer lasers, heavy ion accelerators and z-pinches.
  - Target Technology: The ability to fabricate targets that meet stringent specifications, and to do so with reproducibility and acceptable cost, is an essential element of both research programmes and fusion energy facilities. For a successful power plant, targets must be injected repeatedly into the reactor chamber with high precision by the driver.
- (3) IFE power plant and integration: IFE power plant technology comprises of various plant systems including reaction chamber, blanket, materials behaviour in a radiation environment, cooling systems, tritium and power handling systems, and all of their design constraints and interfaces. Material behaviour under irradiation and plant reliability is important for safety and environmental issues.

The widespread interest in inertial fusion reactors is motivated not only by the quest for a sustainable source of energy but also by the need for an efficient neutron source for various applications including incineration of actinides in nuclear waste and production of nuclear fuel for conventional fission reactors, and fundamental research in high energy density physics.

In this report, the relevant issues and R&D for an integrated Inertial Fusion Energy development are summarized. Advances in all the above mentioned three technical activity areas are effectively demonstrated.

## 1. INTRODUCTION

Inertial Fusion Energy (IFE) research is approaching a critical juncture in its history. Fusion ignition, burn and energy gain are expected in the 2012-2015 timeframe by the National Ignition Facility (NIF), USA, using central ignition. Other facilities will support physics investigations closely related to ignition, such as the Laser Megajoule (LMJ), France, to be operational in 2015, the Fast Ignition Realization Experiment (FIREX), Japan, for electron beam coupling and compression for future fast ignition, the Omega-upgrade in Rochester, USA, the Laser Integration Line (LIL), France, and the VULCAN facility in the UK. At the same time, the development phase of IFE is now shifting attention to the repeated operating mode of drivers and target injection, mass production of targets, knowledge on fusion reactor materials, design of experimental and technological facilities and power plants.

Current prerequisites for efficient target ignition are as follows:

- (1) Improving the implosion and ignition performance of fuel pellets in order to achieve lower ignition threshold and high gain;
- (2) Finding new schemes to reach ignition with innovative concepts.

With regard to engineering developments for rep-rate systems and innovative approaches, a worldwide collaborative network under the auspices of the IAEA has been established through a series of Coordinated Research Projects (CRPs). The need for such a collaborative programme is becoming more important and effective due to the widening of the related fields.

Since the consideration of IAEA collaborative activities in this field, several noteworthy accomplishments have been obtained.

- 1991-1994 – An advisory committee established under the auspices of the IAEA organized a network of international experts to review the state of the art in physics and engineering aspects of inertial fusion energy.
- 2001-2005 – An IAEA-CRP on “Elements of Power Plant Design for Inertial Fusion Energy” took place. A collaborative network was established including scientists from developing countries.
- 2005 – A consultants meeting was held at IAEA headquarters to investigate possible new IAEA activities on IFE.
- 2006-2010 – During the CRP on “Pathways to Energy from Inertial Fusion – an Integrated Approach” several achievements towards the IFE goal have been obtained.

In the global scenario, the world’s most powerful laser and inertial fusion research facility NIF in USA was completed and successfully commissioned in 2009. The achievement of fusion Ignition, Burn and Energy Gain (IBG) is expected in ~2012-2015. Implosion physics has been investigated and databases accumulated for many years with worldwide collaborations and information exchanges resulting in high credibility of IBG scaling on laser energy. The demonstration of IBG will introduce a new era of IFE development that is to move from physics investigations with single shot lasers to IFE power plant development with rep-rate drivers being considered for their overall efficiency and cost for construction and operation.

Advancement in the underlying physics issues and technological developments on NIF have provided the guidelines for the foreseen issues in the development of IFE. Based on the study there are four major research directions toward commercialization of IFE including:

- (1) Realization of an efficient and relatively low cost driver that will operate at a repetition rate of 10 Hz and deliver several hundred kilojoules of energy to the target. The most intensely studied candidate today is the diode pumped solid-state laser (DPSSL). There are actually five large-scale projects under development in the USA, Europe and Japan. The primary goal is construction of a module with an average power of 1 kW delivering ns pulses with about 100 J of energy and it is also motivated by various industrial applications. The difficulties are related to the necessary development of an efficient large scale cooling system for amplifiers and a low cost technology for diode fabrication. Along with the development of solid-state lasers, other lasers such as KrF excimer gas laser, heavy ion beam accelerator, and Z-pinch are also being developed as candidate drivers for IFE power plants. They have their own unique attractive features such as inherently repetitive nature and high efficiency operation.
- (2) Design of an efficient, robust and technologically feasible target with a gain more than 100, which could be mass-produced and ignited with laser energy of a few hundred kilojoules. There are three qualitatively different solutions under study: an up-scaled indirect drive target based on the design studied in the NIF; a direct drive target with conventional or shock driven central spot ignition; and the fast ignition scheme with direct drive implosion and off-center ignition with an energetic electron beam.
- (3) Development of a technological base for mass production of cryogenic targets, a robust system for target delivery to the chamber center and laser with a repetition rate of 10 Hz. IFE power plant fuelling requires ~500,000 targets per day, and should have a cost less than about \$0.30 each. For comparison, the current technology for target fabrication requires about 1 week to produce a single target costing more than \$1000 each. This work is in its beginning – although target fabrication technology has been advanced in the past years, much more needs to be done in the development of a system of target delivery.
- (4) Design of a commercially attractive fusion reactor and the systems of recuperation of fusion energy and tritium recovery. This latter problem has many common features with the work on thermal and radiation resistant materials conducted by the magnetic fusion (MFE) community. Growing collaboration between MFE and IFE research centers on material studies is an important step in the path to nuclear fusion energy.

## 2. OVERALL OBJECTIVES

The CRP overall objectives was set to cover research relevant to further development of IFE and enhance awareness in Member States with regard to Beam-Plasma-Matter interaction, developing building blocks for IFE and on IFE Power plants and integration. The purpose of such research is essentially three-fold: firstly, to improve our understanding of the underlying physical processes; secondly, to demonstrate capability and progress; and finally, of key importance to the pursuit of an integrated IFE power plant design, is the need to translate the results of the research into specifications for the facility itself.

### 2.1. Specific research objectives

The scope of work envisaged is to enhance collaboration and implement a networking approach for exchange of R&D in the following topics:

- Beam-plasma/beam-matter interactions related to target physics and fast ignition.
- Research to address unresolved key issues and/or advance the feasibility and attractiveness of individual drivers, targets and chambers that are part of integrated pathways.
- Research on key interface issues faced when developing integrated power plant systems (e.g., beam propagation through the chamber environment, target survival during injection, beam/target coupling, chamber response to target emission, etc.).

### 3. CRP ACHIEVEMENTS

#### 3.1. Beam/plasma – Matter interaction

Several participating groups in this CRP have concentrated most of their research efforts to various studies of Beam/Plasma – Matter Interaction, either theoretical or experimental. Topics under investigation as well as the results obtained are briefly summarized here. Detailed information can be found in respective reports by the authors.

One of the key phenomena in achieving high gain in inertial fusion is hydrodynamic instabilities. Theoretical investigations are reported by A. R. Piriz (see page 120) and his group. In particular the authors studied the Rayleigh-Taylor and Richtmyer-Meshkov instabilities in ablation fronts directly driven by ion beams. Furthermore, they report experimental studies on Rayleigh-Taylor instabilities relevant to high energy density physics.

Another theoretical work was performed by V. Stancalie (see page 141) in the field of Laser –Atom, Laser –Plasma Interactions related to target physics and fast ignition. In this work the interaction of high intensity laser radiation with atoms and plasmas has been investigated. Laser-atom interaction has been studied in connection with degeneracy and population trapping. Laser-plasma interaction has been considered from the point of view of relations between photon emission rate and ionization or recombination flux, which contribute to opacity effects. These results provide a firm foundation for larger calculations.

Another theoretical work has been described by M.L. Shmatov (see page 124) and concerned optimization of some scenarios of ignitions of micro-explosions in IFE power plants from the viewpoint of target and chamber physics, in particular: (i) Some problems related to fast ignition by laser-accelerated ions, (ii) Possibility and expedience of the use of ions of elements with atomic numbers  $Z > 5$  for heating compressed D-T fuel, (iii) Some advantages of fast ignition targets with two cones. (iv) Optimum variant of using D-D fusion reactions for power production. Further, the report discusses on (i) the use of ignition scenarios (e.g. using two hot spots) for ruggedness in seismic areas, (ii) benefits of IFE studies for development of space propulsion systems, biology and medicine.

Experimental progress on fast electron propagation in cylindrically compressed matter has been reported by R. Jafer et al. (see page 13). This experiment was achieved on the VULCAN laser facility at RAL (UK) using four long pulses beams ( $\sim 4 \times 50$  J, 1 ns, at  $\lambda = 0.53$   $\mu\text{m}$ ) to compress a hollow plastic cylinder. 2D hydro simulations predict a density of 2–5 g/cc and a plasma core temperature up to 100 eV at maximum compression. X ray radiography and proton radiography have been used to measure the compression degree as well as stagnation time. Results are discussed and compared with simulations. Monte Carlo simulations of proton propagation in the cold and in the compressed targets allowed a detailed comparison with 2D numerical hydro simulations.

An experimental study on laser non-uniformity mitigation was reported by T. Desai (see page 22). One of the methods discussed is to combat the growth of instabilities at the laser induced ablation surface. Experiments were performed by using low-density plastic targets embedded with metal particles of micron size and results were compared with *pure* plastic targets. The rear surface target stability was studied using the optical backlighting technique. Shadowgrams of the seeded targets showed a uniform motion of the target rear, whereas pure plastic targets break up under identical conditions. Preliminary investigations reveal the possibility of several simultaneous processes occurring at the ablation surface, which control the growth of the instabilities arising at the ablation surface. Several reasons could be restricting the instabilities and they have tried to analyse the results in the existing knowledge.

J. Wołowski (see page 172) and his team have presented their research related to simulations of proton generation driven by an intense laser pulse. In particular, they studied (i) mechanisms responsible for plasma jet formation by a laser pulse, and (ii) a new indirect method for two-step laser acceleration of the thin foil. The main objective of these works was to study the process of laser-driven proton beams, especially those produced by skin-layer ponderomotive acceleration (SLPA). Such protons can attain parameters relevant to fast ignition of a fusion target. Their report presents exemplary results of PIC simulations of this process. The works connected with laser-produced plasma jet formation and laser driven macro-particle acceleration for ICF applications are also described.

A large international team led by M. Kalal (see page 44), discusses the progress on various research topics: (i) a very simple method of plasma jet formation proposed and applied. This is opening new possibilities for experimental astrophysics and to the studies of mixing of different kinds of plasmas relevant to IFE. (ii) Processes related to the creation of clusters as well as interaction of high-intensity lasers ( $10^{16}$  W/cm<sup>2</sup>) with deuterated clusters (generating fusion neutrons) were studied both experimentally as well as theoretically. (iii) A special Stimulated Brillouin Scattering phase conjugate mirror (SBS PCM) based approach to IFE featuring self-navigation of laser drivers on injected pellets was proposed and tested in experiments. Simplification of the final optics design (having no moving parts) would allow for a higher number of less energetic lasers to be employed. As a consequence, higher repetition rate lasers will be much easier to design. (iv) Theoretical calculations of the experimentally verified beam combination scheme developed by H.J. Kong were performed in order to understand the underlying principles. (v) Theoretical study on Electrorheological Rayleigh-Taylor Instability (ERTI) at the interface between a densely packed saturated poorly conducting couple stress porous layer accelerated by a lighter poorly conducting couple stress fluid in a thin shell in the presence of a transverse electric field and laser radiation was performed and, under certain simplifications, the corresponding dispersion relation for the growth rate of ERTI has been derived.

### **3.2. Developing building blocks for IFE**

Developing building blocks for IFE involves two stages. Viz.

- Drivers (high rep-rate, low cost, high power solid state and gas lasers, heavy ion beams) which will be used to create implosion conditions and ignite fuel.
- Target technology (mass production, handling, low cost, target injection and trajectory, target tracking and shooting, survivability of fuel core). For a successful power plant, targets must be injected repeatedly into the reaction chamber and integrated with the driver with high precision.

These two issues are discussed in the following text.

### 3.2.1. *Drivers*

Solid state lasers: Recent progresses in the key technologies that are fundamental for high power Diode Pumped Solid State Lasers (DPSSLs) include the followings as reported by Nakai (See page 96).

- Progress of high power Laser Diode (LD)
  - 250→700W/cm bar, conversion efficiency 80%.
  - High power Vertical Cavity Surface Emitting Laser (VCSEL) 3.5kw/cm<sup>2</sup>
- Development of ceramic laser materials
  - Ceramic YAG, NdY<sub>2</sub>O<sub>3</sub>
- Development of nonlinear optical materials
  - Growth of KDP, CLBO and organic crystals
- Progress of pulse compression
  - Femtosecond pulses with Petawatt power.
- Progress of fibre laser technology
- Progress of phase conjugate technology for rep-rate operation of solid state lasers

Gas lasers: Recently, the KrF excimer laser has been considered to be a suitable driver for IFE, especially for the ignitor laser due to the intrinsic features of the short wavelength (248 nm) and short duration pulse capability (ps) without any pulse compression system. The high-field laser/matter-plasma interaction physics are under investigation by Foldes et al. with a collaborative work of the scientists of Eastern Europe. (see page 28).

Heavy ion accelerator: A large-scale scientific activity has been started at Darmstadt for IFE research with Heavy Ion Beams under the joint programme of GSI/FAIR. Inertial fusion by focused heavy ion beams has many unique features compared to laser inertial fusion in the beam-plasma-matter interaction and driver technology. Initial experiments on target interaction with a strongly focused U ion beam have been reported. The beam profile has been monitored by gas fluorescence and foil activation. The stopping ranges of ions and the Bragg peak have been clearly observed by the activation method. (report by D.H.H. Hoffmann 38).

Based on the recent progress on the basic technologies related to high average power, high intensity DPSSLs, new projects toward IFE power plant development are providing promising approaches. IFE projects are making significant progress in Europe (the project High Power Laser Research facility – HiPER), in the USA (the project Laser Inertial Fusion Engine – LIFE) and in Japan (the project Fast Ignition Realization Experiment – FIREX). Financial support for these projects is provided by academic laboratories, national and international research organisations and private companies.

### 3.2.2. *Target technology*

The main aspects of IFE target technology include:

1. IFE target production and requirement: target design, fabrication, mass production, robot handling, low cost.
2. Target interface issues: target & robot assembly and transport to the position of the injector, target injection, tracking and shooting, target trajectory and survivability of fuel core.

In addition, target developments for reactor technologies must fulfill the requirement of tritium inventory minimization as well as minimization of human involvement in production processes.

### 3.2.2.1. IFE target production and requirements

Programmes on reactor target production are underway in the Russian Federation, USA, Japan and Europe. In this report we cover the work performed under the present CRP in the Russian Federation.

In the Russian Federation, at Lebedev Physical Institute of the Russian Academy of Sciences (LPI), the issues of IFE target fabrication are focused by I.V. Aleksandrova *et al.* on methods that will scale to high rep-rate and cost-effective target production (see page 77). To realize the goal, an approach based on using Free-Standing Targets (FST) at each production step has been developed at LPI. Currently, the main results are the following:

- (1) It has been shown (theoretically and experimentally) that the fuel layer structure is of crucial importance for the development of the IFE injection scenario. In the optimal case, the fuel layer should be in an isotropic ultra-fine state.
- (2) Experimentally, the FST technologies developed at LPI allow forming cryogenic layers just as isotropic ultra-fine ones. That means that FST technology is promising for the formation of ultra-fine cryogenic layers from DT-mixture.
- (3) A programme on “Multiple target protection methods” includes a number of alternative methods, including outer reflective metal coating, outer protective cryogenic coating (solid Xe, Ne or D<sub>2</sub>), and protective cover (shroud).
- (4) A concept of target factory based on FST technologies has been proposed at LPI.
- (5) A prototypical target factory was accomplished at LPI with the demonstration of filling (fill pressure of up to 1000 atm.), layering (cryogenic layer of up to 100 µm thick) and injection of mm size free-standing targets and repetition rate is ~0.1 Hz.
- (6) Research has shown that FST technologies are suitable not only for spherical cryogenic targets, but also for cylindrical ones (for laser and heavy-ion driven hohlraum targets). Cryogenic cylindrical targets based on this technology are used for LAPLAS experiments on the FAIR facility.

### 3.2.2.2. Target interface issues

Studies of target acceleration and injected target tracking and shooting were performed in the USA as reported by Tillack *et al.*, (see page 165). An electrostatic injection system was tested in which the electrode configuration allows two-dimensional steering. Targets are loaded, charged, released, tracked, accelerated and steered in a vacuum chamber. Acceleration from 12 to 22 m/s<sup>2</sup> has been achieved. Systems also were developed and demonstrated to track direct-drive targets in flight and to steer simulated driver beams onto the targets with the precision required for target ignition. These systems employ active control with crossing sensors, Poisson spot laser, and glint laser. Bench-top experiments were performed in order to demonstrate the feasibility of these systems and to characterize their performance. The system achieved 28 µm accuracy hitting in falling targets on the fly.

A new idea as an alternative approach to resolve this problem using the Main-Laser-Amplifier (MLA) + SBS-PCM system has been reported by H.J.Kong (see page 67). With the SBS-PCM technique, active control is not required so that it takes only several microseconds

for the laser amplification between the glint and the engagement. The principle of this technique is; first, the pellet is injected into the reactor chamber with careful tracking.

When the pellet is approaching the best interaction position, a low-energy pulse (glint) from a seed laser illuminates the pellet. The light scattered from the pellet surface passes through the windows of the reactor chamber and enters the chain of the MLA-SBS-PCM. This MLA-SBS-PCM will amplify the signal beam scattered from the flying target and return back exactly along the same path as its incoming path. This flying target advances more after the glint laser beam illumination during the time for the amplification with the order of microseconds corresponding to the target's advance of the order of  $\sim 100 \mu\text{m}$ , which is negligible for the turbulent flow effect of the previous implosion. This target's advance can be compensated by a Dispersive-Wedge + KDP-crystal located at the last stage of MLA-SBS-PCM that deflects properly the 3<sup>rd</sup> order harmonic imploding beam of the amplified laser beam to the new target position very accurately.

#### 4. IFE POWER PLANTS AND INTEGRATION SYSTEMS

The main systems in a IFE power plant based on Inertial Fusion Energy concept include chamber (first wall, blanket, radioprotection systems), power plant systems (thermal power cycles, heat exchanger, conventional conversion to electrical grid) and tritium cycle (extraction, handling, target manufacturing). Many options are possible for individual materials and technologies, but the design space is constrained and complicated by the need to account for all of the interfaces and interactions between systems. One of the most important design decisions involves the choice of wall protection (*e.g.*, buffer gas, liquid walls, and magnetic diversion) considering the full range of target emissions and its implications on driver and target propagation. Many issues remain in the design, testing, analysis and development of integrated IFE systems. These issues and their R and D include the first wall, structural material to sustain the Spatial and Temporal Radiation Deposition, flow of coolant and breeder (*e.g.*, solid breeder + gas coolant, liquid coolant and breeder) and other options are under discussion (*via* experiments and simulations).

Additional Systems to Blanket include penetration and damage to optical components and diagnostics by target emissions (dose and duration). A large research programme has already started in defining the basic physics problems and the engineering solutions. Simulations on the material response under the appropriate flux of ions, X rays, neutrons and gamma have been reported by Perlado (see page 103).

The main concern for structural materials is that of neutron damage and activation is discussed by Tillack (See page 165). No present material is able to provide the appropriate lifetime. Research on steels (ferritic-martensitic and ODS) and also on SiC composites is needed. These materials are also inside the scope of magnetic fusion research. Facilities for experiments are needed with neutrons.

Khaydarov *et al.* (see page 53) have experimentally analysed some of the processes which take place during the interaction of laser radiation and plasma beams with the materials of reactor chamber. They have studied the effect of target nature on the laser ablation process and on the properties of laser-generated plasma ions using porous targets having different densities. These results show how the charge state, the energy and the intensity of the plasma ions depend on the target density. They also studied the effect of laser frequency on the properties of plasma ions generated at the surface of such porous targets. They investigated the changes in the properties of laser-produced plasma ions after the ablation process, during

the plasma expansion, due to the mutual interaction between the ions of different mass using two-element plasma ions generated from ( $\text{Sc}_2\text{O}_3$ ,  $\text{Ce}_2\text{O}_3$ ,  $\text{Lu}_2\text{O}_3$ ) targets. The last part of the report show that the structural defects caused by the neutron irradiation, influence not only on the efficiency of the process of material evaporation and emission of plasma, but also on the ionization and recombination processes taking place at the initial stage of the plasma formation and expansion.

#### **4.1. Analysis of reactor safety**

IFE reactor systems proceed through accident analysis after evaluation of activation and radionuclide concentrations, safety and radioprotection. In this report by Perlado (see page 111) a set of tasks developed in reactor technologies during this CRP tenure are presented.

- Assessment of target emissions during the laser interaction with the targets: Very different consequences can results from the different schemes on protection of the materials and also in the interior dynamics of the chamber that will influence the repetitive operation of the laser and target injection.
- Knowledge of physics for damage in first wall materials and protection of the chamber walls and optics from debris ions, X rays, alpha particles and shrapnel.
- Provision for lifetime suitability for commercial applications. That implies work to be performed in both areas of Materials: resistant to irradiation and low/reduced activation for minimizing the radioactive waste in the facility.
- Effect of repetitive operation and the potential for re-setting the first wall protection after each shot to a level suitable to permit next shot to be undertaken.
- Minimizing the effect of first wall ablation or aerosol sputtering effects from posting increased challenges to the injection and engagement of a target.
- Radioprotection design of the different areas of the reactor in its different stages (Shielding, penetrations and operation conditions depending of areas, including necessity of remote handling or potential personnel intervention in time intervals)

#### **5. CONCLUSIONS**

The set of results obtained by CRP participants from 16 member states have contributed towards achieving the CRP's overall goal and specific objectives. The Agency's role of providing a platform for international collaboration has been of great value in enabling cross-fertilization on various scientific and technical issues and furthering exchange of resources as well as scientific and technical knowhow. All these scientific and technical achievements demonstrate substantial progress towards the realization of the milestones leading to the design and construction of an inertial fusion energy reactor.

## COUNTRY REPORTS

# EXPERIMENTAL PROGRESS ON FAST ELECTRON PROPAGATION IN CYLINDRICALLY COMPRESSED MATTER

R. JAFER<sup>\*</sup>, D. BATANI<sup>\*</sup>, L. VOLPE<sup>\*</sup>, M. KOENIG<sup>\*\*</sup>, S. BATON<sup>\*\*</sup>, E. BRAMBRINK<sup>\*\*</sup>, F. PEREZ<sup>\*\*</sup>, F. DORCHIES<sup>\*\*</sup>, J.J. SANTOS<sup>\*\*\*</sup>, C. FOURMENT<sup>\*\*\*</sup>, S. HULIN<sup>\*\*\*</sup>, P. NICOLAI<sup>\*\*\*</sup>, B. VAUZOUR<sup>\*\*\*</sup>, K. LANCASTER<sup>†</sup>, M. GALIMBERTI<sup>†</sup>, R. HEATHCOTE<sup>†</sup>, M. TOLLEY<sup>†</sup>, CH. SPINDLOE<sup>†</sup>, P. KOESTER<sup>††</sup>, L. LABATE<sup>††</sup>, L. GIZZI<sup>††</sup>, C. BENEDETTI<sup>†††</sup>, A. SGATTONI<sup>†††</sup>, M. RICHETTA<sup>§</sup>, J. PASLEY<sup>§§</sup>, F. BEG<sup>§§§</sup>, S. CHAWLA<sup>§§§</sup>, D. HIGGINSON<sup>§§§</sup>, A. MACKINNON<sup>#</sup>, A. MCPHEE<sup>#</sup>, Duck-Hee KWON<sup>##</sup>, Y. REE<sup>##</sup>

<sup>\*</sup>Dipartimento di fisica “G.Occhialini, Università di Milano-Bicocca, Italy

<sup>\*\*</sup>LULI, Ecole Polytechnique France

<sup>\*\*\*</sup>Université de Bordeaux - CNRS – CEA, France

<sup>†</sup>RAL, STFC, UK

<sup>††</sup>CNR, Pisa, Italy

<sup>†††</sup>Dipartimento di fisica, University of Bologna, Italy

<sup>§</sup>University of Rome, Italy

<sup>§§</sup>University of York, UK

<sup>§§§</sup>UCSD, California, USA

<sup>#</sup>LLNL, California, USA

<sup>##</sup>Korea Atomic Energy Research Institute, Daejeon, Republic of Korea

## Abstract

In this paper we present the results of an experiment performed at Rutherford Appleton Laboratory. This experiment was achieved on the VULCAN laser facility at RAL (UK) using four long pulses beams ( $\sim 4 \times 50$  J, 1 ns, at  $\lambda=0.53\mu\text{m}$ ) to compress a hollow plastic cylinder. 2D hydro- simulations predict a density of 2–5 g/cc and a plasma core temperature up to 100 eV at maximum compression. A short pulse (10ps, 160 J) beam generated fast electrons that propagated through the compressed matter by irradiating a nickel foil. To infer the hot electron characteristics X ray radiography and proton radiography were implemented in order to estimate the compressed plasma conditions. X ray radiography and proton radiography have been used to measure the compression degree as well as stagnation time. Results are discussed and compared with simulations. Finally, Monte Carlo simulations of proton propagation in the cold and in the compressed targets allowed a detailed comparison with 2D numerical hydro simulations.

## 1. INTRODUCTION

To accomplish the goal of Inertial Fusion Energy (IFE) in attaining fuel ignition condition, several large scale facilities including National Ignition Facility (NIF) in US, Fast Ignition Realization Experiment (FIREX) in Japan, Laser Megajoule Facility (LMJ) in France are performing advanced level experiments. At the same time, an international European facility HiPER [1] is planned in Europe for the same purpose. Many experiments have been done using with different diagnostics [2] to follow the implosion of the target and to study the fast-electron transport inside warm and dense matter [3-5]. Until now, most of the experiments carried out on this subject were designed to study cold planar targets at solid density. Such low-density and/or cold targets may exhibit a different behavior of the hot electrons passing through it, compared with the final design. In particular, the stopping power of fast electrons should be affected by the return current, linked to the collective effects. Till now we have done two different experiments, one at LULI using planar geometry (a detailed report of the main results of this experiment can be found in ref: [6]) and the other at RAL in cylindrical geometry. In this paper we present the results of the experiment performed at RAL to study the electron transport in cylindrically compressed matter, which is a useful geometry to infer different measurements [4, 5]. This experiment was split into two parts: the first one to achieve and study the cylindrical compression. Proton Radiography [2-4] was used in the first phase to record the implosion history of the cylindrical target. In parallel we used X ray Radiography to have a comparison. Simulations were made with the Monte Carlo (MC)

MCNPX Code [7] using density profiles of the imploded cylinder obtained with the 2D-hydro CHIC code [8].

## 2. EXPERIMENTAL SETUP

The experiment has been performed on the VULCAN laser facility (UK). Four long-pulse laser beams (about  $4 \times 50$  to  $4 \times 70$  J in 1 ns) at  $0.53 \mu\text{m}$ , focused to  $150 \mu\text{m}$  FWHM spots through *hybrid* phase plates, were used to cylindrically compress a  $200 \mu\text{m}$  long polyimide tube. This tube had a  $220 \mu\text{m}$  outer diameter and a  $20 \mu\text{m}$  wall thickness, as shown in FIG. 1.

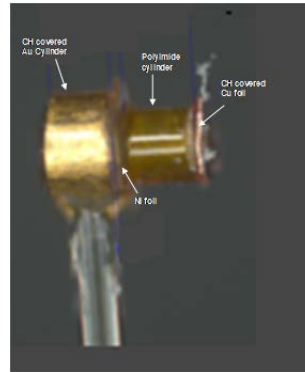


FIG. 1. Example of a target used in the experiment (thanks to Ch.Spindloe, M.Tolley and the entire RAL target prep group).

The target was filled with plastic polymer (TMPTA) at different densities: 0.1 or 0.3 g/cc foam or 1 g/cc solid plastic. Both sides were closed with  $20 \mu\text{m}$  thick foils of Ni and Cu, respectively. To produce the hot electrons, an additional laser (160 J in 10 ps) was focused on the Ni layer at an intensity of  $\sim 5 \times 10^{18} \text{ Wcm}^{-2}$ , using an  $f/3$  off-axis parabola. In order to limit the alteration of the ps beam caused by the low-density plasma generated by the ns pulses, a tube-shaped gold shield was stuck on the Ni foil. The four nanosecond beams had been individually timed to hit the target with a precision better than 100 ps.

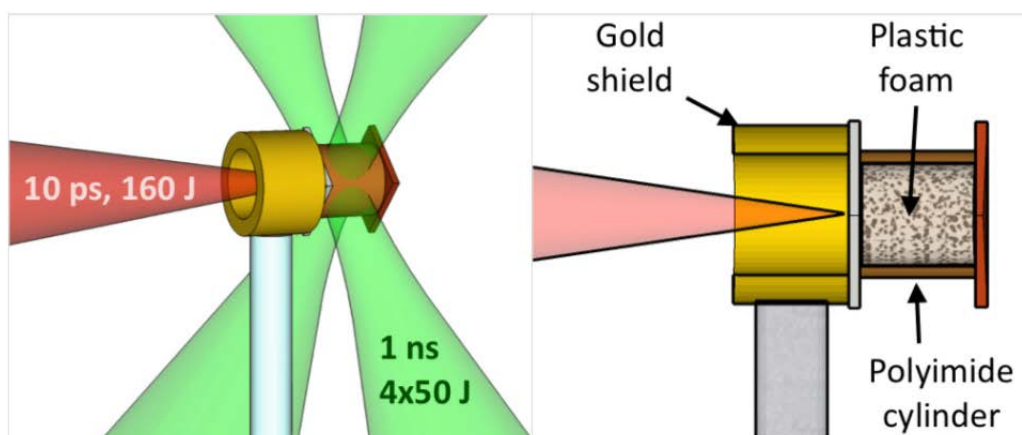


FIG. 2. Schematics of the target and lasers design.

The delay  $\tau$  between the long pulses and the short pulse was adjustable from 0 to more than 3 ns with a jitter of  $\pm 50$  ps. At  $\tau = 0$ , the short pulse hit the target when the long pulses just arrived. The experiment was split into two phases. The first phase objective was to determine the hydrodynamic characteristics of the compressed matter, i.e. temperature and density at optimal compression. In order to determine some of the parameters of the compressed cylinder, an additional laser (100 J in 1 ps, 20  $\mu\text{m}$  FWHM at  $\lambda=1.064$   $\mu\text{m}$ ) was focused on 10 mm distant foils to make an X ray (25  $\mu\text{m}$  Titanium) or proton (20  $\mu\text{m}$  Gold) backlighter for the diagnostics. Transverse point-projection proton radiography [10-13] can be employed to infer the target density in shock-compressed targets. A proton source was produced 10mm away from the target. Laser based protons are characterized by small source, high degree of collimation, short duration and a continuous spectrum up to a high-energy cutoff. Taking radiograph with multi-energetic protons allows recording the implosion history in a single shot. The detector was a radiochromic film (RCF) stack protected by a 12  $\mu\text{m}$  thick Al foil, placed  $\sim 50\text{mm}$  away from the target. The stacks were composed of 5 HD and 10 MD RCFs as shown in FIG. 3

Density measurement was also planned with X ray radiography diagnostic [5, 13]. Using Ti foils 10mm away from the target as backlighters and a quartz crystal to reflect the Ti-K $\alpha$  radiation (at 4.5 keV) that passed through the compressed target, we obtained a magnification of  $\sim 10$ . In order to get sufficient absorption, the plastic foam was doped with 30% Cl in mass. The quartz crystal (interatomic distance of 1.374  $\text{\AA}$ ) was spherically bent with a radius of curvature 380 mm. Imaging plates positioned  $\sim 2\text{m}$  away from this crystal detected the Ti-K $\alpha$  radiation as shown in FIG. 4.

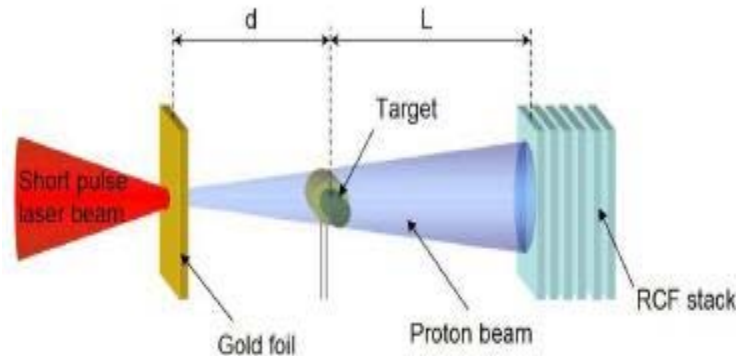


FIG. 3. Schematic of proton Radiography Setup.

The second phase of the experiment was designed to study the hot electron propagation through the compressed matter. The plastic foam inside the cylinder was doped with 10–20% Cu in mass so as to get X ray emission from this region. Two spherically bent quartz crystals with a 1.541 $\text{\AA}$  interatomic distance and a radius of curvature of 380 mm provided 2D monochromatic images, using imaging plates as detector, around the Cu-K $\alpha$ 1 line, i.e. at  $8050 \pm 5$  eV. These crystals were placed to have both side- and rear-view images of the cylinder with a magnification of  $\sim 10$  and a spatial resolution between 10 and 20  $\mu\text{m}$ . A cylindrically bent quartz with a 1.012  $\text{\AA}$  interatomic distances and a radius of curvature of 100 mm produced time- and space-integrated spectra for X ray energies from 7.3 to 9.3 keV in a Von Hamos configuration. It was able to detect both the Cu-K $\alpha$  and Ni-K $\alpha$  lines with a spectral resolution of  $3 \pm 2\text{eV}$ . A second spectrometer consisting of planar Highly Oriented Pyrolytic Graphite (HOPG) monitored the same emission lines with a much higher sensitivity [14], but a lower spectral resolution ( $\sim 50\text{eV}$ ).

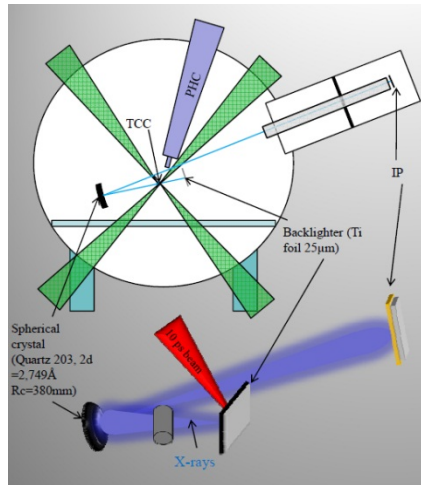


FIG. 4. Schematic of X ray radiography setup.

### 3. EXPERIMENTAL RESULTS

#### 3.1. I Phase: Radiography

The experimental proton radiographs of the reference cylinder as well as of the imploding cylinder at different stages of compressions are shown in FIG. 3.1. The minimum observed diameter is  $\sim 140 \mu\text{m}$  at 2, 3 ns. From experimental analysis it seems that low energy protons are not able to probe dense core so deeply as X rays do as shown in FIG. 6a,b.

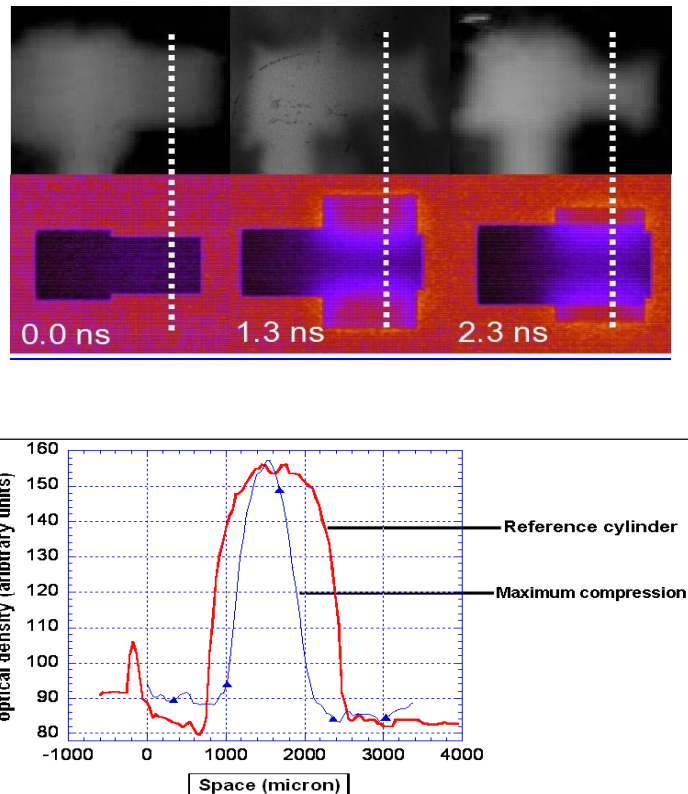


FIG. 5. Compression history obtained by experimental proton radiographs (top) at  $t_1=0 \text{ ns}$ ,  $t_2 = 1.3 \text{ ns}$ ,  $t_3 = 2.3 \text{ ns}$ . The figure below shows the densitometries along the minimum diameters. The uncompressed plastic cylinder ( $t=0$ ) could be fitted with supergaussian (red) while the compressed cylinder ( $t=2.3$ ) fits with gaussian (blue) shape.

## 2D hydrodynamica CHIC code simulations

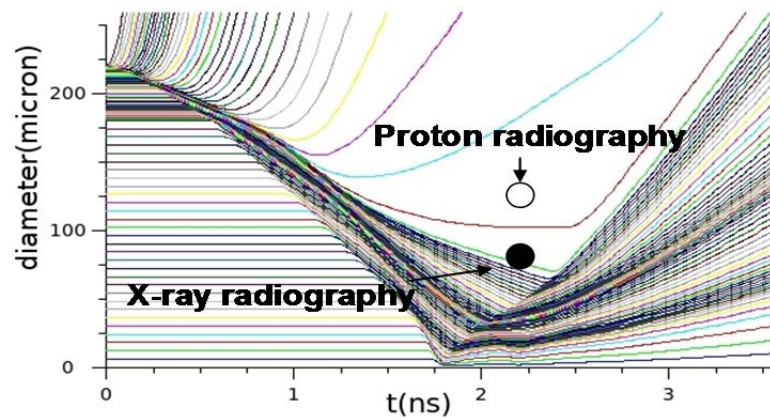


FIG. 6a. The comparison of compressions obtained with Proton and X ray radiography with 2D hydrodynamic CHIC code simulations.

## Proton radiography Vs x-ray radiography for 0.1g/cc

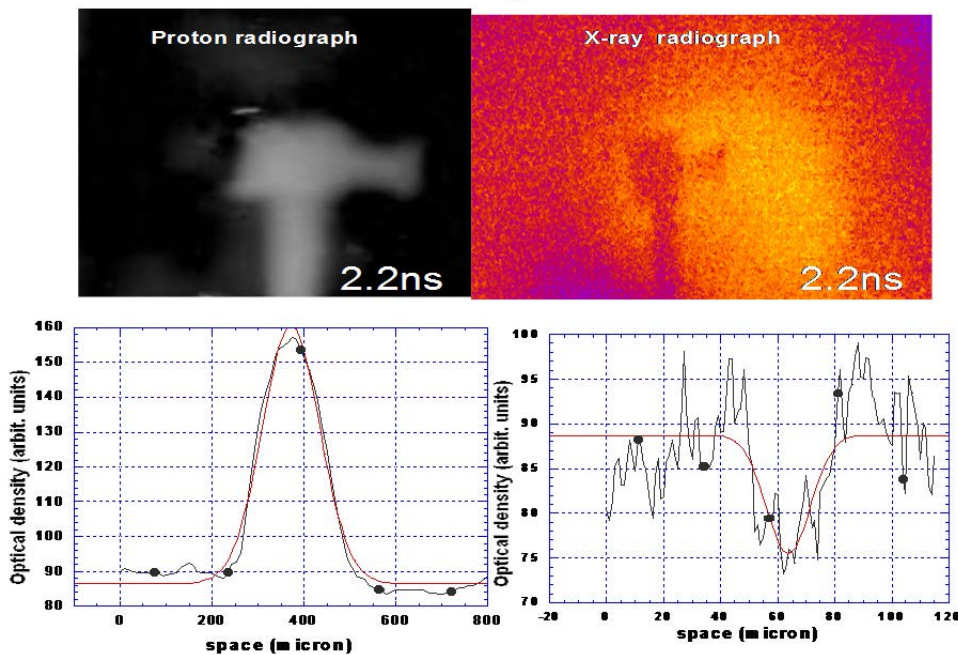


FIG. 6b. proton (left) and X ray (right) radiographies of cylinder at maximum compression and corresponding optical densities profiles.

This can depend on many physical effects among which the most important is the multiple scattering (MS) of protons with the atoms of the target which leads to an increase of the cylinder size on the detector as shown in FIG. 7. In order to investigate MS effects we ran simulation of the process using Monte Carlo code MCNPX prepared by LANL [8].

Stopping power (ST) of protons in the target is described by using Bethe's theory [15] while multiple scattering (MS) effects are described by Rossi's theory [16]. Here we introduced some modifications (a detailed report can be found in ref [17]) in order to account for the differences between Bethe's theory and the actual SP in plasmas [18].

Following the analysis procedure which we applied to experimental data, we have extracted FWHM by using Gaussian fits and in simulations we have got the similar results as shown in FIG. 7, by taking into account the above mentioned physical effects.

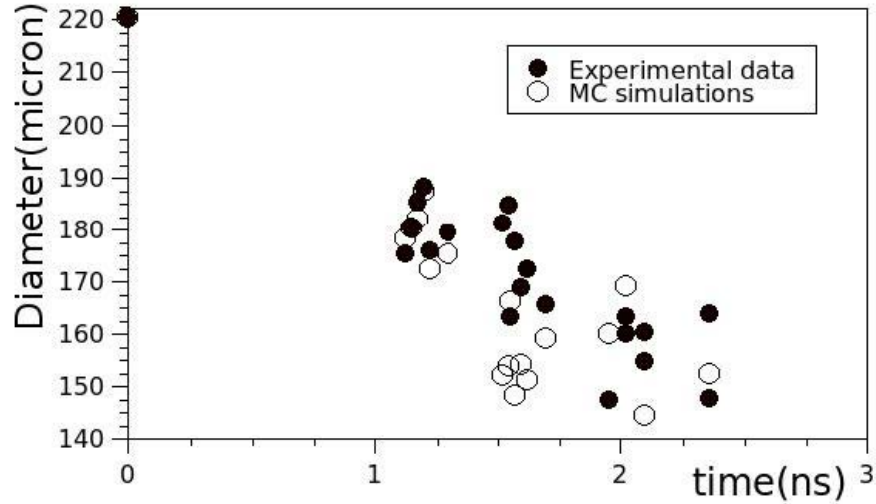


FIG. 7. Comparison of experimental (full circles) and simulation (empty circles) results. The point at 220  $\mu\text{m}$  shows the initial diameter of the cylinder.

### 3.2. II Phase: Electron Propagation in cylindrically compressed targets

In second phase, the two X ray spectrometers detected the  $K_\alpha$  and  $K_\beta$  emission from both Cu and Ni foils. The Ni emission is a good indicator of the electron source. The Cu signal indicates an electron population propagating through the target. The first interesting data are then the ratio between the Cu and Ni signal as it indicates the fraction of the hot ( $>8$  keV) electrons that reached the rear surface of the target. These data are presented in FIG. 8 for different delays, given by the HOPG spectrometer. There is a clear decrease up to  $\tau = 2$  ns, after which the ratio is constant. Furthermore, this effect is identical for the three different initial core densities used. These results, discussed below, are validated by the other spectrometer as well as the two X ray imagers.

The side-view X ray imager produced images of the Cu- $K\alpha$  emission from the rear Cu foil, and from the Cu doping inside the plastic core. In the four images of FIG. 9 the emission from the core is clearly differentiated from the Cu foil one. The vertical size of this core is about  $50\mu\text{m}$  at maximum compression, which is in agreement with the presented simulations. One can also easily see that the horizontal length of the emitting region inside the cylinder decreases with the delay: the penetration depth of the electrons is reduced for a high compression. For the low-density targets, the number of Cu atoms in the foam turned out to be too low to have a significant number of photons coming out of the target.

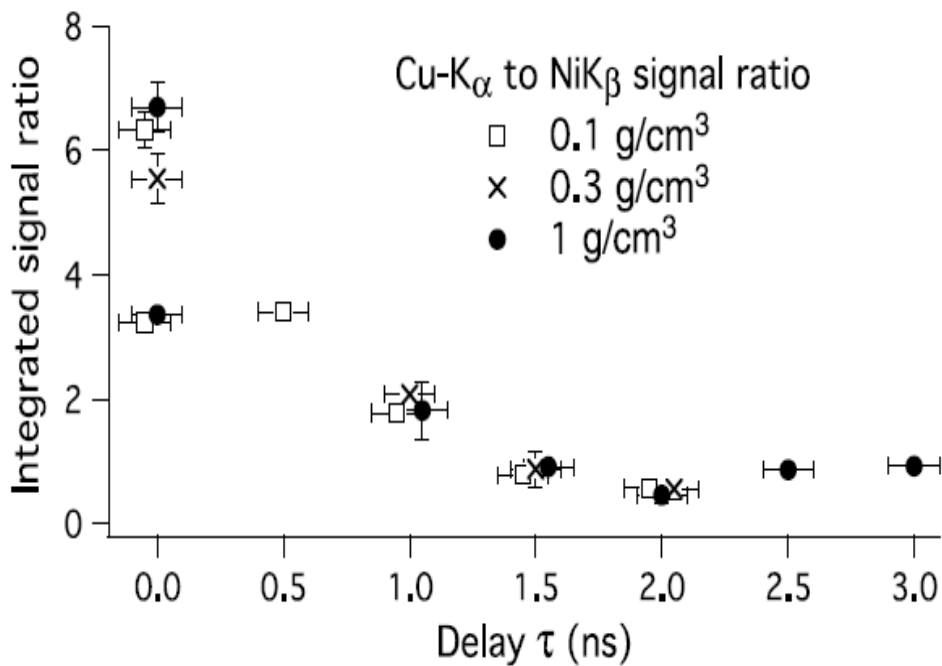


FIG. 8. Ratio between Cu and Ni X ray emissions as measured with the HOPG spectrometer versus the delay  $\tau$ , for different initial core densities.

Now taking into account the rear Cu foil instead of the core, the measurement of the width of this rear surface Cu-K $\alpha$  emission is closely linked to the divergence of the electrons reaching the rear surface. The side-view X ray imager corresponding results are plotted in figure 10. It shows two different behaviours of the hot electron divergence. With low-density targets, the width decreases with the delay. The opposite trend is observed for high-density targets.

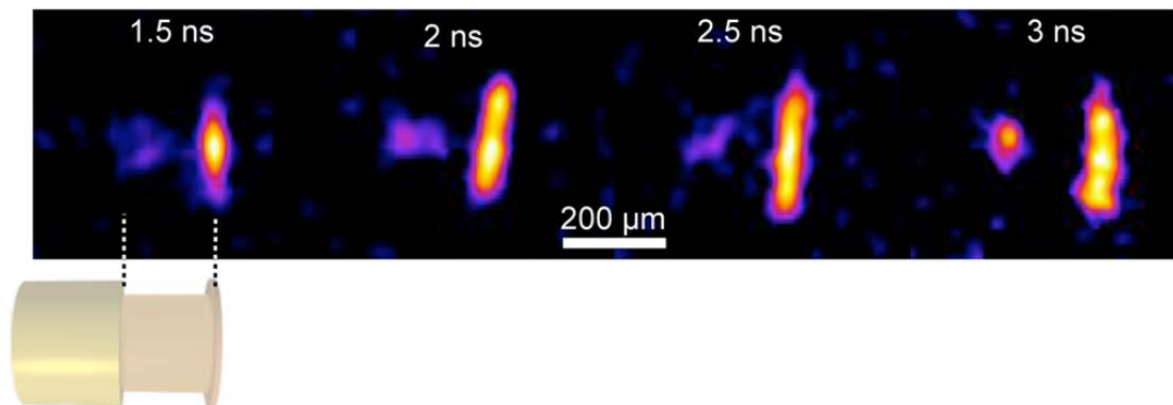


FIG. 9. Side-view X ray images of the Cu-K $\alpha$  emission from the compressed cylinder at different delays (1 g cm<sup>-3</sup> initial density in all cases).

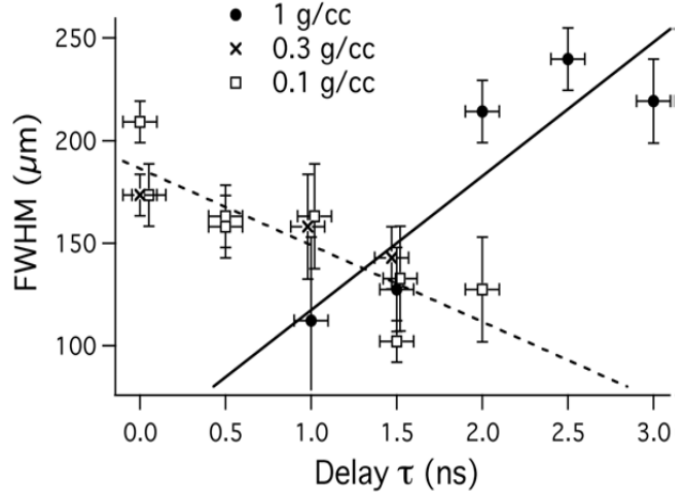


FIG. 10. Side-view imager results for fast-electron beam divergence measurements: rear surface foil width for different target densities. Linear fits are plotted for low- or high-density targets.

#### 4. DISCUSSIONS

Protons and X rays beams have been used to diagnose the implosion of cylindrical targets. X rays seem more penetrating in compressed targets than low energy protons. Simulations are therefore needed to analyse RCF images. Simulated data are able to approximately reproduce the observed size of images on RCF experimental data. The protons do not seem to probe the dense core but the implosion history and the stagnation time is revealed correctly.

The second phase results indicate a decreasing fraction of electrons reaching the rear surface when the compression occurs. It shows that the electrons are slowed down more efficiently with a high compression. For delays above 2 ns, the signal shows a plateau which hints at the presence of a hot electron component reaching the rear surface through the high-density core. This is supported by the side-view images of FIG. 9 as the same integrated signal is always visible on this rear surface. These images also confirm the presence of hot electrons inside the dense target.

To explain the electron divergence behaviour of FIG. 10, a few leads have to be investigated. We observe two different trends: the spot size either decreases or increases with the compression evolution. For the former case, we can formulate the following explanations. Firstly, the increasing density prevents the coldest electrons from reaching the rear surface. The remaining electrons, being more energetic, are less deviated through the plasma, resulting in a lower detected divergence. Secondly, the low-density targets are composed of a shell that is much denser than the core. The corresponding density ratio is about 5: 1 at maximum compression, with a 50  $\mu\text{m}$  diameter core. A resistivity model from [19] and the results from [20] applied to the present case could indicate a resistive confinement of the electrons inside the cylinder core, thus reducing the electron beam size while the cylinder is being compressed. Similarly, collisional processes might be able to prevent the electrons from diverging through the dense shell. Lastly, the electron beam can be truncated by this shell (because of an increased stopping power) thus giving a smaller spot on the rear surface. All these guiding effects may not apply in the case of high-density (solid) targets. However, it is difficult to say whether they are able to reverse the trend, i.e. divergence increasing with the

delay. Indeed, measurements on such a small scale target make their interpretation difficult. To answer this question, electron transport simulations are under consideration.

## 5. CONCLUSIONS

In conclusion, cylindrical compression has been achieved and measured to be in good agreement with the hydrodynamic simulations, and electron transport features have been measured. Within the fast-ignition framework, the presented results indicate that the same numbers of fast electrons able to reach the high-density region are observed for different initial target densities. More surprisingly, the electron divergence appears to depend strongly on the plasma geometries achieved for those different initial densities. In order to understand the above results, electron propagation simulations using electron transport codes still need to be performed. As one of the few experiments on electron transport in compressed matter [21], further studies need to be achieved to complete IFE roadmap. Overall, this experiment was an important test bed for the lasers and diagnostics in such a new configuration, several challenging experimental points have been clarified and fast-electron behaviors in compressed matter have been underlined.

## REFERENCES

- [1] [www.Hiper-laser.org](http://www.Hiper-laser.org).
- [2] STOTT, P.E., WOOTTON, A., GORINI G., and BATANI, D., “Advanced Diagnostics for Magnetic and inertial fusion” edited by Kluwer, Academic/Plenum Publishers, New York; (2002).
- [3] TABAK, M., et al 1994 Phys. Plasmas 1 1626–34.
- [4] NAKAMURA, H., et al 2008 Phys. Rev. Lett. 100 165001.
- [5] PEREZ, F., et al., Plasma. Physics. Control. Fusion, 51, 124035 (2009); B. Vazour, et. al., (2010).
- [6] SANTOS, J.J., et al., Plasma Phys. Controll. Fusion 51 014005 (2009).
- [7] <https://mcnpx.lanl.gov>.
- [8] MAIRE, P.-H., and BREIL, J., Int. J. Num. Meth. Fluids {56}, 1417 (2008).
- [9] LI, C. K., et al. Phy. Rev. Let. 100, 225001 (2008).
- [10] JAFER, R., et al., ULIS proceedings, volume (2009).
- [11] LE PAPE, S., et al 2006 High Energy Density Phys. 21–6.
- [12] MECKINONN A.J., et al. Phy. Rev. Let. 97,045001(2006).; M.Borghesi et al. Plasma physics. Control. Fusion 43(2001) A267-A276.
- [13] BENUZZI-MOUNAIX, A., et al 2008 Phys. Rev. E 77 045402.
- [14] PAK, A., et al 2004 Rev. Sci. Instrum. 75 3747–9.
- [15] BETHE, H. A., Phys. Rev. 89, 1256 (1953).
- [16] ROSSI, B., and GREISEN, K., Rev. Mod. Phys 13 (1941).
- [17] VOLPE, L., et al., to be published (2010).
- [18] MEHLHORN, T.A., J. Appl. Phys., 52, 6522, (1981); T. Peter, J. Meyer-ter-Vehn, Phys. Rev. A, 43, 4 (1991).
- [19] LEE, Y. T., and MORE, R. M., Phys. Fluids 27 1273–86 (1984).
- [20] KAR, S., et al 2009 Phys. Rev. Lett. 102 055001.
- [21] HALL, T. A., et al 1998 Phys. Rev. Lett.



# EXPERIMENTAL STUDY ON LASER NON-UNIFORMITY MITIGATION

T. DESAI

National Research Institute for Applied Mathematics,  
Bangalore, India

## Abstract

One of the methods discussed here is to combat the growth of instabilities at the laser induced ablation surface. We refer to our experiments performed by using low density plastic targets embedded with metal particles of micron size and the results were compared with pure plastic targets. The target stability at the rear surface was studied using the optical backlighting technique. Shadowgrams of the seeded targets show a uniform motion of the target rear, whereas pure plastic targets break up under identical conditions. Preliminary investigations reveal the possibility of several simultaneous processes occurring at the ablation surface which can control the growth of the instabilities arising at the ablation surface. There could be several reasons acting for restricting the instabilities and we have tried to analyse the results in the existing knowledge.

## 1. INTRODUCTION

Laser induced direct drive has the potential to achieve the high gain needed for Inertial Fusion Energy (IFE). One of the major issues in such scheme is a stable ablative compression of spherical fusion pellets filled with DT. Although several alternative schemes have been proposed to overcome these instabilities including Indirect drive as discussed in the progress report, HiPER-2007 [1], fast-ignition by Tabak et al.[2], shock-ignition by Betti et al [3], they are also not free from problems to attain the goal of ignition for commercial purpose. Direct Drive is still an attractive proposal and pursued intensely worldwide.

Direct Drive scheme can be briefly described as follows. A spherical microballoon filled with Deuterium and Tritium (DT) is symmetrically irradiated by multiple high power laser beams. Laser impact on the surface of the microballoon generates few tens of mega bars of intense pressure which isentropically compresses the DT material to few eV and density of the order of 1000 times the liquid DT density. This forms an envelope around the central low density but high temperature plasma  $\sim 5$  KeV due to shock heating. Actually the core plasma serves as an ignitor. In the case of the directly driven inertial confinement fusion  $\sim$ ICF scheme, the ignitor size is 2% of initial target radius. Therefore for efficient fusion reactions, ignitor spawned by the imploding fuel needs to be highly uniform for the stability of the compressed core.

There are several reasons to destroy the symmetry of the fuel compression appearing at different stages at the plasma critical density layer (corresponding to laser wavelength) and at the ablation surface etc. These include Laser non-uniformity, Target surface non-uniformity, Preheat (due to fast electrons and hard X rays), instabilities arising at the ablation surface owing to existing plasma conditions.

Non-uniformities appearing due to laser radiation and target surface non-uniformity can be reasonably overcome with ongoing advancement in the technology. However, existing optical smoothing techniques for reducing laser non-uniformities including RPP, PZP, ISI, SSD etc. offer smoothing of the small scale non-uniformities of the laser beam. For example; using Phase Zone Plates on Prague Asterix Laser System, Prague we can obtain Speckle size  $\sim (f \times \lambda_L) / \text{beam diameter} \sim 2 \mu\text{m}$  (for  $f = 100$  cm,  $\lambda_L = 0.44 \mu\text{m}$  and beam Diameter  $\approx 30$  cm) and such speckles can be easily smoothed by 2-D effects (thermal conduction) according to the following process. These small scale non-uniformities can be reduced as the beam propagates in laser produced plasma by a factor;

$\Gamma = \exp(-\alpha d 2\pi/\lambda_p)$  where  $\alpha \sim 1$ ,  $\lambda_p$  = wave-length of the laser non-uniformity.  
d = distance between laser deposition layer and ablation layer  $\sim I^{14/3} (\lambda_L)^{13/4}$  for planar target.

However, large scale non-uniformities  $\geq 2-3 \mu\text{m}$  persist and imprint on the ablation surface. Smoothing of the non-uniformity profile improves as it propagates the length “d” from laser critical density  $n_c$  layer to ablation layer  $n_a$ .

Ablation surface layer  $n_a$  is also a source for generating certain types of plasma instabilities including Rayleigh-Taylor (RT), Richtmeyer-Meshkov (RM) and Kelvin-Helmholtz (KH) etc. which can not be avoided and we can attempt to reduce their growth rates by adopting appropriate schemes. Low density plasma pushing high density plasma, shock acceleration, and interface shear are the sources for RT, RM and KH instabilities respectively.

Therefore, ablation surface uniformity suffers from non-uniformities introduced by laser and /or target surface and those inherently originating at the ablation surface and mitigating all these simultaneously is a real challenge in direct Drive. To simplify the concept in this work, we assume that the instabilities appear at the ablation-surface are induced either due to laser, heavy ion beam, electron beam interaction etc. as an external source and also due to innate plasma instabilities; thus instabilities are launched at the ablation-surface due to various reasons as shown in FIG. 1. It is also important to ameliorate these early time imprinting of non-uniformities due to laser radiation or target shell surface in an inertial confinement fusion ~ICF Scheme.

The optical smoothing techniques which produce small scale speckles as discussed above interestingly provide an important clue; if the long wavelength instabilities at the ablation surface can be reduced to smaller wavelengths then we can reasonably smoothen the instability profile due to 2-D expansion. If this argument is acceptable then the question is how to can we amend the instability wavelength to small scale length at the ablation surface? In this work we propose to modify the pure target structure like low density pure plastic by doping with 1-2 micron size metal particles. Our experimental results show that the accelerated target is smoother in the case of seeded target compared to pure plastic which shows a break up. These are our preliminary results and analysed in some newer light and we plan detail experiments in future.

## 2. EXPERIMENTS

Two types of planar targets were chosen for laser (1.06  $\mu\text{m}$ ) irradiation, namely, low density pure plastic target  $\sim \rho=0.9 \text{ gm/cc}$  of thickness 20  $\mu\text{m}$  and the same plastic target containing micro-particles of aluminium or gold material keeping  $\rho$  constant. Choice of the low density plastic was to derive the advantage as an ablator that generates few tens of mega bars of pressure isentropically compressing the DT material to few eV and density  $\sim 1000$  times the liquid DT density. Since this forms an envelope around the central low density, high temperature plasma ( $T_e \sim 5 \text{ KeV}$  due to shock heating), high degree of uniformity is required. Therefore the basic interest in the experiments was to study the effect of micro-particles on the hydrodynamic stability of low density plastic target that leads to compression of DT fuel.

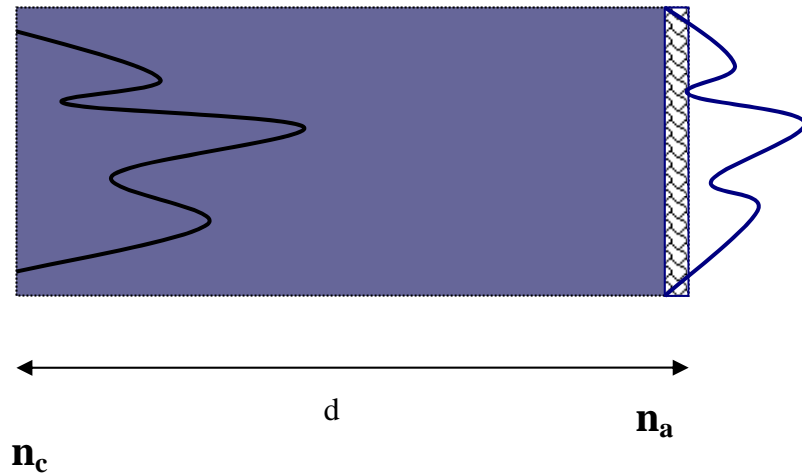


FIG. 1. Laser non-uniformities originating at the critical density layer are partially smoothed as they propagate in the plasma up to the ablation surface covering a distance “ $d$ ”. Various types of plasma instabilities also originate at the ablation surface.

Average aluminium particle size was  $0.4 \mu\text{m}$ , gold particles were of diameter  $\sim 1\text{--}1.2 \mu\text{m}$  whereas tungsten particles were about  $3 \mu\text{m}$ . Each cc of plastic solution contained 50 mg material in particle form and the required targets were prepared. Particle size has variation up to 50% and it was not possible to obtain the particles of exact diameter. In the present experiment, Al particle density was about  $N_{\text{al}} \sim 5.5 \times 10^{11}/\text{cc}$  with an average particle diameter  $\sim 0.4 \mu\text{m}$  and the average particle spacing was  $\sim 0.755 \mu\text{m}$ . Target structure showed not really a uniform placing of the particles but a random distribution in the base plastic target. Each aluminium and gold particle acts as an X ray source for primary emission but absorption and reemission plasma zone can not be established for a point source where the dimension of the source is less than the X radiation mean free path. Therefore X ray emission from isolated aluminium, gold or tungsten particles will not be similar to that of solid Al/ Au/W slab, high Z buffered foam or high Z coated targets. Due to the presence of fewer gold and tungsten particles (corresponding to their higher density as compared to aluminium), the inter-particle spacing was large for gold and tungsten seeded targets. Experimental arrangement is briefly shown in FIG. 2.

Targets with micro-particles will form a super-lattice structure. In the present experiment, Au and tungsten particles emit copious soft X rays  $h\nu \sim 1.5 \text{ KeV}$  and Al particles which are relatively poor X ray emitters compared to Au/W material could provide an understanding on the advantage of X ray in the present experiment. Hence the effect of X rays on mitigation of the instabilities can be studied by comparing the results of Au/W seeded targets with Al seeded target.

Seeded targets have certain advantages over the pure material targets like;

- (1) Micro-particles are an obstacle to the free flow of plasma and how their presence involves in affecting the growth of the instabilities is an important issue to study.
  - (2) High Z metal particles could be treated as an X ray source, and hence one can draw some advantage of short wavelength ablation.
  - (3) X ray emission from such targets is low as compared to pure high-Z materials, and thus higher ablation efficiency.
4. Such seeded targets have been used as a shield against the preheating of the plasma due to hot electrons and hard X rays.

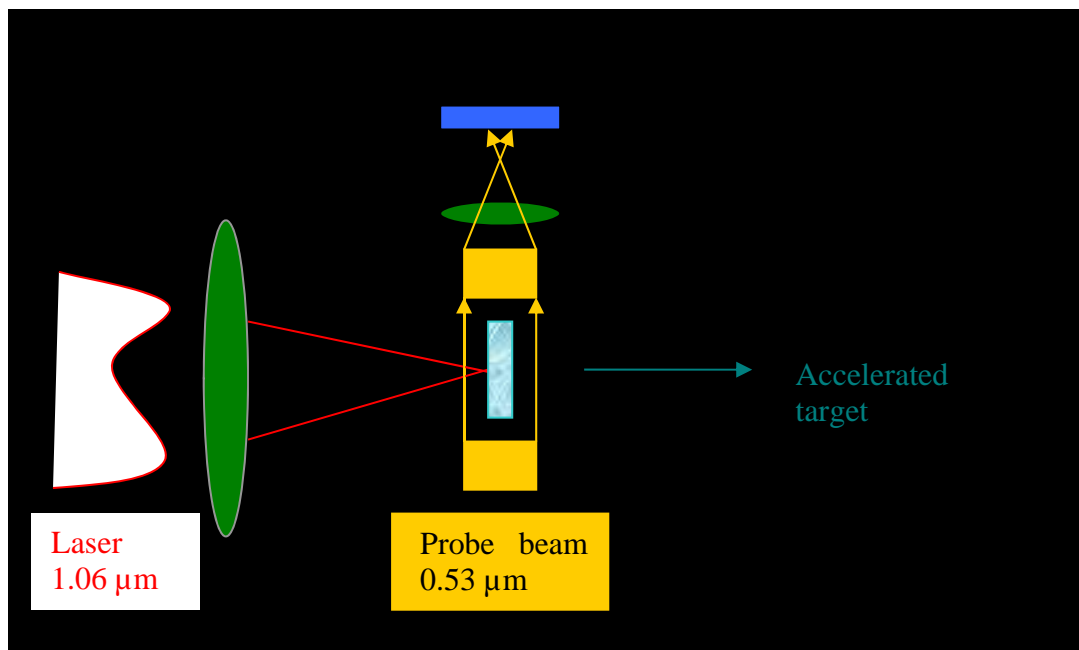


FIG. 2. Experimental setup showing the optical shadowgraphy technique using  $0.53 \mu\text{m}$  probe beam for recording the target front and accelerated target rear surface simultaneously.

### 3. RESULTS AND DISCUSSION

In this report we restrict our discussion to the analysis of the pure plastic and aluminium seeded targets. We simplify the behaviour of the micro-particle with the following assumption.

- Micro-particles are mechanical obstacles and they are relatively stationary and the plasma flows freely through the inter-particle spacing.
- Ionization of the micro-particles is negligible with the on-set of the instability.
- There is no particle to particle and particle to surrounding plasma interaction. Situation will be complex if we involve interaction of the particles and with surrounding plasma as they get ionized at the ablation surface and during the growth of the instabilities.

However, other processes like the following may appear simultaneously in the ablation surface.

- Plasma revolving around the particles may give rise to vortex formation and related process including generation of magnetic field.
- High density and low temperature plasma in the vicinity of the ablation surface may turn out to be Non-ideal.

Many unknown processes may appear during the growth of the instabilities and could be important. Of course, the process may be very complex if it involves interactions between the incident shock and the reflected rarefaction with the front/rear sides of the target. The problem of this transient phase in which the shock is travelling inside the target, followed by the reflected rarefaction is not yet solved even for the simpler case of uniform materials.

Shadowgrams shown in FIG. 3 a,b were recorded at 25 ns after the laser interaction with the target surface. Laser intensity on the target surface was about  $5 \times 10^{12} \text{ W/cm}^2$ . Motion of the target rear surface carries the information of the ablated target and it represents the

processing taking place at the ablation surface. Therefore, rear surface expanding structure is a signature of the instabilities existing at the ablation surface. FIG. 3a is the ablatively accelerated pure plastic target. FIG. 3b is aluminum seeded plastic target which shows a near uniform structure of the accelerated target and a small coronal plasma expansion as compared to pure plastic target under identical conditions. These images clearly show that seeded targets show a better stability of the accelerated target as compared to pure plastic target.

There could be several processes acting simultaneously at the ablation surface in space and time. This is a complex situation for the analysis. Some of these processes can be based on the effect of micro-particles, role of X rays, vortex formation, amplitude saturation due to wave breaking etc. Contribution from these individual processes occurring in time/space domain is difficult to point out. However, the final effect is observed as shown in FIG. 3. In this report we discuss the role of micro-particles at the ablation surface. In reality target behavior at the ablation surface and its vicinity is turbulent.

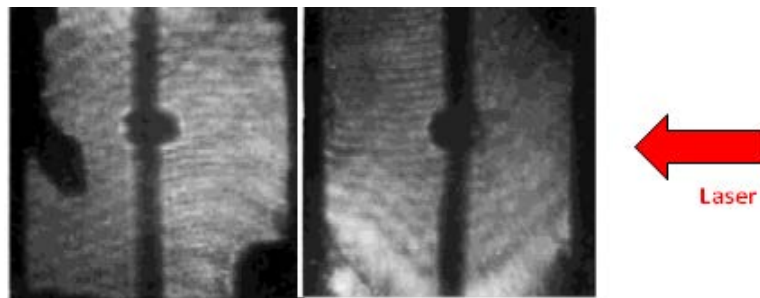


FIG. 3. a) Shadowgram of the ablatively accelerated pure plastic target  $\rho t \sim 18.0 \text{ g/cm}^2$ . b) Aluminum seeded plastic target;  $\rho t \sim 18.4 \text{ g/cm}^2$ .

We treat the presence of the aluminum particles as a mechanical obstacle. We assume particles are heavy and remain stationary during and after the interaction to all types of instabilities appearing at the ablation surface. Their ionization is neglected. Growth of the instabilities is limited due to the restriction imposed by the spacing set by the micro-particles.

By appropriate use of the micro-particles density ( $n$ ) we can approximately define the spacing between the two micro-particles in the target structure. We have performed numerical calculations to estimate the resultant amplitudes of the instabilities growing at different wavelengths for a given inter-particles spacing in the seeded targets. Here the particle dimension is not considered which will be important when we apply the motion of these micro-particles. We consider a plasma disc of 100 micron in diameter and introduce micro particles of  $1 \mu\text{m}$  at a distance of 5, 10 and  $20 \mu\text{m}$  which represent the inter-spacing of the micro-particles. We generate all the possible sinusoidal waves and estimate their resultant. The resultant profile of all these modes provides the amplitude of the instability in the fluid. Preliminary results show that the resultant amplitude of the instability is about  $3 \mu\text{m}$  when the inter-particle spacing is  $10 \mu\text{m}$  and lower for smaller micro-particle spacing. As the spacing increases to  $20 \mu\text{m}$ , amplitude is about  $3.5 \mu\text{m}$  and smoothing of the instabilities above this amplitude is difficult due to 2-d effects. Therefore we restrict our calculation to  $20 \mu\text{m}$  inter-particle spacing. Depending upon the material characteristics of the micro particles including diameter, density, electron configuration etc, we can estimate the particle density ( $n$ ) required for maintaining the spacing between micro-particles.

Gold and tungsten are good emitter of X rays as compared to aluminum and the present results show a good smoothing of the accelerated target with aluminum seeded targets also.

Hence the role of X radiation transport and the amount of X radiation needed for transport is to be understood. Although role of X radiation transport in increasing the distance between critical density layer and ablation layer resulting in enhancing the non-uniformity smoothing is known, its importance and impact are required to be understood in seeded targets.

In our experiments we cannot really differentiate whether instabilities were due to laser/target surface or due to plasma behavior at the ablation surface. What we see is, the accelerated rear target surface is smoothed in seeded plastic target as compared to pure plastic target. This implies seeded plastic target physics is certainly different than pure plastic target behavior.

We would like to emphasize that the behavior of seeded particles in the coronal region during laser interaction and up to the ablation region and, thereafter are still unclear to us. Above report is our effort in understanding one of the possibilities in restricting the growth of the instabilities. We need to perform the experiments by changing various parameters including laser intensity profile, micro-particle properties. This will help us in isolating the contribution from the individual processes mentioned above.

#### 4. CONCLUSION

Laser accelerated thin plastic and plastic target seeded with high z material particles of micron size were experimentally studied. “ $\rho t$ ” (target density x thickness) in all these targets were nearly constant for comparing the results. Optical shadowgraphy technique was adopted to record the accelerated target motion. Experimental results show that aluminum seeded target show a better target stability as compared to pure plastic target under identical conditions. In the present knowledge it is difficult to identify the exact process involved in smoothing the accelerated seeded-targets. However, we expect several processes to act in restricting the growth of the instabilities. It is also difficult to know the exact instability growing at the ablation surface and contributing to the breakup of the accelerated pure plastic target. We have tried to analyze the result due to presence of micro-particles as an obstacle and other possible processes mentioned in the articles need further experiments. When inter-particle spacing is  $\leq 10 \mu\text{m}$ , the resultant amplitude of the instability is  $\leq 3 \mu\text{m}$  which can be smoothed by 2D effects. Is it really particle act as only obstacle or there is more physics is to be investigated.

Aluminum is a poor emitter compared to gold and Tungsten and the present results show a good smoothing of the accelerated target with aluminum seeded targets also. Hence the role of X radiation transport and the amount of X radiation needed for transport is to be understood. The exact role of X radiation transport in increasing the distance between critical density layer and ablation layer and its impact are required to be understood in seeded targets.

#### REFERENCES

- [1] HiPER report; [www.hiper-laser.org](http://www.hiper-laser.org)
- [2] TABAK, M., et al., Ignition and high gain with ultrapowerful lasers, Phys. Plasmas, 1, No. 5, May (1994), 1626–34.
- [3] BETTI, R., et al., Shock Ignition of Thermonuclear Fuel with High Areal Density Phys. Rev. Lett. 98, (2007), 155001.

# SHORT PULSE KrF LASERS FOR INERTIAL FUSION

I.B. FÖLDES

Department of Plasma Physics, Association EURATOM HAS

KFKI Research Institute for Particle and Nuclear Physics of the Hungarian Academy of Sciences

Budapest, Hungary

## Abstract

Possible applications of KrF lasers for the fast ignition scheme of inertial fusion studies are investigated. Besides the theoretical proposal of a new scheme the Hungarian KrF laser system is upgraded to 80mJ / 600fs. Plasma mirror as a possible pulse cleaning method even for the KrF system was demonstrated together with VUV spectroscopic studies of the laser plasmas. Phase-amplitude imaging diagnostics was developed in collaboration. Polarization diagnostics of harmonics from solids generated by a few-cycle OPCPA laser system demonstrated that coherent wake emission harmonics mechanism generated only p-polarized harmonics for p-polarized lasers beams. Spectroscopic studies at the PALS experiments confirmed that jet-like structures occur only for high-Z materials with strong X ray emission.

## 1. INTRODUCTION

Inertial fusion energy production needs high repetition rate laser systems as drivers. The first ignition facility - a flashlamp-pumped solid-state laser system for single-shot operation - the NIF was set into operation in 2009. At present there are two alternatives for high repetition-rate operation. Besides the – at present - favored diode-pumped solid state lasers (DPSSL) KrF lasers represent an alternative as fusion drivers. Energetic, high-quality Krypton-Fluoride (KrF) excimer laser systems of nanosecond pulse durations have been built and successfully used for plasma heating with high-hopes for direct-drive laser fusion in the USA at the Naval Research Laboratory [1]. On the other hand, for the case of short pulse, i.e. femtosecond KrF lasers, the situation is different: In the field of this relatively underdeveloped technology, the weakly bound centers are in Europe, including Hungary.

The KrF laser system of the HILL laboratory in Szeged - where the joint researches of the Department of Plasma Physics of the KFKI Research Institute for Particle and Nuclear Physics of the Hungarian Academy of Sciences and the Department of Experimental Physics of the Szeged University are carried out - serves as a basis for the experimental work in Hungary. The laser system was upgraded during the present CRP and it delivers ~70 mJ energy of 600 fs duration on the 248 nm wavelength.

In the present report first we are going to summarize the work carried out in our laboratory. First the upgrading of the laser system is reported and the parameters like pulse duration, intensity, contrast etc. are summarized. The successes in the development of short pulse KrF systems encouraged us to give a possible scheme for fast ignition with KrF lasers which is summarized here shortly [2]. The ultimate method to clean laser pulses from pedestals has recently been carried out by plasma mirrors. We demonstrated plasma mirror effect for KrF systems the first time, and some possible methods for the applications are given [3]. Plasma properties are investigated from plasma threshold to the optimum of plasma mirror effect and then, up to the intensities where instabilities start to evolve.

Our collaborative activity consists of two parts. Our laboratory is a member of LASERLAB II, i.e. we summarize the experimental work hosted therein. A diagnostic system for B-field measurement in laser-produced plasma, namely the complex interferometry was developed by the researchers of the Technical University of Prague with the additional participation of an Italian student.

Finally, the last part of the present report contains the results of our activities in larger laser laboratories. We carried out soft X ray spectroscopy at the PALS laser in an experiment lead by Jan Badziak from Poland, then the results of the experiments with the LWS20 system of the MPQ Garching is summarized in which case high-harmonics from solid surfaces were first demonstrated by a sub-10 fs laser, and the polarization properties were investigated.

## 2. LASER PLASMA EXPERIMENTS IN THE HILL LABORATORY

### 2.1. Upgrading the laser system

Our original KrF laser system [4] delivered a laser pulse of  $\sim 600$  fs duration with a maximum energy of 15 mJ on the wavelength of 248 nm. The upgraded system has a new amplifier designated as “final amplifier” in FIG. 1. In this case there are only 2 passes in the first amplifier and again 2 passes in the final amplifier after spatial filtering. This arrangement allowed us to obtain 70mJ energy in  $620\pm 10$ fs pulses. The beam could be focused using a Janos Technology off-axis parabola mirror to a spot diameter of  $2.4\text{-}2.5\mu\text{m}$  with 42% of laser energy contained within this central spot. It corresponds to a maximum intensity of  $10^{18}$  W/cm<sup>2</sup>.

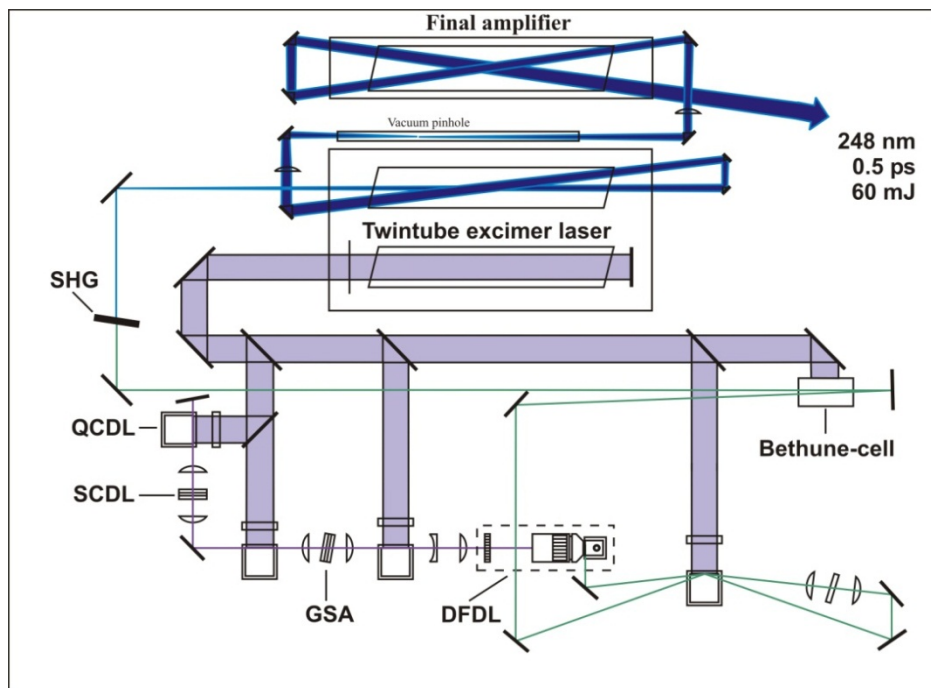


FIG. 1. The upgraded KrF laser system.

In the previously used system 3-pass off-axis direct amplification was used, therefore prepulses (pedestals) arose only from the amplified spontaneous emission (ASE) of  $\sim 15$ ns duration. Therefore the power contrast ( $P_{\text{pulse}}/P_{\text{ASE}}$ ) was  $\sim 3 \times 10^5$  even if the energy contrast ( $E_{\text{pulse}}/E_{\text{ASE}}$ ) was as low as 15. In case of tight-focusing by an off-axis parabola intensity contrast better than  $I_{\text{pulse}}/I_{\text{ASE}} = 10^{10}$  could be obtained because the ASE spot was of several  $100\mu\text{m}$  size. This corresponds to an ASE intensity below  $10^7$ W/cm<sup>2</sup>. It was shown however [5] that at this wavelength even such an ASE pulse may result in free ion generation through photoablation and photoionization. This must be kept in mind when performing ablation experiments, or surface studies for which case the beam is not tightly focused. Then the contrast corresponds only to that of the power contrast. According to the results of mass

spectroscopy [5] it is desirable to keep the prepulse level below  $2 \times 10^6 \text{W/cm}^2$ . The spatial filter of the upgraded system blocks the ASE radiation of directional properties different than that of the main beam, therefore the energy contrast is improved to  $>100$ . On the other hand the ASE transmitted through the pinhole is further amplified, resulting in a lower intensity contrast with  $\sim 10^8$ - $10^9 \text{W/cm}^2$  ASE intensity in the focal plane. It means that whereas at its present state the system can well be used for material studies which require larger spot sizes, in case of tight focusing further pulse cleaning methods are needed, especially for experiments that require very high intensity contrast (e.g. high harmonics from solid surfaces and isochoric heating of dense matter).

## 2.2. Plasma mirror effect with KrF lasers

One of the most efficient methods to remove prepulses is based on the self-induced plasma shuttering or plasma mirror technique. If the intensity of the laser pulse which falling onto a transparent solid material is chosen so that only the leading edge of the main ultrashort pulse is above the threshold for plasma production, the pedestal of lower intensity will be transmitted. The created plasma does not have sufficient time to expand during the rise time of the main laser pulse, therefore it interacts with an overdense plasma of a very steep density gradient. In this way a plasma mirror can improve the contrast with several orders of magnitude. Several successful experiments were carried out, cleaning the pulses of infrared titanium-sapphire and OPA laser systems by plasma mirrors [6,7].

We investigated plasma mirror effect for the 248 nm wavelength of our KrF system. In order to demonstrate high-reflectivity, s-polarized beam was used for the reflection experiments. The laser beam was focused by an F/10 lens onto an antireflexion-coated glass-plate with  $45^\circ$  and  $12.4^\circ$  angle of incidence. The target was moved by stepping motors shot-by-shot. The energy of both the incident and reflected beams were monitored by calibrated photodiodes. The laser energy was kept constant, the intensity was varied by shifting the lens relative to the target, which offered more than 4 orders of magnitude intensity range, from less than  $10^{12} \text{W/cm}^2$  up to above  $10^{16} \text{W/cm}^2$ . The first results were obtained for  $45^\circ$  angle of incidence in which case it was demonstrated the first time that plasma mirror effect really occurs for short KrF laser pulses, i.e. the reflectivity increases logarithmically above the plasma threshold at  $10^{12} \text{W/cm}^2$  and it saturates above  $10^{14} \text{W/cm}^2$  [3] with a maximum reflectivity of  $\sim 35\%$ . The situation improves for  $12.4^\circ$  angle of incidence in which case reflectivity of  $\sim 50\%$  was observed as shown in FIG. 2. Above the optimal intensity the reflectivity drops due to the nonlinear processes and the increased collisional absorption in the longer plasma. This behaviour is similar to earlier results with Ti-sapphire lasers [6] with the difference that the reflectivity – due to the shorter wavelength is less than the 70% therein.

Even in this case plasma mirrors can be applied for cleaning KrF laser pulses. The 50% losses may however be reduced if the plasma mirror is applied before the last amplifier. We can use the fact that KrF amplifiers work in saturation regime. Consequently, if one applies the plasma mirror before the final amplifier the output energy will not be significantly reduced, whereas ASE pedestal from the system before the final amplifier disappears. This ASE due to its linear amplification in a single stage off-axis amplifier does not give a significant contribution in the focus because - due to its larger divergence - it will remain practically unfocused in the focal plane. A further advantage of this setup can be utilized with the plasma mirror positioned to the focal plane. This not only relaxes the energy requirements but - due to the diffraction limited property of the KrF laser beam - the plasma mirror will not deteriorate the beam quality. There is no structure within the diffraction limited focal spot, and thus the plasma mirror acts as a secondary source of radiation operating as a spatial

filter [8]. Such a scheme is capable for cleaning the laser beam from the Fourier-components with higher spatial frequency, thus from the spatial inhomogeneities of the main pulse.

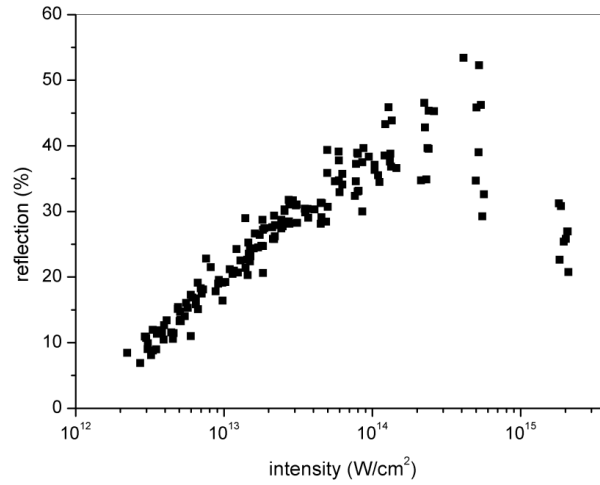


FIG. 2. Intensity dependence of the reflectivity for  $12.4^\circ$  angle of incidence.

### 2.3. VUV spectroscopy of LiF

VUV spectroscopy of LiF was carried out in the 10-40 nm spectral range. This spectral range corresponds to low-ionization states of these low-Z materials, therefore it is appropriate to follow plasma behaviour from plasma threshold to the intensities where plasma mirror effect is optimal, and then saturates due to the initiation of nonlinear processes (i.e. harmonics generation above  $10^{14}$  W/cm<sup>2</sup>). LiF plasmas contain two low-Z ion-components, therefore their investigations can be used as a test for calculations of multiple ion-components as well. This spectral range is also interesting for lithography because Li is a candidate as X ray source for lithography as well. VUV Experiments were carried out using a holographic toroidal grating (550 l/mm, Jobin-Yvon).

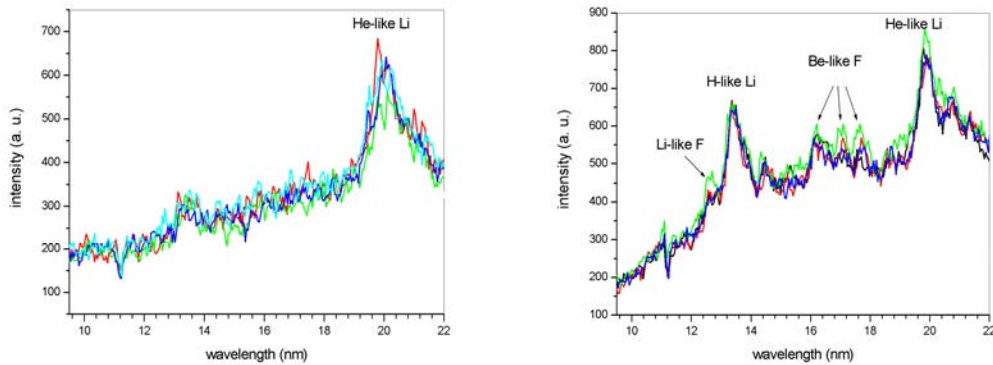


FIG. 3. LiF spectra for  $1.4 \times 10^{13}$  (left) and for  $10^{14}$  W/cm<sup>2</sup> (right).

Plasma generation starts somewhat below  $10^{13}$  W/cm<sup>2</sup> with the appearing He- $\alpha$  line of Li near 20nm. The first ionization potential of Li is 5.392 eV and according to the calculations of Yu. Ralchenko with the kinetic code for mixtures (NOMAD)[9], this corresponds to a temperature of  $\sim 5$ eV . At slightly higher intensity of  $1.4 \times 10^{13}$  W/cm<sup>2</sup> even the Ly- $\alpha$  line appears but still the He-like feature dominates, as seen in FIG. 3. The He- $\beta$  line at 17.8 nm is not seen in each shot, i.e. the density is approximately equal or more than  $10^{20}$  cm<sup>-3</sup> and the

temperature is less than 10eV. Ly- $\alpha$  starts to dominate for intensities above  $5 \times 10^{13} \text{W/cm}^2$ . For the case of the intensity optimal for the plasma mirror effect, i.e. for  $10^{14} \text{W/cm}^2$  – as seen in FIG. 3 – beside the strong Ly- $\alpha$  radiation Be-like F-lines appear between 16 and 18nm., and even the Li-like fluorine feature appears at 12.8nm. The Li-like F lines at 11.3 and at 12.8 nm start above 20eV plasma temperature according to the calculations.

The appearance of the Li Ly- $\beta$  line line refers to the same temperature, too. It must be noted that the spectral measurements were time-integrated, and therefore they have a strong continuum contribution, consequently it is difficult to compare them quantitatively with the calculations. However the appearance and dominance of the different spectral lines allow us to give a good estimation to the maximal plasma temperature, thus we could follow temperature increase with increasing intensities to the optimal intensity for the plasma mirror effect for which case a temperature of 20eV can be estimated[3].

#### **2.4. Fast ignition scheme with KrF laser**

Clearly, the excellent beam quality and the short wavelength of KrF excimer lasers make them good candidates for IFE driver. Due to their short wavelength these lasers could also act as fast ignitors, since they can penetrate into the plasma of a significantly higher density, compared to infrared lasers. If one wants to avoid the use of cones for fast ignitors, short wavelength and thus KrF radiation seems to be the real alternative. Based on a recent proposal which suggested the use of the same KrF amplifiers for driver and ignitor we considered its possibilities for the planned NRL KrF test facility [1] using 0.5MJ driver laser energy. Taking into account the properties of KrF e-beam pumped amplifiers it was shown that a 30% increase of the pump duration is sufficient to reach the required 50kJ energy for the fast ignitor. In contrast to the traditional single-beam fast ignitor a new, multiple-beam scheme was suggested utilizing the special amplification properties of KrF lasers. It consists of hundreds of KrF pulses of ps duration each focused separately onto the fusion pellet. Since the extractable energy from a KrF amplifier is independent of the pulse duration below  $\sim 100\text{ps}$ , the shortest practical pulse duration of  $\sim 1\text{ps}$  is targeted. The energy of the individual beams is chosen so that  $1.8 \times 10^{20} \text{W/cm}^2$  focused intensity for electron acceleration up to 1MeV can be obtained practically by single-beam amplification. This approach reduces the requirements of beam demultiplexing which is the greatest difficulty associated with the usual single-beam (20ps) fast ignitor schemes[2]. A more detailed analysis of this scheme is to be given at the 5th Technical Meeting "Physics and Technology of Inertial Fusion Energy Targets and Chambers".

### **3. COLLABORATIVE ACTIVITY IN HUNGARY, COMPLEX INTERFEROMETRY**

One of the possible explanations of our previous high-harmonics observations, i.e. that they appear either with p- or s-polarized radiation in case of a 600 fs KrF laser beam was that strong self-generated magnetic fields arise even for nonrelativistic intensities. In a collaboration with the Czech Technical University, M. Kálal and M. Martinková started to apply the – by them developed - simultaneous interferometric + polarimetric diagnostics, the phase-amplitude imaging to our system[10]. The 496nm green beam of our dye laser system was used for diagnostics which was separated from the amplified beam with a dichroic mirror, therefore the temporal synchronization of the 2 beams can be set by aligning the path lengths. In a first experimental series interferometric studies of laser-produced plasmas were carried out with an increased international collaboration, with the participation of one more student from the University of Milano Bicocca. Time dependent interferograms were taken from laser

sparks in air and from laser plasmas on glassy carbon rod targets. FIG. 4 illustrates the experimental setup in which the wavefront division is carried out by a Fresnel biprism. Note that in case of measuring the B-field in the plasma the target is situated between two crossed polarizers, in which case only the – by Faraday effect – rotated electric field component will give contribution to the fringe-structure. From the contrast and intensity distribution of the fringes even the B-field can be derived [10].

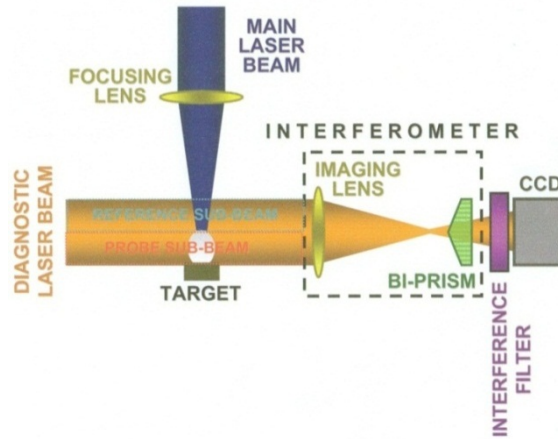


FIG. 4. Experimental arrangement for complex interferometry.

An interferogram of the laser spark and the - from there - derived density distribution can be seen in FIG. 5. The density distribution clearly resolves the hollow density distribution corresponding to the self-focusing of the beam.

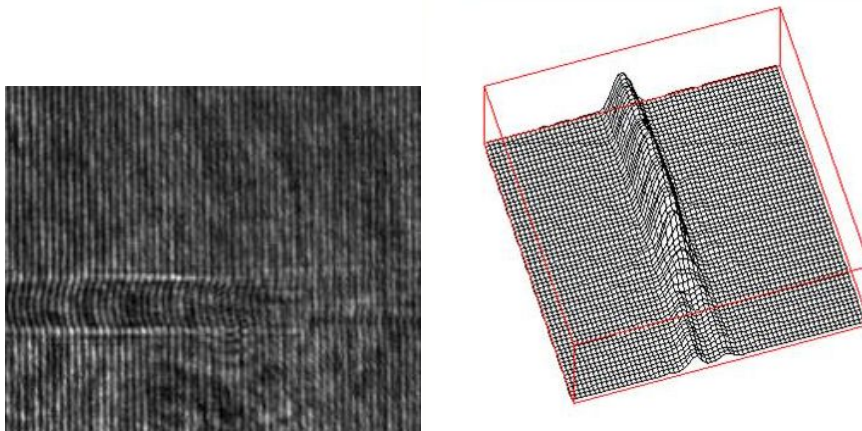


FIG. 5. Interferogram and density distribution of laser spark in air.

After the successful tests in laser sparks experiments were carried out from laser plasmas in solid targets. For these experiments glassy carbon rods (Sigradur) of 0.5 mm diameter were used. FIG. 6 illustrates the resolution of the interferometer for this case. In the following (in the next joint experiments) time dependence of the plasma density will be measured ( $\sim 1$ ps accuracy can be obtained) and then B-field measurements will be carried out for  $10^{16}$  W/cm<sup>2</sup> intensity.

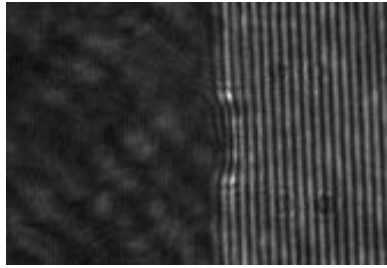


FIG. 6. Interferogram of laser plasma on 0.5mm carbon rod.

#### 4. COLLABORATIVE ACTIVITY OUTSIDE HUNGARY

##### 4.1. Soft X ray spectroscopy at the PALS laser

The experimental series was lead by J. Badziak and T. Pisarczyk of the IFPILM, Warsaw and it was carried out in the PALS Research Centre in Prague. Investigations were carried out on Cu- and Br-doped plastic targets in the intensity range of  $10^{14} - 3 \times 10^{15} \text{W/cm}^2$  of the 250ps, 0.44 $\mu\text{m}$  beam of the PALS laser. Plasma radiation was followed by soft X ray and hard X ray filtered diodes. The contribution of our group was the soft X ray spectrometer for the Cu L-band which was a 10000 l/mm  $\text{SiN}_x$  transmission grating combined with a slit together with a CMOS, and later – as the CMOS detectors were too sensitive to the electromagnetic noise - with BIOMAX film-detector. This type of transmission grating is relatively new. A typical spectrum of Br-doped plastic is shown in FIG. 7 in which an Al filter was used against soft radiation. In contrast to the Au transmission gratings where higher diffraction orders were suppressed,  $\text{SiN}_x$  gratings show strong higher order contributions, especially a strong second order, but the 3rd order is not negligible either and even the 4th order can be seen. A qualitative comparison of our spectroscopic data was however in good agreement with the parallel X ray diode results.

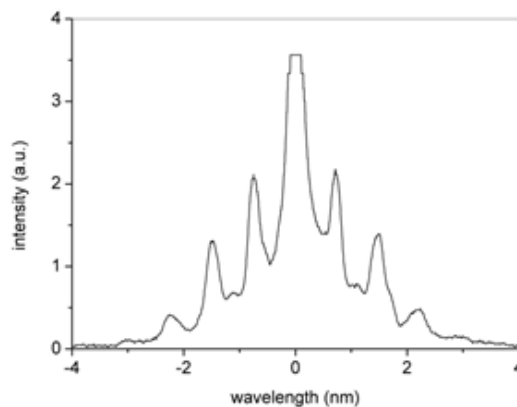


FIG. 7. Br spectra show strong higher order contribution from the transmission grating.

One of the main finding of the experiments was the observation of a highly collimated heavy ion jet for plastic targets doped by high-Z (Cu and Ta) impurities. Ion current up to 100 A and ion current density of  $1 \text{ A/cm}^2$  at 1 m from the target was obtained with an energy conversion efficiency of  $\sim 10\%$  [11]. FIG. 8 illustrates the ion charge density for differently doped targets. In the case of low-Z, i.e. Al-doped plastic no jets could be observed, in the case of higher Z, namely for Cu a featured jet was observed, accompanied by stronger X ray

emission. The annular structure of the laser beam and radiation cooling is the probable mechanism producing the heavy ion jet.

In a parallel experiment[12] thin foil acceleration was investigated, using differently doped thin (10 or 20  $\mu\text{m}$ ) plastic foils, illuminated by 120 J, 0.44  $\mu\text{m}$ , 0.3 ns laser pulse of intensity up to  $10^{15}$  W/cm<sup>2</sup>. The laser-accelerated foil, the so-called “macroparticle” collided with a massive Al target, producing a crater, the volume of which was a measure of the kinetic energy. A high-Z dopant to the plastic foil causes an increase in the ablating plasma density, velocity, and collimation which, in turn, results in a remarkably higher kinetic energy and energy fluence of the flyer foil.

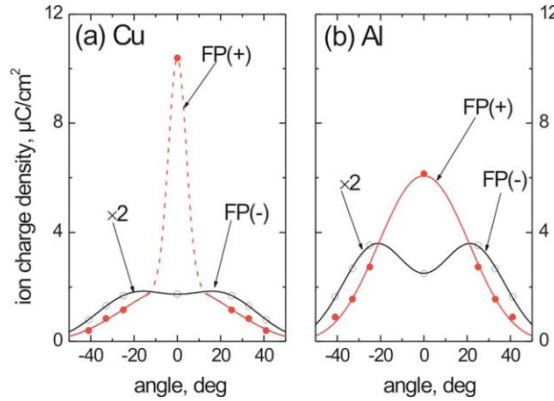


FIG. 8. Angular distributions of ion charge density for ions of velocities in the range of  $0.2\text{--}2\times 10^8$  cm/s.  $E_L=69\pm 2$ J.

FIG. 9 illustrates the results for Br-doped and undoped CH targets. In the case of CH(Br) targets the angular distribution of ion emission was narrower than for the CH targets and the maximum ion emission was usually recorded along the target normal, as opposed to the undoped target for which a distinct maximum was always off the target normal. Significant differences were also observed in the X ray emissions from the two kinds of targets used in the experiment (FIG. 9b.). Note that the X ray data in FIG. 9b is from the X ray diode measurements in agreement with our spectroscopic data from FIG. 7. The additional accelerating mechanism is probably the radiative heat conduction for high-Z dopants which cause stronger ablation and therefore higher acceleration of the foil.

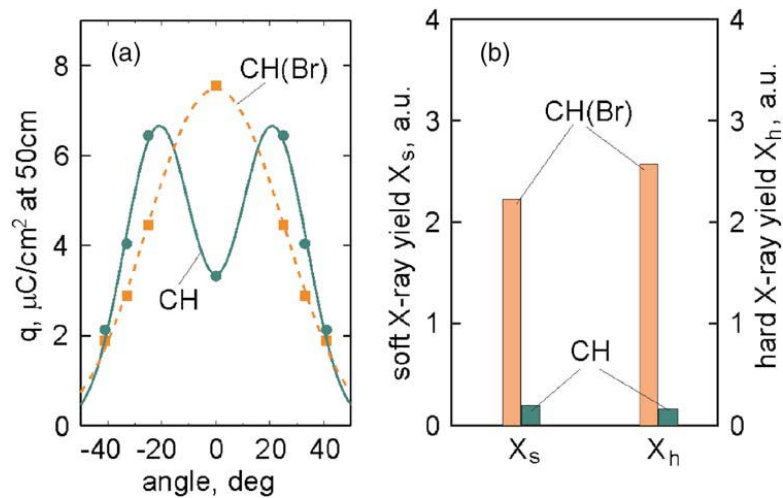


FIG. 9. a) Angular distributions of the charge density of ions of velocities in the range  $0.2\text{--}2\times 10^8$  cm/s for 20 $\mu\text{m}$  thick CH and CH(Br) targets. b) Soft and hard X ray yield for CH and CH(Br)20 targets.  $E_L=120$  J,  $I_L=5\times 10^{14}$  W/cm<sup>2</sup>.

## 4.2. High harmonics generation with a sub 10fs laser on solid surfaces

Our group could participate in the MPQ, Garching in an experiment in which high-harmonics from solid surfaces were generated with the LWS10 and the LWS20 laser systems. This was the first time high-harmonics were generated from solid surfaces with a few-cycle (<10fs) laser pulse. The experiments were led by G.D. Tsakiris, L. Veisz, R. Hörlein, P. Heissler and colleagues in the group of F. Krausz.

The task of our group was the investigation of polarization dependence of harmonics. The laser is based on the OPCPA technique and it provides laser pulses of 8 fs duration up to  $10^{19}$  W/cm<sup>2</sup> focused laser intensities ( $a_L \approx 1.5$ ). The p-polarized beam was focused onto fused silica plates with 45° angle of incidence. The generated harmonic radiation in the specular direction was recorded using a grazing-incidence imaging XUV spectrometer. High harmonics were observed up to  $20\omega$ , where a distinct cutoff was observed, corresponding to the highest harmonic that the plasma density can sustain, thus the responsible mechanism was coherent wake emission (CWE)[13] as expected e.g. from particle in cell (PIC) simulations. Two distinct characteristics in the spectra are noticeable. The individual harmonics are broadened compared to those from a longer pulse and exhibit from shot-to-shot a significant and strongly irreproducible substructure. In contrast, spectra taken with chirped pulses of >20 fs duration reproducibly consist of single peaked harmonics as one would expect from many-cycle pulses. This is unequivocal proof that the structure observed with 3-cycle pulses is due to the shortness of the laser pulse. The shot-to-shot variable substructure is attributed to the carrier-envelope phase variation of the laser pulse [14].

The polarization dependence of harmonics is on the one hand the dependence on the polarization of the incoming beam, and on the other hand the investigation of polarization of the generated harmonics. Polarization properties are important not only as a characteristic of the generating mechanism, but actually it can also be used for polarization gating and thus for the generation of single attosecond pulses [15]. Most of the harmonics experiments rely solely on a linearly polarized laser beam and rotating its angle. In the present experiment it was possible to investigate the dependence on the ellipticity of a circularly polarized beam. This can give new insight into the CWE mechanism. Although polarization gating is considered for the relativistic oscillating mirror mechanism only [15] for higher intensities, it was our interest to investigate its actual applicability for the CWE mechanism. The compressor of the LWS laser systems consists of chirped mirrors and a bulk glass, therefore it does not change the incoming polarization. Therefore broad-band achromatic  $\lambda/2$  and  $\lambda/4$  plates could be used in the uncompressed laser beam. For the analysis of the polarization of harmonics a three-mirror polarization analyser was built consisting of 20 mm diameter gold-coated mirrors [16]. The system makes use of the fact that a plain surface reflects s-polarized light with a higher efficiency than it does for p-polarized radiation. Depending on the orientation of the system relative to the target, the mirrors prefer the reflection of one polarization state over the other by more than an order of magnitude in the 90-130nm spectral range.

FIG. 10 shows the results for 50mJ/8fs laser pulses. When changing the direction of the linear polarization of the beam it is seen in fig 10a that the harmonics intensity drops faster than the near linear intensity dependence expected from the PIC simulations [13] which is shown as the grey-shaded area. The decrease of intensity is still steeper than the expectations when increasing ellipticity (FIG. 10b), but it is not so steep than in the case of FIG. 10a. This leaves open the possibility for polarization gating even for the CWE mechanism.

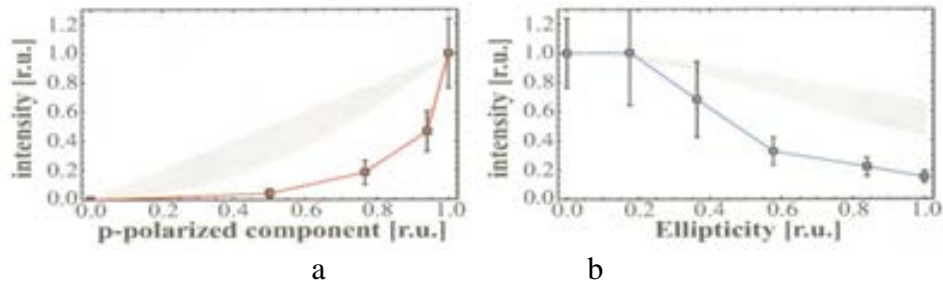


FIG. 10. Dependence of XUV intensity between  $11\omega$  and  $14\omega$  as a function of varying laser polarization for (a) the transition from  $s$  to  $p$  and (b) linear to circular.

Finally the polarization analyzer was successfully tested as shown in FIG. 11. Nice harmonics spectrum was obtained for  $p$ -polarized radiation, whereas no harmonics were observed for  $s$ -polarized incoming beam, and no  $s$ -polarized harmonics were observed in either case within the accuracy of  $\sim$  one order of magnitude suppression. This observation is in full agreement with the theoretical expectations.

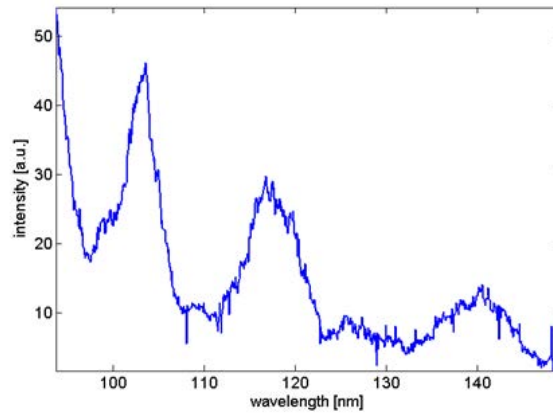


FIG. 11.  $P$ -polarized harmonics spectrum for 80mJ/8fs laser.

## REFERENCES

- [1] OBENSCHAIN, S. P., et al., Phys. Plasmas 13, 056320 (2006).
- [2] FÖLDES, I.B., SZATMÁRI, S., Laser and Particle Beams, 26, 575 (2008).
- [3] FÖLDES, I.B., et al., Radiation Effects and Defects in Solids, 165, 429 (2010).
- [4] SZATMARI, S., Appl. Phys. B 58, 211 (1994).
- [5] FÖLDES, I.B., et al., Laser Physics., 10, 264 (2000).
- [6] ZIENER, Ch., et al., J. Appl. Phys., 93, 768-770 (2003).
- [7] DOUMY, G., et al., Phys. Rev. E, 69, 026402 (2004).
- [8] FÖLDES, I.B., et al., Journal of Physics: Conf. Ser. 244, 032004 (2010).
- [9] RALCHENKO, Yu.V., and Maron, Y., J. Quant. Spectr. Rad. Transfer 71, 609 (2001).
- [10] KALAL M., et al., Applied Optics 26, 1674 (1987).
- [11] BADZIAK, J., et al., Appl. Phys. Lett. 91, 081502 (2007).
- [12] BADZIAK, J., et al., Appl. Phys. Lett. 92, 211502 (2008).
- [13] QUERE, F., et al., Phys. Rev. Lett. 96, 125004 (2006).
- [14] HEISSLER, P., et al.; Appl. Phys. B 101, 511-521 (2010).
- [15] RYKOVANOV, S., et al.; New J. Phys., 10, 025025 (2008).
- [16] VERES, G., et al.; Europhys. Lett. 48, 390 (1999).

# TRANSVERSE DIAGNOSTICS OF INTENSE, FOCUSED HEAVY ION BEAMS

D.H.H. HOFFMANN\*, F. BECKER\*\*, P. FORCK\*\*

\* TU Darmstadt, Germany

\*\* GSI, Darmstadt, Germany

## Abstract

During this CRP project we developed non-intercepting instruments and methods to measure the transverse intensity distribution of energetic heavy ion beams at a focal plane, based on gas fluorescence monitors and pick-up probes. The aim of this project was the development of novel non-intercepting instruments and methods to measure the transverse intensity distribution of energetic heavy ion beams at a focal plane. These instruments and methods are essential for small-emittance high-intensity heavy ion beam handling at high energy accelerators and transport lines for inertial fusion drivers. Precision transverse beam diagnostics at the focal spot is a very important aspect of the high-energy-density physics experiments which are being performed at GSI to investigate intense heavy ion beams as inertial fusion drivers. During the project period, we performed theoretical and experimental work in two different directions: Gas fluorescence monitors: investigations on beam-induced fluorescence of different gases (Ar, Xe, He and N<sub>2</sub>) in the pressure range from 10<sup>-4</sup> to 10<sup>-3</sup> mbar with spatial, temporal and spectral resolution. High-order pickup probes: development of high-resolution electric and magnetic pickup probes to measure quadrupole and high-order geometric moments of the beam intensity distribution.

## 1. INTRODUCTION

Beam induced fluorescence spectra in the range of 300-800 nm were investigated with an imaging spectrograph. Wavelength-selective beam profiles were obtained for a 5.16 MeV/u sulphur beam in nitrogen, xenon, krypton, argon and helium at 10–3 mbar gas pressure. In this paper calibrated BIF spectra of specific gas transitions were identified and corresponding beam profiles presented. The measurement results are discussed for typical applications at the present setup and the future FAIR facility.

As conventional intercepting diagnostics will not withstand high intensity ion beams, Beam Induced Fluorescence (BIF) profile monitors constitute a preeminent alternative for online profile measurements [1]. At present, two BIF monitors are installed at the GSI UNILAC and several locations are planned for the FAIR high energy beam transport lines [2]. For further optimizations accuracy issues like gas dynamics have to be investigated systematically.

Especially the determination of focused beams in front of targets with high line charge densities rely on a careful selection of proper working gas transitions to keep profile distortions as low as possible [3].

## 2. EXPERIMENTAL SETUP

Key issue of this experimental layout using an imaging spectrograph with an area scan intensified CCD (ICCD) camera (FIG. 1) was to have both, the spectral information of specific beam induced gas transitions along the diffraction axis and the spatial information about the beam profile width, transition wise along the imaging axis, see FIG. 2. For 150 mm object distance, a chromatically corrected UV lens of f=50mm and f/2.8 was chosen. A CCD height of 4.9 mm and a total reproduction scale  $\beta_{tot}=0.42$  yield a 19.5 mm field of view.

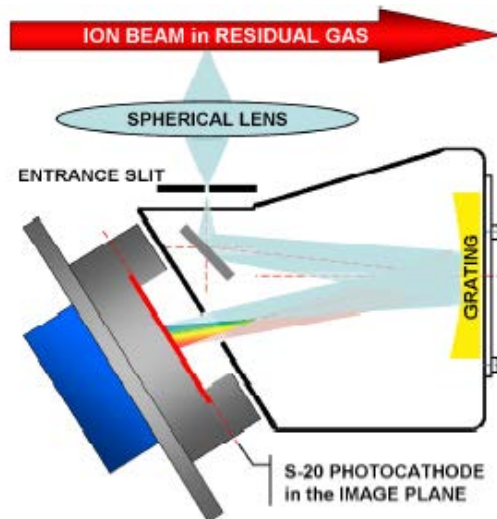


FIG. 1. Top-view of the optical path in the diffractive plane. Length of spectrum in the image plane is 10 mm. 1:1 imaging from slit to image plane. All refractive optics adapted to UV-VIS [5]. ICCD performs single photon detection and has a  $\varnothing$  25 mm UV-enhanced photocathode with a V-stack MCP [6] and digital VGA camera in bluish color [7].

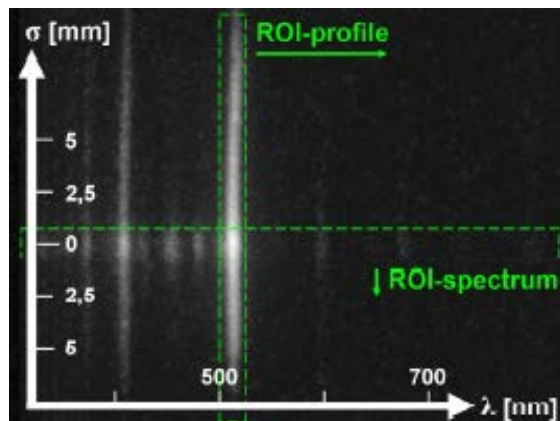


FIG. 2 Spectrographic average image  $n=2000$  of  $3\text{-}^{101}\text{IS}6^+$  ions @ MeV/u in  $10^{-3}$  mbar helium gas,  $\sigma_w=1.8\text{mm}$ . Logarithmic gray-scale for better presentation.

The  $\varnothing$  70 mm spherical mirror with 140 mm focal length is holographically etched and astigmatism corrected. 140 sinusoidal grooves per mm produce a spectral dispersion of 50 nm/mm and an image field of  $8 \times 12$  mm on the vertical imaging axis and the horizontal dispersive axis, respectively. With an optical resolution of 33 lp/mm the ICCD limits the spectral resolution to 1.5 nm for an entrance slit  $\leq 30 \mu\text{m}$ . The total spectral system efficiency includes all single component efficiencies as a convolution, see FIG. 3 (upper plot). Most limiting factors in the wavelength range  $\geq 600$  nm are the tri-alkali ( $\text{Na}_2\text{KSb}$ )Cs photocathode and the decreasing grating efficiency. Investigation of optical gas spectra relays on a sufficient purity of the actual gas species. In order to measure and control impurities, a residual gas analyser (RGA) 'quadrupole mass spectrometer'- type was used [8].

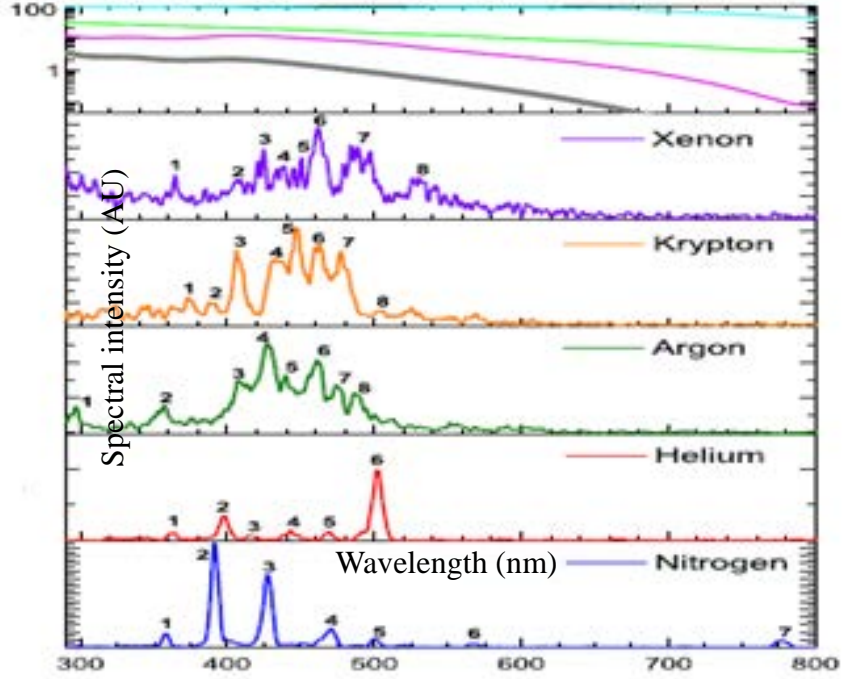


FIG. 1: Optical Beam Induced Fluorescence spectra of  $3 \cdot 10^{11}$   $S6^+$  ions @ 5.16 MeV/u in  $10^{-3}$  mbar residual gases (Xe, Kr, Ar, He, N<sub>2</sub>). Most prominent transitions are indicated and described in Table 1. Spectral efficiencies (upper plot) in descending order: lens (blue), grating (green), photocathode (magenta) and total (gray).

Base pressure of the unbaked vacuum system was  $10^{-7}$  mbar, with the typical fingerprint of hydrogen, water, nitrogen and traces of the previously introduced rare gas species like krypton in an argon atmosphere. Although the gas leak system was flushed carefully after each gas exchange, a significant source of residuals was the pressure reducing regulator. In order to keep relative impurities below 5 %, the working pressure for all experiments had to be set to  $10^{-3}$  mbar N<sub>2</sub>-equivalent. For set pressures, a gas leak system controls a motorized needle valve so that gas flow rate versus the pump rate allows a dynamic equilibrium. To overcome gas specific variations, the ion gauge (5 % reproducibility) was cross-calibrated to a linear temperature corrected capacitance gauge (0.2 % accuracy), so that the relative error in gas pressure  $p_{eff}$  was  $\leq 6$  %.

### 3. DATA ANALYSIS – RESULTS

All optical spectra were recorded during 2000 beam pulses for unchanged accelerator settings. Each single image was recorded as 8-bit bitmap, with the ICCD in photon counting mode. To maintain the dynamic range, the average images were 32-bit float tiffs, see FIG. 2. Further resolution improvement by a factor of  $\sim 4$  was achieved with a cognitive algorithm that determined barycenters of single photon spots and added them as single counts to the VGA-sized matrix [9]. To discriminate spectral peaks against spiky shot noise, Savitzky-Golay fits were applied. Regions of interest (ROI) were chosen like 10 pixel or  $40 \mu\text{m}$  at the beam center for the BIF-spectra in FIG. 3 and like 20 pixel or  $16 \text{ nm}$  for the transitions specific profile plots in FIG. 4 (mid & bottom).

TABLE 1. RESIDUAL GASES (BLOCK-WISE), OBSERVED CHARGE STATES, OBSERVED INTEGRAL INTENSITY I, I<sub>gas</sub> NORMALIZED TO PEFF AND I<sub>gas&Z</sub> NORMALIZED TO PEFF AND THE E--DENSITY (UPPER BLOCK LINE)

gas species	charge state	$\sum I; I_{gas}; I_{gas\&Z} [\%]$
No.) central-wavelength [nm], relative intensity [%]		
<b>Xenon</b>	Xe <sup>+</sup> /Xe	41; 86; 22
1) 363, 4; 2)* 407, 4; 3)* 424, 6; 4)* 438, 5 5) 450, 2; 6)* 462, 12; 7)* 484, 16; 8)* 530, 5		
<b>Krypton</b>	Kr <sup>+</sup> /Kr	45; 63; 25
1) 373, 4; 2)* 388, 3; 3) 407, 10; 4)* 434, 14 5) 447, 12; 6)* 463, 12; 7)* 477, 13; 8)* 505, 2		
<b>Argon</b>	Ar <sup>+</sup>	50; 38; 30
1) 297, 3; 2)* 357, 5; 3)* 407, 11; 4) 427, 19 5)* 440, 8; 6)* 461, 15; 7)* 474, 8; 8)* 487, 7		
<b>Helium</b>	He	21; 4; 26
1) 364, 4; 2) 398, 16; 3)* 415, 3; 4)* 443, 7 5)* 470, 5; 6) 502, 48		
<b>Nitrogen</b>	N <sub>2</sub> <sup>+</sup> /N <sup>+</sup>	100; 100; 100
1) 358, 4; 2)* 391, 45; 3)* 428, 29; 4)* 470, 9 5) 501, 3; 6) 560, 1; 7)* 776, 3		

Corresponding transitions as indicated in FIG. 3, central wavelength and relative intensity with respect to the integral intensity (lower block line). Peaks indicated with No.)\* are superposition of several transition lines.

### 3.1. BIF-Spectra

All spectra were first calibrated to a Hg-Ar-standard and then refined step by step with known transitions of the recorded BIF-spectra. The accuracy for central wavelength is  $\leq 1$  nm. The investigation was performed with 5 ms long beam pulses of 3·10<sup>11</sup> S6+ ions at 5.16 MeV/u, focused to a  $\sigma_w$  of 1.8 mm. Obtained BIF spectra are depicted in FIG. 3. They were not normalized to the spectral efficiency of the optical components, which is therefore given in FIG. 3 as well. In Table 1, the observed charge states, relative integral intensities and most prominent transitions are listed. Different signal-to-noise ratios for the gas species are determined by the observed integral intensity I. Beside nitrogen and helium, where spectral lines of optical transitions are separated, lines appear less intense and clustered in groups. Although nitrogen shows the brightest transitions, gases like xenon and krypton show similar integral intensities I<sub>gas</sub>, normalized with respect to peff. To account for the electronic stopping power, integral intensities I<sub>gas&Z</sub> have been furthermore normalized to the electron density  $\propto Z$ . This way, all rare gases show similar relative integral intensities, except for nitrogen having a four times higher integral intensity value. When the ROI was moved from the center to the beam fringes, spectral intensity decreased homogeneously for all gases unlike helium which showed an unequal decrease for different transitions. For proton beams as well as for much heavier Ta beams, similar results were obtained. A more detailed description can be found in [10].

### 3.2. Transition Dependent Profile Data

The spectrally resolved profile plots are presented in FIG. 4. In the upper plot, all gas-species show corresponding profile width, besides helium that shows a factor 2.5 larger  $\sigma_w$ . Transition-wise profile data is shown in FIG. 4 for N<sub>2</sub> (middle) and He (bottom). In the case of nitrogen, the transitions 1), 5) and 6) show a slightly increased profile width that can be explained by an upscaling of noise in the profile fringes due to the normalization to a common maximum.

He-profile contributions by 1) and 6) show significant shoulders but 2) and 3) do not. Since both He-cases contain weak and strong contributions, noise scaling effects do not explain these results. Assuming excited states of He 1), 2) might have large cross-sections for electron excitation, an 8 mm halo is reasonable, as the mean free path of secondary electrons is in the order of 10 mm, for  $p_{eff}=4 \cdot 10^{-3}$  mbar.

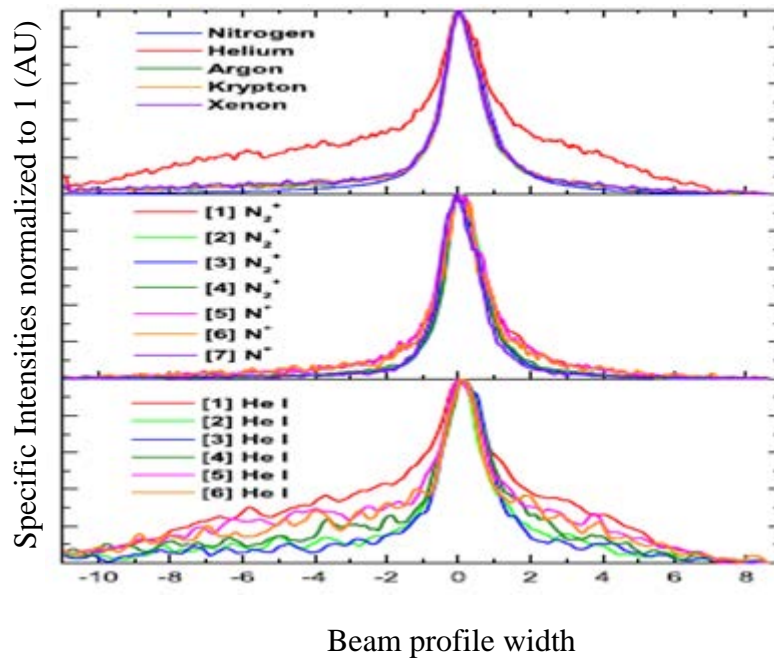


FIG. 4. Gas specific beam profiles (upper plot) and transition specific beam profiles for nitrogen (middle) and helium (bottom) as indicated in FIG. 3.

## 4. CONCLUSION

As first experimental outcome, optical spectra of nitrogen, xenon, krypton, argon and helium have been successfully recorded. They excellently agree with measurements at lower energies  $\leq 10$  MeV/u in the case of nitrogen [11, 12] and higher energies in the range of 50 MeV/u to 25 GeV/u for nitrogen and xenon [13]. Nitrogen seems to be the most appropriate residual gas, because of its spectral concentration between 390 and 430 nm. In addition, nitrogen shows the highest integral intensities. Especially the four times higher  $I_{gas\&Z}$  makes it the right choice, if the stopping power is an issue. For electric fields in the order of 10 kV/mm the trajectories of excited, charged molecules like N<sub>2</sub><sup>+</sup>, will be influenced by the beam's space charge and might falsify the profile reading [14]. Therefore one might focus on different selection criteria as larger molecule masses and shorter transition-lifetimes, provided by rare gases like Xe and Kr. Helium is no alternative due to its wrong profile image in the

considered pressure range. However, for most beam parameters N<sub>2</sub> is the optimal choice because of its high light yield. Moreover it was shown that all nitrogen profiles show the same profile width. Once a residual gas is selected, optical components can be further optimized.

## REFERENCES

- [1] FORCK, P., et al., DIPAC'05, ITTA01, p. 223-227 , 2005.
- [2] SCHWICKERT, M., et al., DIPAC'09 WEOA04, 2009 & FAIR Baseline Technical Report, Vol. 2, p. 148-162 , 2006.
- [3] BECKER, F., et al., DIPAC'07, MOO3A02, p. 33-36 , 2007.
- [4] www.horiba.com, CP140-202 140mm Imaging Spectrograph.
- [5] www.linos.com, inspec.x 2.8/50 UV-VIS apochromatically corrected lens system.
- [6] www.proxitronic.de, BV 2581 QY-V 100N.
- [7] www.baslerweb.com, Type 311-f VGA Sony ICX414AL Sensor.
- [8] www.pfeiffer-vacuum.de, Gauge PKR-261, Valve EVR-116, Controller RVC-300, Calibration-Gauge CMR-264, RGA PrismaPlus.
- [9] software: <http://rsbweb.nih.gov/ij/>, Img. proc.
- [10] BECKER, F., "Non-destructive Beam Profile Measurement of high intense HI-Beams", PhD-thesis, Darmstadt, 2009.
- [11] HUGHES, R.H., et al., Phys. Rev., 123, 2084 (1961)
- [12] LEE, C. S. et al., "Study of N<sub>2</sub> first negative system" Nucl. Instrum. Meth. B 140, p. 273-280, 1998.
- [13] PLUM, M. A., et al., "N<sub>2</sub> and Xe gas scintillation @ Cern PS and Booster", Nucl. Instrum. Meth. A 492, p. 74-91, 2002.
- [14] BECKER, F., et al., BIW'08, California, TUPTPF054, 2008.

# HIGH POWER LASER BASED INERTIAL FUSION ENERGY RESEARCH COORDINATED IN ASSOCIATED LABORATORIES

M. KALAL<sup>\*</sup>, S. YU.GUS'KOV<sup>++</sup>, A. KASPERCZUK<sup>+</sup>, D. KLIR<sup>\*</sup>, E. KROUSKY<sup>\*\*</sup>, J. LIMPOUCH<sup>\*</sup>,  
M. MARTINKOVA<sup>\*</sup>, M. PFEIFER<sup>\*\*</sup>, T. PISARCZYK<sup>+</sup>, Y.J. RHEE<sup>+++</sup>, K. ROHLENA<sup>\*\*</sup>,  
N. RUDRAIAH<sup>§</sup>, J. SKALA<sup>\*</sup>, O. SLEZAK<sup>\*</sup>, J. ULLSCHMIED<sup>\*\*\*</sup>

<sup>\*</sup> Czech Technical University in Prague, Brehova 7, 115 19 Prague 1, Czech Republic

<sup>\*\*</sup> Institute of Physics of the AS CR, Na Slovance 2, 182 21 Prague 8, Czech Republic

<sup>\*\*\*</sup> Institute of Plasma Physics of the AS CR, Za Slovankou 3, 182 21 Prague 8, Czech Republic

<sup>+</sup> Institute of Plasma Physics and Laser Microfusion, Hery 23 St., 00-908 Warsaw 49, P.O.Box 49, Poland

<sup>++</sup> P.N.Lebedev Physical Institute of RAS, Leninski Avenue 53, 119991 Moscow, Russian Federation

<sup>+++</sup> Korea Atomic Energy Research Institute, P.O.Box 105 Yuseong, Daejeon 305-600, Republic of Korea

<sup>§</sup> UGC-Centre for Advanced Studies in Fluid Mechanics, Bangalore University, Bangalore - 560 001, India

## Abstract

This report contains inertial fusion energy (IFE) related research carried out under CRP project in cooperation by our multi-national group of scientists using their respective facilities. Major emphasis in this final period of our research contract went into continuation of studies of laser produced plasma jets from the point of their optimization and better understanding of mechanisms responsible for their generation. Studies were undertaken in order to apply the complex interferometry technique for optimization of fusion neutrons production from Coulomb explosions of deuterium clusters. Continuation of our former research was performed in the field of self-navigation of laser drivers on injected pellets using phase conjugated mirrors generated by stimulated Brillouin scattering. These experimental studies were complemented by the theoretical ones in order to find correct explanation of experimentally well-established phase locking effect of the concave mirror placed behind the stimulated Brillouin scattering cell as used in the laser beam combination technique.

## 1. LASER PRODUCED PLASMA JETS RELATED STUDIES

The issue of the plasma jets generated from massive flat targets has two main points of view. The first one is the generation of these jets as such. So far this has been proven beyond any doubts (at least) at Prague Asterix Laser System (PALS) [1]. The second point is the satisfactory understanding of the underlying physical mechanisms responsible for the generation of these jets under the given experimental arrangements [2]. It should be noted that this second point has not been fully resolved, yet. Looking for the right, widely acceptable, explanation is still causing some concerns. And yet, without this understanding, at least the qualitative one, it might be impossible to guarantee that this generation of cheap high quality plasma jets is a quite common phenomenon and that it is not somehow specific for the PALS conditions only. While trying to find the right answer two possible major mechanisms has been under close investigation.

The first one is the mechanism of a strong radiative cooling of metallic plasma. A major role of this phenomenon could be judged from the fact that only sufficiently high Z targets (where the strong radiative cooling could take place) are suitable for the plasma jet generation (e.g. the jets are of much better quality in case of Cu than Al).

However, taking only this particular mechanism into consideration in computer modeling was not sufficient to get close enough agreements between the experimental and numerical data [3]. Therefore, it has been gradually accepted that for formation of weakly divergent narrow jets generated from flat targets in experiments at PALS it seems indispensable that some annular structure during the laser-plasma interaction should be present supporting the cumulative effect to play its role as well (similar to the case of conical targets) [4].

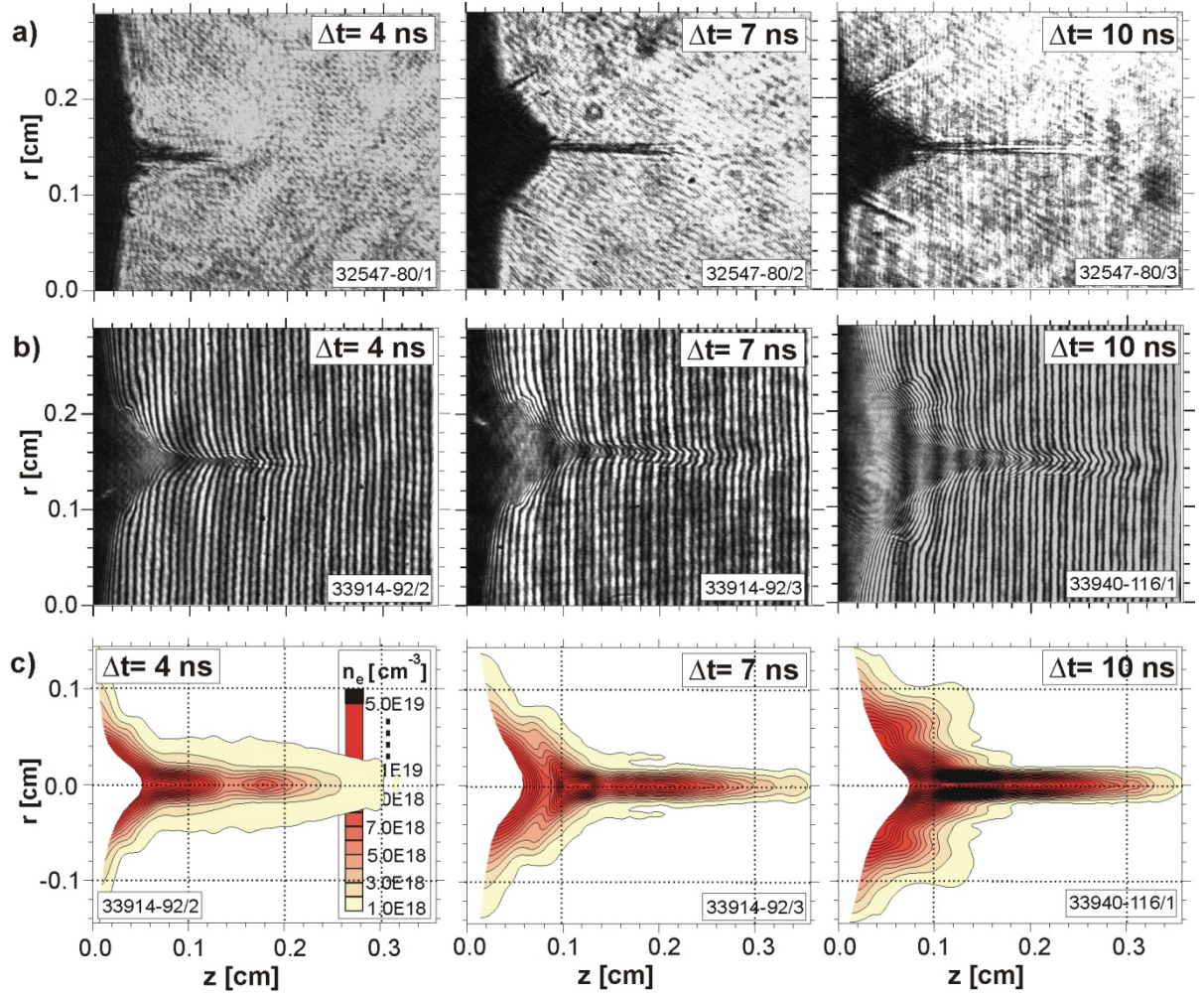


FIG. 1. Sequences of shadowgrams, interferograms and electron equidensitograms illustrative of the typical plasma jet generated from a Cu planar target.

Looking for the origin of such annular structure one obvious possibility would be to find it in the defocused laser beam cross section itself (at least at the target surface). However, even if this would be the case (and some - not yet fully conclusive - studies were already performed in this direction) it would be difficult to attribute the jets creation only to this effect alone. Should this be the reason, good looking jets should be generated both in the case of Al as well as Cu. This, however, would be in contradiction with countless experimentally obtained data. So where to look for this rather mysterious annular structure?

Recently one such explanation was offered. It was based on qualitative studies of created craters supported by ray-tracing. In this case it is presumed that the plasma created at the very beginning of the laser pulse could play a major role in the formation of the annular structure of the interaction region for the remaining part of the laser pulse. Under these assumptions the annular structure would be created only in the case of high Z target materials and it would be quite non-symmetric with respect to the focal plane position (inside versus in front of the target). Should this last scenario be the main reason for the jet creation from the flat targets it would be good news for many other laser laboratories.

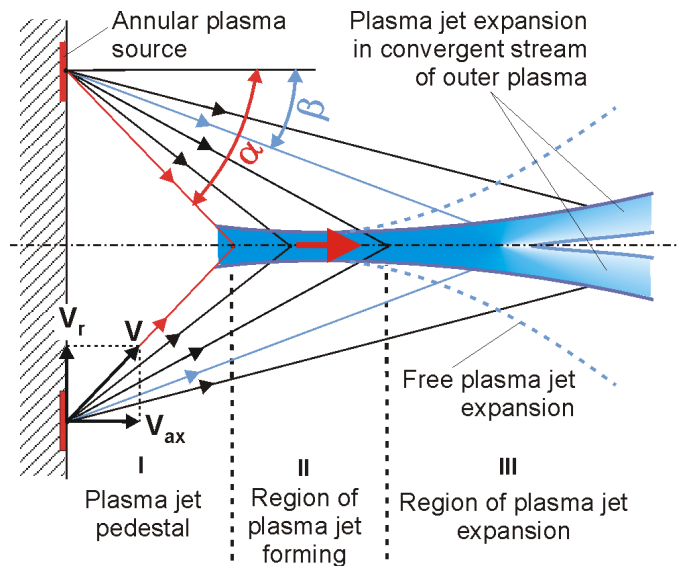


FIG. 2. Schematic geometrical outline of the expected most important mechanism responsible for the plasma jet generation at PALS (annular structure leading to a cumulative effect).

Objections to this mechanism are mainly concerning the width of the plasma layer created during the laser pulse duration regarding it rather too thin to play such an important role. This might be quite a valid objection. However, no laser is perfect from the point of its contrast. And PALS is certainly no exception from the rule. Therefore, the initial plasma layer might not be as thin as expected in the ideal case. And it has been proven beyond any doubts that such pre-plasma can play a very crucial role (e.g. in the case of X ray lasers).

It seems that a very simple method of plasma jet forming proposed by us can open new possibilities for the experimental astrophysics and studies of mixing of different kinds of plasmas relevant to inertial fusion energy (IFE). Whereas the previously applied methods required much higher laser energy in multiple beams and a special geometrical form of targets (making proper laser beams navigation an issue to deal with), our method has, in fact, no obvious technical limitations. The results obtained from the plasma jet - gas-puff interactions are very promising and could deliver many experimental facts for interpretation and numerical modeling [5-8].

## 2. LASER INTERACTION WITH DEUTERIUM CLUSTERS

Interactions of high-intensity femtosecond lasers with deuterium clusters leading to Coulomb explosions and subsequent production of fusion neutrons attracted in recent years considerable attention. In order to maximize the neutron yield, finding a dependence of clusters size and their spatial distribution on experimental conditions becomes very important [9]. In this section a possibility to measure the deuterium clusters spatial distributions experimentally using a complex interferometry diagnostics will be outlined [10]. For this purpose close-to-reality computer generated interferograms were produced which include a small phase shift disturbance modeling the presence of clusters. Subsequent analysis of these interferograms provided results which identified this diagnostics as potentially suitable for such measurements.

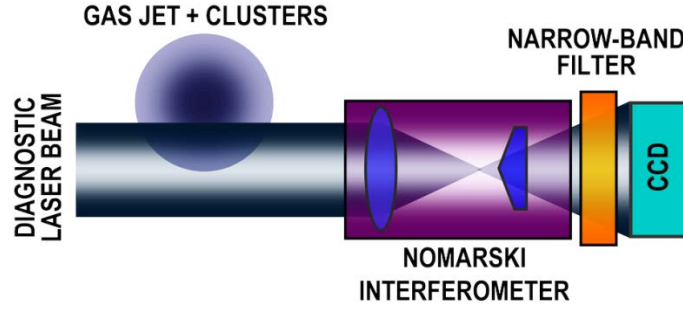


FIG. 3. Experimental setup for spatial distribution of gas/clusters mixture diagnostics.

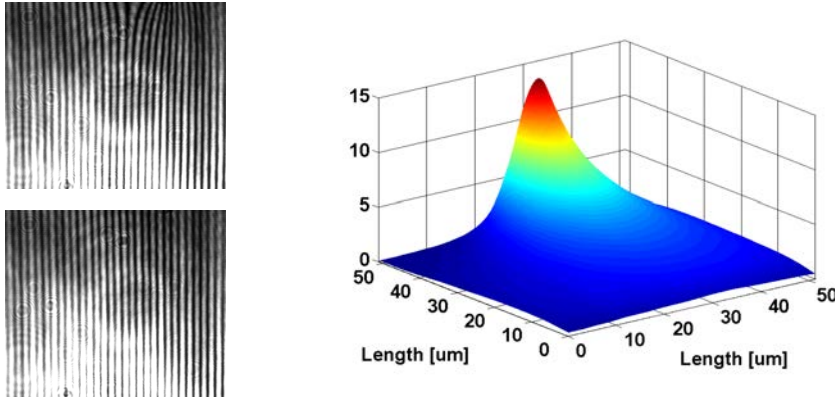


FIG. 4. Examples of two typical experimental interferograms recorded for the gas/cluster mixture in KAERI (45 atm backing pressure): signal (upper left), background (lower left), and the reconstructed phase shift (on the right).

Theoretical background to interferometric measurements of the clusters spatial density distribution will be briefly outlined using a simple model of the mixture of two different gases. Let's consider situation of the injected deuterium gas expanding into vacuum. In the ideal case of the pure gas (without any clusters created), the density profile in the cross-section perpendicular to the gas jet axis of symmetry at the distance  $z$  from the nozzle can be described by some function  $f_1(r,z)$ , where  $r$  represents the distance from the axis of symmetry.

Let's now take into consideration that in the real case, under the right conditions, a certain part of the gas will participate in generation of clusters. Let's denote this density as  $f_2(r,z)$ , thus giving rise to the corresponding clusters density  $f_C(r,z)$ . When  $N$  would be the effective average number of deuterium molecules in one cluster then  $f_C(r,z) = f_2(r,z)/N$ .

Let's also presume that clusters and gas have different values of their respective molar refractivity. Under these assumptions the resulting phase shifts can be obtained from the following expressions:

$$\begin{aligned}\varphi_1(y, z) &= k_1 A[f_1(r, z)] \\ \varphi_2(y, z) &= k_1 A[f_1(r, z)] - (Nk_1 - k_C) A[f_C(r, z)]\end{aligned}$$

where  $\varphi_1(y,z)$  is the phase shift corresponding to the pure gas;  $\varphi_2(y,z)$  is the phase shift of the gas/clusters mixture;  $k_1$  and  $k_C$  are appropriate constants specific for the deuterium gas and the clusters, respectively;  $A[f(r)]$  stands for Abel integral transformation of the function  $f(r)$ .

Provided that both phase shifts  $\varphi_1(y,z)$  and  $\varphi_2(y,z)$  would be known, together with parameters  $k_1$ ,  $k_C$ , and  $N$ , the resulting clusters spatial distribution could be found from the expression:

$$f_c(r, z) = \frac{A^{-1}[\varphi_1(y, z) - \varphi_2(y, z)]}{Nk_1 - k_c}$$

Here  $A^{-1}[\varphi(y)]$  denotes the *Abel inversion* of the function  $\varphi(y)$ . Complete description of this technique and the results obtained will be published [11].

### 3. SBS PCM APPROACH TO SELF-NAVIGATION OF LASER DRIVERS ON INJECTED IFE PELLETS

Experimental studies of our original proposal of embedded SBS PCM based IFE laser driver allowing for its self-navigation on injected pellets as well as an increase of the number of such drivers operating with lower energy (thus easier to design for higher repetition rate) performed during the last 12 months received quite a favorable international reception. Current design of this approach is illustrated in the FIG. 5 where one particular laser channel is displayed during the three distinct stages of its functioning (more details in figure captions).

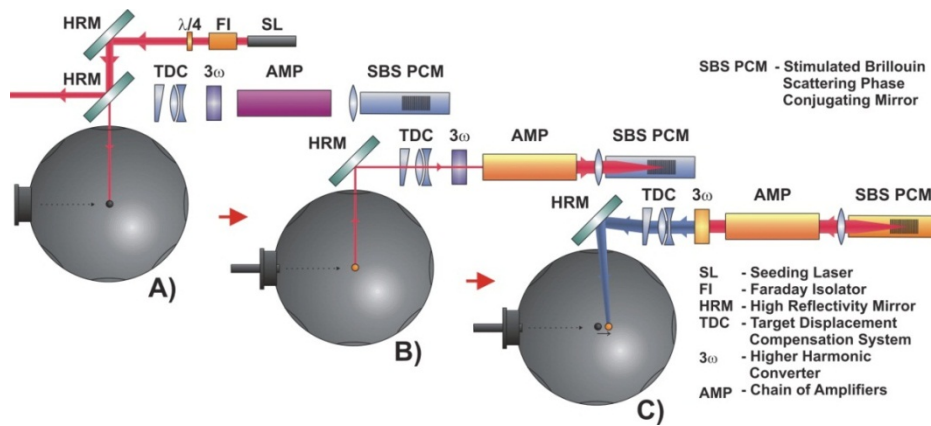


FIG. 5. A) at the right moment (determined by careful tracking) when the injected pellet is approaching its best interaction position, a low energy seeding laser pulse (glint - red line) is sent to illuminate the pellet; B) reflected seeding laser pulse is collected by the focusing optics and amplified on its way to the SBS PCM cell; C) amplified pulse is reflected by the SBS PCM cell, amplified once again, converted to higher harmonic (blue line) and automatically aimed at the moving pellet by the target displacement compensation system (TDC) for its final high power irradiation. TDC is a completely passive system having its optical components appropriately designed for every individual channel taking advantage of their index of refraction dependence on the wavelength.

Our intention is to continue in this research in close cooperation with another CRP member – Prof. Hong Jin Kong from KAIST. One postgraduate student on the Czech side was assigned to continue in this research both in Prague as well as at KAIST. Main concern will be paid to more detailed extension of our recently performed very first successful experiment with direct illumination of the static target (of the size of a real IFE pellet) followed by the reflected light collection, amplification, SBS PCM reflection, second amplification on return, automatic conversion to higher harmonic and change of the final part trajectory to hit the target (which in the real situation would move by an exactly predefined distance). Schematics of the above mentioned experiment are outlined on the FIG. 6.

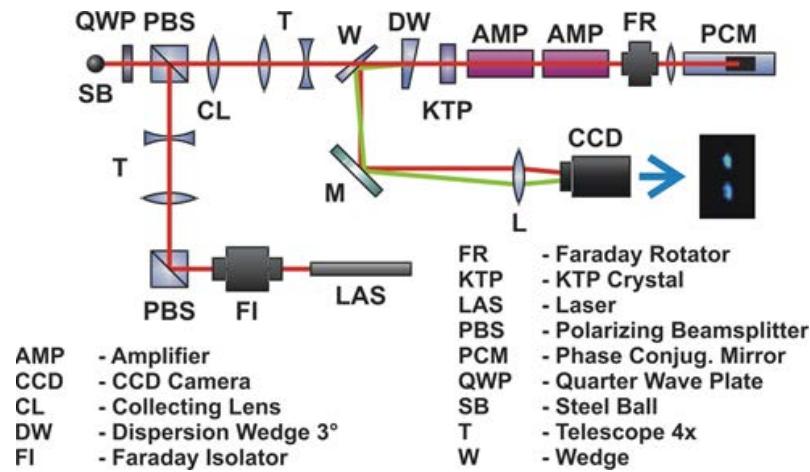


FIG. 6. Schematics of the experimental setup used for verification of the proposed design.

Compared to the successful experiments performed earlier [12] which confirmed the self-navigation principle (the change of the trajectory achieved by the incorporated conversion to the second harmonic - green line) in these new experiments [13,14] the complete individual laser channel setup was assembled - including the pellet realized by the static steel ball. It should be noted that during these tests the laser channel was operating with much lower energies compared to the real ones (so far just below 1 J before irradiating the target). Combining interpretative notes on the FIG. 6 with the figure itself the results presented above should be self-explanatory.

#### 4. PHASE-LOCKING OF SBS BY ELECTROMAGNETIC SEEDING

Among important IFE challenges belongs a construction of high energy high repetition laser driver. One possibility how to achieve this goal would be to combine higher number of smaller lasers into one powerful beam. Probably the most suitable technique (the optics is relatively simple and one can combine, in principle, as many beams as needed) of such beam combination was proposed by Kong et al. and is based on the usage of a phase controlled SBS PCM.

In traditional SBS setup the phase of a reflected Stokes field is random. Kong et al. proposed possibility of using the feedback concave mirror to control the phase of the reflected wave. This phase control technique was successfully experimentally verified and theoretically analyzed. With one exception: a physical mechanism of the traveling acoustic wave excitation by stationary optical interference field remained to be puzzling.

SBS is a nonlinear three wave process. The pumping optical wave is scattered on the acoustic wave in the SBS medium. In standard SBS PCM the acoustic wave randomly arises from the thermal acoustic noise and is amplified via electrostriction by the interference pattern resulting from the interaction of the pumping and the scattered wave. In the SBS PCM scheme shown in FIG. 7 the acoustic wave is not arising from the thermal noise, but it is produced by the interference field in front of the concave mirror. The phase of the acoustic wave, and so the phase of the scattered wave, is then fully controlled by the mirror position. In this Section the process of the acoustic wave excitation using optical interference field and its phase coupling with this optical field will be outlined. Quite a simple approximation will

be used in this case to obtain analytical solution allowing understand just the pure phenomenon itself undisturbed by contribution from any additional mechanisms.

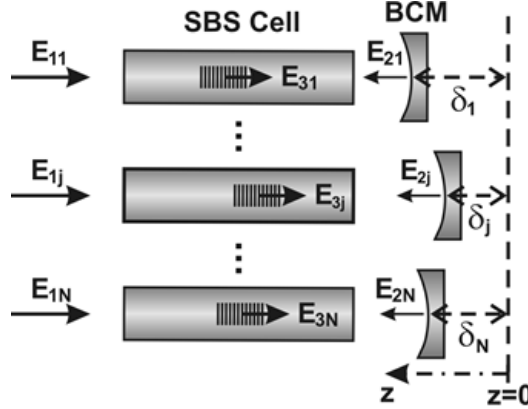


FIG. 7.  $N$  parallel SBS cells with the back-seeding concave mirrors (BCM).  $E_{1j}$  denotes the pump beam,  $E_{2j}$  is the back-seeding mirror reflected beam, and  $E_{3j}$  stands for the SBS backscattered wave.

One important comment to start with is the fact that the electromagnetic standing wave phase in front of the mirror does not depend on the incoming/reflected wave phase. Interference field in the proximity of the back-seeding concave mirror for the  $j$ -th SBS cell can be expressed as

$$\langle E_j^2(z, t) \rangle = \frac{1}{4} |A_j|^2 \left[ \frac{1}{2} (1 + \mu_j^2) - \mu_j \exp[i2k_j(z - \delta_j)] \right] + c.c.$$

Here  $A_j$  denotes the electric field amplitude, and  $\mu_j$  denotes the factor which expresses the amplitude change due to the laser beam focusing. After substitution into the acoustic wave-equation such an interference field acts through electrostriction as a source term for the temporary acoustic wave which converts to the non-oscillating density modulation when this standing wave is completely attenuated.

$$\frac{\partial^2 \rho_j}{\partial t^2} - \Gamma \frac{\partial^2 \rho_j}{\partial z^2} - v^2 \frac{\partial^2 \rho_j}{\partial z^2} = -\frac{\gamma \mu_j}{8\pi} |A_j|^2 k_j^2 \exp[i2k_j(z - \delta_j)] + c.c.$$

Here  $\Gamma$  is the damping constant given by the liquid SBS medium viscosity. Considering the constant density  $\rho_0$  without any perturbations as an initial condition one can find the solution in the form

$$\rho_j(z, t) = \rho_0 - \left\{ \frac{\gamma \mu_j}{32\pi v^2} |A_j|^2 \exp[iq_j(z - \delta_j)] - \frac{\gamma \mu_j}{64\pi v^2} |A_j|^2 \exp\left[-\frac{1}{2}\Gamma_{Bj}t\right] \exp[i(q_j(z - \delta_j) - \Omega_j t)] - \frac{\gamma \mu_j}{64\pi v^2} |A_j|^2 \exp\left[-\frac{1}{2}\Gamma_{Bj}t\right] \exp[i(q_j(z - \delta_j) + \Omega_j t)] + c.c. \right\},$$

Here  $\gamma$  is the electrostriction coupling constant,  $q_j = 2k_j$  denotes the acoustic wave wavenumber,  $\Gamma_{Bj} = \Gamma q_j^2$  stands for the Brillouin linewidth, and  $\Omega_j = q_j v - \Gamma_{Bj}/4$  is the acoustic frequency. The second wave superimposed in the standing wave is the SBS backscattering phase-matched wave.

Initially, the weak spontaneous Brillouin scattering signal occurs on this standing wave structure. The phase matched wave will subsequently interfere with the pump beam and the resulting interference structure will amplify this phase-matched wave via the stimulated scattering process. The second superimposed wave is not going to be amplified and so the resulting wave will start to move (as required). More detailed explanation can be found in the literature [15, 16].

## ACKNOWLEDGEMENTS

Main support to this work comes from the IAEA RC No.: 13781 & 13758. It was also partially supported from various other sources: by the Ministry of Education, Youth, and Sports of the Czech Republic Research Project LC528 & by the grant KONTAKT No. ME933; by the CTU in Prague grant No.: CTU0916314; by the Grant Agency of the Czech Republic grant No.: 202/08/H057; by the EU FP7 joint R&D project "Collaboration on HiPER project" funded by Korean MEST through NRF; by the Nuclear Research & Development Program of the Korea Science and Engineering Foundation (KOSEF) grant funded by the Korean Government (MEST) - grant code: M20090078160 and by R&D Program through the National Fusion Research Institute of Korea (NFRI) funded by the Ministry of Education, Science and Technology.

## REFERENCES

- [1] PISARCZYK, T., KASPERCZUK, A., STENZ, CH., KROUSKÝ, E., MAŠEK, K., et al.: PALS laser-driven radiative jets for astrophysical and ICF applications. In AIP Conference Proceedings Volume 993. Melville, New York: American Institute of Physics, 2008, p. 315-318.
- [2] KASPERCZUK, A., PISARCZYK, T., DEMCHENKO, N.N., S., GUS'KOV, YU., KÁLAL, M., ULLSCHMIED, J., et al., Experimental and theoretical investigations of mechanisms responsible for plasma jets formation at PALS, Laser and Particle Beams. 2009, vol. 27, 415–427.
- [3] NICOLAI, PH., STENZ, C., TIKHONCHUK, V., RIBEYRE, X., KASPERCZUK, A., et al.: Studies of supersonic radiative plasma jet interaction with gases at the Prague Asterix Laser System (PALS) facility. Physics of Plasmas. 2008, vol. 15, no. 8, p. 082701-082718.
- [4] KASPERCZUK, A., PISARCZYK, T., KÁLAL, M., J. et al., Influence of target material on structure of the plasma outflow produced by a partly defocused laser beam, Applied Physics Letters. 2009, vol. 94, p. 081501-081503.
- [5] TIKHONCHUK, V.T., NICOLAI, PH., RIBEYRE, X., et al.: Laboratory modeling of supersonic radiative jets propagation in plasmas and their scaling to astrophysical conditions. Plasma Physics and Controlled Fusion. 2008, vol. 50, no. 12.
- [6] KASPERCZUK, A., PISARCZYK, T., NICOLAI, PH., STENZ, C., et al., Investigations of plasma jet interaction with ambient gases by the multi-frame interferometric and X ray pinhole camera systems, Laser and Particle Beams. 2009, vol. 27, p. 115–122.
- [7] NICOLAI, PH., STENZ, C., TIKHONCHUK, V., et al., Supersonic plasma jet interaction with gases and plasmas, Astrophysics and Space Science. 2009, 322, 11-17.

- [8] NICOLAÏ, PH., STENZ, C., KASPERCZUK, A., et al., Laboratory studies of multi-material radiative astrophysical jets propagation in plasmas, 6th International Conference on Inertial Fusion Sciences and Applications (IFSA 2009), September 6 – 11, 2009, San Francisco, USA ((accepted for publication in the Conference Proceedings in the Conference Proceedings: Journal of Physics: Conference Series).
- [9] KÁLAL, M., SLEZÁK, O., MARTÍNKOVÁ, M., RHEE Y.J., Compact Design of Nomarski Interferometer and its Application in Diagnostics of Coulomb Explosions of Deuterium Clusters, Journal of the Korean Physical Society (2010), 56, No. 1, 287-294
- [10] MARTÍNKOVÁ, M., KÁLAL M., and Y.J. RHEE: Coulomb Explosions of Deuterium Clusters Studied by Compact Design of Nomarski Interferometer, 6th International Conference on Inertial Fusion Sciences and Applications (IFSA 2009), September 6 – 11, 2009, San Francisco, USA (accepted for publication in the Conference Proceedings: Journal of Physics: Conference Series).
- [11] KÁLAL, M., MARTÍNKOVÁ, M., RHEE Y.J., Feasibility Studies of Deuterium Clusters Spatial Density Distribution Measurements by Complex Interferometry (submitted for publication to the Journal of the Korean Physical Society).
- [12] KÁLAL, M., MARTÍNKOVÁ, M., SLEZÁK, O., KONG, H.J. et al., SBS PCM Technique Applied for Aiming at IFE Pellets: First Tests with Amplifiers and Harmonic Conversion, Journal of the Korean Physical Society. 2010, vol. 56, No. 1, 184-189.
- [13] KÁLAL, M., KONG, H. J., KORESHEVA, E., et al., Current Status of the SBS PCM Approach to Self-Navigation of Lasers on IFE Targets, 6th International Conference on Inertial Fusion Sciences and Applications (IFSA 2009), September 6 – 11, 2009, San Francisco, USA (accepted for publication in the Conference Proceedings: Journal of Physics: Conference Series).
- [14] KÁLAL, M., KONG, H. J., KORESHEVA, E., et al., Recent Progress Made in the SBS PCM Approach to Self-Navigation of Lasers on Direct Drive IFE Targets, Innovative Confinement Concepts Workshop (ICCW 2010), February 16-19, 2010, Princeton, New Jersey, USA (accepted for publication in the Conference Proceedings: Journal of Fusion Energy).
- [15] SLEZÁK, O., KONG, H.J., and KÁLAL M., : Phase Control of SBS Seeding by Optical Interference Pattern Clarified: Direct Applicability for IFE Laser Driver, 6th International Conference on Inertial Fusion Sciences and Applications (IFSA 2009), September 6 – 11, 2009, San Francisco, USA (accepted for publication in the Conference Proceedings: Journal of Physics: Conference Series).
- [16] SLEZÁK, O., KÁLAL, M., and KONG H.J., Phase-locked stimulated Brillouin scattering seeded by a transient acoustic wave excited through an optical interference field (submitted for publication to the Journal of the Korean Physical Society).



# INVESTIGATIONS OF INTERACTION OF LASER RADIATION AND PLASMA BEAMS WITH MATERIALS OF REACTOR CHAMBER FOR INERTIAL CONFINEMENT FUSION

R.T. KHAYDAROV, H.B. BEISINBAEVA, M.M. SABITOV, V.B. TERENCEV, G.R. BERDIYOROV,  
T. AKRAMOV  
Institute of Applied Physics  
National University of Uzbekistan  
Tashkent, Uzbekistan

## Abstract

The main purpose of the project was to experimentally analyze some the processes which take place during the interaction of laser radiation and plasma beams with the materials of reactor chamber for the Inertial Confinement Fusion. First, we studied the effect of target nature on the laser ablation process and on the properties of laser-generated plasma ions. As an example we considered porous targets having different densities and showed how the charge state, the energy and the intensity of the plasma ions depend on the target density. We also studied the effect of laser frequency on the properties of plasma ions generated at the surface of such porous targets. We considered possibilities of controlling the intensity and the energy of the ions by changing the frequency of the laser and the density of the target because of the change in laser ablation process. Then we investigated the changes in the properties of laser-produced plasma ions after the ablation process, during the plasma expansion, due to the mutual interaction between the ions of different mass. For this purpose we studied two-element plasma ions generated from ( $\text{Sc}_2\text{O}_3$ ,  $\text{Ce}_2\text{O}_3$ ,  $\text{Lu}_2\text{O}_3$ ) targets. Experiments have shown that structural defects caused by the neutron irradiation, influence not only on the efficiency of the process of material evaporation and emission of plasma, but also on the ionization and recombination processes taking place at the initial stage of the plasma formation and expansion.

## 1. INTRODUCTION

The majority of previous works in the field of controlled thermonuclear fusion has been devoted to the study of comparatively low density thermonuclear fuel (plasma) restrained by specially created magnetic field. More physical problems appear in the inertial confinement scenario related to the field of electromagnetism and plasma physics linked with physics course of thermonuclear fusion reactions in plasma with inertial retention, hydrodynamics and shock waves, transport processes in dense plasmas and the interaction of laser radiation or charged particle beams with plasmas, as well as materials reactor chamber [1, 2]. There are other problems with the technical and applied nature, such as the device features powerful lasers, and laser sources, as well as high-current accelerators of charged particles, the design and production technology of fusion, and target cells, methods of conducting experiments and diagnostics.

At present there are number of works devoted to the study of laser-produced plasma as a source of ions for the inertial confinement fusion (ICF) together with heavy ion accelerators and the systems on the base of powerful impulse of electrical charge, i.e. Z-pinches. Laser ion source (LIS) have been recently designed to load the Heidelberg electron beam ion trap with a pulsed beam of lowly charged ions from solid elements. Due to many characteristics of laser-produced plasmas LIS takes advantages over e.g. a common metal vapor vacuum arc method as a source of ions. Laser-plasma generator – consists of powerful frequency mode laser, the chamber of interaction with the target and a setup for the extraction of high-current ions beams. The system generates beams of large amount of highly charged atoms and nucleus of elements, including rare and radioactive isotopes to inject into the electro-physical equipments [3-5]. Therefore, the investigation of interaction of laser radiation and plasma beams with different kinds of targets gives additional information to improve the characteristics of laser drivers for ICF.

The properties of plasma ions can be improved by changing both the parameters of the laser radiation (intensity, pulse duration, wavelength and polarization, interaction angle etc.) and the parameters of the target itself (e.g., using multi-element targets [5] and targets with different densities [6]). There number of theoretical [7] and experimental [8-10] works which show that charge and energy state of laser-produced plasma ions may change due to the presence of different impurities, as well as due to their distribution in the target.

In this report we present our experimental results, where we studied the plasma formation and expansion processes under the action of laser radiation on the surface of solid targets [10]. Our main goal was to improve and to find a way to control the parameters of the laser-produced plasma ions. We found that the plasma ion characteristics can be improved using porous targets – the maximal change, energy, as well as the intensity of plasma ions is strongly influenced by the target density [6]. However, the origin of some effects e.g. the maximal charge of light elements at low densities and the one of heavy elements at high densities of the target, is still not clear and requires more theoretical investigations.

In Sec. 4 of the report we have shown that the frequency of the laser (i.e. the frequency of the repetition of the laser impulses) also has a strong influence on the plasma ions [9, 10]. For example, the intensity of the plasma ions can be increased considerably for some charge-multiplicity of the ions with increasing the laser frequency. More experimental and theoretical investigations are still necessary to study the effect of the laser frequency on the parameters of charged particles in the plasma, as the change in the frequency makes the laser ablation process more complicated.

We also studied the parameters of the plasma ions generated from the surface of two-element targets (i.e. oxides of elements) [8], where the mass of the main component of the targets changes from 44.9 (Sc) to 174.9 (Lu). As oxygen atoms are present in most of the targets used in such experiments, we mainly focus on the properties of oxygen ions. We show that mass-charge and energy distribution of O ions strongly depend on the nature of the second component of the target, which is related to the mutual interaction of the target components.

Another important topic we have focused within the report is the investigation of the effect of neutron irradiation of the targets with a dose of the neutrons  $10^{15}$ -  $10^{21}$  neutron/cm<sup>2</sup> on the parameters of the laser-generated plasma ions [11]. The irradiation process leads to the formation of defect on the targets and our goal is to study how these defects attribute on the parameters of the plasma ions generated during the action of the laser radiation on the surface of these irradiated targets.

## 2. EXPERIMENTAL SETUP

Experiments were carried out in a laser mass-spectrometer [5] with Niodimum glass laser operates at 1,06  $\mu\text{m}$  wavelength, 15 ns pulse duration, 1-5 J pulse energy and single and multi-shot mode with frequency up to 15 Hz. The laser beam was focused trough a convergent lens on a target placed inside a vacuum chamber at  $10^{-6}$  Tor. The power density of the laser radiation on the surface of the target was in the range  $q=10^8$ - $10^{11}$  W/cm<sup>2</sup>. Plasma currents were measured by the collector method and the plasma ions parameters by time-of-flight mass-spectrometer (the distance was L=100 and 362 cm). Y<sub>2</sub>O<sub>3</sub> and Ho<sub>2</sub>O<sub>3</sub> targets with diameter 1.0 cm and thickness 0.5 cm are used in the experiment, which have density  $\rho_0=1.2$  g/cm<sup>3</sup> (initial condition-powder),  $\rho_1=1.4$  g/cm<sup>3</sup>,  $\rho_2=2.8$  g/cm<sup>3</sup>,  $\rho_3=3.2$  g/cm<sup>3</sup>,  $\rho_4=3.5$  g/cm<sup>3</sup>,

$\rho_5=3.7 \text{ g/cm}^3$ . Other the targets were made of different solid materials with a  $3.14 \text{ cm}^2$  surface and  $1 \text{ mm}$  thickness. The target could be moved vertically with the vacuum feed through, so that each laser shot could hit a fresh surface to avoid the effect of crater formation. The surface morphology of the samples was investigated by electron microscopy.

### 3. INTERACTION OF LASER RADIATION WITH POROUS TARGETS

First, we study the effect of target density on the parameters of laser-produced plasma ions. Targets, made of  $\text{Ho}_2\text{O}_3$ , have densities  $\rho_0=1.2 \text{ g/cm}^3$  (initial condition-powder),  $\rho_1=1.4 \text{ g/cm}^3$ ,  $\rho_2=2.8 \text{ g/cm}^3$ ,  $\rho_3=3.2 \text{ g/cm}^3$ ,  $\rho_4=3.5 \text{ g/cm}^3$ ,  $\rho_5=3.7 \text{ g/cm}^3$ . Plasma is formed on the surface of these targets under the action of laser radiation normal to the target surface and the intensity of the laser was within  $q=10^8\text{-}10^{11} \text{ W/cm}^2$ . Figure 1 shows the maximal charge  $Z_{\text{max}}$  of Ho (solid curves) and O (dashed curves) ions as a function of intensity of laser radiation  $q$  for two different values of target density  $\rho$ . Regardless on the ions mass,  $Z_{\text{max}}$  changes non-linear with increasing  $q$ . However,  $Z_{\text{max}}$  strongly depends on  $\rho$  – maximal charge of heavy (Ho) ions increases and the one of light (O) ions decreases with increasing  $\rho$ .

Figure 2 shows the energy spectra of ions in  $\text{Ho}_2\text{O}_3$  plasma obtained at  $q=10^{11} \text{ W/cm}^2$  for four different values of the target density. For any density of the target, two groups of ions with different spectral range and charge are clearly seen, but the structure and width of energy spectra and intensity and charge of different kind of ions strongly depend on  $\rho$ . At low density of the target [FIG. 2(a)] oxygen ions with charge  $Z=1\text{-}4$  have energies in the range of  $25 - 370 \text{ eV}$ . The maximum charge of Ho ions in this case equals to  $Z_{\text{max}}=3$  and they have wider energy spectra ( $50 - 800 \text{ eV}$ ). With increasing target density O ions with larger charge ( $Z>2$ ) disappear from the spectra and the energy range of oxygen ions considerably decreases (see FIG. 2(b)). For example, the maximal energy of double charged  $\text{O}^{+2}$  ions decreases three times for larger  $\rho=\rho_2$  compared to the reference sample ( $\rho=\rho_0$ ). Ho ions with charge  $Z=4$  are detected for  $\rho=\rho_2$  and there is slight increase of energy diapason of Ho ions. With further increase of  $\rho$  (see FIG. 2 (c)) energy spectra of O ions remain unchanged and energy range of Ho ions increases. The maximal charge of both kinds of ions remains the same.

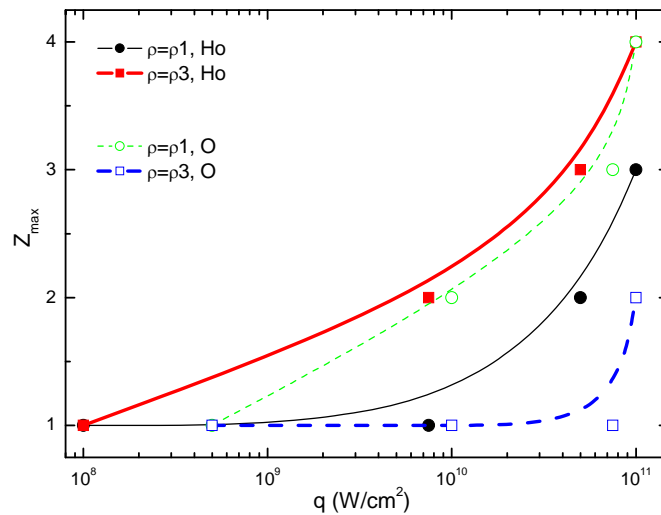


FIG. 1. Dependence of maximal charge  $Z_{\text{max}}$  of Ho (solid curves) and O (dashed curves) ions in  $\text{Ho}_2\text{O}_3$  plasma as a function of intensity of laser radiation for the target density  $\rho_1=1.4 \text{ g/cm}^3$  (thin curves) and  $\rho_3=3.2 \text{ g/cm}^3$  (thick curves).

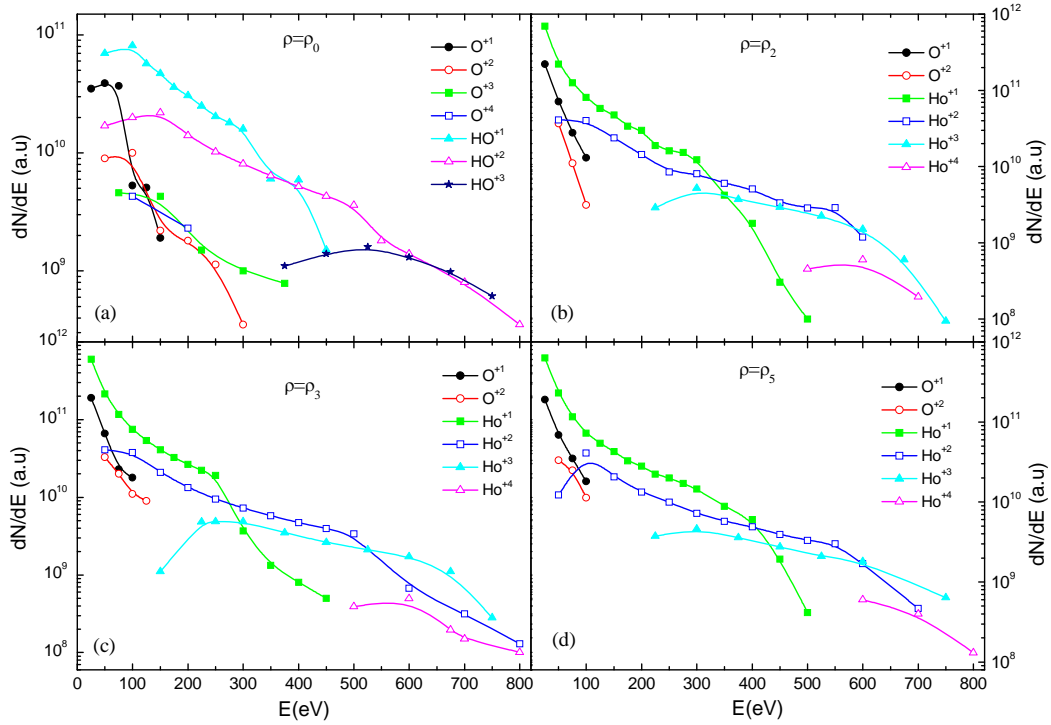


FIG. 2. The energy spectra of ions from two-element  $Ho_2O_3$  plasma for different values of target density:  $\rho=\rho_0$  (a),  $\rho=\rho_2$  (b),  $\rho=\rho_3$  (c) and  $\rho=\rho_5$  (d).

These experimental results can be explained by the nature of the targets. The structure of such porous materials consists of solid particles with different shape alternating with empty spaces. Therefore, the properties of such materials are determined with mass composition, sizes and density of those granules. For small  $\rho$ , most of the laser radiation enter deep inside the sample and the radiation is absorbed “volumetrically” due to the “internal evaporation”. In this case decrease of selective recombination losses takes place for multi-charged  $O$  ions, compared to  $Ho$  ions. Therefore, in this interval of the density  $\rho$  maximal charge of  $O$  ions is higher than the one of  $Ho$  ions. For larger target density  $\rho$  the laser radiation mostly interacts with the surface of the sample. In this case the ionization processes of  $Ho$  ions predominate and the recombination losses of multi-charge  $Ho$  ions decrease compared to the one of  $O$  ions. Therefore, the maximal charge of  $Ho$  ions is higher than the charge of  $O$  ions. We have to mention that the characteristics of laser-produced plasma, like maximal charge, energy and intensity of ions does not change with further increasing  $\rho>\rho_3$ . This indicates that starting from  $\rho=\rho_3$  characteristics of our samples become close to the one of solid targets.

#### 4. EFFECT OF LASER FREQUENCY ON THE PARAMETERS OF PLASMA IONS

Here we present our results on the effect of laser frequency, i.e. the frequency of repetition of 15 ns laser impulses, on the formation of plasma ions on the surface of porous  $Y_2O_3$  targets with densities  $\rho_0=1.2$  g/cm<sup>3</sup>,  $\rho_1=1.4$  g/cm<sup>3</sup>,  $\rho_2=2.8$  g/cm<sup>3</sup>,  $\rho_3=3.2$  g/cm<sup>3</sup>,  $\rho_4=3.6$  g/cm<sup>3</sup> and  $\rho_5=3.7$  g/cm<sup>3</sup>. The results were obtained for the intensity of the laser radiation  $q=10^{11}$  W/cm<sup>2</sup>. From the experimental time-of-flight spectra of ions we constructed energy distribution of ions depending both on the target density and the laser frequency. Figure 4 shows the energy spectra of laser-produced plasma ions for  $\rho=\rho_0$  (a) and  $\rho=\rho_3$  (b) obtained in the mono impulse regime  $\nu=1$  Hz. As we have mentioned in the previous section, for  $\rho=\rho_0$   $O$  ions has largest charge multiplicity ( $Z_{max}=4$ ) and they are mostly located in the low energy

part of the spectrum (FIG. 3 (a)). Y ions occupy large region in the spectra, due to their heavier mass, and the maximal charge of these ions equals to 3. With increasing the target density O ions with larger charge disappear from the spectra and the energy range of these ions considerably decreases (see FIG. 3(b)).

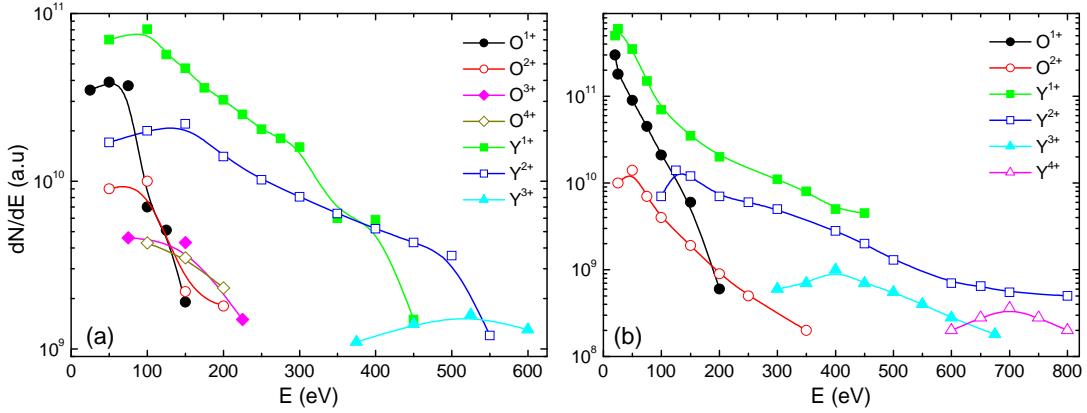


FIG. 3. The energy spectra of ions from two-element  $Y_2O_3$  plasma obtained for  $\rho=\rho_0$  and  $\nu=1\text{Hz}$ .

Let us now consider the effect of the laser frequency on the energy distribution of the plasma ions. Here we give our results for larger density of the target, so that we neglect the influence of  $\rho$ . FIG. 4. shows the energy spectra of ions in  $Y_2O_3$  plasma obtained for the laser frequency  $\nu=3\text{ Hz}$  for two different values of  $\rho$ . As we showed above, for  $\rho=\rho_3$  (FIG. 5 (a)) O ions are located in a narrow range of the energy (20-200 eV) and their maximal charge is unchanged compare to lower density case (see FIG. 4 (b)). Y ions are located in the energy interval 20-800 eV with  $Z_{\text{max}}=3$ . This small increase of the laser frequency affects only on the intensity of the ions: O ions of both charge increases, while the intensity of heavy ions considerably decreases with increasing  $\nu$ .

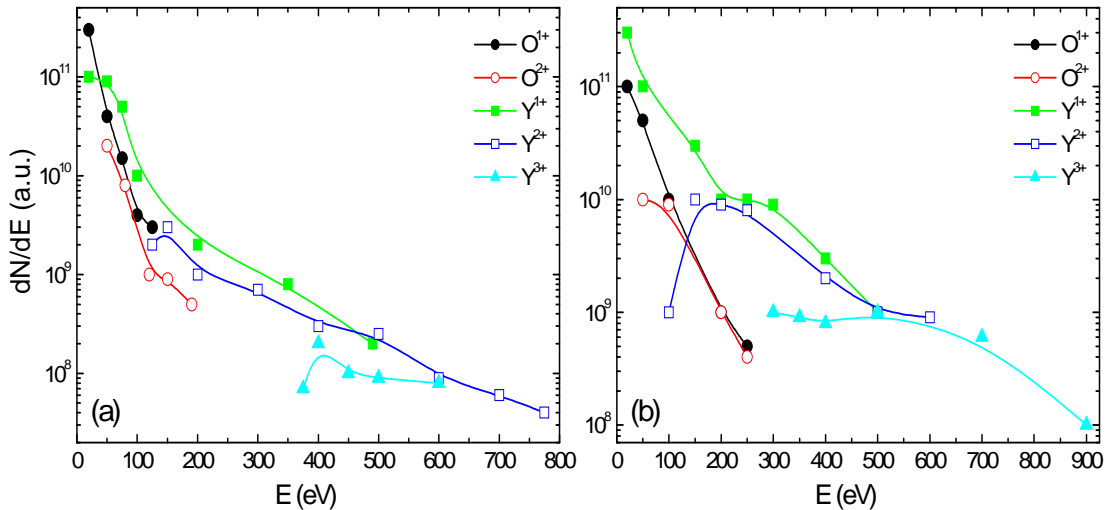


FIG. 4. The energy distribution of ions in two-element  $Y_2O_3$  plasma obtained at  $\nu=3\text{ Hz}$  and for two different target density:  $\rho=\rho_3$  (a) and  $\rho=\rho_5$  (b).

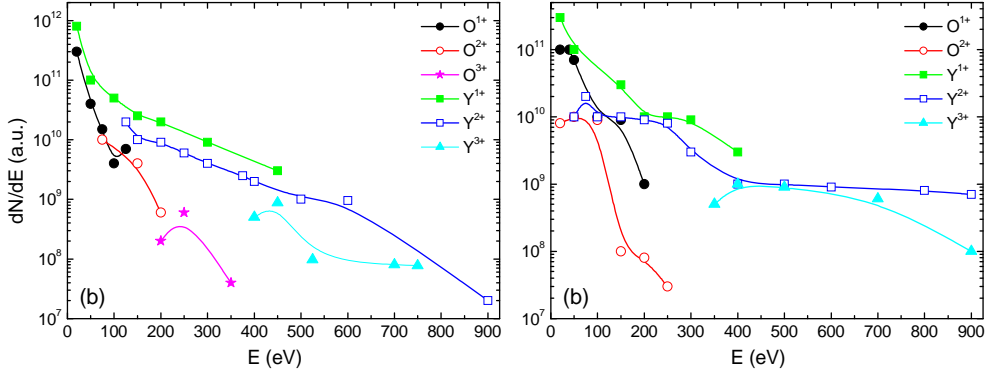


FIG. 5. The same as FIG. 5, but for  $\nu=10$  Hz.

Figure 5(a) shows the energy spectra of ions obtained for larger frequency of the laser ( $\nu=10$  Hz). The effect of the laser frequency is quite evident from this figure. First, O ions with charge  $Z=3$  appears in the spectra. Second, the energy spectra of both light (O) and heavy (Y) ions expand to higher energies. Now O ions can be detected in the energy interval 20-350 eV and Y ions in the energy range 20-900 eV.

We also studied the dependence of the impulse of the ions beam on the laser frequency. Tabs. I and II presents the duration of ions impulse  $t$  for different density of the target and laser frequency. From these data we see a nonlinear dependence of  $t$  on  $\nu$ . For both kind of ions and for all charge multiplicity the largest impulse duration corresponds to the frequency  $\nu=5$  Hz.

TABLE 1. IMPULSE DURATION OF Y IONS FOR DIFFERENT TARGET DENSITY AND LASER FREQUENCY

1.4(gm/cm <sup>3</sup> )				2.8(gm/cm <sup>3</sup> )				3.7(gm/cm <sup>3</sup> )			
3 Hz	5 Hz	0Hz	12 Hz	3 Hz	5 Hz	10 Hz	12 Hz	3 Hz	5 Hz	10 Hz	12 Hz
21.9	30.3	18.2	21.5	17.9	27.1	17.1	21.3	12	18.8	17.7	14.5
18.9	21.4	14.6	17.8	12.7	17.4	15.4	17.7	13.5	11.6	11.1	10.7
8.4	8.2	13.6	5.5	4.9	9	5.2	4.2	15	10	11.7	12.2
					1.3						

TABLE 2. THE SAME AS TABLE I BUT FOR O IONS

1.4(gm/cm <sup>3</sup> )				2.8(gm/cm <sup>3</sup> )				3.7(gm/cm <sup>3</sup> )			
3 Hz	5 Hz	10Hz	12 Hz	3 Hz	5 Hz	10 Hz	12 Hz	3 Hz	5 Hz	10 Hz	12 Hz
31	34.7	33.5	23.8	34.9	36.3	28.7	30.8	39	39.9	32.5	27.2
24.5	29.8	24.9	29.1		24.6	19.2	21.7	26.5		22.1	36.3

We have found that the charge composition and the total current of the ions are strongly affected by the frequency of the laser. This is, to our understanding, due to the change of the focusing condition of the laser radiation on the surface of the targets. The radiation of the

laser working in the frequency mode does not only heats the surface of the target but it also forms craters with noticeable sizes, which can strongly change the focusing condition of the laser radiation during the interaction process [8]. The latter is due to the fact that the ionization process and the expansion of multi-charge ions take place at small time interval than the time between the impulses and additional thermal processes take place on the surface of the target. Therefore, by the change in the focusing condition – the place of the focal spot or formation of craters, as well as using laser in frequency mode, one can control charge and energy spectra of ions obtained from the surface of two-element targets under the action of laser radiation.

In summary, experimental results show strong dependence of plasma parameters of the density of the target – the maximal charge for light ions is reached at low densities, while maximal charge of heavy ions is obtained at higher target densities. This effect is the results of non-equilibrium ionization processes in the plasma due to the changing of the volume, which absorbs laser radiation. We have shown that with increasing the frequency of the laser the charge, energy and intensity of ions increase for a given parameters of the target. Although, this effect is more pronounced for small densities of the target, significant influence of the laser radiation is observed for larger values of the target density. We related this effect to the change in the focusing condition of the laser radiation due the formation of clusters on the surface of the target.

## 5. PROPERTIES OF IONS OF DIFFERENT MASS IN LASER PRODUCED PLASMA

Next we investigate the mutual interaction of plasma ions with different mass. The following targets (in the form of thick disks of diameter 10 mm) have been used in the experiments:  $\text{Sc}_2\text{O}_3$  ( $m=44.955$ ),  $\text{Y}_2\text{O}_3$  ( $m=88.905$ ),  $\text{Ce}_2\text{O}_3$  ( $m=140.11$ ),  $\text{Eu}_2\text{O}_3$  ( $m=151.96$ ),  $\text{Dy}_2\text{O}_3$  ( $m=162.50$ ),  $\text{Tm}_2\text{O}_3$  ( $m=168.93$ ),  $\text{Yb}_2\text{O}_3$  ( $m=173.05$ ) and  $\text{Lu}_2\text{O}_3$  ( $m=174.96$ ). Although the properties of plasma ions show nonlinear dependence on the intensity of the laser radiation (see FIG. 6) we present here experimental results obtained for the maximal intensity of the laser radiation  $q=10^{11}$  W/cm<sup>2</sup>.

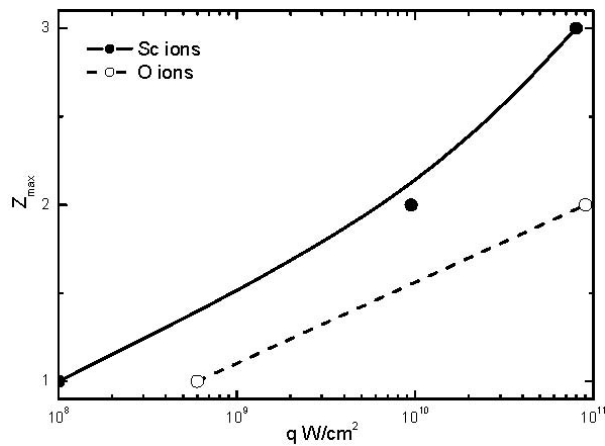


FIG. 6. Dependence of the maximal charge  $Z_{\text{max}}$  of Sc (solid) curve and O (dashed curve) ions in the plasma on the intensity of the laser radiation  $q$ .

Experimentally we obtained mass-charge spectra, i.e. time-of-flight spectra of ions, in two-component laser-produced plasma. From the obtained mass-charge spectra we constructed energy distribution of the ions, which allows us to study the effect of target

composition on the parameters of plasma ions. As an example we plotted in FIG. 7 the energy spectra of ions from  $\text{Sc}_2\text{O}_3$  (a) and  $\text{Lu}_2\text{O}_3$  (b) plasma. As seen from this figure plasma ions have a broad energy spectrum with a single maximum of the distributions. The spectrum consists of different species of ions located in different energy ranges. It is also possible to observe that by increasing the charge-state the energetic distribution is shifted towards higher energy, according to the Coulomb-Boltzmann-shifted model proposed by Torrisi et al. [12]. But the decrease of the ion yields do not follow the exponential law predicted by Shirko-Lotz theory of the ionization cross-sections [13]. O ions with two ionization states are located in low energy part of the spectra, while Sc and Lu ions are located in higher energy part. As expected, the maximal energies of the second component of the target for all charge multiplicity of ions increases with increasing the mass of the ions as illustrated in FIG. 8 for the case of Sc, Ce and Lu elements. The latter is in agreement with the previous theoretical studies [9].

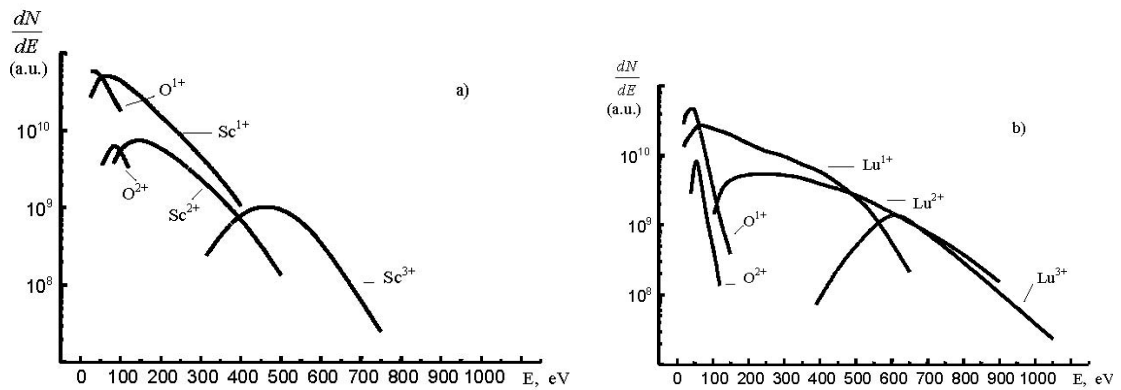


FIG. 7. Energy spectra of ions in two element  $\text{Sc}_2\text{O}_3$  (a) and  $\text{Lu}_2\text{O}_3$  (b) plasma, obtained at  $q=10^{11} \text{ W/cm}^2$ .

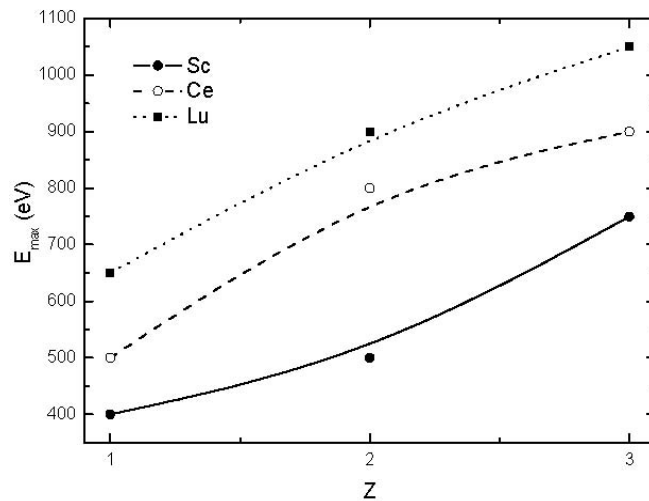


FIG. 8. Dependence of the maximal energy of Sc, Ce and Lu ions on the charge multiplicity of ions.

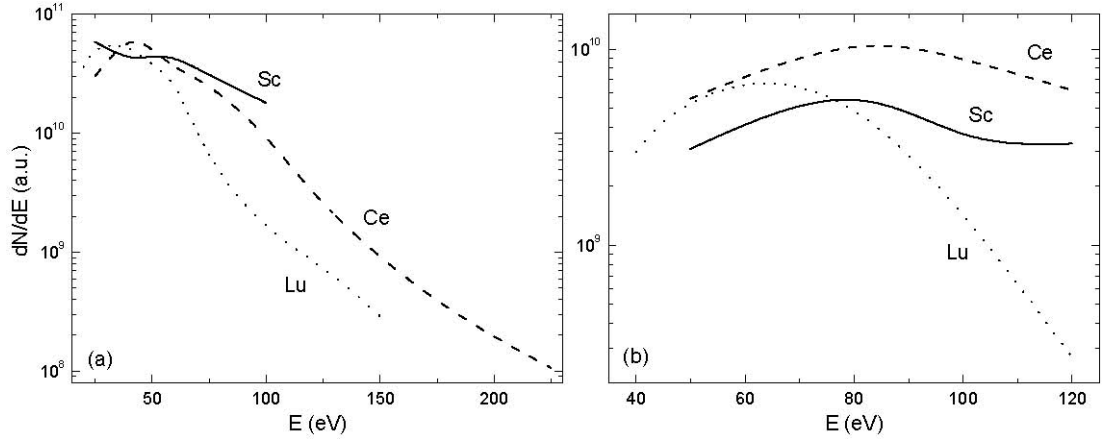


FIG. 9. Typical energy spectra of  $O^{1+}$  (a) and  $O^{2+}$  (b) ions in two element  $Sc_2O_3$  (solid curves),  $Ce_2O_3$  (dashed curves) and  $Lu_2O_3$  (dotted curves) plasma.

Let us now consider the effect of the second component of the target to the energy distribution of O ions in more detail. FIG. 9(a) shows the energy spectra of  $O^{1+}$  ions in the two-element  $Sc_2O_3$ ,  $Ce_2O_3$  and  $Lu_2O_3$  plasma. As we mentioned above character and the width of the energy spectra of O ions and the maximal energy depends on the nature of the target. Single charged  $O^{1+}$  ions have a narrow energy interval ( $E_{max} \sim 100$  eV) for small mass ratio (i.e., Sc ions) (solid curve in FIG. 10 (a)). With increasing the mass of the second component (Ce ions) the maximal energy increases more than two times (dashed curve in FIG. 9 (a)). Although,  $E_{max}$  of  $O^{1+}$  ions slightly decreases with further increasing the mass of the second component of the target, it is still larger than the case of Sc ions. The energy spectra of  $O^{2+}$  ions for different mass of the second component of the target are shown in FIG. 9(b).  $O^{2+}$  ions are mostly located in the interval of the energy between 40 eV and 120 eV and the energy range of the ions in this case does not strongly depend on the target composition.

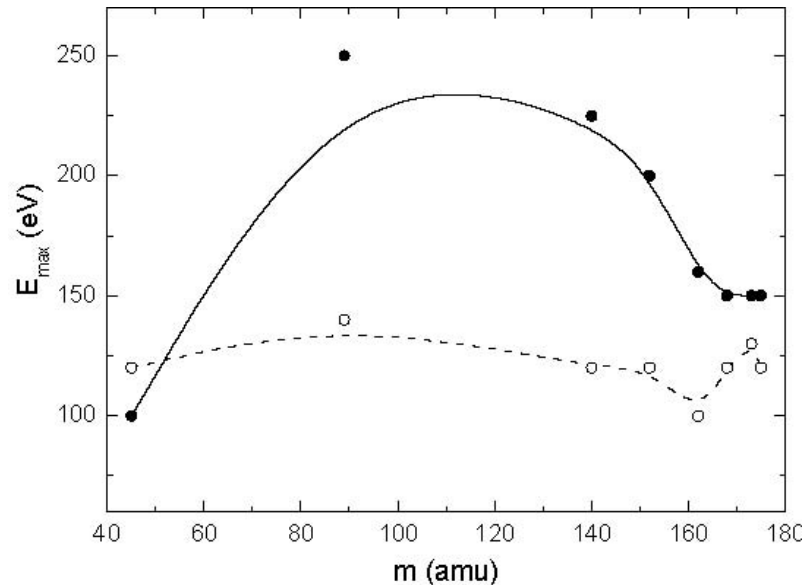


FIG. 10. Dependence of maximal energy  $E_{max}$  of  $O^{1+}$  (solid lines) and  $O^{2+}$  (dashed lines) ions on the mass of the second component of the plasma.

It is noticeable that the increase of the mass of the second component of the target leads to considerable changes in the spectrum of O ions. For example, the intensity and the

maximal energy of O ions increase with increasing the mass of the second component of the target, which we relate to energy exchange between heavy and light components of the plasma. As we mentioned above, this energy transfer was already been shown both theoretically [14] and experimentally [5, 7]. However, in these studies the mass ratio of the plasma particles was fixed. In what follows, we have performed our experiment for large number target composition. FIG. 5 shows the maximal energies of  $O^{1+}$  (solid curves) and  $O^{2+}$  (dashed curves) ions as a function of the mass of the second component of the target. It is seen from this figure that the maximal energy of single charged oxygen ions increases with increasing  $m$ , which is in good agreement with the recent experiments [7]. This may indicate that even light species of the plasma also can gain from the collisions. With further increasing  $m$  the energy decreases and start saturate after  $m > 160$  amu. However, we could not explain this dependence of the maximal energy of the  $O^{1+}$  ions on the mass of the heavier species. The maximal energy of doubly charged oxygen ions do not strongly depend on  $m$ .

Comparative study of O ions and Sc (Ce, Lu) ions shows that the process of formation and expansion of O ions of all charge multiplicity is determined by the composition of the target. In spite of their different thermo-physical parameters, these elements differ with the mass and it is much larger than the mass of oxygen (mass of Sc, Ce and Lu atoms are 3, 9 and 11 times larger than the mass of oxygen atoms). This difference in mass plays considerable role in the formation of two-element plasma, and consequently to the energy exchange between the ions. Due to the lack of the experimental results for pure Sc, Ce and Lu targets, it is difficult to conclude about the effect of the oxygen ions to the properties of the ions of the second component of the target.

In summary, we have reported time-of-flight measurements of ions produced by laser radiation from solid targets consisting of light (oxygen) and heavy components of different atomic mass  $m$ . We found that the maximum charge of plasma ions does not depend on the nature of the target for considered low intensity of the laser radiation. However, the maximal energy and intensity of light elements of all charge state strongly depend on the mass of the heavy component of the target, which we related to the energy-exchange between different kinds of ions.

## 6. INFLUENCE OF IRRADIATION DOSE OF THE TARGET ON THE CHARACTERISTICS OF EMISSION OF MULTI-CHARGE IONS

In this section, we present the results of our recent experiments to investigate the effect of radioactive irradiation of the targets, which leads to defects of lattice structure of the targets, on the parameters of plasma ions. Figure 1 shows the electron microscopy images of the surface of Al(Mn) sample without and with neutron irradiation of different doses. As we see from this figure neutron irradiation leads to the formation of surface defects with sizes around  $1 \mu\text{m}$  (FIG. 11 (b)). However, with further increasing the dose of the radiation the annealing of some of the defects are observed (FIG. 11 (c)).

As shown in FIG. 11, sample irradiation leads to the increase of boundary of the grains and new pore will appear, the size and concentration of which is determined by the dose of the radiation. High-dose of the radiation may lead to annealing. For example, the results of neutron-structural analysis show that the density of Al target decreases by 8 % after irradiation with dose  $10^{21} \text{ n/cm}^2$  compared to non-irradiated case.

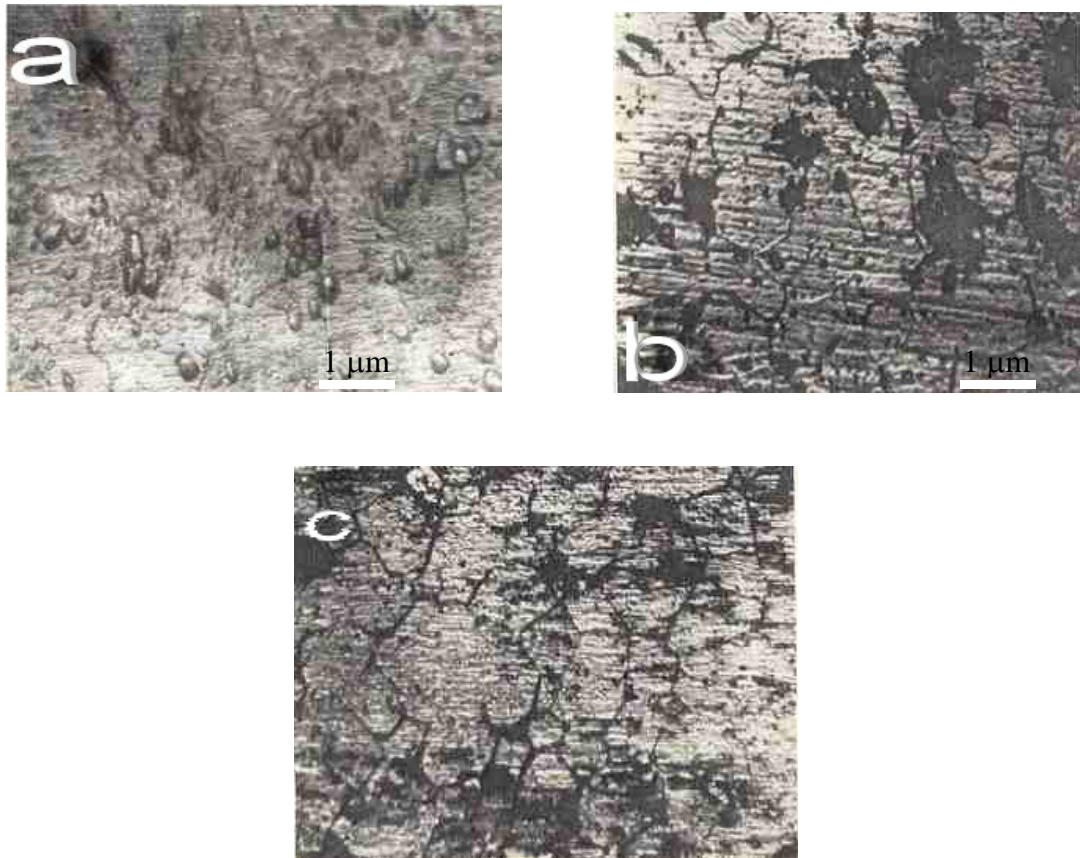


FIG. 11. Microstructure of Al(Mn) targets for different dose of neutron irradiation: (a) without irradiation, (b)  $d=2 \cdot 10^{19}$   $n/cm^2$  and (c)  $d=2 \cdot 10^{20}$   $n/cm^2$ .

The resistance of the targets against the damages by the laser radiation (i.e. the size of the craters formed after the laser incitendt) also dependence on the dose of the radiation  $d$  – it decreases with increasing  $d$ . This resistance also depends on the target composition. For example, the resistance to the laser damages of pure Al target after irradiation with dose of  $10^{19}$   $n/cm^2$  decreased by 10%, while the one of AlMn target by 6%. However, the qualitative behavior of the results obtained during the time-of-flight measurement does not change with including Mn impurities in the Al target. Therefore, in what follows we present the results obtained for Al(Mn) sample.

The energy distribution of  $Al^{3+}$  ions for different values of radiation dose  $d$  is shown in FIG. 12, which shows that the energy spectra of ions expands to high energy ranges with increase  $d$  (compare solid/black and dashed/red curves). However, starting from  $d \sim 10^{19}$   $n/cm^2$  the maximal energy of the ions decreases again (compare dotted/green and dashed-dotted/blue curves). The inset of FIG. 12 shows the dependence of the intensity of  $Al^{3+}$  ions on the radiation dose. The intensity of ions also increases with increasing  $d$ , but starting from some critical dose of the irradiation  $d_c$ , it decreases again. Note that  $d_c$  depends on the charge composition of the ions.

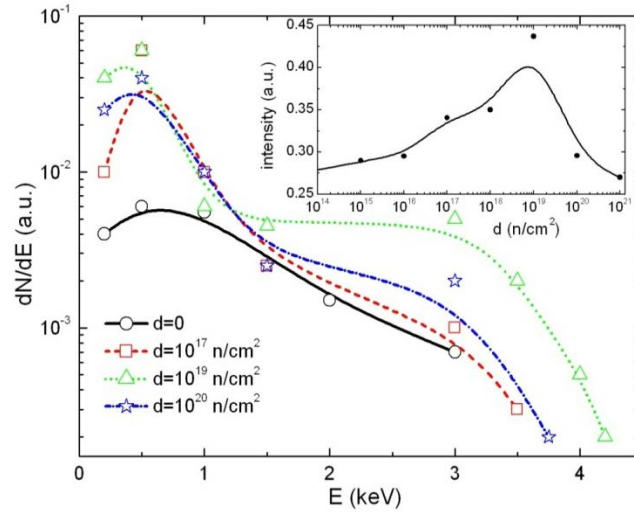


FIG. 12. Energy spectra of  $\text{Al}^{3+}$  ions generated from  $\text{Al}(\text{Mn})$  target at  $q=10^{11} \text{ W/cm}^2$  for different doses of the radiation  $d$ . The inset show the intensity of  $\text{Al}^{3+}$  ions as a function of  $d$ .

We also performed measurements of spatial distribution of laser-plasma ions. Experiment results the irradiation of the targets with doses  $10^{15}$ – $10^{16} \text{ n/cm}^2$  does not have significant influence of the spatial distribution of the ions. Further increase of  $d$  leads to narrowing of the ions distribution and to the shift of the direction of the maximal ions expansion to smaller angles. For the case of irradiated targets with dose  $d \geq 10^{19} \text{ n/cm}^2$  characteristic flow of Al ions is found. Figure 13 shows the spatial distribution of  $\text{Al}(\text{Mn})$  plasma ions for different doses of the neutron irradiation. One of the reasons of narrowing of spatial distribution of ions beam is the decrease of the inertia of the plasma [4]. In our case this means that in the plasma formed with the laser radiation from the irradiated samples, the condition is reached which decreases recombination processes.

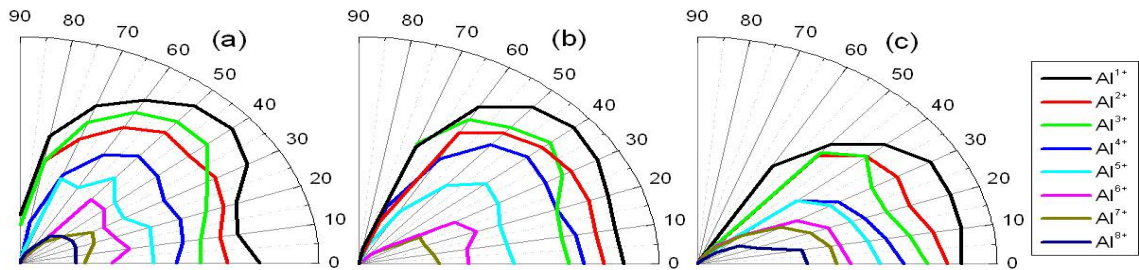


FIG. 13. Spatial distribution of plasma ions generated from  $\text{Al}(\text{Mn})$  target with the laser radiation of intensity  $q = 10^{11} \text{ W/cm}^2$  for the dose of the radiation: (a)  $d=0$ , (b)  $d=10^{19} \text{ n/cm}^2$ , and (c)  $10^{21} \text{ n/cm}^2$ .

Thus, on the base of analysis of experimental results on the dynamics of spatial expansion of ions, formation of energy spectra, as well as plasma currents we conclude that preliminary irradiation of Al targets, further interacted with the laser radiation, leads to the formation of the optimal condition for formation and expansion of plasma. This condition is able to increase efficiency of ionization process and possible decrease of the recombination process.

It is known that the reactor irradiation of the solids leads to the formation of stable structural defects due to breaking of bonds and shift of particles in the lattice points and between them [15]. As a result of shift of crystal particles from their regular position in the

lattice strong potential and local Coulomb field is formed. The interaction of laser radiation with such irradiated targets is different from the interaction with non-irradiated samples because physical properties of irradiated samples are different from the reference sample. The experimental results show that irradiation leads not only to the deterioration of structure of the targets but also to the degradation of the heat and electric conductivity. At the same time the density of the target decreases and micro hardness increases.

Deterioration of electric conductivity properties of the samples means the increase of their ability to absorb the electromagnetic radiation. The increase of the part of the laser radiation absorbed by the target, which has less thermal conductivity than the reference sample, leads to the increase of temperature of the target. The intensity of evaporation process in the sample is determined by the bound energy of atoms [15]. According to the theory of absolute velocity the possibility of elementary evaporation is [16],

$$\Omega = \frac{\kappa T}{h f / f^*} \exp \left\{ -\frac{\lambda_1}{\kappa T} \right\}$$

where  $k$  and  $h$  - Boltzmann and Planck constant,  $f^*$  - statistic sum of activated complex in which the term of "reaction" coordinate is not taken into account,  $f$  - static sum connected with crystalline lattice of atoms,  $\lambda_1$  - activation energy, which equals to the energy for evaporation of one atom at zero temperature,  $T$  - temperature of the layer where evaporation takes place. If we assume  $\lambda_1$  and  $f$  constant, the probability of evaporation is larger due to high temperature. Taking into account the presence of the area with broken and partially weakened bounds in irradiated samples we can assume that these factors also increase the efficiency of the evaporation process. The presence of optimal value of the laser intensity ( $q = 5 \cdot 10^{10} \text{ W/cm}^2$ ), at which the effect of the increase of parameters of the laser plasma confirms the above assumption, as for the given  $q$  the evaporation is caused by thermal mechanism [15].

As a result of increase of density of evaporated material the time of screening of the target surface from the acting laser radiation decreases, which leads to the increase of part of the electromagnetic radiation, which is spent to heat and ionize plasma cloud. At the same time hydrodynamic acceleration of plasma ions increases. The latter effect as well as the formation of dense plasma explains experimentally obtained decrease of the minimal energy of ions formed from the irradiated target. As the plasma itself is heated to high temperatures, the above factors increase its speed of expansion. As a result the time of stay of the plasma in the zone of recombination and the efficiency of recombination processes decrease and ions get out of dense plasma zone with smaller losses of charge and intensity.

## 7. CONCLUSIONS

In summary, generation and characterization of Al ions of high kinetic energies generated during the interaction of laser radiation with the surface of the solid targets, subjected for the neutron irradiation, are carried out. For the same intensity of the laser radiation, the irradiation of Al target with neutrons leads to decrease of plasma formation threshold, as well as to increase of emission, charge and energy of ions and narrowing of the spatial distribution of the ions. The change of properties of irradiated Al targets caused by the formation of structural defects, influences on the efficiency of material evaporation and formation of plasma. Present results can be used to optimize the characteristics of plasma ions for sources of multi-charged ions. This work was supported by IAEA (№13738).

## REFERENCES

- [1] HORA, H., (2004). *Laser Part. Beams* 22, 439-450.
- [2] Conference Report Physics and Technology of Inertial Fusion Energy Targets, Chambers and Drivers IAEA-Conference report- XXXX, ISBN, ISSN© IAEA,2005, Printed by the, IAEA in Austria.
- [3] DUBENKOV, V., SHARKOV, B., et.al.(1996). *Laser and Particle Beams* 14 (3), 385-392.
- [4] ROSMEJ, F.B., HOFFMANN, D.H.H., et.al., (2002). *Laser and Particle Beams* 20 (4), 555-557.
- [5] KHAYDAROV, R.T., et al., *Laser and Particles Beams* 23, 512 (2005).
- [6] KHAYDAROV, R.T., et al., *Plasma and Fusion Science: AIP Conf. Proc.* April 7, 2008, Volume 996, pp. 251-256; DOI:10.1063/1.2917020.
- [7] SRIVASTAVA, S.N., et al., *J. Phys. D: Appl. Phys.* 38, 3643-3653 (2005).
- [8] KHAYDAROV, R.T., et al., *International Journal of Plasma Science and Engineering*, (2008), doi:10.1155/2008/180950.
- [9] KHAYDAROV, R.T., et al., *Nucl.Fusion* ,49 pp7 (2009).
- [10] KHAYDAROV, R.T., et al., *Phys. Plasmas* 9, (2009).
- [11] KHAYDAROV, R.T., et al., *Nucl.Fusion* ,50 (20010)025024(5pp).
- [12] TORRISI, L., et al., *J. Appl. Phys.* 91, 4685 (2002).
- [13] *Electron Impact Ion Sources for Charged Heavy ions*, edited by G.D. Shirkov et al. (F. Vieweg & Sohn, Publ., Gottingen, 1996).
- [14] URBASSEK, H.M., and SIBOLD, D., *Phys. Rev. Lett.* 70, 1886 (1993).
- [15] SAWAN, M.E., MCGEOCH, M. W., IBRAHIM, A., and WILSON, P., *Fusion Science and Technology*, 52, 938 (2007).
- [16] MOIN, M.D., *Russian journal Surface Physics* 26, 2742 (1984).

# THE STUDY OF THE BEAM COMBINATION LASER SYSTEM WITH HIGH POWER/ENERGY AND HIGH REPETITION RATE USING STIMULATED BRILLOUIN SCATTERING PHASE CONJUGATE MIRRORS (SBS-PCMS) FOR LASER FUSION DRIVER

H.J. KONG, J.S. SHIN, S. PARK, K.S. SHIM, S. CHA

Department of Physics

KAIST

Daejeon, Republic of Korea

## Abstract

Beam combining method with stimulated Brillouin scattering phase conjugate mirrors (SBS-PCMs) is a promising technique for achieving a laser fusion driver with high-energy, high power, and high-repetition-rate of  $\sim 10$  Hz. The key techniques for the realization of the beam combination laser system, “the self-phase-control technique” and “the pre-pulse injection technique,” were proposed by H. J. Kong *et al.* and have been developed. In this project, the further developments have been achieved for the practical application of the beam combination system. The active phase control has been performed to stabilize the thermally induced long-term phase fluctuation. And the four-beam combination systems with the amplitude dividing and the wave-front dividing schemes have been constructed and tested. In the four-beam combination systems, the active controls of the SBS-PCMs have made the phase fluctuations less than  $\lambda/30$ . Operating the amplifiers in the wave-front dividing scheme, the phase fluctuation stabilized less than  $\lambda/25$ . As a further study for the pre-pulse injection technique, the relationship between the pre-pulse energy and the delay time for the waveform preservation of the SBS wave has been also investigated experimentally. It has been shown that the minimum pre-pulse energies required for the waveform preservation are 10 mJ, 3 mJ, 2 mJ and 4 mJ for the delay times of 3 ns, 8 ns, 15 ns and 17 ns, respectively.

## 1. INTRODUCTION

Laser Fusion Energy (LFE) is one of the most promising sources of clean energy for mankind. A laser driver for a commercial power plant requires high repetition rate operation of 10 Hz with pulse energy of several mega-joules in a several nanoseconds [1]. The beam combination method can resolve the fundamental thermal problems by combining many small amplifiers that operate at a high repetition rate [2-22]. The small amplifiers operate below the thermal limitation so that the combined beam system can operate with the same repetition rate as the small amplifier.

H.J. Kong *et al.* proposed and have developed the beam combination laser system using stimulated Brillouin scattering phase conjugate mirrors (SBS-PCMs) [2-16]. There are two main obstacles for the achievement of the beam combination system. One obstacle is the random phase of the SBS wave due to its generation from a thermal noise [23]. For the coherent output, the randomness of the SBS wave should be overcome. For this purpose, H. J. Kong *et al.* proposed a new phase control technique, so called “the self-phase-control technique,” and the effectiveness of this technique was demonstrated experimentally [4-6]. With this technique, the phases of the SBS waves can be controlled independently with a simplest optical composition so that the scaling up has no limitation to the number of the beams to be combined. The other obstacle for the beam combination laser is the deformation of the temporal SBS waveform [24]. The SBS wave has a steep rising edge, because the pump beam consumes its front part energy for the generation of the acoustic grating. This waveform deformation can cause optical breakdowns in the optical components. To overcome this problem, “the pre-pulse injection technique” was proposed and demonstrated successfully by H. J. Kong *et al.*, [24].

In this project, the further development has been achieved for the practical application of the beam combination system using SBS-PCMs. An active phase control using the piezoelectric translators (PZTs) has been performed to stabilize the thermally induced long-term phase fluctuation in the beam combination system with amplitude dividing

scheme [12-13]. And the four-beam combination systems with the amplitude dividing and the wave-front dividing schemes have been constructed, and the long-term phase stabilization of the SBS waves have been achieved with the self-phase-control and the active control [14-16]. Besides the phase stabilization of the SBS wave, as a further study for the pre-pulse injection technique, the relationship between the pre-pulse energy and the delay time in the waveform preservation of the SBS wave has been investigated experimentally and theoretically [25].

## 2. LONG TERM PHASE STABILIZATION OF THE SBS WAVE

The self-phase-control technique can control/lock the phase of the SBS wave for every laser shot. However, a thermally induced long-term phase fluctuation has been presented. This long-term phase fluctuation can be effectively stabilized by positioning using a PZT (piezoelectric translator) attached to the feedback mirror as shown in FIG. 1. The active control is carried out as follows. First, the relative phase of the combining beams is measured by analyzing the interfered energy. Then, the PZT-attached concave mirror is controlled to maintain the zero phase difference between the SBS beams.

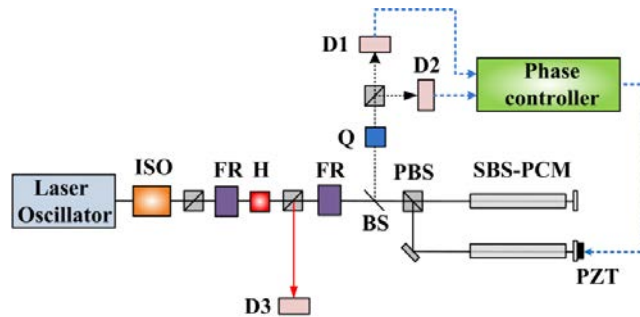


FIG. 1. Experimental setup for the long-term phase stabilization: ISO, optical isolator; FR, Faraday rotators; H, half-wave plates; Q, quarter wave plates; PBS, polarizing beam splitters; BS, beam splitter; D1, D2, and D3, energy detectors; PZT, piezoelectric translator.

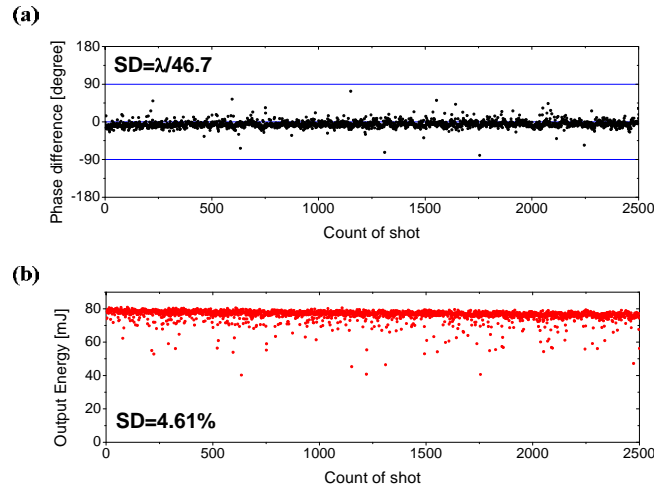


FIG. 2. Experimental results of (a) the phase difference between the SBS beams and (b) the output energy with active control during 2500 laser shots (250 s).

FIG. 2(a) shows the phase difference measured during 2500 shots (250 s) for the case with PZT control, and FIG. 2(b) shows the corresponding output energy. In this case, the phase difference between the SBS beams and the output energy are stabilized quite well. The

phase fluctuation is measured to be  $\lambda/46.7$  and the output energy fluctuation is measured to be 4.61%.

### 3. FOUR-BEAM COMBINATION LASERS

#### 3.1. Amplitude dividing scheme

As a further development of the beam combination laser using SBS-PCMs, the four-beam combination laser system is constructed with the amplitude dividing scheme. FIG. 3 shows the experimental setup. The beam passes through the polarizing beam splitter (PBS) and the quarter wave plate (QWP3). The QWP3 changes the linear polarization to a circular polarization so that the beam is divided into two beams with almost equal energies at the second PBS. Each divided beam is split into two beams again by the PBS after passing through the HWP1 or HWP2. Consequently, the initial beam is divided into four sub-beams with equal energies. The four sub-beams are reflected by the four separated self-phase-controlled SBS-PCMs and recombined again after reflections from the SBS-PCMs.

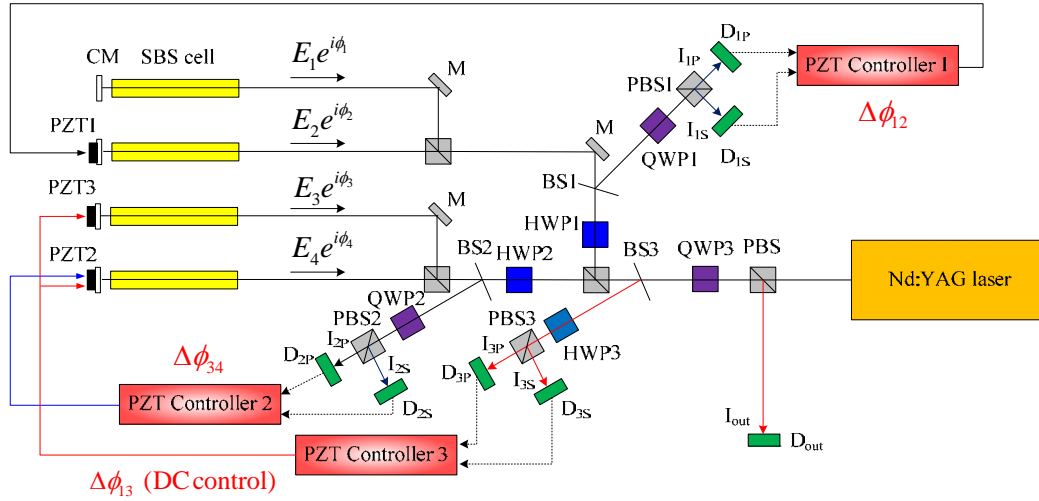


FIG. 3. Experimental setup for the four-beam combination system with amplitude division: PBS, PBS1, PBS2, and PBS3, polarizing beam splitter; HWP1, HWP2, and HWP3, half wave plates; BS1, BS2, and BS3 beam splitters; QWP1, QWP2, and QWP3, quarter wave plates; M, mirrors; CM, concave mirrors; PZT1, PZT2, and PZT3, piezoelectric translators.

To compensate the long-term phase fluctuations of the beams, PZTs are attached to the three concave mirrors as shown in FIG. 3. Since the overall system is essentially a cascaded system of two-beam combination laser, the compensation is done in steps. The phase fluctuations of two sub-beam combination are measured using the interfered energy of them. And the compensation signals are applied to one PZT of each beam combination module. At the same time, the phase fluctuation between the two-beam combination modules is measured in the same manner, and the compensation signal is applied to the two PZTs of the same sub combination module.

The experimental results of the phase differences with the long-term phase stabilization are shown in FIG. 4. The phase differences between the SBS waves are stabilized well during 2000 shots (200 s). The phase difference,  $\phi_{ij}$ , is defined as  $\phi_i - \phi_j$ , where  $\phi_i$  is the phase of the  $i$ th beam. The standard deviations of the fluctuations of  $\phi_{12}$ ,  $\phi_{13}$ , and  $\phi_{14}$  are measured to be  $\lambda/34.3$ ,  $\lambda/37.6$ , and  $\lambda/30.5$ , respectively. FIG. 5 shows the four beam combined

output energy during 2000 shots (200 s). The output energy is also stabilized well and the measured energy fluctuation is 6.16% by standard deviation.

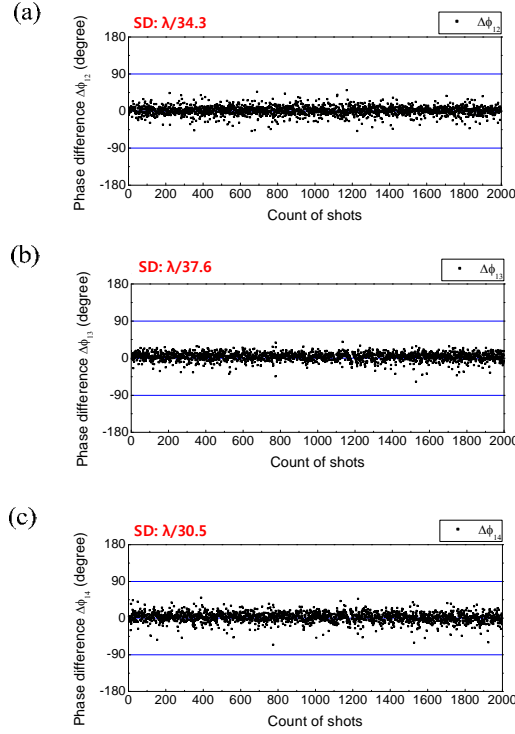


FIG. 4. Long-term stabilized phase differences between the SBS beams during 2000 shots (200 s) between (a) Beam1 and Beam2, (b) Beam1 and Beam3, and (c) Beam1 and Beam4 for the amplitude dividing four-beam combination laser.

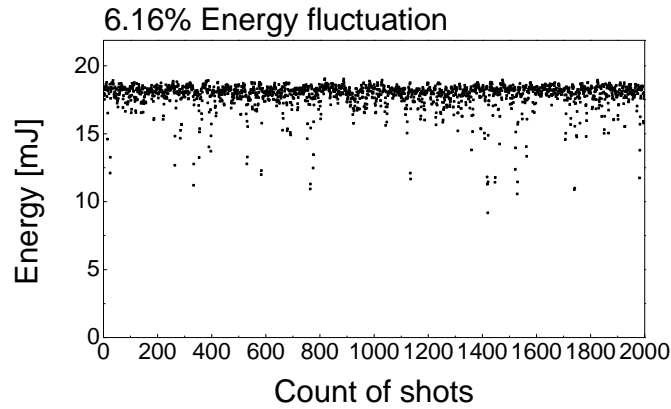


FIG. 5. Long-term stabilized output energy during 2000 shots (200 s) for the amplitude dividing four-beam combination laser.

### 3.2. Wave-front dividing scheme

For another development of the beam combination laser using SBS-PCMs, the four-beam combination laser amplifier system is constructed with the wavefront dividing scheme. FIG. 6 shows the experimental setup. The beam from the oscillator is expanded by four times with spherical lenses with focal lengths of  $f = -50$  mm and  $f = 200$  mm. The expanded beam is spatially divided into four sub-beams after passing through an aperture consisting of a  $2 \times 2$  array of circular holes with 6 mm diameter. After passing PBS, four beams are separated



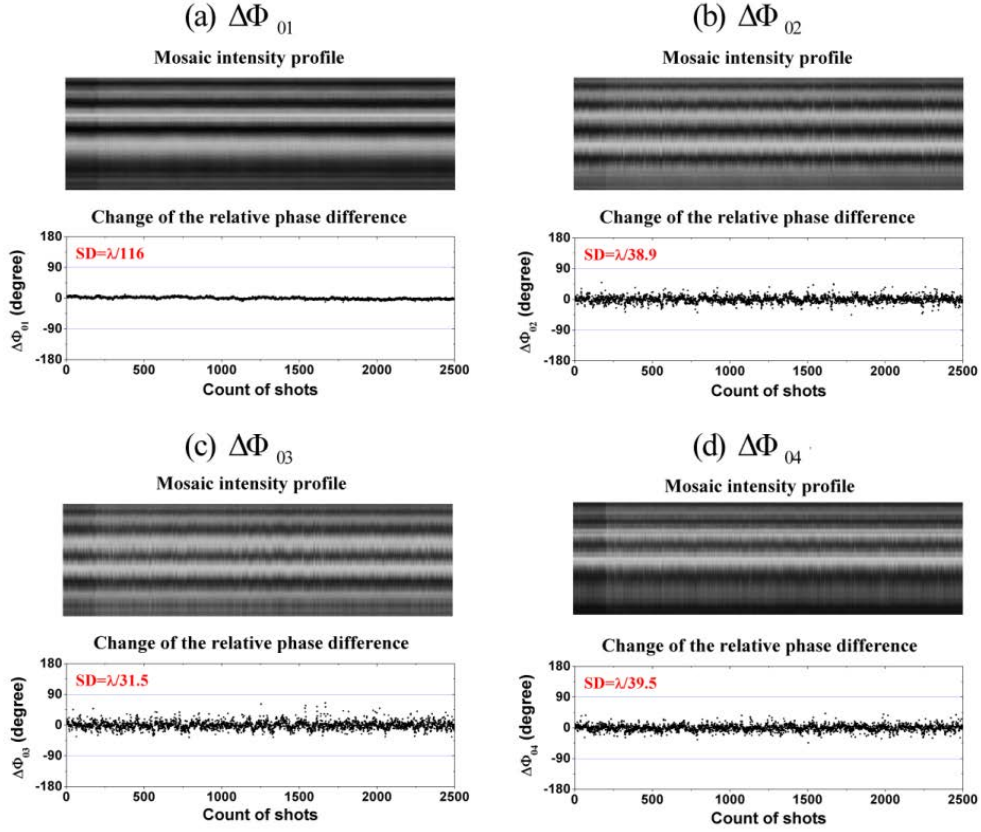


FIG. 8. Measured mosaic intensity profiles of the interference patterns and changes of phase differences between (a) Beam0 and Beam1 ( $\Delta\Phi_{01}$ ), (b) Beam0 and Beam2 ( $\Delta\Phi_{02}$ ), (c) Beam0 and Beam3 ( $\Delta\Phi_{03}$ ), and (d) Beam0 and Beam4 ( $\Delta\Phi_{04}$ ) during 2500 shots (250s) without amplification.

FIG. 8 shows the measured mosaic intensity profiles of the interference patterns and changes in the phase differences between (a) Beam0 and Beam1 ( $\Delta\Phi_{01}$ ), (b) Beam0 and Beam2 ( $\Delta\Phi_{02}$ ) (c) Beam0 and Beam3 ( $\Delta\Phi_{03}$ ), and (d) Beam0 and Beam4 ( $\Delta\Phi_{04}$ ) during 2500 shots (250 s), which are obtained without amplification. In this case, the total output energies of the recombined SBS beams are measured to be  $9.9 \pm 0.5$  mJ for the input energy of  $32.0 \pm 0.3$  mJ. In the experiment, the standard deviations of  $\Delta\Phi_{01}$ ,  $\Delta\Phi_{02}$ ,  $\Delta\Phi_{03}$ , and  $\Delta\Phi_{04}$  are measured to be  $\lambda/116$ ,  $\lambda/38.9$ ,  $\lambda/31.5$ , and  $\lambda/39.5$ , respectively.  $\Delta\Phi_{01}$  shows a very low phase fluctuation, because both Beam0 and Beam1 are generated from the same SBS-cell.  $\Delta\Phi_{02}$ ,  $\Delta\Phi_{03}$ , and  $\Delta\Phi_{04}$  fluctuate according to the degree of the phase control from the independent SBS waves. All the phases of SBS waves are well-stabilized less than  $\lambda/30$ .

FIG. 9 shows the measured mosaic intensity profiles of the interference patterns and changes of the phase differences between (a) Beam0 and Beam1 ( $\Delta\Phi_{01}$ ), (b) Beam0 and Beam2 ( $\Delta\Phi_{02}$ ) (c) Beam0 and Beam3 ( $\Delta\Phi_{03}$ ), and (d) Beam0 and Beam4 ( $\Delta\Phi_{04}$ ) during 2500 shots (250 s), which are obtained with the operation of the amplifiers. In this case, the total output energy is measured to be  $169 \pm 6$  mJ, which corresponds to the gain of 5.3 for the same input energy. In the experiment, the standard deviations of  $\Delta\Phi_{01}$ ,  $\Delta\Phi_{02}$ ,  $\Delta\Phi_{03}$ , and  $\Delta\Phi_{04}$  are measured to be  $\lambda/68.8$ ,  $\lambda/26.5$ ,  $\lambda/28.0$  and  $\lambda/26.1$ , respectively. All the phases of the amplified beams are well-stabilized less than  $\lambda/25$ .

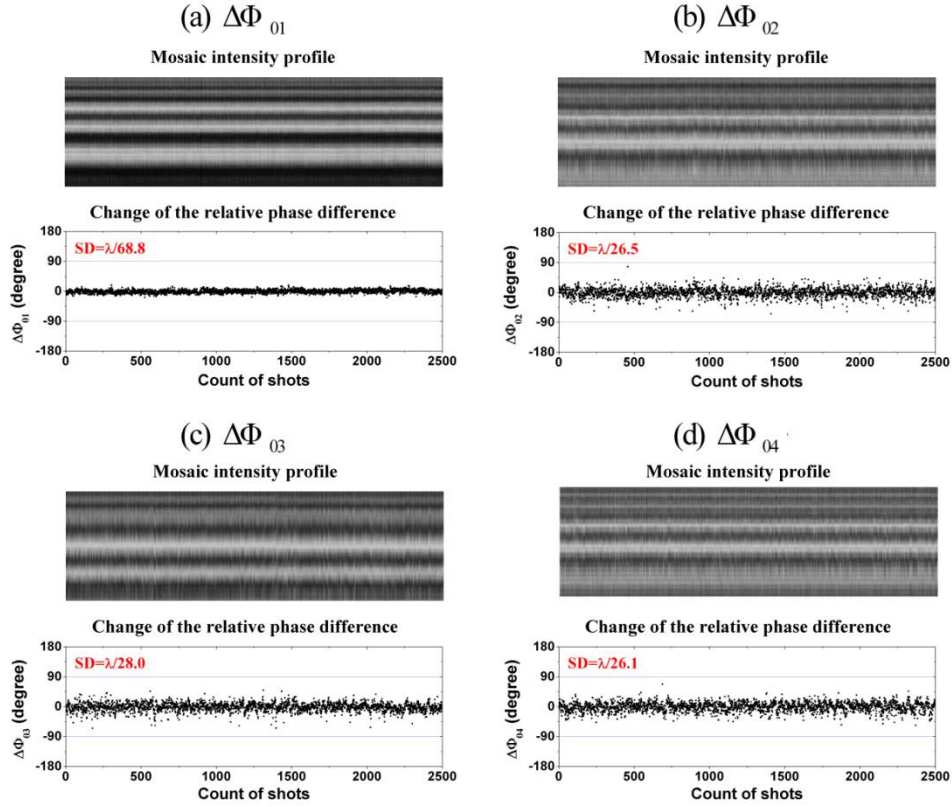


FIG. 9. Measured mosaic intensity profiles of the interference patterns and changes of phase differences between (a) Beam0 and Beam1 ( $\Delta\Phi_{01}$ ), (b) Beam0 and Beam2 ( $\Delta\Phi_{02}$ ), (c) Beam0 and Beam3 ( $\Delta\Phi_{03}$ ), and (d) Beam0 and Beam4 ( $\Delta\Phi_{04}$ ) during 2500 shots (250 s), with the operation of the amplifiers.

#### 4. INVESTIGATION OF THE RELATIONSHIP BETWEEN THE PRE-PULSE ENERGY AND THE DELAY TIME

FIG. 10 shows the experimental setup for measuring the investigation of the relationship between the pre-pulse and the delay time. A single longitudinal mode Nd:YAG laser is used as a laser source. It has a pulse width of  $\sim 7$  ns and a repetition rate of 10 Hz. The beam passes through a half wave plate (HP2) and is divided by the polarizing beam splitter (PBS2) into the two pulses—the main pulse and the pre-pulse. The main pulse energy is fixed at 10 mJ, and the pre-pulse energy is varied using the HP3 and the PBS3. The main pulse is reflected by a plane mirror and passes the delay line twice, and the delay time between the main pulse and the pre-pulse is controlled by adjusting the length of the delay line. After the serial reflection from the SBS-PCM (a lens + FC-75), the pre-pulse is dumped out through the PBS3 while the main pulse is reflected from the PBS4 and arrives at the photodiode (PD). Varying the delay time and the pre-pulse energy, the temporal waveforms of the reflected SBS waves are observed by a fast photodiode (PD).

The experimental results of FIG. 11 and 12 show that the waveform of the SBS wave can be preserved very well by using the pre-pulse injection technique, and the minimum pre-pulse energies required for the waveform preservation are dependent on the delay time. The required pre-pulse energies are measured to be 10 mJ, 3 mJ, 2 mJ and 4 mJ for the delay times of 3 ns, 8 ns, 15 ns and 17 ns, respectively.

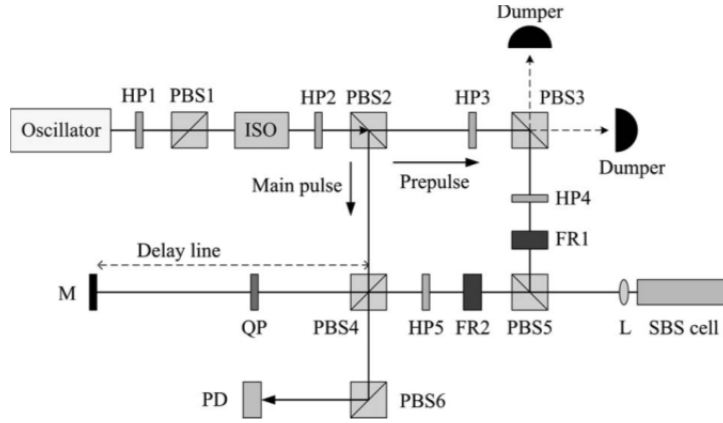


FIG. 10. Experimental setup for the pre-pulse injection method: HP1, HP2, HP3, HP4, and HP5, half-wave plates; PBS1, PBS2, PBS3, PBS4, and PBS5, polarizing beam splitters; ISO, optical isolator; FR1 and FR2, Faraday rotators; QP, quarter-wave plate; M, mirror; L, focusing lens; PD, photodiode.

FIG. 11 is a typical example of the SBS waveform preservation for the 15 ns delay time. The waveform distortion for the non-pre-pulse injection case shows a typical SBS waveform as depicted in FIG. 11(a). The SBS waveform starts to be recovered by increasing the pre-pulse energy, and it is recovered fully when the pre-pulse energy is equal to 2 mJ or more. FIG. 12 shows the required pre-pulse energy versus the delay time. The filled dots represent the experimental results for the minimum pre-pulse energy required for waveform preservation versus the delay time. And the blank dots represent the theoretical simulation results. For the theoretical simulation, it is assumed that the SBS threshold energy is 2 mJ and phonon decay time is 0.9 ns. And it is also assumed that the accumulated phonon energy required for the SBS ignition is equal to the threshold energy. The simulation result also shows a U-shaped curve and qualitatively agrees with the experimental results [25].

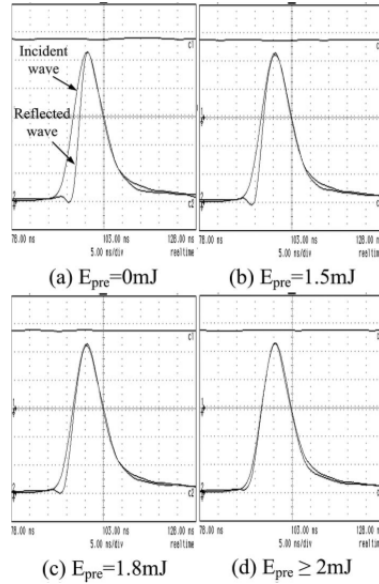


FIG. 11. Reflected SBS waveforms when the delay time is 15 ns and the pre-pulse energy is (a) 0 mJ, (b) 1.5 mJ, (c) 1.8 mJ, and (d) more than 2 mJ.

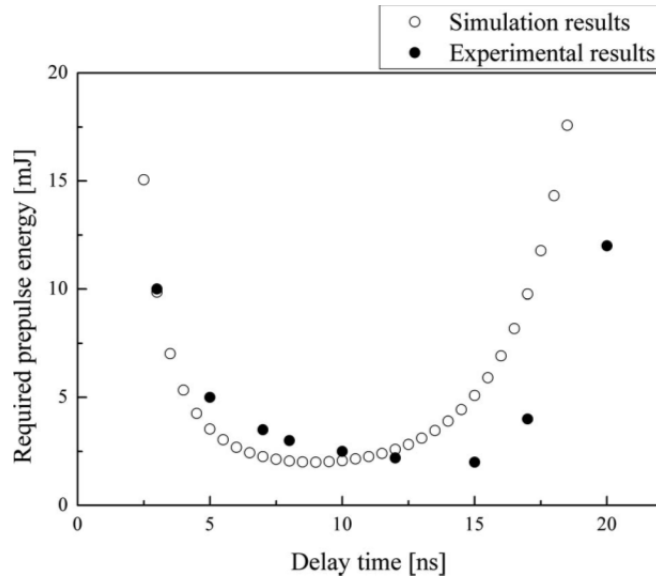


FIG. 12. Required pre-pulse energy versus delay time: the experimental (filled dots) and the simulation result (blank dots).

## 5. CONCLUSIONS

In conclusion, the active phase control has been performed to stabilize the thermally induced long-term phase fluctuation in the beam combination system with amplitude dividing scheme. With the active control, the phase fluctuation of SBS wave is measured to be  $\lambda/46.8$  during 2500 shots (250s) for the 2 beam combination system. And the four-beam combination systems with the amplitude dividing and the wave-front dividing schemes have been constructed and tested, and the phase stabilization of the SBS waves have been achieved with the self-phase-control and the active control systems. In the amplitude dividing and the wavefront dividing schemes, the SBS phase fluctuations are stabilized less than  $\lambda/30$ . Operating amplifiers in the wave-front dividing scheme, the phase fluctuations are stabilized less than  $\lambda/25$ . As a further study for the pre-pulse injection technique, the relationship between the pre-pulse energy and the delay time for the waveform preservation of the SBS wave has been investigated. It has been shown that the minimum pre-pulse energy required for the waveform preservation is dependent on the delay time, and are measured to be 10 mJ, 3 mJ, 2 mJ, and 4 mJ for the delay times of 3 ns, 8 ns, 15 ns, and 17 ns, respectively. Based on these experimental works, it is expected that the beam combination technique can be applied to develop a practical laser fusion driver module in future.

## ACKNOWLEDGEMENTS

This work was supported by the Nuclear Research and Development Program of the Korea Science and Engineering Foundation (KOSEF) grant funded by the Korean government (MEST) (grant code: M20090078160), RandD Program through the National Fusion Research Institute of Korea (NFRI) funded by the Ministry of Education, Science and Technology, the KAIST High Risk High Return Project (HRHRP), and the International Atomic Energy Agency (IAEA) as a part of the coordinated research project “Pathway to Energy from Inertial Fusion – An Integrated Approach” (Research Contract No. 13758/R0).

## REFERENCES

- [1] NAKAI, S., MIMA, K., REP. PROG. PHYS. 67, 321 (2004).
- [2] KONG, H.J., LEE, J.Y., SHIN, Y.S., Opt. Rev. 4, 277 (1997).
- [3] KONG, H.J., SHIN, Y.S., KIM, H., Fusion Eng. Des. 44, 407 (1999).
- [4] KONG, H.J., LEE, S.K., LEE, D.W., Laser Part. Beams. 23, 55 (2005).
- [5] KONG, H.J., LEE, S.K., LEE, D.W., Laser Part. Beams. 23, 107 (2005).
- [6] KONG, H.J., LEE, S.K., LEE, D.W., GUO, H., Appl. Phys. Lett. 86, 051111 (2005).
- [7] LEE, S.K., KONG, H.J., NAKATSUKA, M., Appl. Phys. Lett. 87, 161109 (2005).
- [8] KONG, H.J., LEE, S.K., YOON, J.W., BEAK, D.H., Opt. Rev. 13, 119 (2006).
- [9] KONG, H.J., YOON, J.W., SHIN, J.S., BEAK, D.H., LEE, B.J., Laser Part. Beams 24, 519 (2006).
- [10] KONG, H.J., YOON, J.W., LEE, D.W., LEE, S.K., NAKATSUKA, M., J. Korean, Phys. Soc. 49, S39 (2006).
- [11] LEE, S. K., KONG, H. J., YOON, J.W., NAKATSUKA, M., KO, D.K., J. LEE, J. Phys. IV France 133, 621 (2006).
- [12] KONG, H. J., YOON, J. W., BEAK, D.H., SHIN, J.S., LEE, S.K., LEE, D.W., Laser Part. Beams 25, 225 (2007).
- [13] KONG, H. J., YOON, J.W., SHIN, J.S., BEAK, D.H., Appl. Phys. Lett. 92, 021120 (2008).
- [14] KONG, H. J., SHIN, J.S., YOON, J.W., BEAK, D.H., Laser Part. Beams 27, 179 (2009).
- [15] KONG, H. J., SHIN, J.S., YOON, J.W., BEAK, D.H., Nucl. Fus. 49, 125002 (2009).
- [16] SHIN, J.S., PARK, S., KONG, H. J., YOON, J.W., Appl. Phys. Lett. 96, 131116 (2010).
- [17] BASOV, N.G., EFIMKOV, V.F., ZUBAREV, I.G., KOTOV, A.V., A.B. MIRONOV, S.I. MIKHAILOV, M.G. SMIRNOV, Sov. J. Quantum Electron. 9, 455 (1979).
- [18] ROCKWELL, D.A., GIULIANO, C.R., Opt. Lett. 11, 147 (1986).
- [19] VALLEY, M., LOMBARDI, G., APRAHAMIAN, R.J., Opt. Soc. Am. B 3, 1492 (1986).
- [20] LOREE, T.R., WATKINS, D.E., JOHNSON, T.M., KURNIT, N.A., FISHER, R.A., Opt. Lett. 12, 178 (1987).
- [21] RIDLEY, K.D., J. Opt. Soc. Am. B 12, 1924 (1995).
- [22] BOWERS M.W., BOYD, R.W., IEEE J. Quantum Electron. 34, 634 (1998).
- [23] BOYD, R.W., RZEWSKI, K., NARUM, P., Phys. Rev. A 42, 5514 (1990)
- [24] KONG, H. J., BEAK, D.H., LEE, D., Opt. Lett. 30, 3401 (2005).
- [25] YOON, J.W., SHIN, J.S., KONG, H. J., LEE, J., J. Opt. Soc. Am. B 26, 2167 (2009).

# OPTIMIZING CRYOGENIC LAYERING FOR INERTIAL FUSION ENERGY (IFE) TARGETS FOR PROVIDING TARGET SURVIVAL DURING THE INJECTION PROCESS

I.V. ALEKSANDROVA, A.A. BELOLIPETSKIY, E.R. KORESHEVA, A.M. OPARIN,  
I.E. OSIPOV, A.A. TONSHIN  
Lebedev Physical Institute of RAS,  
Moscow, Russian Federation

## Abstract

In this report, the results on fabrication of isotropic ultra-fine condensed layers for IFE fuel targets are overviewed. In our investigations, dependencies on degree of microstructure regularity and bulk fuel properties are demonstrated. We have shown the potentialities of creating the isotropic ultra-fine layers having an increased mechanical strength and thermal stability. Application of such layers allows minimizing the risk of fuel layer destruction during target delivery as compared with an anisotropic crystalline fuel. Our experimental researches have proved that isotropic thermo-stable ultra-fine fuel layer can be formed by FST method developed in the Russian Federation under the following conditions: cooling rate  $\sim 1\div 50$  K/sec, layering time  $\leq 15$  sec, using high-melting additives as stabilizing agents in the amount of  $\sim 3\div 20\%$  (note that for DT mixture, tritium stands as a high-melting additive relative to deuterium). Thus, the application of a fuel layer in an isotropic ultra-fine state is very promising in IFE because this allows to solve the target survival problems and to provide the shock wave propagation through the isotropic solid fuel, which is of critical importance for the stable compression of IFE targets.

## 1. INTRODUCTION

International research into inertial confinement fusion (ICF) is aimed at constructing by the year 2040 a demonstration reactor operated in the pulse-periodic mode at a frequency of 0.1-10 Hz [1-3]. The first stage of the program is to obtain by 2015 a high energy gain in the mode of single-shot irradiation of fuel targets.

It is assumed that the demonstration of thermonuclear (fusion) ignition, burn and positive energy gain in various ICF schemes with a laser driver shall be achieved on high-power facilities constructed in the USA, France, Japan and the Russian Federation [3-6]. The scaling experiments performed at present at the 30-kJ, 60-beam OMEGA laser [7,8] are to confirm the possibility of producing a high energy gain in future experiments on the high-power National Ignition Facility (NIF).

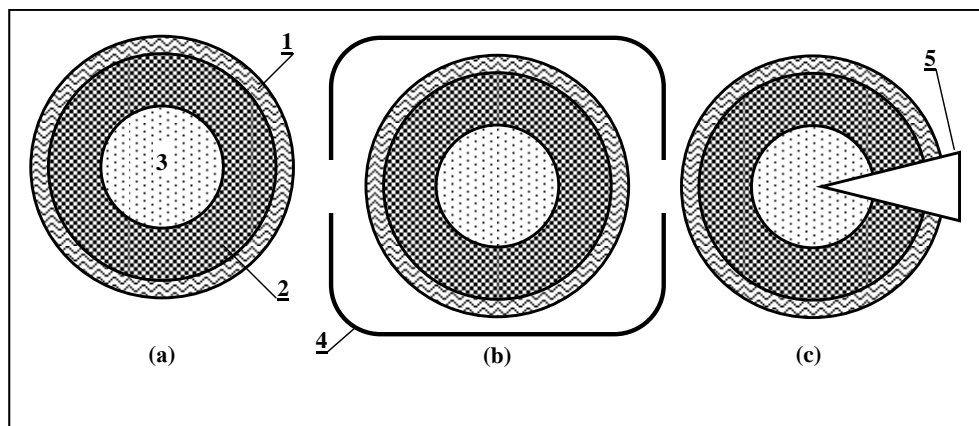


FIG. 1. Schematics of fuel targets for different concepts of irradiation: (a) direct-drive target, (b) indirect-drive target, (c) target for fast ignition; 1 – shell wall, 2 – layer of DT-fuel, 3 – DT-vapor, 4 – cylindrical converter, 5 – guiding cone.

Three possible schemes of irradiating the target with a laser light are considered at present: direct drive, indirect drive and fast ignition. The structure and parameters of the target essentially depend on irradiation energy and also on the scheme of interaction of the

laser-target pair, as the result of which a high compression and heating of DT fuel is achieved. However, as seen in FIG. 1, the targets for each of the above schemes have a common component, a spherical capsule (or shell usually fabricated from a polymer material), which contains DT fuel. In the direct drive scheme, this component represents a cryogenic target in its classical configuration.

For the laser-target interaction to have a required effect, the fuel should be compressed with a high speed and at minimal entropy. As the first shock wave, when moving through fuel with density  $\rho$  under the action of pressure  $P$ , introduces entropy of the order of  $s \sim P/\rho^{5/3}$  into the substance, the fuel to be used should be the one with a maximum possible initial density, i.e., condensed.

The use of condensed fuel not only ensures the optimal regime of fusion target compression, but is the only practical possibility of realizing a state-of-the-art laser experiment and the operation of future reactors. Indeed, the amount of fuel in targets for the acting OMEGA laser facility, high-power facilities being built (NIF, ISKRA-6 & UFL-2M, HiPER) and the reactor is such that at room temperature the pressure of fuel gas inside the thin polymer shell is within the range of 100 up to 1000 atm. As the shell does not withstand more than (5-40) atm at  $T = 300$  K, it is evident that this high internal pressure would inevitably result in its rupture.

The only possibility to avoid the shell rupture and the radioactive fuel leakage is to condense the fuel onto the inner shell wall, bearing in mind that the pressure of saturated vapors over the condensate surface is rather small:  $\sim 0.19$  atm for a DT mixture and  $\sim 0.17$  atm for  $D_2$  (the triple point data [9]).

According to the current views, the direct irradiation of a spherical target is the most promising configuration of an energy station using laser irradiation to achieve the fuel ignition and burn conditions. The requirements to the quality of the components that constitute a direct-drive target are the most stringent (as compared with the other irradiation protocols). In particular, the parameters of the cryogenic fuel layer should satisfy the following quality criteria [11, 12]:

- (1) Thickness variation (layer non-uniformity): no more than 2%
- (2) Free surface roughness: no more than 1.0 - 0.5  $\mu\text{m}$
- (3) Temperature:  $\sim 1.5$  degree lower than the fuel triple point

The fulfillment of the above conditions enables reducing the development of hydrodynamic instabilities in compression and avoiding the mix-up of cold and hot fuels in the central zone of the compressed target (hot spot), i.e., producing in the centre the densities and temperatures required to ignite self-sustaining fusion reactions (the ignition conditions for DT fuel:  $\rho R \sim 1\text{-}3$  g/cm<sup>2</sup>,  $T \sim 5\text{-}8$  keV).

At current stage of the ICF program, the major requirements to the production cryogenic targets with DT fuel are as follows [13, 14]:

- (1) Formation of a smooth and uniform solid layer inside the fuel core.
- (2) The fuel layer should be resistant to the environmental effects during target delivery from the formation zone to the irradiation zone.

- (3) The formation method should satisfy the requirements on the tritium inventory minimization in the target system, i.e., the minimization of the time and space scales of each operation.

The problems of using the cryogenic targets in ICF experiments are conditioned by the peculiarities of standard layering technologies based on the fuel layer formation in the equilibrium crystalline state (temperature variation onto the outer target surface  $< 1$  mK; cooling rates  $q < 1$  mK/min) [15,16].

Such a layer preserves its quality only near the triple point ( $T_{tp}$ ) of fuel and does not exist in the required temperature region (1.5 degrees below the triple point ( $\sim 18$  K for DT)). Cooled only 0.1- 0.3 K below the triple point  $T_{tp}$ , the DT layer cracks due to the stresses caused by fuel density changes. The instability is a consequence of the anisotropy of the crystalline hydrogen isotopes, and also of a decrease in the strength of the DT layer due to the bubble defects because of the evolution of  $^3\text{He}$  in the  $\beta$ -decay of tritium.

Besides, the layering time in such an approach is rather long (5-to-24 hrs), which leads to a high tritium inventory in the target system. Application of nano-structured materials allows surviving the samples under conditions of periodical thermal and mechanical stresses arising in the process of power plant operation. Therefore, it is recommended to use nano-structured materials in the main building blocks of inertial fusion energy (IFE) power plant, namely: chamber wall [17], laser [18], and fuel target [19, 20].

This means that a part of work should be devoted to one more important issue – application of advanced materials with prescribed properties, including those used for fuel layer formation (ultra-fine solid hydrogen isotopes).

Note that the term “ultra-fine” layer relates to material state, which is characterized by an ultra-fine micro-structural length or grain size. It can be classified into the following structural states: near-nano (submicron) crystalline state (grain size 0.1-to-0.3  $\mu\text{m}$ ), nano-crystalline state (grain size  $\leq 150$ -200 nm), amorphous state (characteristic scale or order parameter  $\sim 1$  nm).

Very often, submicron (near-nano) crystalline state is called “fine-grained” crystalline. Depending on a formation method (more specifically, on a cooling rate) the solid fuel layer can be in the state with a different level of dispersion: ultra-fine layers in a high-dispersed state (fine-grained crystalline, nano-crystalline, amorphous) and anisotropic molecular crystals (real single crystals, coarse-grained crystalline).

As the size reduces into the nanometer range, the materials exhibit peculiar and interesting mechanical and physical properties, e.g. increased mechanical strength and thermal stability, enhanced diffusivity, higher specific heat and electrical resistivity compared to conventional coarse-grained counterparts. In many cases, even near-nano crystalline materials are increasingly finding application in engineering systems.

Therefore, the layer formation as nano-structured solids holds much promise for solution of the problem of survivability of fuel layers under conditions of the environmental effects.

Preliminary researches carried out at the Lebedev Physical Institute of RAS (LPI) [19, 21, 22] have shown that using ultra-fine fuel layers offers the following advantages before traditionally applied crystalline ones (real single crystals, coarse-grained crystalline):

- (1) They give rise to a significant shortening of the layering time (from tens of hours to tens of seconds) and, thus, tritium inventory minimization.
- (2) They are less sensitive to the g-loads due to its higher mechanical strength.
- (3) They are less sensitive to the heat-loads due to its isotropy.

Such properties of ultra-fine fuel layers reduce the cost of the production steps related to the target formation and delivery, and provide for reliable operation and service safety. This indicates that IFE power plant can have more attractive cost, safety and environmental features.

Despite a basic understanding, the relationship between the details of ultra-fine microstructure of the hydrogen isotopes and layer bulk response is generally unknown. Therefore, a thorough analysis of fundamentals underlying the processes of ultra-fine fuel layer formation and stabilization has been carried out at LPI over the period of 4 Years activity from September 15, 2006 – March 20, 2010 in the frame of the IAEA Technical Contract №13871 [23-26]. The results obtained in the scope of this problem are described below.

## 2. RESULTS OF THE 1<sup>ST</sup> YEAR ACTIVITY

Our researches have turned to numerical simulation to gain insight into the relationship between fuel layer microstructure and bulk properties of the layer. Therefore, the overall objective of the 1<sup>st</sup> Year was to understand how one can lower the fuel layer sensitivity to the environmental effects due to application of the isotropic solid layers. It is a very challenging computational task and, to date, such simulations have not been reported.

The research program included the following topics:

- (1) Modeling of the fuel layer degradation depending on the layer structure, including:
  - (a) Layer strength dependence upon the defect density of the fuel ice structure.
  - (b) Growth rate of the surface roughness caused by fuel ice anisotropy.
- (2) Comparative analysis of the experimental results on formation of heat-resistant high-dispersity layers stabilized with a small additive (0.03-3%).
- (3) Theoretical analysis of allowable tritium pauperization in the DT-mixture designed to tritium inventory minimization in the reactor target system.
- (4) Extension of the method of non-equilibrium state stabilization with a small additive (0.03-3%) in case of 10-25%. Purpose: method adaptation to DT-layer formation with a long-lived quality. Realization of proof-of-principle experiments.

The research work of the 1<sup>st</sup> Year has shown that the application of ultra-fine solid fuel in cryogenic reactor targets allows lowering the fuel layer sensitivity to the environmental effects. This conclusion based on the following results obtained during the reported period [23]:

- The modeling results on degradation of the cryogenic fuel layer have shown that an isotropic layer is the most stable under the heat loads, which appear during the process of cryogenic targets storage or delivery to the burn area (Table 1).
- Analysis of the issue of optimal choice of the solid-fuel layer structure has shown:

There are two different ways of obtaining high strength materials: (a) zero-defects crystalline structure creation, and (b) creation of ultimate disordered structure with a high density of defects.

TABLE 1. CALCULATED TIMES OF REACHING A CRITICAL LEVEL OF ROUGHNESS ( $0.5 \mu\text{M}$ ) AT DIFFERENT VALUES OF ANISOTROPY ( $\xi$ )

$\xi$ [%]	25	50	75	100
t [ms]	8,87	4,45	2,97	2,23

- Obtaining zero-defects macro crystals is almost impractical in the laboratory as this needs extremely slow rates of cooling and experimental conditions maintenance during all the time of layer formation (Fig. 2). Slow cooling realized in practice leads to the defect accumulation (Fig. 2), and, as a consequence, the strength of real crystals decreases. The traditional approach to D2 or DT layer formation inside the target relates to layer formation just at slow cooling. The compression experiments with such targets confirm a high sensitivity of the crystalline layer to the environmental effects [15]. This is due to the presence in such crystalline layers the preferential plane of low glide dislocations. Because of the same reason, the coarse-grained crystalline layers have low strength as well (Fig. 2).
- On the contrary, the ultra-fine materials with a large defect density ( $n$ ) have no natural glide planes and, as a consequence, their mechanical strength rises sharply, proportionally to  $n$  (see Fig.2). The structural defects in the crystals are considered as grain boundaries. One of the mechanisms of strengthening the ultra-fine materials is crack braking inside the grain body.
- Thus, we can achieve considerable strength increase when the grain size of the layer structure is scaled back into the nanometer range.
- One of the ways to obtain the ultra-fine of materials is to realize extremely high cooling of the melt. The cooling rates of 1-100 K/sec (method FST) allow forming the cryogenic layers from hydrogen isotopes as ultra-fine solids [28, 29].
- The modeling results on strengthening of the cryogenic fuel layer have shown that: (a) the ratio  $(\sigma/\rho)$  is the main parameter, which defines the value of permissible overloads ( $\sigma$  is the tensile strength and  $\rho$  is the fuel layer density); (b) the more the ratio  $(\sigma/\rho)$ ; the more the permissible overloads.

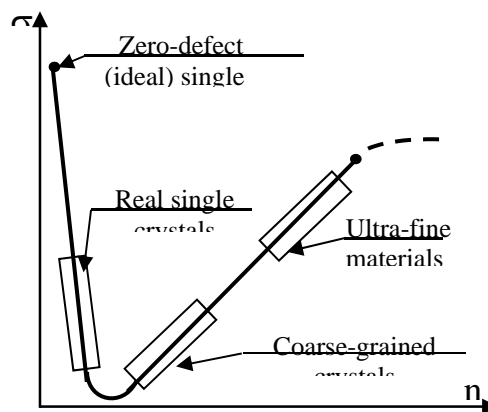


FIG. 2. The sample strength  $\sigma$  vs. the defect density.

- The results of theoretical analysis using the improved code ALFA [30] predicts that tritium pauperization in the DT-mixture to 10-20% does not influence sufficiently on the energy gain of a target. The obtained results show that:
  - For D2 fuel with small tritium additives the burning regimes with a high thermonuclear yield and complete tritium reproduction are available.
  - For realization of the mixture ignition, the confinement factor at the moment of ignition beginning must be  $\langle \rho R \rangle = 25\text{-}30 \text{ g/cm}^2$  (low bound).
  - The ignition temperature is essentially lower than the ignition temperature of pure D<sub>2</sub> fuel and, if the confinement factor  $\langle \rho R \rangle \geq 20\text{-}30 \text{ g/cm}^2$ , it practically coincides with the ignition temperature of the standard DT-fuel (4-5 keV). The above listed results coordinate with the results obtained by other authors [31].
- Proof-of-principle experiments on H<sub>2</sub>/HD, H<sub>2</sub>/D<sub>2</sub> and D<sub>2</sub>/Ne mixtures freezing by FST method have shown the possibility of transparent cryogenic layer formation inside the free-standing targets in time less than 15 sec. Optimal cooling rate was in the range of 1-to-50 K/sec. The amount of high-melting additives was from 5-10% to 20%.

The layers are in an ultra-fine (probably nano-structured) state and have a required thermal stability. Basing on the above results we consider that the FST method holds much promise for the stable ultra-fine cryogenic layer formation from DT-mixture, in which the amount of tritium is 10-20%. Tritium here stands as a high-melting additive relative to deuterium (FIG. 3).

Dependencies on degree of microstructure regularity and fuel layer sensitivity to the environmental effects are demonstrated. The theoretical and experimental researchers of the 1<sup>st</sup> year have shown that:

- (1) Nano-layering technology developing is one of the key moments of the target survival problem (we mean that the grain size should be scaled back into the nanometer range).
- (2) FST method developed at LPI can be used as a base for nano-layering technology development.
- (3) Further insight into the physics underlying the processes of formation and delivery the IFE target with a different fuel structure is urgently needed.

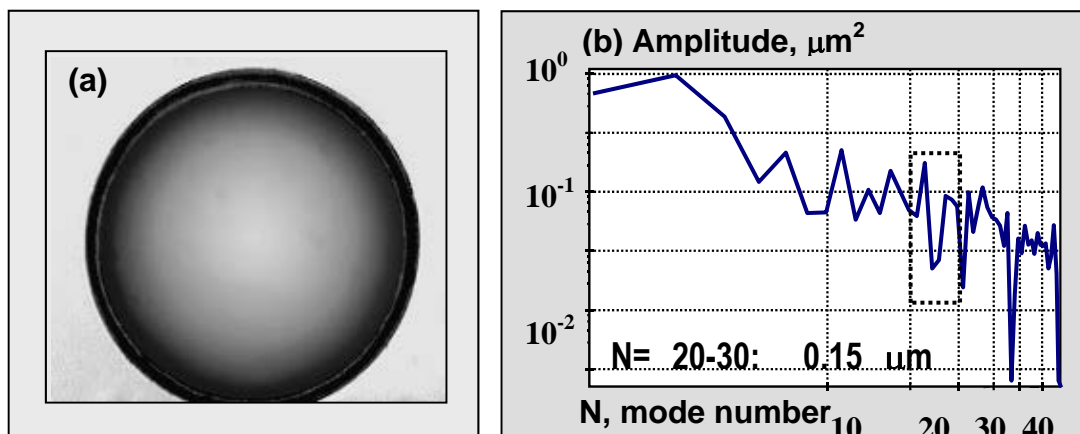


FIG. 3. The results of combined application of the FST layering method and fuel with a high concentration of neon as additive: (a) CH shell ( $2R = 1230 \mu\text{m}$ ) filled with 80%D<sub>2</sub>/20%Ne mixture up to 275 atm at 300 K, cryogenic layer is 41 μm-thick; (b) Fourier-spectrum of the bright band shows that the layer roughness does not exceed 0.15 μm (modes 20-30).

### 3. RESULTS OF THE SECOND YEAR ACTIVITY

The IFE target fabrication program in LPI has been focusing on methods that will allow forming cryogenic layers with inherent survival features. Therefore, a central feature of the 2<sup>nd</sup> Year of the project was the survivability of fuel layers with a different anisotropy under conditions of thermal overloads during target delivery into the reaction chamber. The title of the 2<sup>nd</sup> Year researches was “*Multicriteria optimization for the delivery process of IFE targets with a different fuel structure*”. The degrading effect of radiation heat transfer from the hot chamber wall to the fuel core was of primary importance in our study.

The work is divided in the following research topics:

1. Elucidation of the physical fundamentals underlying the nano-layering technology operation.
2. Study on cryogenic target degradation inside IFE chamber for different fuel layer structures (what effect target heating has on the roughness conditions)
3. Computer code development for technologic forecasting and in-depth analysis of cryogenic target survival during its flight inside the reactor chamber.
4. “Band-pass-windows” for a set of injection parameters, which ensure survivability of layers with a different structure under conditions of the environmental effects.

The following results have been obtained [24]:

- There were performed theoretical and experimental researches in the scope of the nano-layering technology development (FIG. 4). The research objective is more precise definition of the nature of thermo-stable transparent cryogenic layers of hydrogen isotopes obtained by FST method in the presence of high-melting additives. There also have been made an extended analysis of the scientific literature over the problems of formation and stabilization of the ultra-fine materials on the basis of metals, semiconductors and alloys ( see FIG. 5). There have been performed a comparative analysis of our data with the data found out in the scientific literature. The obtained results allow considering the thermo-stable transparent cryogenic layer from hydrogen isotopes as layer characterized by the micro-structural length close to a nano-scale.

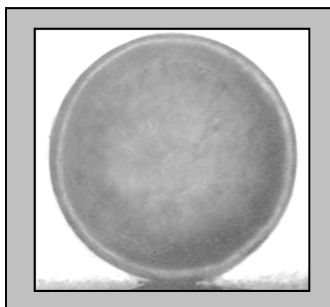


FIG.4. Target protection developments: 1500- m diameter CH shell with a 50- $\mu\text{m}$  thick layer of  $\text{D}_2 + \text{Ne}$  (3 % additive). The shell is covered by the outer reflective layer of Pt/Pd (200 Å thick).

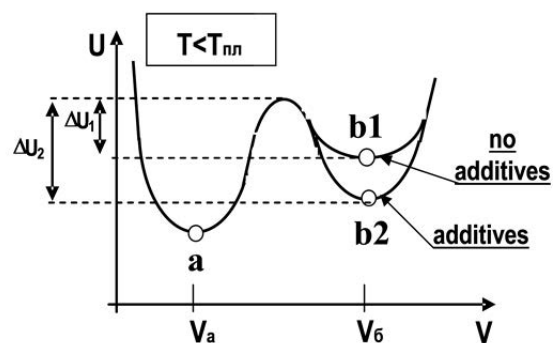


FIG.5. Stabilization of the ultra-fine materials: (a) stable crystalline state; (b1 and b2) meta-stable high-dispersed state; (b2) the potential well becomes deeper, and the power barrier  $\Delta U$  becomes higher.

- There was created a physical concept and performed a mathematical modeling of the roughness growth of the cryogenic layer with a different structure (anisotropic crystalline, isotropic ultra-fine state) under the influence of a thermal load onto the outer target wall (stage of target injection into the reaction chamber). An approach based on Stephen's problem for singularly perturbed simultaneous equations for thermal conductivity with semi-linear boundary and initial conditions is advanced to model the process of fuel layers degrading due to uniform radiative heating during target injection. The calculations were performed for the «Nakai» target: classical high gain target with a 4-mm diameter CH shell and a 45- $\mu\text{m}$  thick wall, the solid layer thickness is 200  $\mu\text{m}$  [32]. The target is exposed to a uniform radiative heating from the hot chamber wall at absolute temperature  $T_0 = 1758$  K. The heat flux absorbed by the target is in the range of  $J_t = 5.0 - 0.5$  W/cm<sup>2</sup>. For a detailed analysis, we assume that a minimal injection time  $\Delta t_{cc}$  is defined by the ratio of chamber radius (6.5 m, like SOMBRERO chamber [33]) to injection velocity ( $\sim 400$  m/sec, near the maximum practical velocity), which is about 16 ms.

The obtained results (Tables 2 and 3) are presented in terms of time of surface roughness growth from a “zero level” to 0.5  $\mu\text{m}$  versus variation in the layer anisotropy ( $\xi_1$ ) and the heat fluxes absorbed by the target ( $J_t$ ). Table 2 reveals a general tendency: the roughness growth slows down for a weaker anisotropy.

- The developed computer program *CDEGRADATION* with a user interface allows calculating the time of layer roughness growth above the rated value *versus* the cryogenic layer structure and the reactor target delivery conditions.

With the help of the *CDEGRADATION* program there were determined the “band-pass-windows” for a set of injection parameters in the case of Nakai target delivery at the chamber center SOMBRERO-like reactor. The targets contain the cryogenic fuel layer of different structure: (a) crystalline layer with anisotropy level  $\xi=7-20\%$ , (b) isotropic ultra-fine layer ( $\xi=0$ ). The delivery conditions are as follows (Tables 2 and 3):

(a) Crystalline layer:  $\xi=20\%$  – in no case;  $\xi=7-9\%$  –  $T_{inj} = 17$  K,  $V_{inj} = 400$  m/sec

(b) Ultra-fine layer:  $\xi = 0\%$  –  $T_{inj} = 5-17$  K,  $V_{inj} = 130-400$  m/sec

Closing this section, note that the obtained results determine specifically that our approach to form ultra-fine solid fuel is timely in the IFE target fabrication programs. Existing and developing target fabrication capabilities and technologies must take into account the structure particularities of solid fuel. A spherically symmetric layer with a uniform thickness and acceptable surface quality must have such a structure, which supports the fuel layer survivability during target acceleration and injection into the reaction chamber.

In this connection, we emphasize yet again that application of ultra-fine fuel layers allows one:

- To reliably perform the target injection into the reaction chamber (without failure of the cryogenic fuel quality under conditions of on-target heat-loads). This is due to such properties of a thermo-stable ultra-fine layer as isotropy and wide temperature range of the layer lifetime (from 5 K to the fuel triple point);

- To reliably perform the target acceleration stage without fuel layer mechanical destruction;
- To shorten the basic acceleration length of a target (as compared with the crystalline layer) to reduce considerably the overall dimensions of the injector.

TABLE 2. ROUGHENING OF THE LAYER (TIME IN MS) VERSUS LAYER ANISOTROPY FOR A RANGE OF HEAT FLUXES ABSORBED BY THE TARGET

$\xi_1, \%$	INJECTION TEMPERATURE $T = 10 \text{ K}$			
	$J_t = 5 \text{ W/cm}^2$		$J_t = 0.5 \text{ W/cm}^2$	
	$D_2$	$DT$	$D_2$	$DT$
1	11.7	9.8	27.6	23
5	4.7	4	11.5	9.7
10	3	2.6	7.6	6.5
15	2.4	2	6.1	5.1
20	2	1.7	5.1	4.4

TABLE 3. \*ROUGHENING OF THE LAYER (TIME IN MS) VERSUS LAYER ANISOTROPY FOR A RANGE OF INJECTION TEMPERATURE

Heat flux absorbed by the target					
$J_t = 0.5 \text{ W/cm}^2$					
$T_i, \text{ K}$	10	12	14	16	18
$\xi_1=7\%$	8.3	10.5	12.9	16.2	21
$\xi_1=8\%$	7.7	9.7	11.9	15	19.5
$\xi_1=9\%$	7.2	9.1	11.1	14	18.3

\*/ Times of surface roughness growth are presented for DT fuel.

**Resume.** The theoretical and experimental researchers of the <sup>second</sup> year have proved that the probability of ultra-fine layer destruction under the influence of thermal and mechanical loads is minimal as compared with the commonly used crystalline layer. The application of IFE targets with an ultra-fine layer allows advancing the reliability of injection process and considerably reducing the overall dimensions of the injector at the expense of shortening the basic acceleration length of a target.

#### 4. RESULTS OF THE THIRD YEAR ACTIVITY

The third year activity has been directed toward elucidation of fundamentals underlying the gas condensation stage and liquid cooling stage during ultra-fine fuel layer formation. There are special conditions of the first-order phase transitions (condensation, crystallization) during FST layer formation inside the shell:

- Presence of temperature gradient in the system (this is realized in the FST method),
- Separation of «fuel + additive» mixture into several components may occur (we have observed this effect in a number of experiments).

Under these conditions, the uniform distribution of additive by fuel volume may be disturbed, and then, the method of obtaining the thermo-stable ultra-fine layer becomes ineffective.

Therefore, the research program of the third year included the following directions:

- (1) Theory: development of the physical model of some individual stages of the FST-layering in the presence of additives (gas condensation stage; liquid cooling stage):
  - Heterogeneous condensation in volume: estimation of drop-seeding rate inside the shell under variation of the gas density.
  - Separation of fuel mixture (fuel + additive): estimation of fuel mixture separation effect due to thermo-diffusion.
- (2) Experiment (in support of theoretical investigations):
  - Study of peculiarities of “gas-liquid” phase transition at different regimes of fuel mixture cooling inside the spherical hollow shell.
  - Study of peculiarities of “liquid-solid” phase transition at different regimes of fuel mixture cooling inside the spherical hollow shell.
- (3) Application: Determination of “band-pass-windows” for a set of layering parameters, which ensure the formation of thermo-stable ultra-fine fuel layer inside the spherical hollow shell.

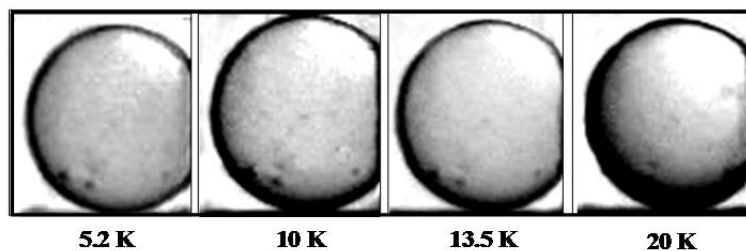


FIG. 6. Transparent solid layer does not re-crystallize when heated within the temperature range from 5 K up to the triple point of  $H_2$  (13.96 K).

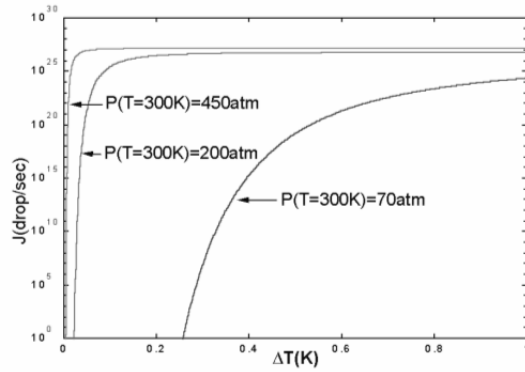


FIG. 7. Generation rate of seeds with critical radius ( $J$ ) vs. overcooling degree ( $\Delta T$ ) at different fill pressures ( $P$ ) (1 mm shell filled with hydrogen).

The following key issues have been determined theoretically and proved experimentally [25]:

- (a) The formation of an ultra-fine thermo-stable layer by FST is possible due to the presence of high-melting additives that are uniformly distributed by fuel volume (FIG. 6, the glass shell diameter is 500  $\mu\text{m}$ , the layer composition is: 99.47%  $\text{H}_2$ ,  $(0.53 \pm 0.11)\%$  HD,  $D_2 < 1\%$ )
- (b) Under “gas–liquid” transition the heterogeneous condensation inside the shell is a way to obtain a uniform rate of fuel mixture. Therewith, the molecules of high-melting additives play a role of seeds for this process initiation.

It has been theoretically shown that the more the density (fill pressure), the less the required rate of gas overcooling to initiate droplet-seed condensation inside the shell (FIG. 7). This result coincides with the results observed experimentally (Table 4). The above case (FIG. 7) relates to the homogeneous condensation, when we use the material without any additives. Physical basis of this process initiation refers to density fluctuations in the gas volume that at a certain degree of overcooling leads to the generation and growth of condensation centers (FIG. 8). When there are impurities of another material of a greater molecular weight, the density fluctuations increase and the gas condensation progresses at smaller overcooling. We have observed this regularity in  $\text{H}_2/\text{HD}$  and  $\text{D}_2/\text{Ne}$  mixtures.

- (c) During further target cooling and liquid layer symmetrization by FST, the target moves randomly inside the layering channel. Owing to this fact the temperature gradient is not stable and the mixture separation (including the additives) does not occur due to the thermo diffusion.
- (d) The presence of high-melting additives slows down the growth of solid layer roughness.

As a result of the third year activity, the topical issue of free-standing targets (FST) technology has been solved, namely: the “band-pass-windows” (or optimal parameters) of the FST experiment have been found (see Table 5), which allow one to produce ultra-fine cryogenic layers inside free-standing spherical hollow shells.

TABLE 4. HYDROGEN CONDENSATION INSIDE THE SHELL AT DIFFERENT FILL PRESSURES  $P_F$

Hydrogen isotopes	$P_F$ , atm	$\rho$ , mg/cc	$T_s$ , K	$t$ , s	$dT/dt$ , K/s	In-volume condensation
H <sub>2</sub>	450	28.5	32.5	1.0-3.0	0.18-0.20	+
H <sub>2</sub>	450	28.5	32.5	6.0-7.0	0.01	+
H <sub>2</sub>	200	14.5	31.5	0.1-0.2	~ 110	+
H <sub>2</sub>	200	14.5	31.5	1-2	~10	+
H <sub>2</sub>	200	14.5	31.5	-	0.15-0.20	-
H <sub>2</sub>	70	5.5	27	-	0.18-0.20	-
H <sub>2</sub> +5%HD	275	19.0	32	6.0-7.0	0.20-0.40	+

$\rho$  - gas density,  $T_s$  - phase separation temperature,  $t$  - typical time of condensation in volume

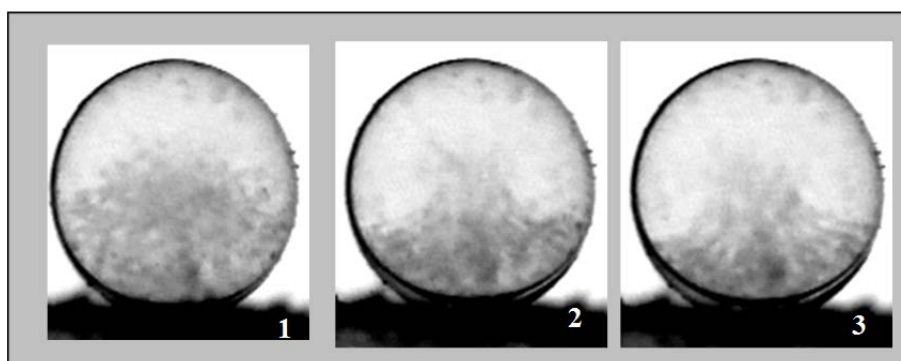


FIG. 8. Homogeneous condensation in volume initiated during glass shell cooling ( $\varnothing$  500  $\mu$ m, gas density is 14.5 mg/cc, substrate cooling rate is ~ 10 K/s): (1)  $t=80$  ms after the cooling.

## 5. RESULTS OF THE FOURTH YEAR ACTIVITY

TABLE 5. BAND-PASS-WINDOWS FOR A SET OF LAYERING PARAMETERS, WHICH ALLOW FORMING THERMO-STABLE ULTRA-FINE FUEL LAYER USING THE FST METHOD

Parameter		Band-pass-windows
Material of additives		The additive triple point must be higher than that of the main isotope. For example: HD or D <sub>2</sub> additives for H <sub>2</sub> , T <sub>2</sub> or DT additives for D <sub>2</sub> , T <sub>2</sub> for DT – mixture.
Amount of additive		0.3-to-20 %
Cooling rate	Gas-liquid transition	$\geq 0.01$ -0.4 K/sec (depends on gas density)
	Cooling of liquid phase	$\leq 1$ K/sec (depends on symmetrization rate)
	Melt cooling	1-to-50 K/sec

The main goal of the fourth year is further elucidation of fundamentals underlying the process of formation of thermo-stable ultra-fine fuel layer.

The execution work plan of the fourth year is as follows:

- Experiments with a rapid cooling rate.
- Experiments with a moderate cooling rate.
- Experiments with a slow cooling rate.
- Analysis of peculiarities of “liquid-solid” phase transition at different rates of fuel mixture cooling inside spherical hollow shell.

**Methodologies to solve the tasks of the project:** free-standing target technology, cooling rate variations under target heating and cooling, video recording and high resolution optics application for diagnostics of the experimental results.

**Expected output of the year:** FST-layering parameters optimization during “liquid-solid” phase transition. This ensures the formation of ultra-fine, thermo-stable solid fuel layer with a certain amount of high-melting additives.

Details of the experiments shown in FIG. 9 are as follows: (a) fine-grained layer obtained by FST in the presence of the heat exchanging helium inside the layering channel (rapid cooling); (a)–(d) fine-grained layer evolution during the heating; (e) deuterium melting at  $T=18.65$  K; (f) state of the mixture components inside the shell at  $T=21$  K: Ne – solid,  $D_2$ – liquid; (g) completion of the melting process of Ne at  $T=23.8$  K; (h) solidification of Ne at slow cooling of the shell (0.05 K/sec); state of the mixture components inside the shell at  $T=20$  K: Ne – solid,  $D_2$  – liquid; (i) solidification of the deuterium during further slow cooling of the shell (0.05 K/sec); state of the mixture components in the shell at  $T=15.9$  K: Ne – solid,  $D_2$ – solid.

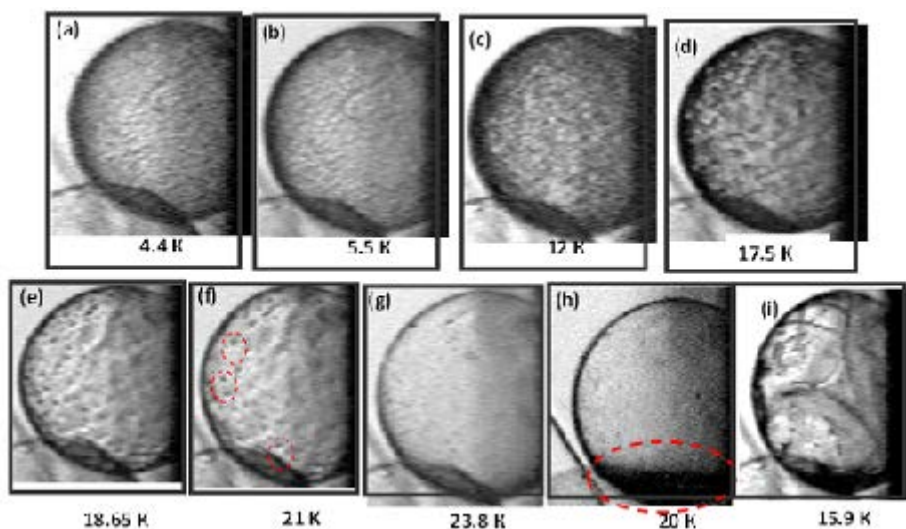


FIG. 9. Features of the thermal evolution of the cryogenic layer from the 80%D2/20%Ne mixture: heating process (a) – (g), cooling process (g) – (i); 3 mTorr of heat-exchanged helium inside the test chamber.

Below we discuss the results obtained over the period of September 8, 2009 – March 20, 2010 (7 months).

In the experiments there were used the polystyrene shells of 1.0-to-1.2 mm diameters filled with D<sub>2</sub>/Ne mixture up to fill pressure of 125÷300 atm. The mixture contained of 80%D<sub>2</sub> and 20%Ne.

The main results achieved in the 4<sup>th</sup> year are as follows [26]:

A) Slow mixture cooling at a rate of  $\sim 0.05$  K/сек: the target is placed on the slowly cooled substrate; the heat removal from the shell surface realizes both through the area of contact and the heat-exchanging helium (3 Torr).

In this case, the mixture components freeze out onto the inner wall of the polystyrene shell independently of each other – at first the component with a higher triple point (Ne), and then with a lower triple point (D<sub>2</sub>). In the process, it is seen that Ne does not wet the polystyrene surface whereas D<sub>2</sub> wets it well. Thus, in the given regime it is impossible to achieve the uniform additive distribution by the condensed layer volume and to freeze a fine-grained solid layer (FIG. 9, h-i).

B) Rapid cooling at a rate of  $\sim 100$  K/sec: the target drop inside the layering channel; heat removal from the shell surface is realized both through the area of contact and the heat-exchanging helium (3 Torr).

In this case, the cryogenic layer has a typical fine-grained structure and consists of two different matters: pure solid deuterium and deuterium/neon solid solution. The estimations have shown that only a small part of deuterium (less then 4% of the total amount of D<sub>2</sub> in the mixture) is involved in the formation of a solid solution. Moreover, the distribution of this solution in the cryogenic layer has a specific form of an array of the “local grains” that uniformly covers the inner shell surface (FIG. 9, a). Peculiarities of the layer evolution upon the shell heating are shown in FIG. 9 (a-g).

C) Moderate cooling at a rate of 1÷50 K/sec: the target drop inside the layering channel (evacuation – 35 mTorr); the heat removal from the shell surface is realized only through the area of contact (experimental conditions of FST layering).

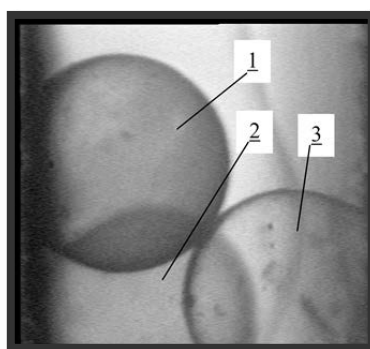


FIG. 10. Homogeneous transparent layer formation from 80%D<sub>2</sub>/20%Ne mixture inside the polystyrene shells. The shells №1-3 is in the optical chamber after their drop in the spiral layering channel (residual gas pressure is 35 mTorr,  $T=4.4$  K).

In this case, the homogeneous transparent layer from the solid D<sub>2</sub>/Ne solution is formed onto the shell wall. Just that very regime allows obtaining the solid transparent layer, which is resistant to heat (FIG. 10).

The observed regularities confirm the fact that in the conditions of the FST technology, the neon additive (the high-melting component imitating the presence of tritium in the DT mixture) in the solid deuterium slows down the growth of crystal grains and, thus, promotes the formation and stabilization of homogeneous fine-grained structure of the cryogenic layer.

A milestone due in Inertial Fusion Energy (IFE) research is a target that must be delivered to the target chamber center at a rate of about 1–10 Hz. Therefore, the IFE target fabrication is focusing on methods that will scale to a high rep-rate and cost-effective target production.

The top-level requirements to successful target fabrication and injection are target material selection and fuel layer structurization. The following aspects are of key importance:

1. Target mass-production.

- Target fabrication capabilities and technologies must take into account the structure particularities of solid hydrogen fuel (high cooling rates combined with high-melting additives to fuel content).
- Target materials must satisfy a wide range of required and desirable characteristics. Optimal micro-structural design and materials selection allow one to obtain chemical, physical and mechanical characteristics for specific applications.
- Tritium inventory minimization (minimization of time and space for all production steps)

2. Survivability of a fuel core → minimization of risk of target destruction at each production and delivery step.

- Layers with inherent survival features (fuel layer structurization – the grain size should be scaled back into the nanometer range)
- Multiple target protection methods (e.g., outer protective cryogenic layers, metal coatings of different configurations and compositions, nano-coatings with super hardness, co-injection of a special protective shroud ahead of the target, etc)

Taking in mind the extreme importance of application of ultra-fine fuel layers in IFE targets, we would like to emphasize that further elucidation of fundamentals underlying the processes of formation of thermo-stable ultra-fine fuel layers in the reactor-scaled targets is of great value. For this reason, our activity, which has been started in the IAEA TC #13871, was continued in the frame of other international collaboration, namely:

1. In the frame of HEDgeHOB collaboration (cylindrical cryogenic targets): we have implemented the R&D project “Design and feasibility study on fabrication and manipulation of HEDgeHOB cryogenic targets” [34].
2. In the frame of HiPER project (spherical cryogenic targets of a reactor scale):
  - we make a proposal on the development of high rep-rate cryogenic target facility (targets fabrication and delivery) [35]
  - we have started the feasibility study on creating the FST-layering module for high-rep-rate production of cryogenic targets of a HiPER-class [36]

The top priority issues, which yet to be studied in the area of IFE targets physics and technology as follows:

- IFE target physics. Theoretical estimation and experimental research of the shock wave propagation and instability growth in the accelerated phase in the targets with fuel layer material of a different structure (anisotropic crystalline state, isotropic ultra-fine state).
- IFE target technology. Technology development for production targets with specified thermo-physical and mechanical properties. In particular, nano-layering technology development for forming stable ultra-fine fuel layer in the targets of a reactor scale, including the targets with foam layer. The issues listed above may be the topics for further international collaboration. The results obtained have been published in [37, 38] and reported in [39-45].

## 6. SUMMARY

A suitable approach to fuel layering based on using free-standing targets (FST) at each production step has been developed at the Lebedev Physical Institute of Russian Academy of Sciences (LPI). Our experimental researches have proved that isotropic thermo-stable ultra-fine fuel layer can be formed by FST method under the following work parameters: cooling rate  $q \sim 1 \div 50$  K/sec, layering time  $t \leq 15$  sec, high-melting additives in the amount of  $3 \div 20\%$ , which allow stabilizing a meta-stable ultra-fine fuel layer. The expertise carried out in the frame of the IAEA TC #13871 permit to come to a conclusion that the application of a fuel layer in the ultra-fine state (submicron or near-nano grain size, nano-crystalline, amorphous) is very promising in IFE. In particular, our theoretical researches have shown that application of isotropic ultra-fine fuel layer allows minimizing the risk of fuel layer destruction during target delivery as compared with an anisotropic crystalline fuel.

## REFERENCES

- [1] MEIER, W.R., An Integrated Research Plan for IFE Technology, in: Book of Abstracts, 1<sup>st</sup> IAEA-TM on Physics and Technology of Inertial Confinement Fusion Energy Targets and Chambers (Madrid, Spain, June 7-9, 2000).
- [2] STEINMETZ, K., Coordination of IFE Keep-in-touch Research Activities in Europe, in: Book of Abstracts, 1<sup>st</sup> IAEA-TM on Physics and Technology of Inertial Confinement Fusion Energy Targets and Chambers (Madrid, Spain, June 7-9, 2000).
- [3] NAKAI, S., Investigation Toward Inertial Fusion Energy at ILE Osaka, in: Book of Abstracts, 1<sup>st</sup> IAEA-TM on Physics and Technology of Inertial Confinement Fusion Energy Targets and Chambers (Madrid, Spain, June 7-9, 2000).
- [4] MOSES, E.I., C.R.Wuest. The National Ignition Facility: Status and Plans for Laser Fusion and High-Energy-Density Experiments. *Fusion Sci. Technol.* 43, N3 420-427, 2003.
- [5] ANDRE, M.L., Laser Megajoule Project Status. In *Inertial Fusion Science and Applications 1999* (eds. C.Labaune et al.), Elsevier, 32-39, 2000.
- [6] KIRILLOV, G.A., ET AL. Overview of Laser Fusion Program at Russian Federal Nuclear Center – VNIIEF. Report, 1<sup>st</sup> IAEA-TM on Physics and Technology of Inertial Confinement Fusion Energy Targets and Chambers. (Madrid, Spain, June 7-9, 2000); S.G.Garanin et al. Concept of the laser facility UFL-2M. Report, 39<sup>th</sup> International Conference on Plasma Physics and ICF (Zvenigorod, Moscow sub., Russian Federation, Feb. 6-10, 2012).
- [7] TOWN, R.P.J., et al. OMEGA Cryogenic Target Designs. *Laboratory for Laser Energetics (LLE) Review, Quarterly Rept.* 82, 49-55, 2000.
- [8] MCKENTY, P. W., et al. Direct-drive cryogenic target implosion performance on OMEGA. *Physics of Plasmas*, 11, N5, 2790-2797 (2004).

- [9] RODER, H. M., CHAILDS, G. E., MCCARTY, R. D., AND ANGERHOFFER P. E. Survey of the Hydrogen Isotopes below their Critical Temperatures, NBS Technical Note, Monograph 74 (1965).
- [10] TOLLEY, M.K., et al. Microtarget requirements, production and delivery for HiPER. Report IF/P7-2, 22<sup>nd</sup> IAEA Fusion Energy Conference, Geneva, 12-18 October 2008.
- [11] MONSLER, M.J., MERKULIEV, YU.A., NORIMATSU T., Target Fabrication and Positioning, p.151, in: Energy from Inertial Fusion, IAEA, Vienna (1995).
- [12] SCHULTZ, K.R., GOODIN, D., NOBILE A., IFE target fabrication and injection achieving “Believability”. Nucl. Instrum. Methods A, 464, 109-117, 2001.
- [13] Elements of Power Plant Design for Inertial Fusion Energy. Final Report of a Coordinated Research Project 2000--2004, IAEA--TECDOC-1460, IAEA, Vienna, 133-138, 2005.
- [14] ALEKSANDROVA, I.V., BELOLIPETSKY, A.A., KORESHEVA, E.R., State of the Problem of Cryogenic Targets in the Current Inertial Fusion Program, Vestnik RAEN 7(2), 37-42, 2007 (in Russian).
- [15] HARDING, D.R., et al., Formation of Deuterium--ice Layers in OMEGA Targets. LLE Review, Quarterly Rept. 99, 160-182, 2004.
- [16] MARSHALL, F.J., et al., Direct-drive, cryogenic target implosion on OMEGA. Phys. Plasmas, 12, 056302-(1-7), 2005.
- [17] PERLADO, M., Inertial fusion energy research in target design, safety, environment and materials for targets and blankets in experimental facilities and reactors. Proceed. 1<sup>st</sup> IAEA RCM on Pathways to Energy from Inertial Fusion (Vienna, Austria, 6-10 November 2006).
- [18] NAKAI, S., Developments of Integrated IFE System and its Application to Industry. Proceed. 1<sup>st</sup> IAEA RCM on Pathways to Energy from Inertial Fusion (Vienna, Austria, 6-10 November 2006).
- [19] KORESHEVA, E.R., Optimizing cryogenic layering for IFE targets for providing target survival during the injection process. Proceed. 1<sup>st</sup> IAEA RCM on Pathways to Energy from Inertial Fusion (Vienna, Austria, 6-10 November 2006).
- [20] RUDRAIAH, N., Effects of laser radiation, nanostructured porous lining and electric field on the control of Rayleigh-Taylor instability at the ablative surface of IFE target. Proceed. 31<sup>st</sup> IAEA Fusion Energy Conference (Chengdu, China, 16-21 October 2006)
- [21] ALEKSANDROVA I.V., et al. An efficient method of fuel ice formation in moving free standing ICF/IFE targets. J.Phys.D: Appl.Phys. 37, 1-16, 2004.
- [22] KORESHEVA E.R., et al. Progress in the Extension of Free- Standing Target Technologies on IFE Requirements. Fusion Sci. Technol. 35, N3, 290-300, 2003.
- [23] First year progress report on the implementation of the IAEA contract number 13871/RBF “Optimizing cryogenic layering for inertial fusion energy (IFE) targets for providing target survival during the injection process”, September 15, 2006 – June 15, 2007. Contractor: Lebedev Physical Institute of RUS, Moscow, Russian Federation.
- [24] Second year progress report on the implementation of the IAEA contract number 13871/RBF “Optimizing cryogenic layering for inertial fusion energy (IFE) targets for providing target survival during the injection process”, Title of the 2<sup>nd</sup> year “Multicriteria optimization for the delivery process of IFE targets with a different fuel structure”, August 15, 2007 – June 15, 2008. Contractor: Lebedev Physical Institute of RUS, Moscow, Russian Federation.

- [25] Third year progress report on the implementation of the IAEA contract number 13871/RBF“Optimizing cryogenic layering for inertial fusion energy (IFE) targets for providing target survival during the injection process”, Title of the 3<sup>rd</sup> year “Elucidation of fundamentals underlying the process of formation of thermo-stable ultra-fine fuel layer”, September 1, 2008 – July 1, 2009. Contractor: Lebedev Physical Institute of RUS, Moscow, Russian Federation.
- [26] Fourth year progress report on the implementation of the IAEA contract number 13871/RBF“Optimizing cryogenic layering for inertial fusion energy (IFE) targets for providing target survival during the injection process”, Title of the 2<sup>nd</sup> year “Further elucidation of fundamentals underlying the process of formation of thermo-stable ultra-fine fuel layer”, September 8, 2009 – March 20, 2010. Contractor: Lebedev Physical Institute of RUS, Moscow, Russian Federation.
- [27] MARTIN, M., GAUVIN, C., CHOUX, A., PASCAL G., A way to reach cryogenic’s temperature and roughness requirements for the Laser MegaJoule Facility. Fusion Sci.Technol. **51**, N4, 747-752, 2007; M. Martin et al. Fusion Sci.Technol. **49**, 600, 2006
- [28] ALEKSANDROVA I.V., et al. Free-Standing Target Technologies for ICF. Fusion Technology. **38**, N1, 166-172, 2000.
- [29] ALEKSANDROVA I.V., et al. Cryogenic fuel targets for inertial fusion: Optimization of fabrication and delivery conditions. J. Russian Laser Research **28**, N3, 37-42, 2007
- [30] OPARIN, A.M., Numerical modeling of hydrodynamic and kinetic processes at high energy density. PhD Thesis, Moscow-1995, 11p.
- [31] KAWATA, S., NAKASHIMA H., Tritium content of a DT pellet in inertial confinement fusion. Laser Part. Beams **10**, 479-483, 1992.
- [32] ZAKHAROV, V.P., GERASIMENKO V.S., Strukturnye osobennosti poluprovodnikov vamorfnom sostoyanyi. Kiev: Naukova Dumka, 1976, 280 p. (in Russian).
- [33] PETZOLDT, R.W., IFE Target Injection and Tracking Expt.Fusion Tech. **34**, 831, 1998
- [34] KORESHEVA, E.R., et al. A Study on fabrication, manipulation and survival of cryogenic targets required for the experiments at the Facility for Antiproton and Ion Research: FAIR. Laser Part. Beams **27**, 255-272, 2009.
- [35] KORESHEVA, E.R., High rep-rate target factory for HiPER: cryogenic target mass production and delivery with a rate of 0.1-to-10 Hz. 3<sup>rd</sup> MWTA, Round table “European project HiPER and international collaboration” (October 18, 2007, Moscow, Russian Federation).
- [36] ALEKSANDROVA, I.V., et al. FST- technologies for high rep-rate production of HiPER scale cryogenic targets. SPIE, 2011 (paper 8080C-128).
- [37] ALEKSANDROVA I.V., BELOLIPETSKIY, A.A., KORESHEVA E.R., AND TOLOKONNIKOV S.M., “Survivability of fuel layers with a different structure under conditions of the environmental effects: Physical concept and modelling results. Laser Part. Beams, 26 (4), 643-648, 2008.
- [38] ALEKSANDROVA, I., et al. Thermal and mechanical responses of cryogenic targets with a different fuel layer anisotropy during delivery process. J. Russian Laser Research, 29 N5, 419-431, 2008.
- [39] KORESHEVA, E.R., ALEKSANDROVA, I.V., BELOLIPETSKIY, A.A., . Optimizing cryogenic layering for inertial fusion energy target for lowering fuel layer sensitivity to the external parameters variations arising during target delivery into reactor chamber. Report, XXXIV International conference on Plasma Physics and ICF (Zvenigorod, Moscow sub., Russia, February 12-16, 2007).
- [40] KORESHEVA, E.R., An overview of cryogenic target fabrication and delivery in Russian Federation. Report, 30<sup>th</sup> European Conf. on Laser Interaction with Matter (ECLIM-2008, August 31-September 6, 2008, Darmstadt, Germany).

- [41] KORESHEVA, E.R., High rep-rate fabrication, characterization and delivery of free-standing moving cryogenic targets: overview on researches developed at LPI. Report, 2<sup>nd</sup> European Target Fabrication Workshop (2<sup>nd</sup> ETFW), October 27-28, 2008, Abingdon, UK.
- [42] ALEKSANDROVA, I.V., et al. High rep-rate fabrication of free-standing cryogenic targets with isotropic solid fuel layer. Report, 36<sup>th</sup> International Conference on Plasma Physics and ICF (Feb. 9-13, 2009, Zvenigorod, Moscow sub., Russian Federation).
- [43] KORESHEVA, E.R., Aleksandrova, I.V., An overview of the results obtained at LPI RAS in the area of high-rep-rate fabrication and delivery of cryogenic fusion targets. Report, XXXVII International Conference on Plasma Physics and ICF (Feb. 8-12, 2010, Zvenigorod, Moscow sub., Russian Federation).
- [44] KORESHEVA, E.R., IAEA TC #13871 (2006-2010): Optimizing cryogenic layering in IFE targets for providing target survival during the injection process. 3<sup>rd</sup> IAEA RCM for CRP “Pathways to Energy from Inertial Fusion – An Integrated Approach”, March 22-24, 2010, Vienna, Austria.
- [45] KORESHEVA, E.R., ALEKSANDROVA I.V., A path toward IFE targets high-rep-rate fabrication and safe delivery. 5<sup>th</sup> IAEA TM on Physics and Technology of IFE Targets and Chambers, Vienna, Austria, March 24-26, 2010.



# PATHWAY TO ENERGY FROM INERTIAL FUSION — AN INTEGRATED APPROACH

S. NAKAI<sup>\*\*\*</sup>, K. MIMA<sup>\*\*</sup>, H. AZECHI<sup>\*</sup>, N. MIYANAGA<sup>\*</sup>, M. NAKAI<sup>\*</sup>, K. TANAKA<sup>\*\*</sup>

<sup>\*</sup>Institute of Laser Engineering, Osaka University

<sup>\*\*</sup>Faculty of Engineering, Osaka University

<sup>\*\*\*</sup>Graduate School for Creation of New Photonics Industries

Tokyo, Japan

## Abstract

In this article we report the developments and physics of lasers as suitable drivers for implosion of a DT filled IFE target. We discuss new applications to the industries such as the manufacturing, nuclear material processing, and medical engineering with the rep-rate high power laser of industrial grade.

## 1. INTRODUCTION

The fusion Ignition, Burn, and Energy Gain (IBG) with the central ignition is highly expected to be demonstrated in 2010 ~ 2012 by the NIF at LLNL of the US. It will open the new era of IFE developments that is the engineering development of the IFE power plant with rep-rate drivers. The increasing understanding on the implosion physics has enabled us the optimized design of the fuel pellet target and the corresponding laser pulse specification for a specific performance. The demonstration of the efficient coupling from the high intensity, short pulse laser to the compressed core shows the feasibility of the concept of the fast ignition which would give us higher energy gain with smaller laser energy.

The remarkable progress on the solid state laser technology based on Diode Pumped Solid State Laser (DPSSL) gives us a feasible prospect toward the driver for a power plant, which requires rep-rate operation with high efficiency and robustness in operation and maintenance.

Now the laser driven implosion and fast heating of high density target both with rep-rate operation are opening new fields of engineering which may have many important applications in science and technology, especially in the nuclear technology. The construction of an integrated IFE system is investigated aiming for the development of IFE power plant and also for the industrial application of an intense neutron source.

## 2. PATHWAY TO IFE – PHYSICS INVESTIGATIONS AND ENGINEERING DEVELOPMENTS

The road map to IFE power plant is shown in Fig 1. The NIF at LLNL will demonstrate the laser fusion Ignition, Burn and Energy Gain (IBG) at around 2010-2012. The commissioning of the system was reported at IFSA2009 in San Francisco showing the spherical implosion of cryogenic targets with 192 beams. The LMJ in France is under construction with the scheduled completion of the system to be 2016. FIREX-I (fast ignition realization experiments) has completed and the initial experiments on the PW, kJ igniter beam coupling with compressed fuel by GEKKO XII were successfully performed in 2009 at ILE, Osaka.

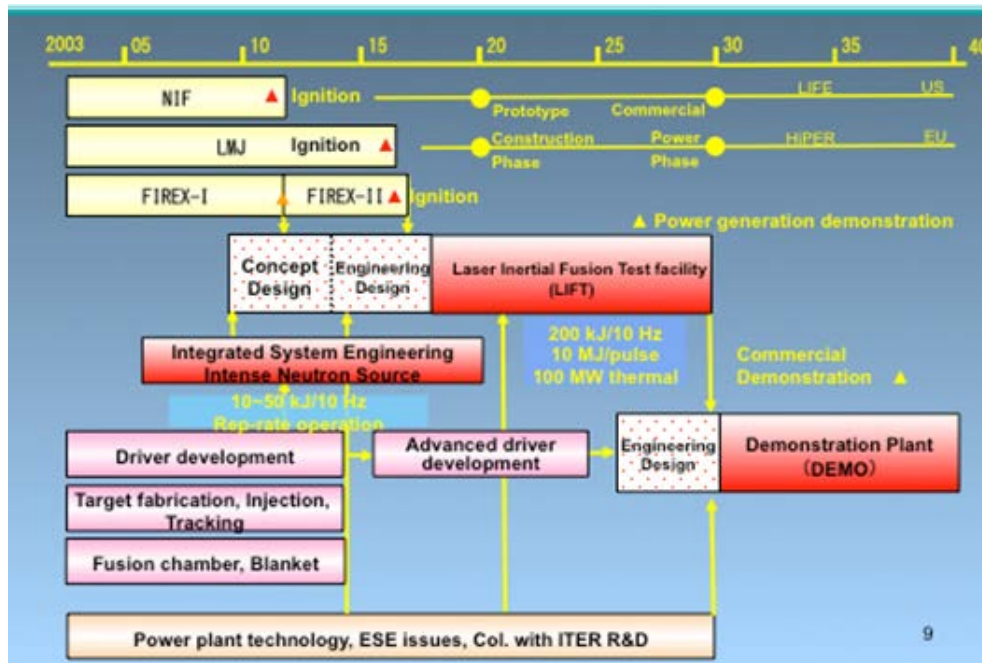


FIG. 1 Road map to IFE Power Plant.

There are many data bases which have been accumulated over many years by many laboratories throughout the world relating to the elementary processes such as laser matter interaction, energy transport by radiation, thermal and non-thermal particles, ablation and hydrodynamics, and the stabilities related to the implosion process. The experimental results of the pellet implosion and fusion reaction have been compared with the numerical simulation results, which were reinforced by the individual verification for the each elementary process. The demonstration of IBG by NIF is really the ultimate goal of the physics research on the inertial fusion.

In the new era after the demonstration of IBG the main efforts on IFE development should be on the engineering issues for the rep-rate integrated system. The key elements are (A)driver, (B)target (C)fusion chamber and (D)blanket all with the rep-rate operations for the consideration of the power plant. The separability of the element blocks of the driver, target, and chamber enables us the independent development keeping the close connection and collaborations of the independent groups of the world. The IAEA Coordinated Research Project (CRP) would be effective and could be the core for the worldwide collaborations in IFE developments especially in the new era.

Based on the developments of the element blocks, the engineering for the integrated system must be developed which include the interface issues between the element blocks such as driver, target and chamber. This integrated system which is shown at the middle in Fig1 could be also the intense neutron source for the fusion material test and also for the industrial application. Beyond this integrated system engineering phase, the power generation demonstration systems are proposed such as LIFE (Laser Inertial Fusion Engine) in US, HiPER in EU which are marked on the future line of the NIF and LMJ in Fig1, and LIFT (Laser Inertial Fusion Test facility) in Japan.

### 3. INTEGRATED IFE SYSTEM AND REP-RATE DRIVER

#### 3.1. Integrated IFE system

The concept of a integrated IFE system is shown in FIG. 2. It consists of: (A)driver system, (B)fuel target system, and (C)reaction chamber system. Surrounding the reaction chamber, neutron diagnostics and application instruments are installed depending on the research program.

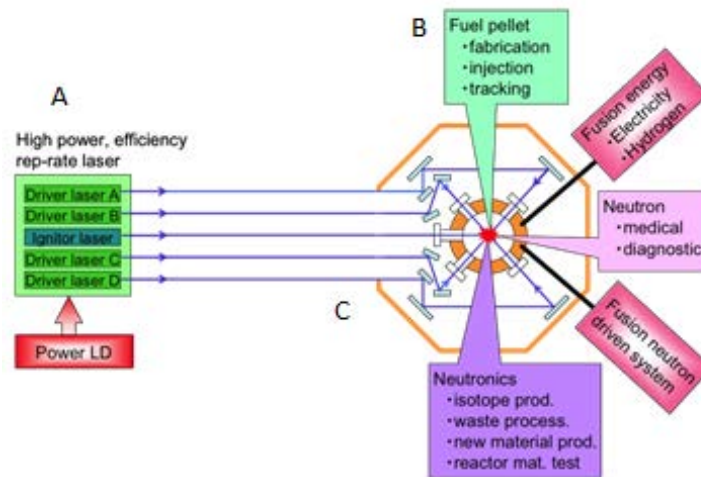


FIG. 2. Integrated IFE system and its application to industries.

For the integrated system with a rep-rate operation the required specification for the key elements of driver, target, and chamber are different from the research facility of a single shot operation. Specifically the interface issues between the key elements must be considered and investigated. They are target tracking and shooting by lasers, influence of chamber environment to the target injection and laser beam propagation, final optics on the beam port etc. Within the key technical issues, the most critical issue is the driver development for which innovative technologies are essentially important.

#### 3.2. Driver development

For the IFE power plant, high efficiency, rep-rate operation, long life, and low cost driver have to be developed. We can see remarkable progresses in high power laser technologies which can improve the design and performance of the power plant driver. The recent innovative achievements of them are listed in Table 1. The most important achievements are:

- (1) The high power LD with high conversion efficiency of 80% at CW operation has been achieved, and further improvement is expected. For the cost reduction of high power LD struck, VCSEL (Vertical-Cavity Surface-Emitting Laser) is preferable as shown in Fig 3, where the monolistic process on wafer base could make the high power emitter array. It has been reported that the enough high output power density of 3.7 kW/cm<sup>2</sup> at 100μs and 0.3% duty cycle for the laser pumping has been achieved with VCSEL[2].

(2) New laser materials are under development including crystal, glass, and ceramic materials. The Yb:YAG ceramic demonstrated very high potentiality for IFE driver with temperature control for optimizing the emission cross section and thermal shock parameter as shown in Fig 4. New laser material based on silica glass has been developed as shown in Fig 5 which shows high peak power operation [3].

TABLE 1. RECENT PROGRESS OF HIGH POWER LASER

- Progress of high power LD
  - 255 W/cm bar, Conversion efficiency 80%
  - high power VCSEL 3.5 kw/cm<sup>2</sup> → Efficiency & Cost
- Development of ceramic laser material
  - Ceramic YAG, NdY<sub>2</sub>O<sub>3</sub> → Higher energy density
- Development of Nonlinear Optical Material
  - CLBO, Organic crystal
- Progress of pulse compression
  - fs, PW
- Progress of Fiber Laser Technology
- Progress of Phase Conjugate Technologies for Rep-Rate

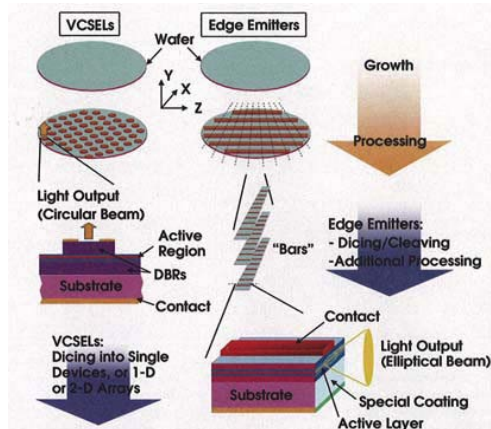


FIG. 3 VCSEL and Edge Emitter.

The future prospect of the high average power driver with high efficiency, and low cost for the IFE will open new industrial applications such as intense neutron source and particle accelerator by high peak intensity laser.

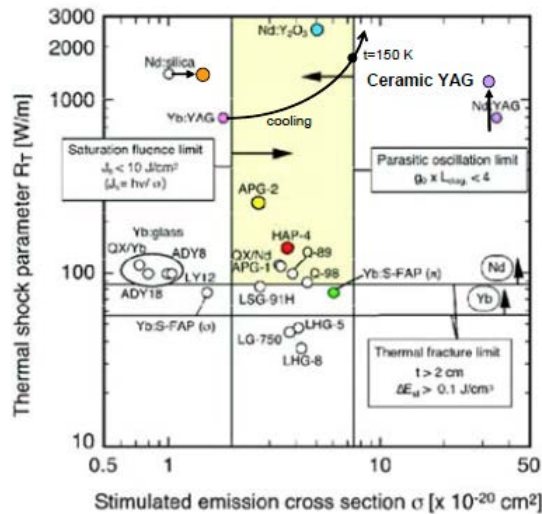


FIG. 4 Laser material mapping.

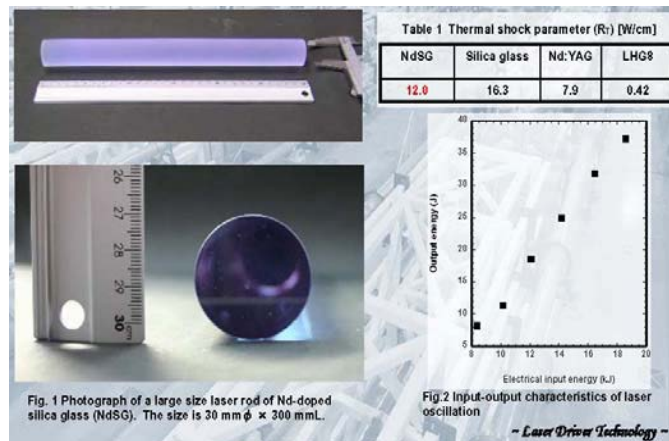


FIG. 5 High-peak-power laser material based on silica glass.

#### 4. APPLICATION OF LASER NEUTRON SOURCE

##### 4.1. Generation of neutrons by high Power Laser

Neutron generation by short pulse laser of order of ns to fs has been well investigated for many years. The physical models of typical examples are shown in Fig 6. They are  $\oplus$  gas cluster target,  $\ominus$  thin film target,  $\odot$  spherical pellet target for implosion. There are many optimized structures of each target such as density control, composite material and Z number optimization, layered structure etc. The pulse width and shape are also optimized according to the type of the targets and structures, the features of which are also shown in Fig 6.

### Generation of Neutron and Beams by High Power laser

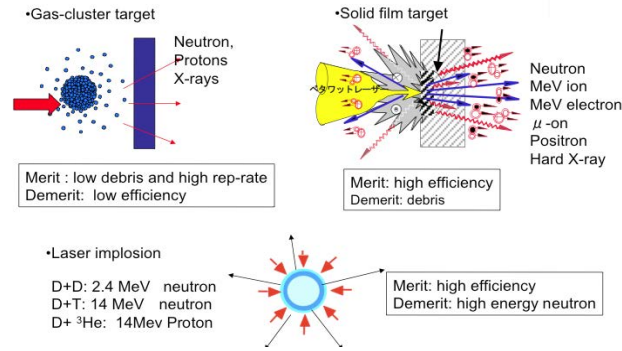


FIG. 6 Generation of Neutron and Beam by High Power laser.

Fig 7 shows the compiled data of neutron generation as a function of injected laser energy with different pulse width depending on the related physical processes. The data points are basically single shot results. The rep-rate operation is needed for the industrial application as a neutron source. For this purpose, repeatable target feeding is also needed. The right vertical axis shows the neutron fluence per second when the neutron production shots are repeated at 10 Hz to 1 kHz. It should be noted that fusion ignition can enhance the neutron production beyond the line  $Q=1$  where the fusion energy is equal to the incident laser energy.

#### 4.2. Industrial applications of laser neutron source

The applications of neutron sources span over wide fields of material science and technology, nuclear energetic, medical, and new methodology in diagnostics, especially in measurements of light elements such as Hydrogen and Li.

The required source neutron intensity is evaluated from the necessary neutron energy and flux density at the sample of the specific application, and the design of energy moderation and guiding of neutrons. It is summarized in Table 2. For the diagnostics of Li-ion battery and fuel cell, the source neutron intensity of  $10^{10} \sim 10^{12}/\text{sec}$  is required. For the medical applications like BNCT, the intensity is  $10^{12} \sim 10^{13}/\text{sec}$ . For semiconductor doping (NTD), the intensity is  $10^{14} \sim 10^{15}/\text{sec}$ . For material processing like annihilation of radioactivity, fusion material test, and fusion-fission hybrid, the intensity higher than  $10^{15}/\text{sec}$  is required.

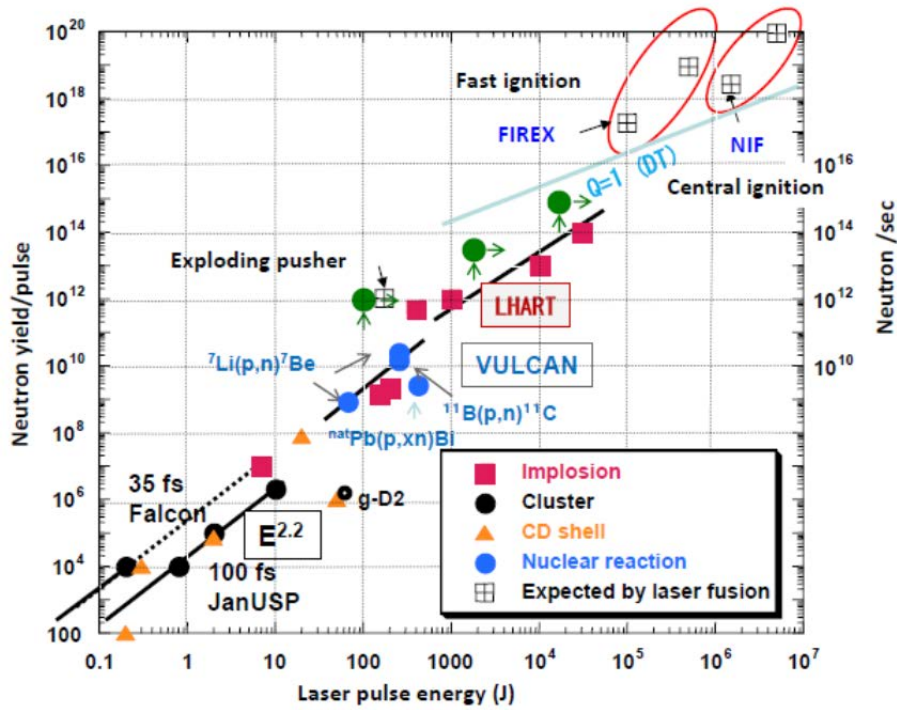


FIG. 7. Neutron Yield Scaling with respect to Laser Energy.

TABLE 2. INDUSTRIAL APPLICATION OF LASER NEUTRON SOURCE AND LASER SPECIFICATION

Field of Application	Nuclear Analysis	Medical	Nuclear Processing
Purpose	•Li ion battery •Proton in Hydrogen energy system	•Boron neutron capture therapy (BNCT)	•Neutron transmutation doping for S:(NTD)
Neutron flux on the sample	$>10^5 \text{ n/s.cm}^2$	$>10^9 \text{ n/s.cm}^2$	depend on the configuration
Neutron source intensity	$10^{10} \sim 10^{12} \text{ n/s}$	$10^{12} \sim 10^{13} \text{ n/s}$	$10^{14} \sim 10^{15} \text{ n/s}$
Laser	$10 \text{ J}(10^8) \times 1 \text{ kHz}$ $100 \text{ J}(10^{10}) \times (10 \sim 100) \text{ Hz}$	$1 \text{ kJ}(10^{11}) \times (10 \sim 100) \text{ Hz}$	$10 \text{ kJ}(10^{13}) \times (10 \sim 100) \text{ Hz}$

## 5. SUMMARY

For IFE power plant developments, the dominant efforts are focused on the driver engineering issues. They are the elements of the building blocks and interface issue. Along with the engineering development for the IFE power plants, growing new applications to industries are such as the UV radiation source for the lithography, the high-energy charged particle acceleration, and the intense neutron source are discussed.

## REFERENCES

- [1] NAKAI, S., IFSA Proceeding, Journal of Physics: Conference Series 112, 042070(2008).
- [2] SEURIN, J.F., DASORO L.A., and GHOSH, C., Photonics spectra July 66(2007)
- [3] SATO T., FUJIMOTO, Y., OKADA, H., YOSHIDA, H., NAKATSUKA, M., UEDA, T., and FUJINOKI, A., Appl.Phys. lett. 90,221108(2007).
- [4] MIMA, K., Report of the Committee on industrial Application of Laser Neutron Source, ILE Osaka University, (In Japanese) February (2010).
- [5] NAKAI, S., *et al.* IFSA Proceeding, Journal of Physics: Conference Series (to be published in 2010).

# THE ROLE OF THE SPATIAL AND TEMPORAL RADIATION DEPOSITION IN INERTIAL FUSION CHAMBERS

J.M. PERLADO  
Instituto de Fusión Nuclear (DENIM)  
Universidad Politécnica de Madrid (UPM)  
Madrid, Spain

## Abstract

In this article, we present the simulations considering the reactor chamber relevant to HiPER. The first wall armor for the reactor chamber of HiPER will have to face short energy pulses of 5 to 20 MJ mostly in form of X rays and charged particles at a repetition rate of 5-10 Hz. Armor material and chamber dimensions have to be chosen to avoid/minimize damage on the chamber, assuring the proper functioning of the facility during its planned lifetime. The maximum energy fluence which the armor can withstand without risk of failure will be determined by how radiation deposits its energy in time and space in the material. In this paper, simulations on the thermal effect of the radiation-armor interaction are carried out with an increasing definition of the temporal and spatial deposition of energy to prove this critical point. These calculations will lead us to present the first simulated values of the thermo-mechanical behaviour of the tungsten armor designed for the HiPER project under a shock ignition target of 48 MJ. The results will show that only the crossing of the plasticity limit in the first few microns might be a threat after thousands of shots for the survivability of the armor.

## 1. INTRODUCTION

Fusion reactions in inertial confinement devices are characterized by short (some ns long) and very energetic explosions (from some tens to some hundreds of MJ) which yield neutrons, gamma and X rays and high energy ions. Among those products, neutrons account for around 70% of the fusion energy and show almost no interaction with the first wall of the reaction chamber. If no protection scheme is devised (ion deflector or a high Z gas), the remaining 30% of the energy in the form of X rays and ions is deposited on the inner wall of the chamber and the front-end optics. Thus, dry-wall designs rely on large chamber dimensions (usually 5-6 m in radius) and an inner wall armor to typically withstand heat loads of 1-6 J/cm<sup>2</sup> and powers of some GW/m<sup>2</sup>. From the thermo-mechanical point of view, this armor has to be made of a material with a high thermal conductivity and melting/sublimation point and with good properties to mechanical stress and fatigue. The goal is to avoid or at least to minimize the mass loss and cracking leading to mechanical failure. The materials under consideration for that purpose are tungsten and carbon based composites. However, nowadays, the tritium retention problem of carbon compounds makes tungsten the standard option on most armor designs [1]. A look at the bibliography shows that, the now canceled American HAPL project [2] relied on a tungsten armor for the 7.5 m radius chamber to absorb the energy from 150 MJ targets (average wall load 5.5 J/cm<sup>2</sup>) at a 5-10 Hz repetition rate. The Japanese Falcon D design [3] also considered tungsten as the most adequate armor material for the reaction chamber. In their design, they planned a 5-6 m radius chamber to house 40 MJ (an average wall load of 2 J/cm<sup>2</sup>) fusion targets at a repetition rate of 30 Hz. The European inertial fusion project, HiPER [4], is meant to use targets of intermediate energies (some tens of MJ up to 100 MJ maximum) at a repetition rate of 5 to 10 Hz. For an initially planned chamber of 5 m radius and a 50 MJ target, tungsten will have to accommodate heats load of around 4 J/cm<sup>2</sup> per shot.

This paper presents the first simulation numbers are made considering the reactor as HiPER project on the thermo-mechanical behaviour of tungsten armor for the proposed 5 m radius chamber under the explosion of a shock ignition target of 48 MJ. First, the characterization of the products of a shock ignition target are described. Then, a series of simulations is presented to highlight the importance of a proper modeling of the time profile

of the delivered energy and its spatial deposition. Finally, the resulting thermo-mechanical behaviour of the tungsten armor when the spatial and temporal profile of the energy deposition is accurately accounted for is shown. Some final conclusions based on the simulation results are discussed.

## 2. FUSION PRODUCTS OF A SHOCK IGNITION TARGET

Fusion targets are filled with deuterium and tritium which, when compressed and ignited, generate 14.1 MeV neutrons and 3.5 MeV He ions. Through different processes, that energy is redistributed among the non-burnt ions (D and T and atoms from the target plastic cover, typically C and H) and in form of X rays. To study the thermo-mechanical effects of the chamber armor against this radiation, the total amount of energy deposited on the wall is not sufficient. As shown later, it is necessary to accurately know the distribution and energy spectra of the different products which be calculated using a radiation-hydrodynamic code.

One of the goals of the HiPER project is to reduce the required laser energy to achieve fusion compared to current approaches (for example, NIF [5]). Thus, HiPER is initially opting for Fast or Shock ignition targets which, in principle, require around 1/3 of the energy of the central ignition targets. For the studies presented in this work, we have chosen the product spectra of a 48 MJ shock ignition target obtained using the LASNEX code [6,7]. In table 1, the energy distribution among the different species is summarized and one can already identify the most relevant particles in the plasma-armor interaction. Since neutrons do not interact with the armor, deuterium, tritium and helium are the main species responsible for the delivery of energy on the armor. Carbon atoms are the next species but their contribution to the total deposition of energy on the wall will be obviated in the thermo-mechanical study. (Carbon content and its energy spectra is very dependent on the target design and its inclusion would influence the validity of the results for a general case). X rays deliver only a 1.4% of the fusion energy to the armor but, as it will be shown, they play an important role in the simulations due to their prompt deposition of energy and consequently high power load on the walls. Other species such as gamma rays, protons and isotopes will be excluded for their minor effect.

TABLE 1. ENERGY DISTRIBUTION OF A 48 MJ SHOCK IGNITION TARGET

	Energy (J) Total= $48 \times 10^6$	
X rays	X rays	X rays
$6.8 \times 10^5$ 1.42%	$6.8 \times 10^5$	1.42%
Neutrons	$3.6 \times 10^7$	75.03%
Deuterons	$2.9 \times 10^6$	6.04%
Tritons	$3.5 \times 10^6$	7.29%
He	$3.6 \times 10^6$	7.5%
C	$1 \times 10^6$	2.08%
Gamma rays H, $^3\text{He}$ , $^{13}\text{C}$	$3 \times 10^5$	0.63%

Figure 1 shows a detailed description of the distribution and energy spectra of the relevant particles to our thermo-mechanical study of the armor. D,T, He and X rays deliver in total a energy of 10.7 MJ to the wall.

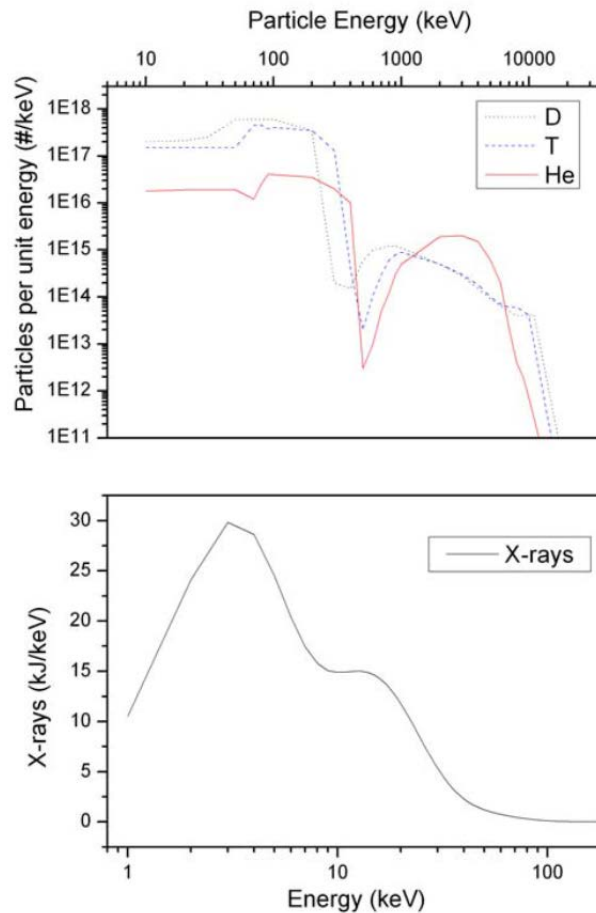


FIG. 1. (Upper) Energy spectra of D,T and He, and (lower) X rays of a 48 MJ shock ignition target.

As it will be shown later, the characterization of the temporal profile of energy deposition is required for a proper simulation of the thermo-mechanical study of the armor. In the case of ions, this temporal profile can be calculated from their kinetic energy spectra of figure 1. Considering a reaction chamber of 5 m in radius, the arrival time of D, T and He particles is represented in figure 2. In the case of the X rays in which all photons travel at the same speed, the temporal profile comes determined by the time span in which they were created. According to previous calculations, the X ray pulse duration has been estimated to be around 1 ns [8].

Figure 2 shows how the different species contribute to the deposition of energy in time steps of 25 ns for a 5 m radius chamber. As it can be seen, X rays arrive almost immediately after the ignition, depositing their energy (6.3% of the 10.7 MJ) at around 17 ns. Then, the fast D, T and He involved in the ignition arrive at around 150 ns after the explosion. Those fast particles have deposited their energy (50% of the 10.7MJ) in the armor before the first  $\mu$ s. Finally, slow D and T particles and thermal He arrive to the armor after the first  $\mu$ s and deposited their energy (the remaining 44%) during 1.5  $\mu$ s. In around 2  $\mu$ s, all the fusion energy which will be delivered to the armor, 10.7 MJ, is deposited.

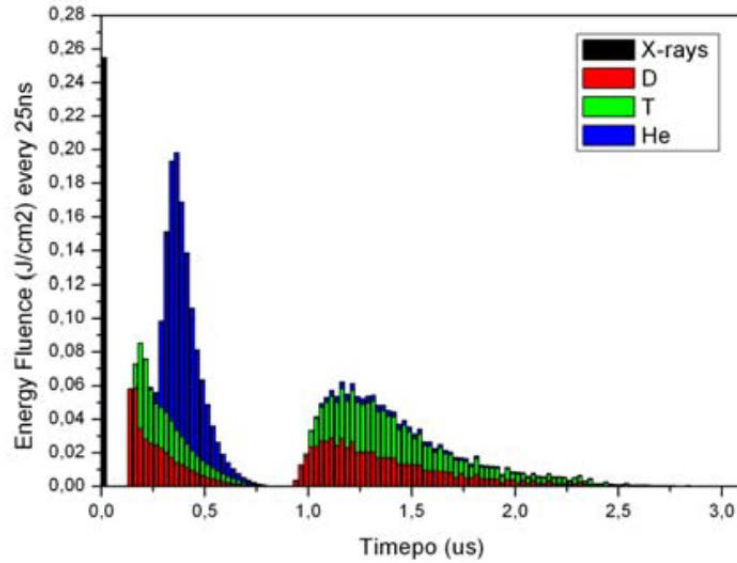


FIG. 2. Temporal profile of the energy deposition of X rays, He, D and T on a 5 m radius chamber for a 48 MJ shock ignition target. Histograms correspond to time intervals of 25 ns. Bars of the different species are added up to show the total energy deposition on each time step.

Finally, the spatial deposition of that energy in the armor is also relevant for an accurate simulation of the thermo-mechanical behaviour of the armor. The spatial energy profile of the different ions can be calculated using the SRIM code [9]. Considering tungsten as the armor material, SRIM simulations are presented in figure 3. In the case of X rays, the spatial deposition has been estimated using the absorption coefficient tables [10] of X ray on W in our spectral region of interest (figure 2). It is important to notice that more than 50% of the total energy is deposited just in the first micron. In the first two microns around 66% of the energy is deposited. This implies that all energy deposited at higher depths (as is the case of fast D and T ions which penetrate some hundred microns, or energetic X rays which travel some tens of microns) will play very little role in the thermo-mechanical behaviour of W. A rough estimate indicates that around 15 to 20% of the arriving energy will be deposited in the W armor with almost no thermo-mechanical effect.

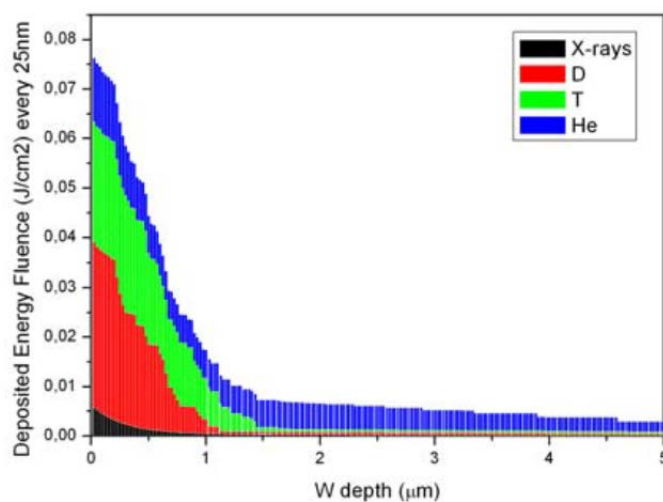


FIG. 3. Spatial distribution of the deposited energy for the indicated particles.

### 3. SIMULATION RESULTS

In principle, HiPER has been proposed as a spherical chamber of 10 m in diameter with a 1 mm tungsten armor as inner wall. In order to simulate the thermal effects on the armor due to its exposure to radiation, we consider three different scenarios:

Scenario 1 – Energy is deposited on the surface during some  $\mu\text{s}$  continuously.

Scenario 2 – Energy is deposited on the surface following the real temporal distribution.

Scenario 3 – Energy is deposited taking into account the penetration depth of the different particles and the real temporal profile.

This exercise will show the importance of an accurate description of the spatial and temporal deposition of energy in the case of simulations for inertial fusion. The heat load on plasma facing materials takes place in such short pulses and with such broad energy spectra of species that approximations as the ones used in magnetic confinement fusion (constant deposition of energy in the first micron of the material) are not valid. Thus, parameters as the Heat Flux value [11] and the roughening and melting limits for tungsten should be handled with care.

The calculations have been carried out using the multi-physics open software CODE ASTER [12]. This software allows to vary the physical and mechanical constants as a function of temperature which has been implemented for our calculations using the ITER material handbook [13]. In all cases and for simulation purposes, the 1 mm W armor is in contact with a fictitious coolant at a constant temperature of 600 K. Also note that in these simulations, no other effect but the deposition of energy in the first wall is considered. Thus, atomistic effects such as sputtering, production of defects and changes in the chemical composition of the armor are not taken into account.

#### 3.1. Scenario 1 – Energy is deposited on the surface during some us continuously

The simplest scenario possible in the deposition of energy on the armor is to consider that all the radiation energy is deposited evenly in time on the surface. Thus, for our case, the total amount of energy delivered by the X rays, D, T and He ions is 10.7 MJ, which corresponds to an energy fluence of 3.4 J/cm<sup>2</sup> for a 5 m radius chamber. This energy can be considered as deposited in a time of 2  $\mu\text{s}$  (see figure 2). This one-dimensional heat equation problem has analytical solution and yields a maximum temperature value on the surface of 1900 K. Taking into account the temperature dependence of the physical properties of W, the simulation was performed using the CODE ASTER software. Figure 4a shows how temperature reaches a maximum of 2200 K at the end of the pulse. After the 2  $\mu\text{s}$ , the temperature decreases rapidly due to the high thermal conductivity of W (173 W/m/K), reaching the base temperature of 600 K after 10 ms. Without further discussion, we can say that, since W can displace heat so quick, the fact that the time profile of the deposition of energy is not considered will give us an underestimation of the maximum temperature.

#### 3.2. Scenario 2 -Energy is deposited on the surface following the real temporal distribution

The first refinement in our simulations to be considered is to include a proper temporal profile of the energy deposition on the W armor. As expected, simulations (figure 4b) yield quite different results from that of the scenario 1. The first evident conclusion is that the temperature evolution of the armor follows the time structure of the radiation pulse, reaching at certain points higher temperatures and dropping to the base temperature after some ms. The

most remarkable results is that, according to the simulations, the fast energy delivery of the Xray pulse leads to temperatures above the melting point (3600 K). However, experiments with X ray sources have shown that W starts to melt at much higher energy fluences [14]. This time, one must realize that the deposition of energy only on the surface obviates the fact that the radiation energy has a spatial profile inside the W according to the penetration depth of the different particles. This simplification in the modelling leads to an overestimation of the maximum temperatures.

### 3.3. Scenario 3 – Energy is deposition taking into account the penetration depth of the different particles and the real temporal profile

In this scenario, we consider the temporal and spatial profile of the energy deposition of the radiation in the W armor. A detailed description of the temporal and spatial distribution of energy differs from previous scenarios (figure 4c). The temperature evolution at different depths clearly shows similar results to those obtained for other W armors [2] and the highest temperature does not reach 1800 K. Once again, the W armor diffuses away all heat before the next pulse.

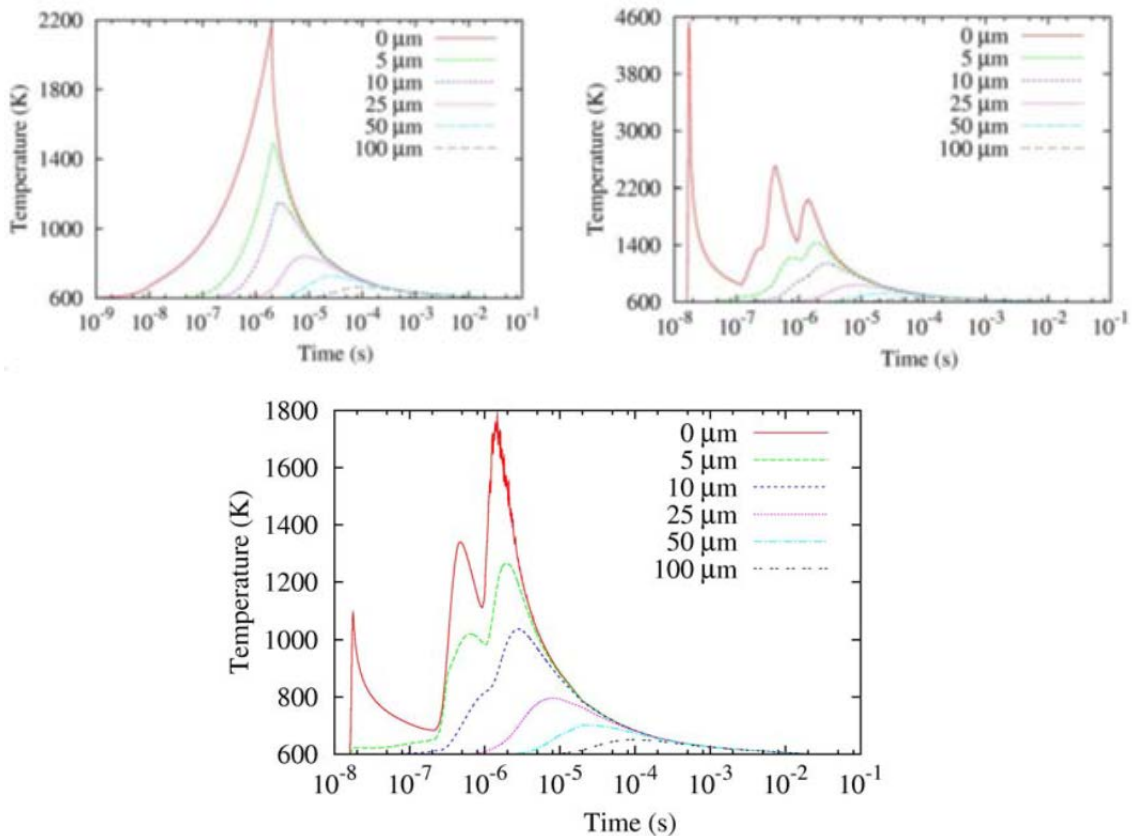


FIG. 4. Temperature evolution at different tungsten depths for a heat load of 3.4 J/cm<sup>2</sup> under a) scenario 1 (upper) , b) scenario 2 (mid) and c) scenario 3 (lower).

Under these proper conditions for the deposition of energy, we also carried out a 2D analysis on the mechanical behaviour of the W armor with CODE ASTER. The observed increase of temperature generates a measurable expansion of the W which, in turn, causes compressions in the wall. The main compression is tangent to the surface of the wall because W only can expand in radial direction due to geometrical considerations.

Figure 5 shows temperature and Von Misses stress ( $\sigma_{VM}$ ), which measure the stress compression into the wall, as function of the depth at a fixed time of 1.5  $\mu$ s. When temperature increases, the expansion of the material produces an increase in the stress. The presented stress has been obtained considering the hypothesis that tungsten behaves as an elastic material, so when the Von Misses stress is higher than the Yield Strength (also represented in figure 5), the tungsten suffers plastic strain. The fact that at high temperature the Yield Strength decreases makes that crossing more favourable. Thus, plastic strain is located in the first microns of the wall, reaching around 18  $\mu$ m in times after 1.5  $\mu$ s. When the temperature decreases and W returns to its initial volume, there are residual traction stress in this layer. As detailed by Blanchard and Martin [15], fatigue due to cycle plastic strain might produce cracks at the surface. The possibility that these cracks, together with other atomistic effects, influence on the survivability of the W armor with increasing fusion shots is under debate [15].

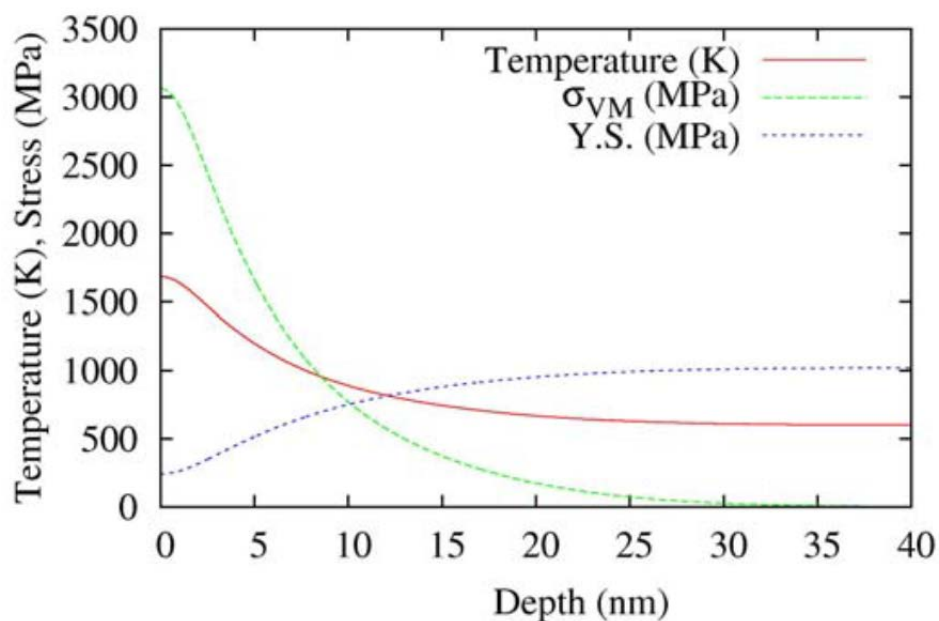


FIG. 5 – Temperature, Von Misses stress and Yield Strength as function of depth at 1.5  $\mu$ s, of simulation.

#### 4. CONCLUSIONS

The inner wall of an inertial fusion reaction chamber will have to withstand high power loads five to ten times a second. With no ion or X ray protection, only relative large chambers (5-8 m radius) and wall armors made of high resistant materials to thermal loads and mechanical stresses (as tungsten) can handle this harsh environments. In order to appropriately study the thermo-mechanical effects of the fusion radiation on the armor, one has to fully account for the precise temporal and spatial deposition of the radiation on the material. Avoiding to do that will underestimate or overestimate the energy fluence limit (J/cm<sup>2</sup>) to preserve the lifetime of the armor. This point has been clearly demonstrated on these pages. Moreover, this work shows the first thermo-mechanical studies on the W armor for the HiPER project under the radiation of a 50 MJ shock ignition target. Calculations reveal that, W armor will work well below its melting point. Only mechanical effects due to transitions of W to its plasticity phase could affect its performance. Fatigue and eventually crack formation under hundred/thousand fusion shots might end in mass loss and irreversible damage.

## REFERENCES

- [1] Kaufmann, M., ,Neu, R., Fusion Engineering and Desing 82 (2007) 521.
- [2] Raffray, A.R., et al., Snead, Fusion Engineering and Design 81 (2006) 1627.
- [3] GOTO, T., Nucl. Fusion 49 (2009) 075006.
- [4] <http://www.hiper-laser.org/>.
- [5] MOSES, E. I., Energy Conversion and Management 49 (2008) 1795.
- [6] ZIMMERMAN, G., et al., Journal of the Optical Society of America 68 (1975) 549.
- [7] PERKINS, J., Internal report.
- [8] PERKINS, J., Internal report <http://www.docstoc.com/docs/54806737/Temperature-Response-and-Ion-Deposition-in-the-1-mm> ).
- [9] <http://www.srim.org/>.
- [10] <http://www.nist.gov/physlab/data/xraycoef/index.cfm>.
- [11] LINKE, J. et al. J. Nucl. Mater. 367-370 (2007) 1422 .
- [12] <http://www.code-aster.org/>.
- [13] Tungsten properties ITER Material Handbook <http://aries.ucsd.edu>.
- [14] TANAKA, T. J., et al. J. Nucl. Mater. 347 (2005) 244.
- [15] BLANCHARD, J.P., AND MARTIN, C.J., J. Nucl. Mater. 347 (2005) 192.

# **CHAMBER RESPONSES AND SAFETY AND FUSION TECHNOLOGY IN INERTIAL FUSION ENERGY (IFE) REACTOR RELATED TO HIPER: A REFERENCE STUDY**

J.M. PERLADO  
Instituto de Fusión Nuclear (DENIM)  
Universidad Politécnica de Madrid (UPM)  
Madrid, Spain

## **Abstract**

In continuation of our effort to study safety of fusion technology, we again consider reactor design for HiPER - The proposed European Laser-Driven Fusion Facility is actually being developed in collaboration with many European (and also international) laboratories. The project was upgraded to the present state of two clear steps in proposing funding for next phase development to arrive finally to an inertial fusion power plant. In addition to laser, target (defining and manufacturing, injection and tracking), chamber design is a key aspect in this new phase in which the project has entered. An overview of the state of art of different options of Chamber, their necessary assessments with the safety and environment considerations will be presented together with proposals for fusion technology experiments.

## **1. INTRODUCTION**

The HiPER project final goal is to design an inertial fusion facility based on Fast Ignition concept where demonstration of ignition and gain (in the range of 44 compression beams giving 200 kJ in 5 ns and a PW beam line of 70 kJ in 10 ps) will be combined with a complementary exploration of longer term research in Inertial Fusion Energy and different spin-off in basic physics, astrophysics, nuclear physics, high density matter, etc. To get those purposes several steps are being envisioned.

From already general criteria we will need to consider aspects such as: i) withstand earthquakes; ii) be resistant to debris, radiation, shrapnel and neutrons effects from experiments; iii) maintain deep vacuum and ultra-freezing environments required for experiments; iv) accommodate the many diagnostic instruments, beam lines, and associated optics and equipment; v) maintain as low as possible the activation of the materials component of the chamber in order to induce the minimum radioactivity and make easy the operation and maintenance; vi) take into account tritium permeation, diffusion, contamination in that phase of operation. We will present the main criteria when designing the main chamber: fabrication (thickness of shell, welding...); the installation of penetration in the chamber and vacuum leak checking; chamber shielding and uncertainties in it; and the chamber survey and alignment for location of optics and laser ports.

From calculations available in different type of targets we are extracting data of energy yields from debris, X rays, and neutrons, also considering the different energy spectra. The capsule design will be critical together with the calculation of those numbers, but even with no actual final design for fast ignition, CHAMBER research is imperative. A potential low fraction of X rays could come from the fact that targets are fully ionized at the end of the burn and bremsstrahlung is the dominant emission. An important difference is also the angular dependence of X rays, and particles emission (this aspect could be very critical for fast ignition conical targets). A key aspect will appear when considering the repetitive operation in HiPER, even at lower energies, because the effects on some of the components are not well known. It is already known that for some frequencies there could be differences in the material performance but no experimental proof has already been done. Multiscale Modelling already done will be presented adequate to HiPER proposal.

From the point of view of safety and environment of the facility we are calculating the evolution of the activity (associated magnitudes are contact dose rate and index of waste disposal) accumulated in the chamber along the period of operation before the cleaning of the chamber and evacuation of fuel residual. A second question is to determine the activity accumulated in the storage facility that collects the activated material which is discharged from the chamber annually during its lifetime. For the problem related to the accumulated activity, we need to define the scenario of irradiation (HiPER designs (a) and (b)) in the internal surface of the first wall (where the material of the burn fuel is deposited) and inject different types of materials in the times scheduled by the programming of shots during the operational year before the discharge. Related to the activity of the storage facility, that is a pure cooling problem, and the material to be injected is that accumulated during operation time from addition of that yearly discharged. We will need to determine the target material (and positioner) accumulated after a defined period of time in the interior of the chamber, including its temporal evolution, photon production, and contact dose rate in the internal surface of the chamber together with the disposal ratio.

We plan to present the methodology to follow in these aspects in HiPER designs and the strategy for assess the viability of such number of chambers, including primary and secondary activation of the chambers. HiPER can provide essential data for IFE in areas in Fusion Technology: Target chamber phenomena and materials responses to target emissions; Prototypical IFE fusion power technologies in the chamber area; Performance testing of IFE target fabrication and injection methods. HiPER would thus play a critical role in providing the basis for design of the follow-on Engineering Test Facility in these areas. Using well established HiPER target output, we will get beneficial knowledge of future technologies with some modification of HiPER main chamber design to allocate these experiments. That is the goal in this phase.

These experiments include important tests in the areas of IFE-specific target physics and IFE fusion power technologies (nuclear heating, transport, activation and shielding, tritium management, IFE materials science, and safety/environment). This group constitutes the majority of IFE experiments, and the majority of IFE-specific shots. Thus, the main impact to consider is their contribution to the total HiPER shot envelope and allowed chamber activation, along with all other user-group shots.

## 2. PROPOSALS OF CHAMBERS

After the first phase of HiPER basic knowledge of potential chambers and discussion on what will be available from the point of view of Technology, Safety and Radio Protection, some expected definition of new phases are open that include the design of an Engineering Facility operated in the burst mode (100 shot per operation / no continuous repetition) named HiPER 4a. Finally, the goal of European initiative HiPER is the Phase 4b devoted to build a power plant (reactor) to demonstrate commercial viability of laser-fusion. The present duration of such Technological Phase (or Risk Reduction) is estimated in approximately seven years as it is envisioned in next Figure where other development of phase Power Plant is also included.

In addition to this initiative there are, in full coincidence on time, the LIFE (Laser Inertial Fusion Engine) project at the Lawrence Livermore National Laboratory (USA) and LIFT (Laser Inertial Fusion Technology) from Institute of Laser Engineering (ILE) of the University of Osaka (Japan) together with other Japanese institutions.

Therefore, the HiPER 4b facility requires a robust reactor assembly that is suitable for a commercially acceptable period of operation in order to demonstrate Reliability, Availability and Maintainability requirements for energy generation, without undergoing major overhaul.

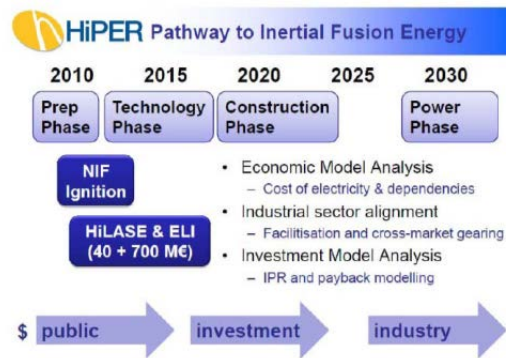


FIG. 1. Estimated progress of HiPER project.

The basic elements of reactor consist of the final optic assembly (including the moving “engagement” mirror), the target engagement control system, the injector, the reactor outer containment, and blanket, energy extraction system to the primary heat exchanger, tritium handling systems and the first wall. The considered optimal strategy is also to define an Engineering Systems (HiPER 4a) in which it would be possible to test in burst mode all the technologies necessary for a reactor, mainly repetition of laser and injection, under a CHAMBER with less requirements and no blanket (heat extraction and tritium breeding) in it.

The CHAMBER research is thought to be conducted through independent facilities where the areas mentioned below could be demonstrated, and finally integrated in an experimental frame in such phase. The key aspect here is to reduce very strongly the risk associated to the final build up of the Power Plant going to such phase of HiPER 4b with a high degree of success. At the same time the goal is to get the large interest of industries and governments in an ENERGY initiative based in a realistic demonstration, as expected, of ignition and gain as soon as 2011 in National Ignition Facility (NIF) at Lawrence Livermore National Laboratory (USA), and in Laser MegaJoule (LMJ) in Commissariat l’Energie Atomique (CEA) in Bordeaux (France) probably first experiments in 2014.

Certainly, in addition to the CHAMBER design, the laser needed for real efficient/repetitive reactor will be design and the target (whatever option is selected) clearly defined for gain operation together (if possible) with adequate manufacturing, injection and tracking. Current ignition scheme options include Fast Ignition (FI), Shock Ignition (SI) and Central Ignition (CI) with Direct Drive (DD) and Indirect Drive (ID). HiPER design (as mentioned) is based on Fast/Shock Ignition schemes, and demonstration of those potentialities is critical for the Project as a Pan European and also international project; in that sense follow up of present experiments at OMEGA-EP (Laboratory for Laser Energetic/ Rochester University, USA) and FIREX (Institute Laser Engineering / Osaka University, Japan) in this present time are absolutely critical. Certainly in Europe experiments in French facility PETAL when available will also be decisive for this HiPER idea; but other present, or close to be in operation, facilities such as GEMINIS, HILASE, ELI will be critical. In previous works we identify the dry wall and wet wall reactor options that are currently (and in the next years) to be evaluated for HiPER (perhaps gas protection?).

It draws on the work performed in reactor design discussing the merits and demerits of each design type. It reviews the suitability of these different reactor types for the different ignition schemes and target designs currently being considered, and comments on possible solutions for use in HiPER. We need a down select decision to be made for the HiPER Phase 4b reactor. That will be (and it has already started) in close collaboration with LIFE and LIFT.

IFE power plant conceptual design studies have been performed for over thirty years, essentially in USA (SOLASE (1977), SOMBRERO (1991), PROMETHEUS, HAPL (2001-8), HYLIFE-2, LIFE (2010) and a long list), but also in Japan (SENRI, KOYO, KOYO-F, FALCON). In Europe, there have been also design studies such as HIBALL I-II, LIBRA and LIBRA \_LITE, HIDIF. From these studies a lot of ideas have appeared from different laboratories, some of the key aspects have been lighted now, and in some cases experiments for proof of principles have been performed. For HiPER next steps there are essentially two main chamber types, wet and dry wall. The HiPER reactor would be significantly complex probably being circa 50 laser beam entries, potentially more than one injector, a number of diagnostic ports and entry points for remote maintenance access. The number of penetrations would be subject to detailed design, this being concluded during HiPER 4a operations circa 2020 to 2030. In addition to these problems is key to design very carefully the RadioProtection Systems (Shielding concerning the different areas of the Reactors. During the operation of HiPER first engineering facility, up to  $2 \cdot 10^5$  MJ per year of fusion neutrons yields are foreseen. This irradiation level could be distributed in 100MJ detonations, accounting up to 100 detonations in a single burst, with 10Hz repetition rate. A burst would take place every month.

The dose rates are computed and different concrete shields are evaluated within the target bay. During the operation of the facility the stays inside the bioshield are exclusion areas. Between bursts, manual maintenance might be performed inside the bio-shield but outside the final optics (FO) shield. Inside the FO shield the residual dose rates are so high that only remote maintenance is allowed. The FO shield reduces the delivered dose rate in a factor of 435.5

As mentioned several reactor configurations are actually considered based on dry or wet walls. Dry Wall reactors operate with a base pressure of approximately 10-4 mbar ( $\sim 0.1$  mTorr) and rely on wall distance (but other options such as special geometries, materials are explored) from the fusion event and wall material properties to resist the huge fluxes stemming from every explosion. In order to minimize the chamber dimensions, different Gas Protection scenarios have been proposed. They rely on a certain density of gas (typically Xe) inside the chamber, in the order of 10-2 mbar (tens of mTorr) @ST. With the current knowledge, gas protection scenarios appear incompatible with FI schemes due to non-linear interactions between the PW ignition laser pulse and the gas.

In other ignition schemes, in particular with ID target, gas protection is an option, and we will need to explore. We will not consider a high gas density because it can affect laser transport (not only in FI scheme) and target injection, especially in the case of DD targets. Wet Wall reactors of all variants rely on the low vapour pressure liquid coating of internal reactor walls mitigating the effects of operation. They are very attractive due to the self-healing nature of liquid. However, some drawbacks have been reported. In particular, aerosol formation can affect laser transport, target tracking and engagement. Further research must be devoted to these topics. Finally, some works propose to use magnetic intervention for ion deflection. Detailed calculations indicate that a properly designed magnetic field may lead all

generated charged particles to a divertor out of the chamber. Despite some disadvantages such as its complexity, cost and divertor-related problems this idea must not be ruled out.

No solution is optimal yet for HiPER 4b, and that is one of major objective for European laboratories, in particular as present responsible in HiPER. During phase 3 and 4a of HiPER, physics schemes, target packages, materials and modeling research and prototyping will be undertaken to find technologically safe solutions. Maybe the most favored reactor option now would be a dry wall chamber which could be suitable for all ignition schemes currently under consideration and their associated target types. Limitations of currently available first wall materials to meet the operation demands seem solvable by means of further R&D programs in this topic. Within the R&D still necessary, this area appears as one of the most easily successful in the coming years. In addition, (undesired) enhance of chamber dimensions or magnetic intervention could work if an appropriate solution for first wall materials is not found.

### 3. STRATEGIC LINES AND RESULTS

HiPER, both options of 4a (Engineering) and 4b (Power Plant), has many areas in CHAMBER design where put emphasis, which could be different depending on what facility it can be talking about. We list now a systematic approach of list task to be developed by groups in this field:

- (a) Knowledge of physics for damage in materials and protection of the chamber walls and optics from debris ions, X rays, alpha particles and shrapnel
- (b) Provision of a working life suitable for commercial applications. That implies work to be performed in both areas of Materials resistant to irradiation and being of low/reduced activation minimizing the radioactive waste in the facility
- (c) Operation at repetition rate and the potential for re-setting the first wall protection measures after a shot to a level suitable to permit another shot to be undertaken
- (d) Minimising the effect of first wall ablation or aerosol sputtering effects from posing increased challenges to the injection and engagement of a target
- (e) Breeds tritium at a minimum breeder ratio of 1.1 to permit continued operation with minimum tritium inventory.
- (f) Ensuring that the chamber size and port arrangements make achievable:
  - (a) final optic protection from ions
  - (b) laser spot size and accuracy of pointing on target
  - (c) diagnostic protection
  - (d) target survival
  - (e) target engagement
  - (f) Radioprotection design of the different areas of the reactor HiPER in its different options (Shielding, penetrations and operation conditions depending of areas, including necessity of remote handling or potential personnel intervention in time intervals).

Then, key issues for creating an operating reactor with a matched ignition scheme are:

- First wall life;
- Target survival in the environment;
- Ability to engage lasers appropriately with target;
- Final optic life assuming that neutrons, X rays,  $\gamma$ -rays and shrapnel will hardly be avoided, in particular in evacuated chambers;
- Structural material performance under intense pulsed neutron irradiation.

From that list Chamber design inside HiPER has started to identify key aspect correlated with experiments proposed in the near future. Those experiments and proposal are both for HiPER 4a and 4b, in spite that we will have different conditions and work very special need to be define the type of blanket in HiPER.

The major difficulty to make accurate predictions on materials performance stems from the simultaneous interactions (synergetic effects) of different types of radiation (neutrons, energetic photons, charged particles) with the surrounding materials. In particular, for Inertial Confinement Fusion (ICF) reactors with targets such as those expected for HiPER, the major threats to target facing materials come from the arrival of high fluxes of a large variety of energetic particles (mainly D, T, He and C) shortly after the deposition of a high power pulse of X rays and the subsequent passage of a high flux of neutrons (energy up to 14 MeV/neutron). We want to assess in fig.2 where we are in potential experiments in Inertial Fusion:

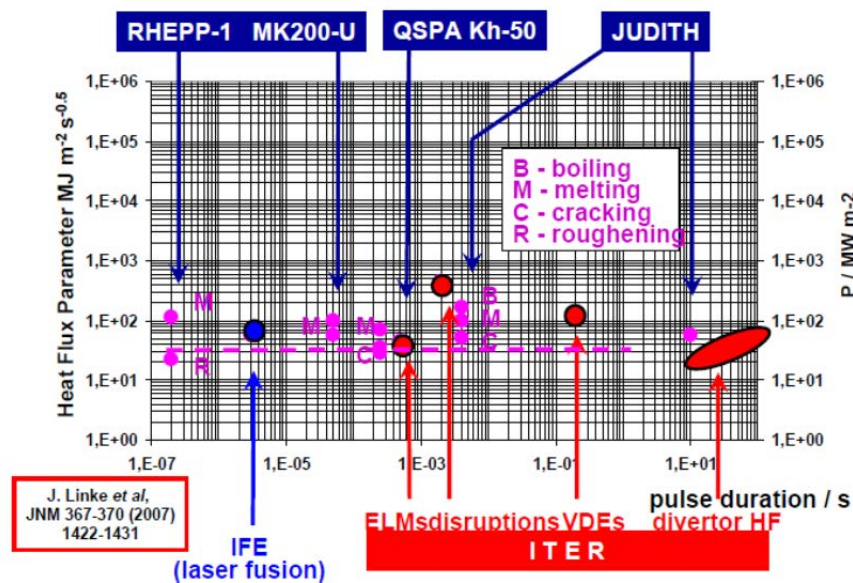


FIG. 2. Assessment of the potential experiments in Inertial Fusion.

In order to study the combined effect of light species (D/He) and heavier ions (C) on first wall materials and final optics components subjected to ICF radiation conditions, one needs to use a multi-beam system. It is proposed to use the double beam facility available at the group of *Ion Physics in Forshcugzentrum Rossendorf*.

For the final optics, we will need to compare high quality optical graded silica samples with KU1 silica, well known for its radiation degradation resistance. In addition, we need to consider the performance of (unavoidable) anti-reflective coatings (e.g. hafnia) subjected to ICF ion irradiation. For this purpose a plan proposed by Instituto Fusion Nuclear of UPM is to

reproduce the effects due to simultaneous implantation of C-He/D typical of an ICF reactor. The study will be carried out at different sample temperatures and up to doses of  $10^{17}$  cm<sup>-2</sup>, which are equivalent to 100000 shots of 20 MJ direct drive targets (as those planned for the first phases of HiPER). The diffusion and retention (depth profiling) of light atoms will be studied by resonance nuclear reaction analysis (RNRA) as a function of temperature and thermal desorption spectroscopy (TDS). The structural and morphological properties of implanted samples will be investigated by X ray diffraction (XRD), atomic force microscopy (AFM) and transmission electron microscopy (TEM).

The combined use of these techniques will make possible the understanding of the combined effects of damage and gas retention (bubble formation) and the development of macroscopic detrimental effects such as swelling and blistering under realistic ICF conditions. The mechanical (W) and optical (silica) properties will also be investigated after irradiation to relate the observed effects.

As first option W is a promising candidate for the reactor first wall due to its high melting temperatures, good thermal conductivity, low sputtering and low tritium retention. The implanted-induced effects of H, D and He as single light species in W have been widely studied. However, as far as we know, synergetic effects which may reduce significantly the operational window of W as a first wall material have been only reported for Magnetic Fusion (MF) conditions at room temperature. Moreover, the interaction with C poses additional risks on material performance.

The work the Instituto (DENIM) intend to carry out (in facilities such as *Jannus* or *TIARA facilities*) is related to the study of the combined effect of light species (D,3He) and heavier ions (12C) on first wall materials for ICF reactors. In particular, we will co-implant D, 3He and 12C in single- and poly-crystalline W samples. In order to simulate a prototypical IF energy ion, the implantation energies would be selected to be 0.75 MeV for 12C, 1.51 MeV for 3He and 0.5 MeV for D. The fluences used for implantation will range from  $1 \times 10^{15}$  to  $1 \times 10^{17}$  cm<sup>-2</sup>. The implantation would be done at different temperatures (from room temperature up to above 1000 °C). These conditions are very similar to those expected for the first phases of HiPER. The second part of the work is related to the characterization of the diffusion and retention (depth profiling) of light atoms immediately after co-implantation. For this purpose, we intend to carry out resonance nuclear reaction analysis (RNRA) by using the  $3\text{He}(d, p)4\text{He}$  and the  $12\text{C}(d, p)13\text{C}$  nuclear reactions.

The effect of tritium is critical and will be in Power Plants; then proposals such as following (by Insituto Fusion Nuclear, DENIM) is the study of diffusion and retention (depth profiling) of light atoms, H, which can be produced by transmutation or introduced by interaction with the plasma, in the materials to be used in future fusion reactors. The understanding of this phenomena is crucial in order to be ready for the design of the future reactor HiPER 4b, and it is one of the significant differences between fusion technologies and other related areas (fission or spallation sources, for example). To this end  $\text{Li}_2\text{SiO}_3$ ,  $\text{Li}_4\text{SiO}_4$ ,  $\text{Li}_2\text{TiO}_3$ ,  $\text{Li}_2\text{ZrO}_3$  and ODS steel samples were grown under different conditions in order to achieve a different microstructural configuration and implanted with deuterium at different energies (the projected ranges of the implanted hydrogen ions were calculated with the TRIM code to be around 0.8  $\mu\text{m}$  and 1.6  $\mu\text{m}$  for 50 keV and 100 keV energies, respectively), at different doses (up to  $5 \times 10^{16}$ cm<sup>-2</sup>) and at room temperature.

In order to study the hydrogen diffusion not only as a function of microstructural properties but also as a function of annealing temperature some of the samples were annealed after implantation at different temperatures in the interval between 100 and 400°C.. The

microstructure of the samples has been investigated by XRD prior to and after ion-implantation. The work that we intended to carry out in *Rosendorf* is related to the hydrogen depth profiling characterization in as-implanted and post-annealed implanted samples. To this end we will perform depth profiling experiments by using H ( $^{15}\text{N},\text{He}$ ) $^{12}\text{C}$  nuclear reaction. Depth profiling of deuterium in deuterium-implanted fusion materials (Lithium-compounds ceramics and ODS steels with different microstructure and annealed at several temperatures in the range from 300 to 700°C). The work that we intended to carry out in Katholieke Universiteit Leuven (KUL) is related to the deuterium depth profiling characterization in as-implanted and post-annealed implanted samples. To this end we are intended to perform depth profiling experiments by using the  $\text{D}(^3\text{He}, \text{p}) ^4\text{He}$  nuclear reaction. In order to look for the optimal analysis conditions we ask for three days to analyse the most representative samples and to study the feasibility of the experiment.

From the Radio Protection in HiPER, we have studied the implications of a preliminary proposal of design from the standpoint of internal and shielding requirements of CHAMBER. The reference case is considered to be the most exigent irradiation scenario conceived for HiPER 4a. We will start with HiPER 4b defining in near future the Blanket structure and accommodation in the system. 100MJ neutron yields per shot, with 100 shots at 10 Hz in a single burst, one burst every week or month (other more realistic is 20MJ neutron yields, with 5 events in a 100 non-explosive shots per bursts at 10 Hz (explosions occur at 0.5 Hz)). A fully defined geometry has been used for very detailed 3D geometry considering penetrations and different areas.

Materials as SS304L, EUROFER and Al5083 has been considered with a borated concrete shield after that structure with a thin first wall of W. The expected lifetime of the facility for this scenario is 20 years. We have computed the prompt dose rates (PDR) and residual dose rates (RDR) delivered to the workers/public during the operation and in the period between bursts; we also computed the prompt dose delivered to the Final Optic Assembly (FOA), as a sensitive part of the facility.

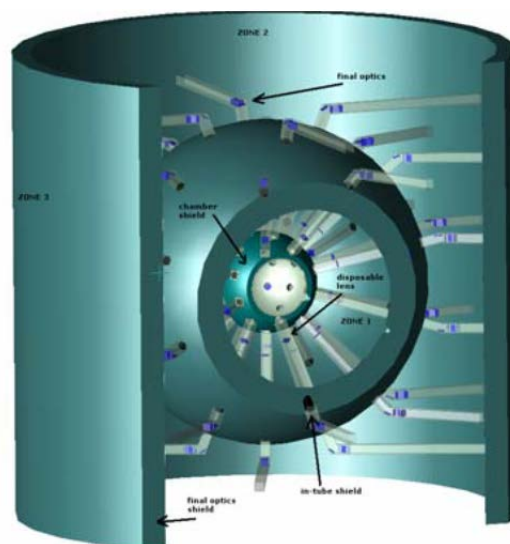


FIG. 3. Preliminary proposal design of HiPER facility.

The shields that have been proposed behave reasonably well, creating free-restriction areas outside the target bay, and allowing manual maintenance 36 hours after the shutdown in

some stays. The FOA receives a dose rate 30 times lower in the presence of the FOA shield. We compute the quantities with the same design undergoing a softer irradiation scenario, resulting a waiting time to access to the restricted area shorter than one day. The FOA receives 20 times lower dose rates. We have also considered different materials for the tubes which transport the beams, as they are the main responsible for the RDRs. The choice of material for the reaction chamber is discussed for commercial and reduced-activation steels, with regards to waste management performance.

## ACKNOWLEDGEMENTS

The authors acknowledge the International Atomic Energy Agency (IAEA) and the support of the Funding Agencies undertaking this work (EC FP7 project number 211737): EC, European Commission, MSMT, Ministry of Education, Youth and Sports of the Czech Republic and STFC, Science and Technology Facilities Council of the United Kingdom. It has been also partially supported by Plan Nacional de I + D + I (2008 - 2011) Fusion Nuclear ENE2008-06403-C06-02 MICINN. This work is mainly consequence of group of people at Instituto Fusion Nuclear doing present proposals, and first author thanks J. Alvarez, A. Rivera, R. Gonzalez-Arrabal. S. Cuesta, D. Garoz. R. Juarez, J. Sanz for all the material in their specific articles and here.

## REFERENCES

- [1] <http://www.hiper-laser.org/index.asp>.
- [2] JUAREZ, R., et al., Overview on Neutronics, Safety and Radiological Protection of HiPER Facility, IAEA FEC 2010, Daejon, October 10-17, (2010) IFE/P6-22.
- [3] ALVAREZ, J., et al., The Role of the Spatial and Temporal Radiation Deposition in Inertial Fusion Chambers, IAEA FEC 2010, Daejon, October 10-17, (2010) IFE/P6-23.
- [4] CUESTA, S., et al, Modeling Advanced Materials for Nuclear Fusion Technology, IAEA FEC 2010, Daejon, October 10-17, (2010) IFE/P6-24.
- [5] GONZÁLEZ-ARRABAL, R., et al., Study of diffusion and retention of light species (H and He) in pure W and W-based materials, IAEA FEC 2010, Daejon, October 10-17, (2010) IFE/P6-25.
- [6] Information on Laser Inertial Fusion Engine (LIFE) from Lawrence Livermore National Laboratory from Ed. Moses in IAEA FEC 2008, J. Latkowski, IAEA CRP Vienne 2010, W. Meier SOFT 2010, T. Díaz de la Rubia, Madrid Conference at UPM, 2009.



# HYDRODYNAMIC INSTABILITIES IN INERTIAL FUSION SYSTEMS AND HIGH ENERGY DENSITY PHYSICS

A.R. PIRIZ\*, J.J. LÓPEZ CELA\*, S.A. PIRIZ\*\*, N.A. TAHIR\*\*\*

\* E.T.S.I. Industriales, Universidad de Castilla-La Mancha, 13071 Ciudad Real, Spain

\*\* Facultad de Ciencias Físicas, Universidad Complutense de Madrid, 28040 Madrid, Spain

\*\*\* GSI Helmholtzzentrum für Schwerionenforschung Darmstadt, 64291 Darmstadt, Germany

## Abstract

We report our research work performed during the period 2007-2009 on hydrodynamic instabilities that affect the design of experiments on inertial fusion and high energy density physics. In particular we have studied Richtmyer-Meshkov and Rayleigh-Taylor instabilities in the framework of experiments on high energy density physics and Rayleigh-Taylor instability in ablation fronts directly driven by ion beams.

## 1. INTRODUCTION

Richtmyer – Meshkov (RM) instability occurs when a shock wave goes through an interface between two media or when the shock is launched into a medium from a free surface ( $y = 0$ ). Instead, Rayleigh-Taylor instability occurs whenever a medium with density  $\rho_1$  pushes and accelerates another medium with higher density  $\rho_2$  ( $\rho_2 > \rho_1$ ). In the reference frame of the interface we have a constant gravitational field  $g$ .

Hydrodynamic instabilities in solids with elastic-plastic (EP) properties are of great importance in high energy density physics (HEDP) both, because they affect the performance of the experiments, and also because their application as a tool for investigating the mechanical properties of matter under extreme conditions.

The implosion stability in the LAPLAS (Laboratory of Planetary Sciences) experiment on HEDP that is planned at GSI can be controlled by the high tensile strength of the shell. Inertial fusion capsules can also benefit from the constitutive properties of the material. Besides Rayleigh-Taylor instability is at present the main tool for the experimental evaluation of the yield strength  $Y$  of accelerated solids. Richtmyer-Meshkov instability could also be used as a tool for HEDP.

## 2. RICHTMYER-MESHKOV INSTABILITY IN ELASTIC PLASTIC SOLIDS

We consider a free surface at  $y = 0$  with a small sinusoidal perturbation of amplitude  $\xi_1$  and wave length  $\lambda$  ( $k\xi_1 \ll 1$ ;  $k = 2\pi/\lambda$ ). A shock driven by a constant pressure  $p_0$  is launched from this surface. Then, we study the time asymptotic evolution of the interface corrugations. This evolution can be described by the following equation [1,2]:

$$\frac{\rho}{q} \frac{dv_y}{dt} = -S_{yy} ; \quad S_y = \frac{S_{yy}}{\sin kx} = \begin{cases} \sqrt{\frac{2}{3}} \frac{Y}{\alpha|M} ; k\xi > 0 \text{ and } \xi \geq \xi_p \\ 2 \frac{k}{\alpha} G(\xi - \bar{\xi}) ; k\xi < 0 \text{ or } \xi \leq \xi_p \end{cases}$$

where  $1/q$  is the characteristic length of decaying of the surface modes,  $\rho$  is the density of the shocked material,  $v_y$  is the normal component of the perturbed velocity field,  $S_{yy}$  is the deviatoric part of the stress tensor  $\xi_p$  is the amplitude for which the elastic limit is achieved and  $\bar{\xi}$  is the initial amplitude when the material is stress-free. For calculating the deviatoric

part  $S_{ij}$  of the stress tensor  $\sigma_{ij} = -p\delta_{ij} + S_{ij}$ , we have assumed a Prandtl-Reuss rule with the von Mises yield stress criterion.

By integrating the equation of motion of the interface we obtain the time evolution of the perturbation amplitude. For times  $t_0 \leq t \leq t_m$  the perturbation amplitude grows in a parabolic trajectory up to the maximum amplitude  $\xi_m$  in the time  $t_m$  (FIG. 1).

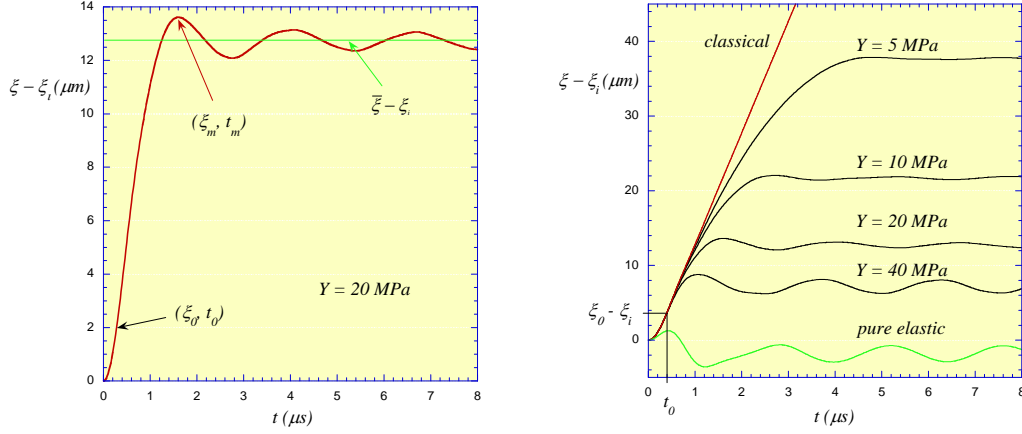


FIG. 1. Time evolution of the perturbation amplitude in RMI in elastic-plastic solids.

### 3. RAYLEIGH-TAYLOR INSTABILITY IN ELASTIC PLASTIC SOLIDS

The linear evolution of the perturbation amplitude  $\eta$  is given by the Newton second law [1,3-6]:

$$\frac{d}{dt}[(m_1 + m_2)\dot{\eta}] = \delta\Pi_{yy}^{(2)} - \delta\Pi_{yy}^{(1)} \quad ; \quad \delta\Pi_{yy}^{(v)} = \delta p + \delta\dot{m}_v v_v + \dot{m}\delta v_y^{(v)} - S_{yy} \quad ,$$

where  $\delta\Pi_{yy}^{(v)}$  is the vertical component of the perturbation of the momentum flux density tensor  $\Pi_{ik}^{(v)} = p^{(v)}\delta_{ik} + \rho_v v_i^{(v)} v_k^{(v)} - \sigma'_{ik}^{(v)}$  in the medium  $v$ .  $S_{ik}$  is the perturbation of the deviatoric part  $\sigma'_{ik}$  of the stress tensor  $\sigma_{ik} = -p\delta_{ik} + \sigma'_{ik}$ ; and  $m_v$  is the mass per unit area of the medium  $v$  involved in the motion due to the instability.

For a solid plate of thickness  $h$  accelerated by a rippled pressure  $p = p_0[1 + (\xi_0/h)e^{ky} \sin kx]$ , we have ( $k$  is the perturbation wave number):  $\dot{m}_v = 0; m_1 = 0; m_2 = \rho/k; \delta p = \rho g(\eta + \eta_0); \eta = \xi(t)e^{ky} \sin kx$ . Then, the evolution of the interface is described by the following equation:  $(\rho/k)\ddot{\eta} = \rho g(\eta + \eta_0) - S_{yy}$ . Using again the Prandtl-Reuss constitutive model for an elastic plastic solid and assuming the perturbed velocity field for an ideal fluid ( $v_y = \dot{\eta} = \dot{\xi}(t)e^{ky} \sin kx; v_x = \dot{\xi}(t)e^{ky} \cos kx$ ) we obtain the following equation of motion for the interface [5,6]:

By solving this differential equation with the initial conditions  $\xi(0) = 0$  and  $\dot{\xi}(0) = 0$  we obtain the complete solutions for the evolution of the interface and, in particular, the conditions for marginal instability and for the transition from the elastic to the plastic regime

(FIG. 2). We find that transition to the plastic regime is a necessary condition for instability ut

not a sufficient one.  $\frac{\rho}{k} \ddot{\xi} = \rho g(\xi + \xi_0) - S_{yy}$ ;  $S_{yy} = \begin{cases} 2kG\xi & \text{for } \xi \leq \xi_p \\ \frac{\alpha Y}{\sqrt{3}} & \text{for } \xi \geq \xi_p \end{cases}$ ;  $\xi_p = \frac{\alpha Y}{2\sqrt{3}kG}$ ;  $\alpha = e^{k|y_p|} \equiv 3$

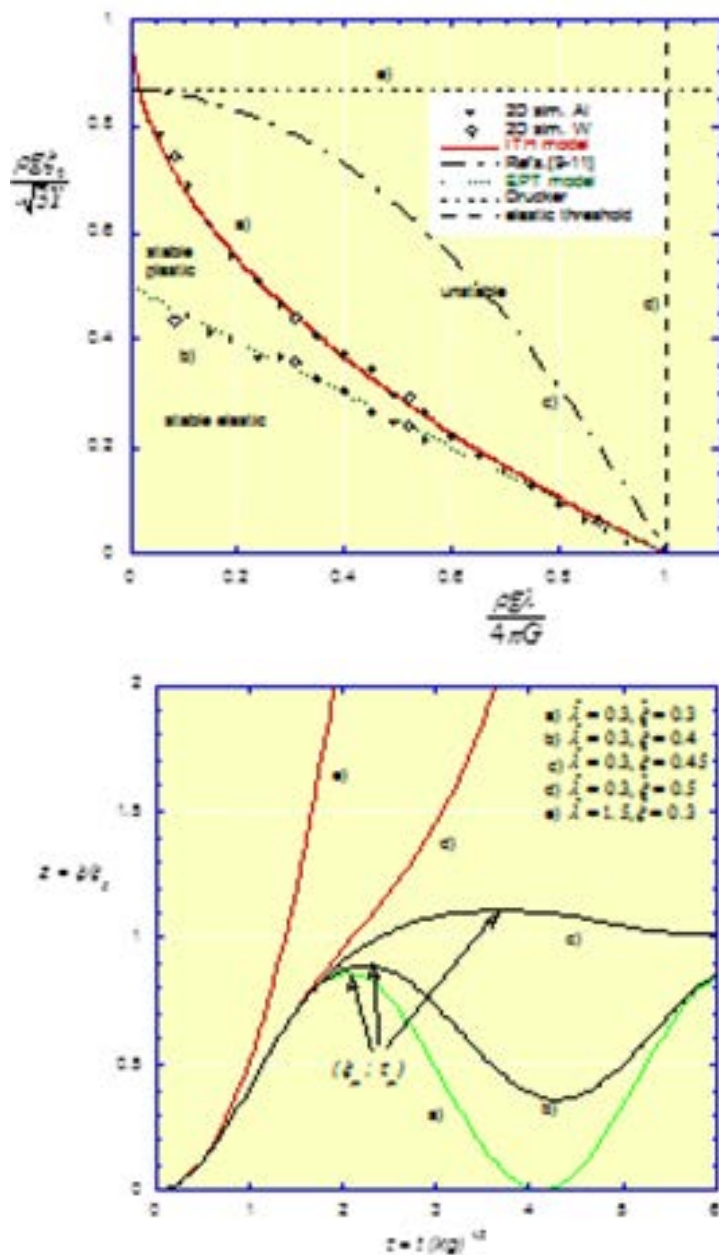


FIG. 2. Stability diagram (left) and time evolution of the interface for the stable and unstable solutions (right).  $\hat{\xi} = \rho g \xi_0 / \sqrt{3}Y$  and  $\hat{\lambda} = \rho g \lambda / 4\pi G$ .

#### 4. RAYLEIGH-TAYLOR INSTABILITY IN ABLATION FRONTS

Researchers at Berkeley have recently reconsidered inertial fusion ablatively driven by ion beams on the basis of the high rocket efficiency that is achieved during one-dimensional shell target implosions. However, RTI during the implosion process is an issue of concern in inertial fusion. In ablative implosions driven by electromagnetic radiation (lasers, blackbody radiation), the ablation process plays an essential role in mitigating the instability effects. In ablation driven by ion beams there are no “critical surface” in the corona and the beam energy

is transported up to the ablation front by means of a non-diffusive process of Coulombian collisions. Therefore, the results known for RTI in ablation driven by radiation cannot be extrapolated to the case of ablation driven by ion beams.

By applying the previously discussed approach for the analysis of RTI to the case of an ablation front we get now the following expressions to be introduced into the equation of motion of the interface:  $\delta p^{(v)} = \rho_v g \xi$ ;  $\delta \dot{m}_1 = -\delta \dot{m}_2 = \delta \dot{m}$ ;  $\delta v_y^{(1)} = -\delta v_y^{(2)} = \dot{\xi}$ ;  $\dot{m} = \rho_v v_v$  and  $m_v = \rho_v / k$  and therefore the equation of motion reads [7]:

$$\frac{\rho_2 + \rho_1}{k} \ddot{\xi} = (\rho_2 - \rho_1) g \xi - 4\dot{m} \dot{\xi} - \delta \dot{m} (v_1 + v_2)$$

Actually, this equation applies to any situation in which we have flow of mass through the interface, including the case with mass diffusion and any case of ablation fronts. That is fronts driven by different mechanisms of energy transport. So, in order to specify that we are dealing with an ablation front we have to introduce the fundamental boundary condition that sets that the ablation front is an isotherm [8]:  $\delta \varepsilon = -\xi d\varepsilon / dy)_{y \approx 0}$ . And for determining  $\delta \dot{m}$  we must specify the particular process of energy transport that drives the ablation. For the case of ablation driven by thermal conduction we get  $\delta \dot{m} / \dot{m} \approx k \xi$  and we retrieve the well known results for RTI in an ablation front driven by thermal conduction [8,9]. For the case of ablation driven by an ion beam we have  $\delta \dot{m} / \dot{m} \ll k \xi$  and the equation of motion becomes:

$$\ddot{\xi} + \frac{4kv_2}{1+r_D} \dot{\xi} - A_T kg \xi = 0.$$

As we can see, the absence of a diffusive mechanism of energy transport prevents the existence of the cut-off wavelength resulting that the front is unstable for any perturbation wavelength.

## REFERENCES

- [1] PIRIZ, A. R., et al., Richtmyer – Meshkov flow in elastic solids, Phys Rev. E. 2006, vol.74, 037301.
- [2] PIRIZ, A. R., et al., Richtmyer – Meshkov instability in elastic-plastic media, Phys. Rev. E. 2008, vol. 78, 056401.
- [3] PIRIZ, A. R., et al., Rayleigh - Taylor instability in elastic solids, Phys. Rev. E. 2005, vol.72, 056313.
- [4] PIRIZ, A. R., et al., Rayleigh - Taylor instability in elastic solids, Am. J. Phys. 2006, vol. 74, 1095.
- [5] PIRIZ, A.R., LÓPEZ J., CELA, J., Tahir N.A., Rayleigh-Taylor instability in elastic-plastic solids, J. Appl. Phys. 2009, vol.105, 116101.
- [6] PIRIZ, A.R., LÓPEZ, J., CELA, J., and N.A. TAHIR: Linear analysis of incompressible Rayleigh-Taylor instability in solids Phys. Rev. E. 2009, vol.80, 046305.
- [7] PIRIZ, S. A., PIRIZ, A.R., and TAHIR, N.A., Rayleigh-Taylor instability in ion beam driven ablation fronts Phys. Plasmas. 2009, vol.16, 082706.
- [8] PIRIZ, A. R., SANZ J., and IBÁÑEZ, L. F., Rayleigh-Taylor instability of steady ablation fronts: The discontinuity model revisited, Phys. Plasmas. 1997, vol. 4, 1117.
- [9] Betti, R., et al., Self-consistent stability analysis of ablation fronts in inertial confinement fusion, Phys. Plasmas. 1996, vol 3, 2122.

# OPTIMIZATION OF SOME SCENARIOS OF IGNITIONS OF MICRO-EXPLOSIONS IN INERTIAL FUSION ENERGY (IFE) POWER PLANTS

M.L. SHMATOV  
IOFFE Physical Technical Institute  
St. Petersburg, Russian Federation

## Abstract

Several problems related to the efficiency of fast ignition of the D-T microexplosions in IFE power plants, the use of the D-D fusion reactions for power production, and the usefulness of IFE studies for development of space propulsion systems, biology and medicine are considered.

## 1. INTRODUCTION

The expedience of the creation of the large number of the IFE power plants will depend crucially on the cost of electricity produced by them (see, e. g., Refs. [1,2]). In turn, the cost of electricity will depend strongly on the scenario of ignition of microexplosions (see, e. g., Ref. [2]). The main results of the studies on optimization of some scenarios of ignition of microexplosions in IFE power plant from the viewpoint of target and chamber physics under the IAEA Research Contract No. RUS 13722 are presented below.

## 2. SOME PROBLEMS RELATED TO FAST IGNITION BY THE LASER-ACCELERATED IONS

### 2.1. Possibility and expedience of the use of ions of elements with the atomic numbers $Z \geq 6$ for heating compressed D-T fuel

Fast ignition by the laser-accelerated ions is widely discussed in the literature (see, e. g., Refs. [3-20]). The main attention is given to the scenarios with the use of the equimolar D-T fuel [3-20]. To provide the possibility and the high efficiency of fast ignition, the flux and, therefore, the source of the ions should obey several requirements. First of all, the intensity  $I_{bomb}$  of bombardment of the hot spot should be sufficiently high [3-22]. For the equimolar D-T fuel, an increase in the typical range  $R_{ion}$  of the ion above  $1.2 \text{ g/cm}^2$  increases the necessary values of  $I_{bomb}$  [21,22]. However, when heating the compressed D-T fuel by the laser-accelerated protons and, may be, some other ions of elements with the relatively low atomic numbers  $Z$ , the choice of  $R_{typ} > 1.2 \text{ g/cm}^2$  can be expedient [20]. The reason is that an increase in  $R_{ion}$  will be accompanied by an increase in the efficiency  $\eta_{ac}$  of acceleration of the ions and other useful effects (see Ref. [20] and Subsection 2.2). In some situations  $I_{bomb}$  will be sufficiently high only if the bombarding ions are focused [3,7-11,20]. The necessity of focusing results in the necessity to place the ion source sufficiently far from the hot spot surface and, therefore, can make the difficulties, related to a decrease in  $I_{bomb}$  due to spread of the ion velocities and the divergence of the ion flux, more important compared with the situations when the ion source is placed relatively close to the hot spot surface (Refs. [3, 7]).

It is desirable to realize the scenarios with the relatively low energy  $E_{las}$  of the laser pulse(s) accelerating the ion, because such scenarios correspond to the relatively low cost of the installation igniting the microexplosions (see also Ref. [2]).

At  $R_{typ} \approx 1.2 \text{ g/cm}^2$ , that probably correspond to the minimum sufficient values of  $E_{las}$  in the scenarios with more or less uniform heating the hot spot, the necessity of focusing disappears when  $Z$  is sufficiently high (here it is assumed that the compressed fuel density  $\rho$  is of the order of  $100 \text{ g/cm}^3$  or higher) [7,11,20]. The reason is that the main dependence of  $R_{typ}$  on  $Z$  is being described by the factors that equals  $Z^{-2}$  or is about this value (see Refs. [4,5,7,14,20] and Subsection 2.2). The absence of the necessity to focus the ions will simplify space modulation of heating the hot spot [11]. Such a modulation can provide a substantial decrease in the minimum sufficient values of sum  $E_{hs}$  of the kinetic energies of the ions hitting the hot spot and  $E_{las}$  [15,22-24]. An increase in  $Z$ , at least up to about 6, will also reduce the minimum sufficient value of  $E_{las}$  in the scenarios with more or less uniform heating the hot spot (see Refs. [5,7,11,20 and Subsection 2.2]).

It was assumed that the maximum acceptable value of  $Z$  would be limited by the necessity to provide the sufficiently low radiative losses of energy due to bremsstrahlung and a small spread of the ionization stages of the bombarding ions [4]. It should also be noted that the realization of the relatively high  $\eta_{ac}$  at  $Z \geq 6$  will be possible only if the intensity  $I$  of irradiation of the ion source is relatively high (see also Refs. [5,7,12,13,17,18,20] and Subsection 2.2).

It has been shown that at least at  $Z \leq 30$ , the radiative losses of energy from both the hot spot and the ion source and the ionization losses in the ion source are acceptable [7,14]. The acceptability of the radiative losses of energy from the hot spot at  $Z \leq 30$  follows from the fact that these losses, corresponding to one ion and the optimum time  $t_{opt}$  of bombardment of the hot spot, are much less than the ion kinetic energy  $\varepsilon$ , corresponding to the time when the ion hits the fuel and the ion range  $R \approx 1.2 \text{ g/cm}^2$  [7,14].

The range of the ion in the uniform equimolar D-T fuel can be estimated as

$$R[\text{g/cm}^2] \approx 5.15 \times 10^{-2} \frac{A(T_e[\text{keV}])^2}{Z_s^2} \int_{u_0}^{u_1} \frac{udu}{\Lambda G}, \quad (1)$$

where  $A$  is the atomic mass of the ion,  $T_e$  is the electron temperature,  $Z_s$  is the stage of ionization of the ion at the stage of its stopping in the fuel,  $u_0 = 3m_e / m_i \approx 1.65 \times 10^{-3} / A$ ,  $m_e$  is the mass of the electron,  $m_i$  is the mass of the ion,  $u_1 = m_e \varepsilon / (m_i T_e) \approx 0.549 \times \varepsilon [\text{MeV}] / (A T_e [\text{keV}])$ ,

$$\Lambda \approx 6.08 - \ln \{ Z_s \sqrt{\rho [\text{g/cm}^3]} [1 + 5.49 \times 10^{-4} \times Z_s / (A u)] (T_e [\text{keV}])^{-3/2} (1 + u)^{-1} \},$$

$$G \approx \int_0^u dt \sqrt{t} \exp(-t) - 5.49 \times 10^{-4} \sqrt{u} \exp(-u) / A$$

Eq. (1) and other afore mentioned formulae are taken from [14]. Eq. (1) is an analog of an equation from Ref. [5], the difference is that Eq. (1) takes into account the possibility of the incomplete ionization of the ion at the stage of its stopping in the fuel. Note that in many situations this difference will not be important due to quick stripping of partly ionized ion in the fuel (see Ref. [14]).

Note also that for some of the thermonuclear targets being discussed in the literature,  $\varepsilon$  can be significantly less than the initial kinetic energy of the ion due to deceleration of the ion in the plasma that has a relatively low density and surrounds the main blob of the compressed fuel [13,18]. This plasma will arise from the fuel and, in some situations, from the material of ablator and other construction elements. Below we will consider the situations when such deceleration is insignificant, that can be provided, in particular, when the ion source is placed in the cone (see also Refs. [4,6,7,10]), and  $R_{typ} \approx R(\varepsilon = \varepsilon_{typ})$ , where  $\varepsilon_{typ}$  is the typical initial kinetic energy of the laser-accelerated ion. Eq. (1) yields that  $R$  increases with  $T_e$  (see also Refs. [4,5] and Subsection 2.2).

For the D-T fuel cooling due to the inverse Compton effect (see, e. g., Ref. [25]) is not important. Therefore, the upper boundary of the bremsstrahlung radiation losses, related to “doping” the hot spot by the bombarding ions, can be found using the approximation of the optically thin plasma [7,14].

Let us consider the product of the bremsstrahlung radiation intensity  $I_{br}^{\max}$  that corresponds to one totally ionized immovable ion, immersed into the fuel with  $T_e = 12$  keV, on  $t_{opt}$ . The hot spot should be heated to  $T_e \approx 12$  keV [21,22], while the bremsstrahlung radiation intensity increases with  $T_e$  [26]. Thus, the product  $I_{br}^{\max} t_{opt}$  can be used as the upper boundary of the bremsstrahlung radiation losses corresponding to one ion and the time  $t_{opt}$  [7,14]. Using  $t_{opt}(\rho = 300 \text{ g/cm}^3) \approx 21$  ps [21,22] and describing  $I_{br}^{\max}$  in the Born approximation (see Refs. [7,27]), we obtain [14]

$$(I_{br}^{\max} t_{opt})(\rho = 300 \text{ g/cm}^3)[\text{MeV}] \approx 1.76 \times 10^{-2} Z^2. \quad (2)$$

In many situations the acceptability of the radiative losses due to the bound-bound transitions in the bombarding ions immersed into the fuel can be demonstrated using the model taking into account only the 2p-1s transitions in the hydrogen-like ions [14]. The reason is that even these transitions turn out to be rather slow and, as a result, the emission power corresponding to them turns out to be relatively low. At least at  $Z \leq 30$ , “the reserve of smallness” of this power shows that both the changes of the bound state energies and transition rates due to the influence of the free electrons and binding of two or more electrons with one nucleus cannot result in a “catastrophic” increase in the radiative losses.

In a cavity filled with thermal radiation with the temperature  $T_R$ , a hydrogen-like ion in the 2p state is a radiation source with the power

$$P_Z = P_Z^{sp} \{1 + 1/[\exp(\Delta E/T_R) - 1]\}, \quad (3)$$

where  $P_Z^{sp} \approx Z^6 \times 1.01 \times 10^{-9}$  W is the power of the spontaneous radiation and  $\Delta E \approx Z^2 \times 10.2$  eV [14] (see also Ref. [28]).

Eqs. (1,2) yield, for example, that for the  $^{39}\text{K}^{+19}$  ion and  $\rho = 300 \text{ g/cm}^3$ ,  $\varepsilon(T_e = 12 \text{ keV}, R = 1.2 \text{ g/cm}^2) \approx 1.8$  GeV,  $I_{br}^{\max} t_{opt} \approx 6.4$  MeV [14]. Eq. (3) yields that for the  $\text{K}^{+18}$  in the 2p state  $P_Z(T_R = 12 \text{ keV}) t_{opt}(\rho = 300 \text{ g/cm}^3) \approx 24$  MeV [14]. Thus, in the situation under consideration the radiative losses from the fuel are acceptable. In Ref. [14],

other examples are presented and the problems related to the accuracy of Eq. (1) are considered.

The acceptability of the radiative losses from the ion source is demonstrated in Refs. [7,14]. The ionization losses in the ion source are also acceptable (see Ref. [14]).

## 2.2. Expedience of the choice of $R_{typ} > 1.2 \text{ g/cm}^2$

The expedience of the choice of  $R_{typ} > 1.2 \text{ g/cm}^2$  was analyzed using Eq. (1), ion acceleration model based on equations from. Ref. [5], and the requirements on  $I_{bomb}$  from Ref. [22].

Let us denote the intensity of the flux of the laser-accelerated ions near their source as  $I_{i0}$ . In order to estimate the dependencies of  $I_{i0}$  and  $\varepsilon_{typ}$  on  $I$ , let us use the equations

$$I_{i0}[\text{W/cm}^2] \approx 1.7 \times 10^{16} \sqrt{Z_a \lambda [\mu\text{m}] / A} \times [I / (10^{18} \text{ W/cm}^2)]^{5/4} \quad (4)$$

and

$$\varepsilon_{typ}[\text{MeV}] \approx 0.5 Z_a \lambda [\mu\text{m}] \sqrt{I / (10^{18} \text{ W/cm}^2)}, \quad (5)$$

where  $Z_a$  is the stage of ionization of the ion at the stage of its acceleration,  $\lambda$  is the wavelength of the accelerating radiation. These equations are the analogs of the equations from Ref. [5], the difference is that Eqs. (4,5) take into account the possibility of the incomplete ionization of the ion at the stage of its acceleration [20].

The instantaneous value of  $\eta_{ac}$  equals  $I_{i0} / I$  [5].

Let us consider the situation when the hot spot is being heated by the ions with the sufficiently small spread of  $\varepsilon$  and, as a result, at any time the ranges of all of the ions can be considered equal approximately to  $R_{typ}$  corresponding to the current  $T_e$ , any value of  $R_{typ}$  is not less than  $0.3 \text{ g/cm}^2$ , the hot spot has a shape of a cylinder and is transversally uniform.

$I_{bomb}$  should obey the condition

$$I_{bomb} \geq I_{bomb}^{\min} f_R(R_{typ}), \quad (6)$$

where  $I_{bomb}^{\min}$  is the parameter that depends on  $\rho$  and the hot spot radius  $r_{hs}$ ,  $f_R(0.3 \text{ g/cm}^2 \leq R_{typ} \leq 1.2 \text{ g/cm}^2) = 1$ ,  $f_R(R_{typ} \geq 1.2 \text{ g/cm}^2) = (R_{typ}[\text{g/cm}^2]) / 1.2$  [22]. If during the whole time of hot spot heating  $R_{typ}$  either remains in the range from  $0.3$  to  $1.2 \text{ g/cm}^2$ , or is a constant exceeding  $1.2 \text{ g/cm}^2$ ,  $E_{hs}$  should obey the conditions

$$E_{hs}(\min R_{typ} \geq 0.3 \text{ g/cm}^2, \max R_{typ} \leq 1.2 \text{ g/cm}^2) \geq E_{hs}^{\min}, \quad (7)$$

$$E_{hs}(R_{typ} = \text{const} > 1.2 \text{ g/cm}^2) \geq E_{hs}^{\min} f_R(R_{typ}), \quad (8)$$

where  $E_{hs}^{\min}$  is the parameter that depends on  $\rho$  and  $r_{hs}$  (see Ref. [22]).

The formulae (6-8) yield that the lowest necessary values of  $E_{las}$  correspond to the highest values of the parameter  $\eta = \eta_{ac} / f_R(R_{typ})$  (see also Ref. [20]).

In some cases the technical difficulties, related to the necessity to provide hit of the sufficiently large number  $N_{ion}$  of ions in the hot spot, can arise (see, e. g., Ref. [18]). The smallest values of  $N_{ion}$  correspond to the largest values of the parameter  $\varepsilon_{eff} = \varepsilon_{typ} / f_R(R_{typ})$  (see also Ref. [20]).

At  $\varepsilon \ll (m_i / m_e)T_e$ , Eq. (1) takes the form

$$R[\text{g/cm}^2] \approx 0.114 \frac{\sqrt{A}}{Z_s^2} \frac{1}{\Lambda'} (T_e[\text{keV}])^{3/2} \sqrt{\varepsilon[\text{MeV}]}, \quad (9)$$

where  $\Lambda' \approx 6.08 - \ln\{Z_s \sqrt{\rho[\text{g/cm}^3]} / (T_e[\text{keV}])^{3/2}\}$  (see also Refs. [5,7]).

Formulae (1,4,5,9) yield that an increase in  $R_{typ}$  in the range from 0.3 to 1.2 g/cm<sup>2</sup> corresponds to the increases in  $\eta$ ,  $I_{i0}$  and  $\varepsilon_{eff}$  (in such situations  $\eta = \eta_{ac}$ ,  $\varepsilon_{eff} = \varepsilon_{typ}$ ; see also Refs. [3,5]). The high values of  $I_{i0}$  at  $R_{typ} \leq 1.2$  g/cm<sup>2</sup> and, in a general case, the high values of  $I_{i0} / f_R(R_{typ}) = \eta I$  are desirable due to several reasons. For example, formula (6) yields that they either simplify focusing of the ions on the hot spot, either make this focusing unnecessary at all. The realization of the scenarios with  $R_{typ} < 1.2$  g/cm<sup>2</sup> will be justified mainly in the situations when the ions of elements with relatively high atomic numbers  $Z$  are used and the larger  $R_{typ}$  are unattainable due to the limited  $I$  (see Eqs. (1,5,9) and Refs. [5,7]).

According to (4,5,9),

$$\eta(R_{typ} \geq 1.2 \text{ g/cm}^2, \varepsilon_{typ} \ll (m_i / m_e)T_e) \approx 0.25 \frac{Z_s^2 \Lambda'}{A(T_e[\text{keV}])^{3/2}}, \quad (10)$$

$$\varepsilon_{eff}(R_{typ} \geq 1.2 \text{ g/cm}^2, \varepsilon_{typ} \ll (m_i / m_e)T_e)[\text{MeV}] \approx 92 \frac{Z_s^4 \Lambda'^2}{A(T_e[\text{keV}])^3} R_{typ}[\text{g/cm}^2]. \quad (11)$$

Formulae (4,5,10,11) yield that an increase in  $I$  in the range, corresponding to  $R_{typ} \geq 1.2$  g/cm<sup>2</sup>, does not increase the lower boundary of  $E_{las}$  and is accompanied by the useful effects, i. e., by the increases in  $I_{i0} / f_R(R_{typ})$  and  $\varepsilon_{eff}$ .

Eq. (1), describing the dependence of  $R_{typ}$  on  $\varepsilon_{typ}$  with the higher accuracy, yields that an increase in  $R_{typ}$  above 1.2 g/cm<sup>2</sup> is accompanied by a decrease in  $\eta$ . The examples, corresponding to heating the equimolar D-T fuel with  $\rho = 300$  g/cm<sup>3</sup> by protons and carbon-12 ions with  $Z_a = Z_s = 6$  at  $\lambda = 1 \mu\text{m}$ ,  $T_e = 5$  и 10 keV, are presented in Tables 1 and 2. At the chosen  $\rho$  and the optimum  $r_{hs}$ ,  $I_{bomb}^{\min} \approx 6.82 \times 10^{19}$  W/cm<sup>2</sup> [21,22]. This corresponds to the necessity to focus protons at, for example,  $T_e = 10$  keV,  $R_{typ} < 2.81$  g/cm<sup>2</sup> and any distance between their source and the hot spot. This also corresponds to the absence of the necessity to focus carbon ions at the sufficiently short distance between their source and the hot spot and  $R_{typ} \approx 1.2$  g/cm<sup>2</sup> (see Eqs. (1,4,5), Tables 1 and 2, and Ref. [7]).

The data from Table 1 show that the choice of  $R_{typ} > 1.2$  g/cm<sup>2</sup> is justified, first of all, for the late stages of heating the hot spot by protons. For example, at  $T_e = 10$  keV an increase

in  $R_{typ}$  from 1.2 to 2.5 g/cm<sup>2</sup> is accompanied by about a ten-fold-increase in  $\eta I$ , that simplifies focusing of protons significantly, and a relative decrease in the instantaneous value of  $\eta$  only on 11.5 %, while an increase in  $R_{typ}$  above 2.81 g/cm<sup>2</sup> will result in the disappearance of the necessity to focus protons at the optimum  $r_{hs}$ .

TABLE 1. SOME PARAMETERS DESCRIBING HEATING THE HOT SPOT IN THE EQUIMOLAR D-T FUEL WITH  $\rho = 300$  G/CM<sup>3</sup> BY PROTONS AT  $\lambda = 1 \mu\text{m}$

$T_e$ , keV	$R_{typ}$ , g/cm <sup>2</sup>	$\varepsilon_{typ}$ , MeV	$\varepsilon_{eff}$ , MeV	$I$ , W/cm <sup>2</sup>	$\eta_{ac}$ , %	$\eta$ , %	$\eta I$ , W/cm <sup>2</sup>
5	1.2	16.0	16.0	$1.02 \times 10^{21}$	9.61	9.61	$9.82 \times 10^{19}$
	1.5	20.7	16.5	$1.71 \times 10^{21}$	10.9	8.74	$1.49 \times 10^{20}$
	2	27.6	16.6	$3.05 \times 10^{21}$	12.6	7.58	$2.31 \times 10^{20}$
	2.5	33.7	16.2	$4.55 \times 10^{21}$	14.0	6.70	$3.05 \times 10^{20}$
10	1.2	4.81	4.81	$9.25 \times 10^{19}$	5.27	5.27	$4.88 \times 10^{18}$
	1.5	7.12	5.70	$2.03 \times 10^{20}$	6.42	5.13	$1.04 \times 10^{19}$
	2	11.5	6.92	$5.33 \times 10^{20}$	8.17	4.90	$2.61 \times 10^{19}$
	2.5	16.4	7.85	$1.07 \times 10^{21}$	9.72	4.67	$4.99 \times 10^{19}$
	2.81	19.4	8.29	$1.51 \times 10^{21}$	10.6	4.52	$6.82 \times 10^{19}$

TABLE 2. SOME PARAMETERS DESCRIBING HEATING THE HOT SPOT IN THE EQUIMOLAR D-T FUEL WITH  $\rho = 300$  G/CM<sup>3</sup> BY CARBON-12 IONS AT  $Z_a = Z_s = 6$ ,  $\lambda = 1 \mu\text{m}$

$T_e$ , keV	$R_{typ}$ , g/cm <sup>2</sup>	$\varepsilon_{typ}$ , MeV	$\varepsilon_{eff}$ , MeV	$I$ , W/cm <sup>2</sup>	$\eta_{ac}$ , %	$\eta$ , %	$\eta I$ , W/cm <sup>2</sup>
5	1.2	419	419	$1.95 \times 10^{22}$	14.2	14.2	$2.77 \times 10^{21}$
	1.5	504	403	$2.82 \times 10^{22}$	15.6	12.5	$3.52 \times 10^{21}$
	2	626	375	$4.35 \times 10^{22}$	17.4	10.4	$4.53 \times 10^{21}$
	2.5	731	351	$5.94 \times 10^{22}$	18.8	9.01	$5.35 \times 10^{21}$
10	1.2	213	213	$5.05 \times 10^{21}$	10.1	10.1	$5.12 \times 10^{20}$
	1.5	294	235	$9.63 \times 10^{21}$	11.9	9.53	$9.17 \times 10^{20}$
	2	425	255	$2.00 \times 10^{22}$	14.3	8.59	$1.72 \times 10^{21}$
	2.5	546	262	$3.31 \times 10^{22}$	16.2	7.78	$2.57 \times 10^{21}$

The problem of expedience of the choice of  $R_{typ} > 1.2$  g/cm<sup>2</sup> in the scenarios with heating the hot spot by ions of carbon, those of other elements with  $Z > 1$  (see Refs. [4-7,12-14,17,18]), and deuterons and tritons, accelerated in the fuel (see Refs. [16,19]), requires the additional studies.

Attaining the high values of  $\eta I$  and  $\varepsilon_{eff}$  by means of the choice of  $R_{typ} > 1.2$  g/cm<sup>2</sup> can also be useful for the scenarios with a reduction of  $E_{hs}$  and  $E_{las}$  by means of shaping the hot spot (see Refs. [15,22-24]).

In some situations, the simultaneous increases in  $\eta_{ac}$  and  $\varepsilon_{typ}$  also occur when the duration of the accelerating pulse increases [9]. This can turn out the additional reason of expedience of the choice of the relatively large  $R_{typ}$ .

### 2.3. Scattering of ions in the material of the protective membrane of fast ignition, indirect compression target without cone

The targets, proposed for fast ignition by the laser-accelerated ions, usually contain the protective membranes or/and cones, preventing damage of the ion source by plasma particles

and radiation at the stage of compression of the fuel [3,4,6-10,17,18]. Passage of the ions through the protective membrane or cone will cause their scattering [3,10]. The ions will also scatter in the evaporated material of these construction elements. The authors of Ref. [10] have presented an example when scattering of protons in the 10-  $\mu\text{m}$ -thick gold layer, placed at the distance  $d = 100 \mu\text{m}$  from the compressed fuel, does not cause the significant deterioration of the geometry of the hot spot. Below it is shown that at the indirect compression of the fuel the strong negative manifestation of scattering of the ions in the non-evaporated and evaporated material of the protective membrane of the target without cone is possible. For example, this effect results in the inexpedience of the power production with the use of targets without cones with  $d \geq 1 \text{ cm}$  and heating the hot spot by the ions of carbon and lighter elements.

Scattering of ions in the material of the protective membrane of indirect compression target can be analyzed using the Molière theory (see, e. g., Refs. [10,29,30]). According to this theory, after passage of the completely ionized ions of element with the atomic number  $Z$  through the uniform foil consisting of atoms of one element with the atomic number  $Z_f$  and the atomic mass  $A_f$  the angular distribution of the ions is determined by the parameter

$$\gamma_1[\text{rad}] = \left[ \frac{0.157 Z_f (Z_f + 1) Z^2 \times t_f [\text{g/cm}^2]}{A_f \times (pv) [\text{MeV}]} \right]^{1/2}, \quad (12)$$

where  $t_f$  is the surface density of the foil or, in other words, its thickness measured in  $\text{g/cm}^2$ ,  $p$  and  $v$  are the ion momentum and the ion velocity corresponding to its average kinetic energy in the foil, and the parameter  $B$  that is the root of the equation  $B - \ln B = b$ , where

$$b = \ln \left[ \frac{6680 \times t_f [\text{g/cm}^2]}{\beta^2} \times \frac{(Z_f + 1) Z_f^{1/3} Z^2}{A_f (1 + 3.34 \alpha^2)} \right], \quad (13)$$

$\beta$  is the ratio of  $v$  to the velocity of light,  $\alpha = ZZ_f e^2 / (\hbar v)$ ,  $e$  is the absolute value of the electron charge and  $\hbar$  is the Planck constant [29,30]. According to Ref. [30], the Molière theory is applicable at  $B \geq 4.5$  (see also Refs. [10,29]).

We will use the value  $\gamma_0 = \gamma_1 \sqrt{B}$  as the typical angle of scattering of the ions. About 62 to 63 % of the scattered ions will have the angle between the vector of the velocity and the initial direction of motion in the range from zero to  $\gamma_0$ , while about 73 to 75 % of the scattered ions will have this angle in the range from zero to  $1.2\gamma_0$  [30].

When analyzing scattering of the ions in the two-layer obstacle consisting of the non-evaporated and evaporated membrane material, we will assume that a partial ionization of the evaporated material does not affect scattering significantly and will use Eqs. (12,13) with the substitution  $t_f = k_{ex} \rho_m l_m$ , where  $k_{ex}$  is a coefficient taking into account a possible decrease in the surface density of the evaporated material due to its transversal expansion,  $\rho_m$  is the density of the membrane and  $l_m$  is its thickness. Probably,  $k_{ex}$  is not less than 0.5 to 0.7.

The requirements on the composition and thickness of the protective membrane of the indirect compression target without cone are close to those on these parameters of the layer confining radiation in hohlraum of this target. Therefore, the membrane should be made of the material(s) with the high atomic number(s), if the membrane has the usual solid-state density,  $l_m$  should be of the order of 10  $\mu\text{m}$  (see Refs. [3,8,9]).

The examples of  $\gamma_0$  for scattering of protons and  $^{12}\text{C}^{+6}$  ions in the gold membranes with  $\rho_m = 19.32 \text{ g/cm}^3$  (see, e. g., Ref. [31]) are presented in Tables 3 and 4, respectively.

TABLE 3. SOME VALUES OF  $\gamma_0$  [RAD] FOR SCATTERING OF PROTONS

$\varepsilon$ , MeV $\rightarrow$ $k_{ex}l_m$ , $\mu\text{m}$ $\downarrow$	3	10	15	20	30
10	$1.41 \times 10^{-1}$	$4.23 \times 10^{-2}$	$2.83 \times 10^{-2}$	$2.12 \times 10^{-2}$	$1.42 \times 10^{-2}$
20	$2.09 \times 10^{-1}$	$6.30 \times 10^{-2}$	$4.21 \times 10^{-2}$	$3.16 \times 10^{-2}$	$2.12 \times 10^{-2}$
30	$2.64 \times 10^{-1}$	$7.94 \times 10^{-2}$	$5.30 \times 10^{-2}$	$3.98 \times 10^{-2}$	$2.67 \times 10^{-2}$
40	$3.10 \times 10^{-1}$	$9.34 \times 10^{-2}$	$6.24 \times 10^{-2}$	$4.69 \times 10^{-2}$	$3.14 \times 10^{-2}$

TABLE 4. SOME VALUES OF  $\gamma_0$  [RAD] FOR SCATTERING OF  $^{12}\text{C}^{+6}$  IONS

$\varepsilon$ , MeV $\rightarrow$ $k_{ex}l_m$ , $\mu\text{m}$ $\downarrow$	100	200	400	500	825
10	$2.54 \times 10^{-2}$	$1.28 \times 10^{-2}$	$6.43 \times 10^{-3}$	$5.17 \times 10^{-3}$	$3.17 \times 10^{-3}$
20	$3.78 \times 10^{-2}$	$1.90 \times 10^{-2}$	$9.58 \times 10^{-3}$	$7.70 \times 10^{-3}$	$4.73 \times 10^{-3}$
30	$4.76 \times 10^{-2}$	$2.39 \times 10^{-2}$	$1.21 \times 10^{-2}$	$9.69 \times 10^{-3}$	$5.95 \times 10^{-3}$
40	$5.60 \times 10^{-2}$	$2.81 \times 10^{-2}$	$1.42 \times 10^{-2}$	$1.14 \times 10^{-2}$	$7.00 \times 10^{-3}$

At  $\gamma_0 \ll 1$ , the typical displacement of the point of hit of the ion on hot spot due to scattering is about  $\gamma_0 d$  [10].

For the transversally uniform hot spot an increase in  $r_{hs}$  above its optimum value  $r_{opt} \approx (60 \mu\text{m}) \times [\rho / (100 \text{ g/cm}^3)]^{0.97}$  results in an increase in  $E_{hs}$  [22]. Note that  $r_{opt}(\rho \geq 300 \text{ g/cm}^3) \leq 21 \mu\text{m}$ .

In some of the proposed scenarios  $d \geq 1 \text{ cm}$  [12,13,17,18]. At least at  $\rho \geq 300 \text{ g/cm}^3$ , such  $d$  correspond to  $\Delta > r_{opt}$  and, as a result, to the large values of  $r_{hs}/r_{opt}$  and  $E_{hs}$  (see Ref. [22]). For the IFE power plants this will be unacceptable.

For the shaped hot spot the acceptable value of  $\Delta$  will be of the order of 1  $\mu\text{m}$  (see also Ref. [15]). The data presented in Table 3 show that for the indirect compression targets without cones with heating the hot spot by protons the realization of such values of  $\Delta$  will be impossible even at  $d \approx 1 \text{ mm}$ .

## 2. SOME ADVANTAGES OF FAST IGNITION TARGETS WITH TWO CONES

In recent years, several designs of fast ignition thermonuclear targets with two cones were proposed [14, 24, 32-35]. Such targets have several advantages related to the ignition physics [14, 24, 32, 33, 35]. For some of the IFE power plants and other facilities, the presence of two cones in one target will also provide or simplify solution of the technical problems that are not related directly to ignition and can be considered as those of IFE reactor chamber physics or/and target production [33-35]. The expedience of the use of the targets with two cones in IFE power plants will depends on several factors. First of all, the following problems are important.

Some of the proposed fast ignition scenarios involve attempts to create two hot spots in one blob of the compressed fuel [32, 35-37] (see also Refs. [4, 12, 13, 17, 18]). Below the scenarios of such a kind will be called “scenarios with two hot spots”, while those with the attempts to create one hot spot in one blob of the compressed fuel will be called “scenarios with one hot spot”. Realization of the scenarios with two hot spots is one of the applications of the targets with two cones [32, 35]. When heating the compressed fuel with the special driver, the scenarios with two hot spots duplicate the requirements on the total power of this driver compared with those with one hot spot and the same compression of the fuel.

Some more or less similar fast ignition scenarios, for example, those with heating the hot spot by the laser-accelerated ions, can probably be realized using the targets with two cones, or one cone, or without cone at all. Note that the targets without cones can be used in several scenarios with two hot spots (see Refs. [12, 13, 16-19, 37]). In some situations the cost of a target with two cones will be higher than that of a similar target with one cone or without cone. Thus, the targets with two cones will be used for power production only if their advantages are sufficiently important. For example, they should either compensate for an increase in the cost of the targets and/or equipment necessary for ignition and/or some other purposes, or provide realization of the attractive scenario(s) that cannot be realized with other targets.

In some situations the scenarios with two hot spots will provide the higher fuel burning efficiency, averaged over all of the attempts to ignite the microexplosions, than similar scenarios with one hot spot and the same compression of the fuel [35, 37]. This is due to two effects. Firstly, creation of the second hot spot in the blob of the compressed fuel can enhance the maximum fuel burning efficiency [37]. Secondly, for the scenario with two hot spots, the probability  $p_f$  of failure of ignition (or, in terms being used in Ref. [2], “a dud rate”) can be less than that for a similar scenario with one hot spot. Note that according to Ref. [2], for the targets with cones  $p_f$  can be as high as 40 % (in Ref. [2] the targets with two cones are not mentioned, thus, this value seems to be related to the targets with one cone). The scenarios with two hot spots will be attractive for IFE power plant if the cost of the drivers, necessary for them, is acceptable [35]. This may correspond, first of all, to the methods of hot spot heating with the use of the relatively long duration, low intensity laser pulses (see Refs. [7, 32, 38, 39]) or without the use of the special laser or particle beam(s) at all (see Refs. [32, 36, 40]).

However, it should be emphasized that the reliable conclusion about the feasibility and efficiency of any of these methods will be possible only after the additional studies. For example, creation of the circular cumulative jet by the striker moving in the cone

(see e.g. Refs. [41, 42]) may prevent or at least complicate significantly the realization of the method called “impact fast ignition” (see Refs [35, 38]).

In some situations, the realization of the scenarios with one hot spot and two different cones will be expedient. First of all, the additional truncated cone with the open tip can provide leakage of gas or/and plasma from the central region of the fuel capsule during the implosion and, thereby, improve compression of the fuel [24].

The presence of the cones in the targets may result in the necessity to use the liquid fuel [43]. For example, there is an assumption that “the insertion of a reentrant cone into a spherical shell introduces new, perhaps insurmountable problems for beta layering of solid D-T as well for target fabrication” [43]. Note that some problems related to production of the targets with cones and solid D-T fuel are considered in Ref. [44].

The liquid fuel can be confined between the solid ablator and thin solid inner shell (see Refs. [35, 43]) or in the low-density foam (see Refs. [43,45]). For some of the targets, the use of both the foam and the solid inner shell may be expedient [35]. One of the reasons is that the inner shell will reduce the density of the gas and/or plasma arising in the central region of the fuel capsule during its implosion and, thereby, will improve compression of the fuel [33, 35]. The presence of two cones in one target will be a factor facilitating fixing the inner shell [33, 35].

Heating the liquid fuel of the fast ignition, direct compression target during its flight in the reactor chamber may be unimportant at all. The situations when at the high temperature in the reaction chamber protection of the capsule with the liquid fuel by the cones or by the cones and the reflective coating (see, e. g., Ref. [46]) is sufficient seem also to be possible. The possibility of the relatively quick filling the target by the liquid fuel is also important. The use of the liquid fuel may enable acceleration of the relatively simple targets on the short paths.

If the use of the D-T ice in the IFE targets is possible and even desirable, the presence of two cones in one direct compression target will simplify providing survival of the target in the reactor chamber [34]. For example, the cones and the construction elements connecting them can serve as a frame supporting the protective membrane isolating the fuel capsule from the reactor chamber environment [34].

### 3. THE USE OF THE IGNITION SCENARIOS WITH TWO HOT SPOTS AND ONE HOT SPOT IN ONE IFE POWER PLANT OPERATING IN THE SEISMIC AREA

The possibility to use the scenarios with two hot spots and one hot spot in one IFE power plant will be a factor increasing the stability of the electric power supply [35]. The scenario with two hot spots should serve as the main one. The scenario with one hot spot will be used when realization of the former is impossible, but the total halt of operation of the plant is not necessary. This can be caused by the damage of some parts of the driver heating the hot spots or/and some equipment of the target production facility or by the maintenance works [35].

Note that according to some projects of IFE power plants, each laser being used to irradiate the thermonuclear targets has a redundant partner [47,48]. This redundancy was proposed as a measure to achieve high reliability and ease of maintenance of the plant, the

laser beams irradiating the targets were considered as generated by the different lasers rather than by the different parts of one laser [47,48].

The possibility to use the scenarios with two hot spots and one hot spot in one IFE power plant will be especially useful in the seismic area, for example, in Japan and California [35]. It is worth noting that the expected influence of the earthquakes on the nuclear power plants is being described by the parameters of two earthquakes [49]. One of them corresponds to the possibility to turn off the plant safely, another corresponds to the possibility not to halt operation of the reactor [49].

The targets for the scenario with one hot spot can differ from those for the scenario with two hot spots. However, in some situations the use of the same targets in both scenarios can be expedient or even unavoidable.

If the methods of hot spot heating with the use of the relatively long duration, low intensity laser pulses or without the use of the special laser or particle beam(s) are feasible and acceptable for the IFE power plants, both drivers and target production facilities of such plants will probably be relatively stable to the influence of the earthquakes of low magnitudes. Thus, the hot spot heating methods, that seem to be the best for the use of the scenarios with two hot spots for power production from the viewpoint of the cost of the drivers, seem to be the best from the viewpoint of reliability of the IFE power plants operating in the seismic areas.

Note that the seismicity of the area of location of the IFE power plant will also have the influence on the design of the plant through the choice of the liquid for tritium breeding, transfer of heat from the reactor chamber, and, if necessary, protection of the reactor chamber walls. For example,  $\text{Pb}_{83}\text{Li}_{17}$  has the high density and, as a result, "difficulty meeting seismic design standards" [50]. The comparison of Li and flibe requires the analysis of manifestations of the flammability of Li and the chemical toxicity of flibe at the different levels of damage of the IFE power plants by the earthquakes (see also Ref. [50,51]).

#### 4. OPTIMUM VARIANT OF USING D-D FUSION REACTIONS FOR POWER PRODUCTION

The possibility of using D-D fusion reactions for power production is being discussed for many years (see, e. g., Refs. [33,48,52-58]). The main advantage of the power plants employing these reactions to those where only the D-T fusion reaction is physically important consists in a lower amount of tritium involved in the process [48,52-58]. This is desirable due to the reasons related to safety, ecology and economics [48,52-58].

Ignition of the D-D fusion reactions is a more difficult task compared to the ignition of the D-T fusion reaction [33,48,52-58]. For power plants with the magnetic plasma confinement, the use of the D-D and D-He<sup>3</sup> fusion reactions in the observable future will probably be impossible or at least inexpedient [57].

Ignition of deuterium explosions by the fission explosions is the most technically simple approach to using the D-D fusion reactions for power production [56]. However, this approach seems to be politically unacceptable.

The problem of using microexplosions with physically important reactions of D-D fusion for power production was discussed in several papers (see, e. g., Ref. [33,48,52-55, 58]). Potential fuels for these microexplosions include pure deuterium, D-T mixtures with small average atomic fraction  $\langle x_T \rangle$  of tritium and mixtures of deuterium with small amounts of tritium and He<sup>3</sup> [33, 48, 52-55,58].

The compression of a fuel with small or zero  $\langle x_T \rangle$  using laser or other driver with very high parameters, and, hence, very high cost (see, e. g., Refs. [53-55]) is only one of the possible approaches. The most effective approaches are those in which the compression of such fuel is caused entirely or mostly by thermal radiation of one or several D-T microexplosions (see, e. g., Refs. [25, 33, 52, 58-60]). This results partly from the following. Up to 20 – 25 % of the yield of the D-T microexplosion ignited with the indirect compression of the fuel will correspond to the energy of X ray flux [2, 58, 60-62]. The temperature and the typical time of emission of this flux will obey, at least if appropriate simple measures are taken, to the requirements related to compression of the fuel [48, 58, 60]. For realization of these approaches, the driver with the parameters corresponding to ignition of D-T microexplosions with the yields of about 1 GJ or less will be sufficient [58]. Note that in some situations compression of the fuel can be caused by both radiation from the D-T microexplosion and one or several auxiliary drivers that improve the symmetry and temporal profile of compression [33,58,62]. Some other problems, related to compression of thermonuclear fuel by thermal radiation from the D-T microexplosions, are considered in Ref. [25, 52, 58-60, 62].

## 5. USEFULNESS OF IFE STUDIES FOR DEVELOPMENT OF SPACE PROPULSION SYSTEMS, BIOLOGY AND MEDICINE

The progress of IFE studies will be useful for creation of space ships, accelerated by thermonuclear microexplosions, and some devices that can serve as the tools for the biology and medicine.

Space propulsion and electrical power production are the main possible applications of thermonuclear microexplosions. It is worth noting that E. Teller considered the use of thermonuclear microexplosions for space propulsion to be more feasible than IFE [1], the statement of such a kind about the laser igniting the microexplosions was done by L.P. Feoktistov [59(p. 306)]. However, the political and some other factors may correspond to the first priority of creation of IFE power plants. For example, Ref. [63] (p. 147) contains the following statement: “If somehow the most promising mission for fusion were to be viewed as space propulsion, then the urgency of fusion research could be decreased even further than it is currently”.

In any case, many of the already obtained results of the studies devoted initially to one of the aforementioned applications of thermonuclear microexplosions are useful for optimization of scenarios of another one. This will also take place in the future. Other manifestations of the mutual usefulness of the works on the different applications of thermonuclear microexplosions are also quite possible. For example, production of He<sup>3</sup> for space propulsion systems by the terrestrial IFE power plants may become feasible and expedient [33].

For diagnostics of the high-density, high temperature plasma in the experiments on optimization of the scenarios of ignition of thermonuclear microexplosions, the lasers operating on the wavelength  $\lambda$  of about 40 Å and less will be useful [64]. The reason is that

the high brightness of the laser radiation will provide diagnostic of the plasma even in the situations when the intensity of the spontaneous radiation emitted by this plasma is rather high, while the sufficiently short  $\lambda$  will provide penetration of the radiation into the plasma with the density of the order of  $100 \text{ g/cm}^3$  [64] (for example, the product of the plasma frequency of the equimolar D-T fuel with  $\rho = 300 \text{ g/cm}^3$  on  $\hbar$  equals 316 eV; such photon energy corresponds to  $\lambda \approx 39 \text{ \AA}$ ). The laser radiation with the wavelength of about  $40 \text{ \AA}$  and less will also be useful to study the structure of the living biological cells [64-67].

Till now, the laboratory X ray lasers generating the stimulated radiation with  $\lambda \approx 40 \text{ \AA}$  operate only on the  $4d - 4p$  transitions in Ni-like ions [65-67]. Improving the efficiency and other parameters of such lasers with the mirror, providing the double-pass amplification, is highly desirable, because improving their parameters by means of lengthening the active medium is difficult or even impossible due to the high requirements on the energy of pumping [64-67]. Note that many X ray lasers were pumped by the lasers created for the experiments on inertial confinement fusion [65-67].

The attempts to achieve the double-pass amplification of radiation with  $\lambda \approx 44.83 \text{ \AA}$  on the  $4d - 4p$  transitions in Ni-like ions of Ta were unsuccessful [65-67]. The amplification was possible during the time that was estimated as about 250 or 350 ps [65,67]. The smallness of this time required placement of the mirror at the distance  $b \leq 2 \text{ cm}$  from the end of the active medium [65-67]. The experiments were performed at  $b = 2$  and  $6 \text{ cm}$  [65-67]. In the former situation the damage of the mirror was so quick that the reflection of the single-pass laser pulse did not occur, in the latter one the reflection of this pulse without its significant amplification was observed [65-67].

The experiments were performed both with and without the use of the protective filter placed between the active medium and the mirror [65-67]. In the former situation the mirror was damaged by the scattered pumping radiation [66]. The filter consisted of plastic and aluminum, had a transmission of about 75 – 80 % at  $44.83 \text{ \AA}$  and cut off the scattered pumping radiation almost completely [66,67]. When using the filter, the main damage of the mirror at  $b = 2 \text{ cm}$  was caused by the spontaneous X rays from the active medium [65-67].

It has been shown that the use of the protective filter containing carbon or potassium as the main component will provide the acceptable transmission at  $44.83 \text{ \AA}$  and at least the two-fold attenuation of irradiation of the mirror by the spontaneous X rays in the spectral regions that bring the significant contribution into its quick damage resulting in suppression of the double-pass amplification [68]. The data from Refs. [65-67] allow us to assume that this will provide the realization of the effective double-pass amplification on the  $4d - 4p$  transitions in Ni-like ions of Ta [68].

Other manifestations of usefulness of IFE studies for biology and medicine are also possible (see, e. g., Ref. [9,69]).

## 6. CONCLUSION

Heating the compressed fuel by the laser-accelerated ions of elements with  $Z$  of about 6 and higher seems to be one of the best versions of fast ignition.

The realization of the methods of hot spot heating with the use of the relatively long duration, low intensity laser pulses or without the use of the special laser or particle beam(s) is

highly desirable, but the reliable conclusion about the feasibility and efficiency of any of these methods will be possible only after the additional studies.

The analysis of the attainable parameters of the IFE power plants should take into account the possibility of compression of the tritium-lean fuels by radiation from the D-T microexplosions and by such radiation and the auxiliary drivers that improve the symmetry and temporal profile of the compression.

Usefulness of IFE studies for development of space propulsion systems, biology and medicine is the factor that can provide the additional financial support of these studies.

I would like to thank B.V. Litvinov, P. Mulser, V.A. Ovsyannikov and V.T. Tikhonchuk for useful discussions and the International Atomic Energy Agency for a partial financial support of the studies on the use of microexplosions for power production under IAEA Research Contract No. RUS 13722.

## REFERENCES

- [1] TELLER, E., "A future ICE (thermonuclear, that is!)", IEEE Spectrum **10**, No. 1, 60-64 (1973).
- [2] MEIER W.R., and HOGAN, W.J., "Power plant and fusion chamber considerations for fast ignition", Fusion Sci. Technol. **49**, 532-541 (2006); corrigenda: **52**, 118 (2007).
- [3] ROTH, M., et al., "Fast ignition by intense laser-accelerated proton beams", Phys. Rev. Lett. **86**, 436-439 (2001).
- [4] GUS'KOV, S.Yu., "Direct ignition of inertial fusion target by a laser-plasma ion stream", Kvantovaya Elektronika 31, 885-890 (2001) [Quantum Electronics 31, 885-890 (2001)].
- [5] BYCHENKOV, V.Yu., et al., "Fast ignition concept with fast ions", Fizika Plazmy 27, 1076-1080 (2001) [Plasma Physics Reports 27, 1017-1020 (2001)].
- [6] ATZENI, S., et al., "A first analysis of fast ignition of precompressed ICF fuel by laser-accelerated protons", Nucl. Fusion 42, L1-L4 (2002).
- [7] SHMATOV, M.L., "Some problems related to heating the compressed thermonuclear fuel through the cone", Fusion Sci. Technol. 43, 456-467 (2003).
- [8] RAMIS R., and RAMÍREZ, J., "Indirectly driven target design for fast ignition with proton beams", Nucl. Fusion 44, 720-730 (2004).
- [9] BORGHESI, M., et al., "Fast ion generation by high-intensity laser irradiation of solid targets and applications", Fusion Sci. Technol. 49, 412-439 (2006).
- [10] KEY, M.H., et al., "Proton fast ignition", Fusion Sci. Technol. 49, 440-452 (2006).
- [11] SHMATOV, M.L., "Comment on 'Assessment of potential for ion-driven fast ignition'", Fusion Sci. Technol. 52, 116-117 (2007).
- [12] ALBRIGHT, B.J., et al., "Studies in capsule design for mid-Z ion-driven fast ignition", J. Phys.: Conf. Ser. 112, 022029 (2008).
- [13] FERNÁNDEZ, J.C., et al., "Progress on ion based fast ignition", J. Phys.: Conf. Ser. 112, 022051 (2008).
- [14] SHMATOV, M.L., "Factors determining the choice of the laser-accelerated ions for fast ignition", J. Phys.: Conf. Ser. 112, 022061 (2008).
- [15] M. TEMPORAL, R. RAMIS, J.J. HONRUBIA and S. ATZENI, "Fast ignition induced by shocks generated by laser-accelerated proton beams", Plasma Phys. Control. Fusion 51, 035010 (2009).

- [16] NAUMOVA, N., et al., “Hole boring in a DT pellet and fast-ion ignition with ultraintense laser pulses”, *Phys. Rev. Lett.* 102, 025002 (2009).
- [17] FERNÁNDEZ, J.C., et al., “Progress and prospects of ion-driven fast ignition”, *Nucl. Fusion* 49, 065004 (2009).
- [18] HONRUBIA, J.J., et al., “Fast ignition of inertial fusion targets by laser-driven carbon beams”, *Phys. Plasmas* 16, 102701 (2009).
- [19] TIKHONCHUK, V.T., et al., “Fast ignition with ultra-intense laser pulses”, *Nucl. Fusion* 50, 045003 (2010).
- [20] SHMATOV, M.L., “The optimum values of the typical ranges of laser-accelerated ions in compressed equimolar deuterium-tritium fuel”, Preprint of Ioffe Physical Technical Institute No. 1802 (2010).
- [21] ATZENI, S., “Inertial fusion fast ignitor: Igniting pulse parameter window vs penetration depth on the heating particles and the density of the precompressed fuel”, *Phys. Plasmas* 6, 3316-3326 (1999).
- [22] ATZENI S., and TABAK, M., “Overview of ignition conditions and gain curves for the fast ignitor”, *Plasma Phys. Control. Fusion* 47, B769-B776 (2005).
- [23] HERRMANN, M., HATCHETT S., and TABAK, M., “Reducing ignitor energy for fast ignition by controlling energy deposition”, *Bull. Amer. Phys. Soc.* 46, No. 8, 106-107 (2001).
- [24] HATCHETT, S.P., et al., “Hydrodynamics of conically guided fast ignition targets”, *Fusion Sci. Technol.* 49, 327-341 (2006).
- [25] FEOKTISTOV, L.P., “Thermonuclear detonation”, *Uspekhi Fiz. Nauk* 168, 1247-1255 (1998) [*Physics – Uspekhi* 41, 1139-1147 (1998)].
- [26] SPITZER, L., JR. *Physics of Fully Ionized Gases*, 2<sup>nd</sup> revised ed., New York, London: Interscience Publishers (1962).
- [27] BERETETSKII, V.B., *Kvantovaya Electrodinamika [Quantum Electrodynamics]* (L.D. LANDAU and E.M. LIFSHITZ, *Teoreticheskaya Fizika*, Vol. 4 [Course of Theoretical Physics, Vol. 4]), 2<sup>nd</sup> ed., Moscow: Nauka (1980) [in Russian].
- [28] BETHE H.A., and SALPETER, E.E., *Quantum Mechanics of One- and Two- Electron Atoms*, Berlin, Göttingen, Heidelberg: Springer – Verlag (1957).
- [29] BETHE, H.A., “Molière’s theory of multiple scattering”, *Phys. Rev.* 89, 1256-1266 (1953).
- [30] BICHSEL, H., “Charged-particle interactions”, *Radiation Dosimetry*, 2<sup>nd</sup> ed. (ed. by F.H. ATIX and W.C. ROESCH), Vol. 1, pp. 157-228, New York, London: Academic Press (1968).
- [31] BERDONOSOV, S.S., “Zoloto [Gold]”, *Fizicheskaya Encyclopedia [Physical Encyclopedia]* (Editor-in-Chief A.M. PROKHOROV), Vol. 2, p. 87, Moscow: Sovetskaya Encyclopedia (1990) [in Russian].
- [32] VELARDE, G., et al., “Progress in inertial fusion energy modelling at DENIM,” Preprint UCRL-CONF-20815, Lawrence Livermore National Laboratory (2004).
- [33] SHMATOV, M.L., “Some thermonuclear power plants as the possible sources of He<sup>3</sup> for space propulsion systems,” *JBIS* 60, 180-187 (2007).
- [34] SHMATOV, M.L., “Advantages of the fast ignition, direct compression targets with two cones from the viewpoint of IFE reactor chamber physics,” *IFSA 2007 Abstracts* (Kobe, Japan, September 9-14, 2007), abstract ThPoIAEA101, p. 209 (2007).
- [35] SHMATOV, M.L., “Advantages of fast ignition scenarios with two hot spots for space propulsion systems”, *JBIS* 62, 219-224 (2009).
- [36] MARTINEZ-VAL, J.M., et al., “Jet-ignited indirect-drive inertial fusion targets,” *AIP Conf. Proc.* No. 406, 208-215 (1997).
- [37] HAIN S., and MULSER, P., “Fast ignition without hole boring,” *Phys. Rev. Lett.* 86, 1015-1018 (2001).

- [38] MURAKAMI M., and NAGAMOTO, H., “A new twist for inertial fusion energy: impact ignition”, Nucl. Instr. Methods Phys. Res. A 544, 67-75 (2005).
- [39] WINTERBERG, F., “Magnetic booster fast ignition macron accelerator”, Phys. Plasmas 13, 112702 (2006).
- [40] WINTERBERG, F., “On Impact Fusion”, AIP Conf. Proc. No. 406, 198-207 (1997).
- [41] CHARAKHCH'YAN, A.A., “Numerical investigation of circular cumulative jets compressing deuterium in conical targets”, Plasma Phys. Control. Fusion 39, 237-247 (2005).
- [42] KRASYUK, I.K., et al., “Use of conic targets in inertial confinement fusion,” Kvantovaya Elektronika 35, 769-777 (2005) [Quantum Electronics 35, 769-777 (2005)].
- [43] HANSON, D.L., et al., “Liquid cryogenic targets for fast ignition fusion”, Fusion Sci. Technol. 49, 500-516 (2006).
- [44] NORIMATSU, T., et al., “Fabrication, injection, and tracking of fast ignition targets: status and future prospects”, Fusion Sci. Technol. 49, 483-499 (2006); corrigenda: 52, 118 (2007).
- [45] SACKS R.A., and DARLING, D.H., “Direct drive cryogenic ICF capsules employing D-T wetted foam”, Nucl. Fusion 27, 447-452 (1987).
- [46] STEPHENS, E.H., et al. “Optimizing high-Z coatings for inertial fusion energy shells,” Fusion Sci. Technol. 43, 346-352 (2003).
- [47] BOOTH A., and FRANK, T.G., “A Technology Assessment of Laser-Fusion Power Production,” Preprint LA-UR-76-2076 (1976).
- [48] DUDERSTADT J.J., and G.A. MOSES, Inertial Confinement Fusion, New York: John Wiley and Sons (1982).
- [49] BOLT, B.A., Earthquakes. A Primer, San Francisco: W. H. Freeman and Co. (1978).
- [50] BLINK J.A., and MONSLER, M.J., “Status of Inertial Fusion and Prospects for Practical Power Plants,” Atomkernenergie-Kerntechnik 44, 205-208 (1983).
- [51] SHMATOV, M.L., “Some problems related to toxicity of Flibe”, Preprint of Ioffe Physical Technical Institute No. 1769 (2004).
- [52] WINTERBERG, F., “Inertial confinement fusion using only deuterium”, J. of Fusion Energy 2, 377-382 (1982).
- [53] MILEY, G.H., “Advanced fuels for heavy-ion beam fusion”, Nucl. Instr. Methods Phys. Res. 278, 281-287 (1989).
- [54] TABAK, M., “What is the role of tritium-poor fuels in ICF?”, Nucl. Fusion 36, 147-157 (1996).
- [55] ATZENI S., and CIAMPI, M.L., “Burn performance of fast ignited, tritium-poor ICF fuels”, Nucl. Fusion 37, 1665-1677 (1997).
- [56] IVANOV, G.A., et al., Vzryvnaya Deiterievaya Energetika [Explosive Deuterium Energetics], Snezhinsk: Izdatel'stvo RFYaTs – VNIITF (2004) [in Russian].
- [57] STOTT, P.E., “The feasibility of using D-<sup>3</sup>He and D-D fusion fuels”, Plasma Phys. Control. Fusion 47, 1305-1338 (2005).
- [58] SHMATOV, M.L., “Optimum variant of D-D fusion ignition for thermonuclear power plants”, Pis'ma v ZhTF 36, No. 8, 82-87 (2010) [Tech. Phys. Lett. 36, 386-388 (2010)].
- [59] FEOKTISTOV, L.P., Iz Proshlogo v Budushchee: Ot Nadezhd na Bombu k Nadezhnomu Reaktoru (Vospominaniya, Izbrannye Stat'i) [From the Past to the Future: From Hopes on Bomb to a Reliable Reactor (Memoirs and Selected Papers)], Snezhinsk: Izdatel'stvo RFYaTs – VNIITF (1998) [in Russian].
- [60] SHMATOV, M.L., “Space propulsion systems utilising ignition of microexplosion by distant microexplosion and some problems related to ignition of microexplosion by microexplosion”, JBIS 53, 62-72 (2000).
- [61] MÖLLENDORF, U., in “The HIDIF Study”, Report GSI-98-06, pp. 177-183, Darmstadt (1998).

- [62] SHMATOV, M.L., “Creation of directed plasma fluxes with ignition of microexplosions by and with the use of distant microexplosions”, JBIS 57, 362-378 (2004).
- [63] McCARTHY, K., et al., “Nonelectric applications of fusion”, J. of Fusion Energy 21, Nos. 3/4, 121-153 (2002).
- [64] Elton, R.C., X ray Lasers, Boston: Academic Press, Inc. (1990).
- [65] EDER, D.C., et al., “Cavity issues for Ni-like Ta X ray lasers”, SPIE Proc. 1551, 143-149 (1991).
- [66] MacGOWAN, B.J., et al., “Short wavelength X ray laser research at the Lawrence Livermore National Laboratory”, Phys. Fluids B 4, 2326-2337 (1992).
- [67] MacGOWAN, B.J., et al., “Problems in the implementation of X ray optics”, Inst. Phys. Conf. Ser. No. 125, 269-274 (1992).
- [68] SHMATOV, M.L., “Possibility of protecting a mirror of a laser on the 4d-4p transitions of nickel-like tantalum ions against spontaneous  $\gamma$ -rays by means of a filter”, Kvantovaya Elektronika 39, 1041-1044 (2009) [Quantum Electronics 39, 1041-1044 (2009)].
- [69] NAKAI, S., “Development of integrated IFE system and its industrial application as intense neutron source”, J. Phys.: Conf. Ser. 112, 042070 (2008).



# LASER-ATOM, LASER-PLASMA INTERACTIONS RELATED TO TARGET PHYSICS AND FAST IGNITION

V. STANCALIE

National Institute for Laser  
Plasma and Radiation Physics  
Bucharest, Romania

## Abstract

Presence of carbon in polymer target materials and aluminum material are of importance in laser irradiated cryogenically cooled pellet target design. Therefore X radiation emission study from aluminum and carbon material is important. This work discusses the non-perturbative method which has been used to study the interaction of high intensity laser radiation with aluminum and carbon ions. The intensity-dependent behavior of the resonance profiles is also discussed. Separate account is given of relation between photon emission rate and ionization or recombination flux which contribute to the opacity effects on a plasma emission lines.

## 1. INTRODUCTION

The study of laser-atom interactions at high intensities is an excited area of atomic physics related to fusion researches. Rapid advances in this domain have become possible due to the development, using the “Chirped Pulse Amplification” (CPA) scheme [1] of lasers capable of yielding intensities of the order exceeding the value corresponding to the atomic unit of electric field strength. Such laser fields are strong enough to compete with the Coulomb forces in controlling the electron dynamics in atomic systems. As a result, atoms and molecules in intense laser fields exhibit new properties which have been discovered via the study of multiphoton processes [2]. These properties generate new behavior of bulk matter in intense laser fields, with wide ranging potential applications such as the study of ultra-fast phenomena, the development of high frequency (XUV and X ray) lasers, the investigation of the properties of plasmas and condensed matter under extreme conditions of temperature and pressure, and intense field control of atomic and molecular reactions. Over the last ten years, laser intensities have increased by four orders of magnitude, up to  $10^{20}$  W cm<sup>-2</sup> where relativistic effects in laser-atom interactions become important [3-6].

On the theoretical side, the development of supercomputers has made it possible to perform calculations of unprecedented complexity, which have led to the prediction of novel properties of atomic systems in strong laser fields. While dense matter is typically electrically neutral, the light pressure of these ultra-intense laser pulses can separate electrons from ions completely, at least over spatial distances of order  $c/\omega_p$ , thus generating huge space charge fields in which charged particles are accelerated [7-9]. Fast ignition entails assembly of compressed fuel followed by fast heating. The simulation of the effects of the relativistic electron beam produced by the laser requires the modeling of the electron source and the transport of relativistic electrons in high-density materials. Theoretical calculations are the primary source of information on electron collisions with many atomic and molecular systems. Accurate understanding and interpretation of phenomena involves the knowledge of atomic and molecular processes dynamics in electromagnetic field.

In the last years, with the development of new instruments and technology able to measure spectra in the X-UV region, this activity made an unexpected progress. In simple gas targets, this may lead to the “bubble” regime, in which an electron-void volume trailing a short laser pulse self-traps electrons and accelerates them to hundreds of MeV. Corresponding electron pulses are now observed by many groups. Guiding the laser pulse in capillaries, thus

extending the acceleration distance, has led to the production of GeV electrons. At solid interfaces, the space charge fields accelerate ions to multi-MeV energies.

These beams have been observed with remarkably low emittance, and much of the current discussion concentrates on how to make mono-energetic ion pulses. Recent theoretical works show that ultra-thin foils and clusters can be accelerated as a whole close to the velocity of light, with pushed electrons dragging all ions [10]. Complementary to electron-void regions, one finds dense electron fronts moving with high relativistic velocities. These fronts may backscatter optical photons and convert them into X rays. At steep surfaces, oscillating relativistic mirrors compress incident laser light into attosecond flashes, corresponding to high harmonic spectra. It looks feasible to even focus these flashes, thereby reaching intensities close to the Schwinger limit for pair production from the vacuum. It is the first time that we have a realistic option to achieve electric fields of the order of  $10^{16}$  V cm<sup>-1</sup> at which light significantly disturbs the vacuum.

In the presence of an intense laser field, atomic and molecular states are dressed in the continuum. This can promote a discrete state into a photoionization continuum. Such a process, referred to as a laser-induced continuum structure (LICS), has been studied by Knight [11] and Kylstra *et al.* [12]. A LICS creates a tunable ‘pseudo-autoionizing resonance’ of adjustable position and width. Shao *et al* [13] also showed that it is possible to induce a LICS by exciting Rydberg states into the continuum. They have observed LICS in the ionization spectrum of sodium. Laser-induced degenerate states (LIDS) are different from LICS in that they involve two laser dressed atomic states. If for a particular laser frequency and intensity, the dressed autoionizing state and the dressed ground state (LICS) are degenerate (have the same energy and width), they form what is called a LIDS. Pumping an atom from the ground state into an excited state with the help of a laser is usually performed by tuning the laser to resonance and waiting sufficiently long. This process can be understood in terms of a simple two-level model atom, in which the laser coupling induces Rabi oscillations of the population between the two states. In principle, population can be transferred to 100% by choosing the pulse length appropriately ~‘ $\pi$  pulse’. Decay processes can be included in this model, for example the spontaneous decay, which destroys the coherence, but still allows at least 50% population transfer. When laser-induced ionization of the atom becomes important, however, in particular when the ionization rate of the upper level becomes comparable to the Rabi frequency, it is not evident that population can be transferred through Rabi oscillations.

A general feature of a laser plasma X ray spectrum is the presence of the so-called satellite lines on the longer wavelengths side of each resonance line. These lines, for which the ion levels involved in the transition are the same as for the corresponding resonance lines, are emitted as a consequence of the dielectronic recombination process. The presence of a further bound electron in an excited state causes the emission to occur at a slightly longer wavelength. Opacity issues are of crucial importance when modeling X ray spectra from laser-plasmas. Experimental and theoretical determinations of the radiative opacity have long been of interest. Many physical effects which have been treated approximately or ignored in theoretical models may affect the accuracy of opacity. Some discrepancies are supposed to be a consequence of line saturation effect.

Vitally important in almost all plasma environments are collisions between electrons and ions, particularly those that involve the transfer of energy. Theoretical efforts have produced much of the existing data. The proper description of electron scattering from open

shell ions must involve an adequate description of electron correlation as well as radiation damping. This problem has been solved a number of times using different tools. Method and codes exist for wide range of electron-impact excitation and ionization processes: the Convergent Close Coupling (CCC) theory and method is meant to be applicable at all energies for the major excitation and ionization processes [14] A recent development is a surface integral approach to scattering theory that is valid for short and long-range potential including Coulomb potential. The Plane-Wave Born (PWB) and first order many body perturbation theories (FOMBT) [15] and methods have also shown good agreement in some cases but very large differences for forbidden transitions in electron impact excitation. Resonances are not treated correctly by either PWB or FOMBT and require the use of the R-matrix method or of the CCC method.

Excitation can be a direct process or a result of resonant dielectronic capture followed by autoionization leaving the target ion in an excited state. Resonant enhancements to the cross section are significant in optically-forbidden transitions and can dominate the direct contribution by an order of magnitude or more near threshold. Direct configuration interaction (CI) and indirect interactions with a common continuum have shown [16] to produce interference between nearby resonances and have a strong effect on the resonance contributions to the cross sections as calculated in the close coupling formulation. It has been found that the resonance structure is sensitive to the exact energies of the individual resonances.

The increasing sophistication of collision calculations carried out over the last years has depended to a considerable extent on rapidly increasing power of the supercomputers available to such research. The difficulties in theoretical calculations of these processes come from the interference effects between the direct and the indirect processes. One approximation widely used to treat these phenomena is the Distorted Wave Born approximation (DWBA) [17]. Following this approximation the intermediate resonance state is independent of its decay. A second approximation [18] uses the R-matrix method to evaluate excitation cross section to the autoionizing states. In this case the interference effects with the direct process are neglected. The R-matrix method with one suitably chosen pseudo-state (RMPS) to represent continuum electrons [19] accurately includes both direct and indirect processes as well as the interference effects between them. As in the CCC approach, this method approximates the effects of higher-lying discrete and target continuum states by a set of pseudostates, which are incorporated into the R-matrix programs.

Doubly excited states (resonances) offer a very suitable laser frequency regime within which to undertake investigative calculations has already attracted interest. The resonance regions have been studied in the context of multiphoton transitions. There have been several theoretical methods introduced to describe multiphoton processes in atoms. Of these calculations only those employing the R-matrix Floquet [20,21] method couple the field to the ion non-perturbatively and only those of Latinne *et al.*[22, 23] explicitly investigated the laser induced modification of doubly excited states, that is to say, the interplay of laser-induced degenerate states (LIDS). Specifically, the frequency and the intensity of the light field can be adjusted such that the energy and the width of the dressed ground state coincide with the energy and the width of the dressed autoionizing state. The motion of the complex energies in the complex plane as function of the field intensity for different frequencies and atomic parameters gives complementary information on the role of LIDS on resonances obtained by laser. It was shown that the rate of the 'ground' excited Rydberg state will first increase with the intensity and then exhibit a typical 'stabilisation', namely a decrease of the ionization rate

with increasing intensity. The most interesting is the critical region where a crossing (or an avoiding crossing) occurs.

Pumping an atom from the ground state into an excited state with the help of a laser is usually performed by tuning the laser to resonance and waiting sufficiently long. This process can be understood in terms of a simple two-level model atom, in which the laser coupling induces Rabi oscillations of the population between the two states. In principle, population can be transferred to 100% by choosing the pulse length appropriately ~“ $\pi$  pulse”. Decay processes can be included in this model, for example the spontaneous decay, which destroys the coherence, but still allows at least 50% population transfer. When laser-induced ionization of the atom becomes important, however, in particular when the ionization rate of the upper level becomes comparable to the Rabi frequency, it is not evident that population can be transferred through Rabi oscillations. In the present work we focused on the Li-like Al and C ions interacting with an intense laser field. Aluminum material and presence of carbon in polymer target materials are of importance in laser irradiated cryogenically cooled pellet target design. Therefore X radiation emission study from aluminum and carbon material is important.

The high-lying single-particle states, in one-photon transfer reaction, manifest themselves as broad ‘resonance’-like structures superimposed on a large continuum. In general one associates double-resonant processes with processes induced by two lasers. In our work, instead of using a probe laser to reach a high-lying state in the continuum, this state is reached by choosing the energy of the incident electrons to be at resonance with the resonant state of the composite electron-atom system. An intense laser is then used to strongly couple the autoionizing state to another state. The advantage of such approach is that it allows flexibility: tuning the energy of the electrons over a wider energy range is easy, while lasers operate in restricted frequency intervals. Additionally, resonant states of all symmetries can be excited, not only the dipole selected states. Our description of the laser field assumes that the following conditions hold: (i) the number of photons per mode (in our case there is only one mode) of the laser is large so that the field may be treated classically; (ii) the wavelength of the laser is large compared with the spatial extent of the atom so that the dipole approximation is applicable; and (iii) the pulse duration is long compared to typical scattering times. Floquet theory calculates quasistationary solution of time dependent Schrodinger equation (TDSE) for a monochromatic field equation. In the RMF approach, the time-dependent wavefunction is written in a Floquet-Fourier form, so that the TDSE is transformed into a time-independent eigenvalue equation, in which atom-field coupling is treated in a fully non-perturbative manner.

This implies that all resonant couplings, as well as non-resonant and high-order laser-induced coupling, are fully accounted for. The laser dresses the autoionizing state, and the projectile electron, and we assumed the following: at resonance this dressing is dominated by the resonant coupling between these states so that we can ignore the influence of the remaining states. Models of this type have been able to reproduce well a variety of *ab initio* calculations of multiphoton ionization processes involving autoionizing states. The resulting quasienergies are complex with the imaginary part being equal to minus one half times the ionization rate of the state. This represents a quasi-stationary picture in which the atom decays exponentially in time.

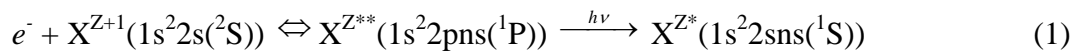
The work is structured as follows: Section 2 gives our model for studying the high intensity laser pulse interaction with Li-like Al and C ions. Section 3 presents our procedure

for analyzing resonances in laser assisted atomic collision, which exploits the analytic properties of the R-matrix Floquet theory to obtain the intensity dependence of resonance profile. We explore the possibility of using developed two-state model in conjunction with Fano theory in order to investigate intensity dependence of resonance profiles in ultra-short, high intensity laser-atom interaction. Section 4 gives results from the opacity calculation.

A general feature of a laser plasma X ray spectrum is the presence of the so-called satellite lines on the longer wavelengths side of each resonance line. These lines, for which the ion levels involved in the transition are the same as for the corresponding resonance lines, are emitted as a consequence of the dielectronic recombination process. The presence of a further bound electron in an excited state causes the emission to occur at a slightly longer wavelength. Opacity issues are of crucial importance when modeling X ray spectra from laser-plasmas. We derived atomic data for opacity model including the contribution of the bound-free and bound-bound transitions. Line broadening caused by autoionization and the core-valence correlation contribution to the oscillator strength was investigated and included into the model. An R-matrix calculation was carried out for Al XI ion. The weighted oscillator strengths for selected strong transitions and their contribution to the absorption in the plasma was investigated related to the opacity issue. Section 5 gives our concluding remarks and future works.

## 2. NON-PERTURBATIVE TREATMENT OF IONS IN LINEARLY POLARIZED ELECTROMAGNETIC FIELD: THE TWO STATE MODEL FOR LASER INDUCED DEGENERATE STATES (LIDS). APPLICATION TO LITHIUM ISO-ELECTRONIC SEQUENCE

The calculation reported here is part of a general investigation which started with studies of  $\Delta n = n' - n = 0$ ,  $n, n'$  ranging from 5 to 12 for  $C^{2+}$  and from 9 to 12 for  $Al^{9+}$  [24] and  $\Delta n = 2$  in Be-like carbon [25]. We only recall here the principal ideas of the theory and the numerical methods. Only the relevant equations will be repeated here. The basic process of interest is:



In the above equation  $X^{Z+1}$  signifies the Li-like C ion, of nuclear charge Z, in its ground state, and  $X^{Z+**}$  is the doubly excited state of the corresponding Be-like ion of nuclear charge Z.

## 3. THEORETICAL APPROACH

An initial calculation based on the QDT and the standard R-matrix has been done. This is to calculate the  $1s^2 2s^2$  and  $1s^2 2p^2$  ground states for Be-like ions, including full description of the electron-electron correlation and exchange effects. The energies belonging to the corresponding Rydberg excited states  $1s^2 2snl$  and  $1s^2 2pn'l$  have been taken from the Opacity Book or evaluated from the QDT, if missing. The  $1s^2 2pn'l$  state energy has been evaluated relative to  $^2P$  ionization threshold while, the energy of the excited 'bound' state  $1s^2 2snl$  is evaluated relative to  $^2S$  ionization threshold.

The atomic system was then dressed by a monochromatic mono-mode linearly polarized laser field the intensity of which is given by the field strength of the core transition  $2s-2p$  and the frequency by the energy of the core transition. The laser dresses the autoionizing state, and the projectile electron, and we assume the following: at resonance this dressing is dominated by the resonant coupling between these states so that we can ignore the influence of the

remaining states. This represents a quasi-stationary picture in which the atom decays exponentially in time.

### 3.1. Theoretical results

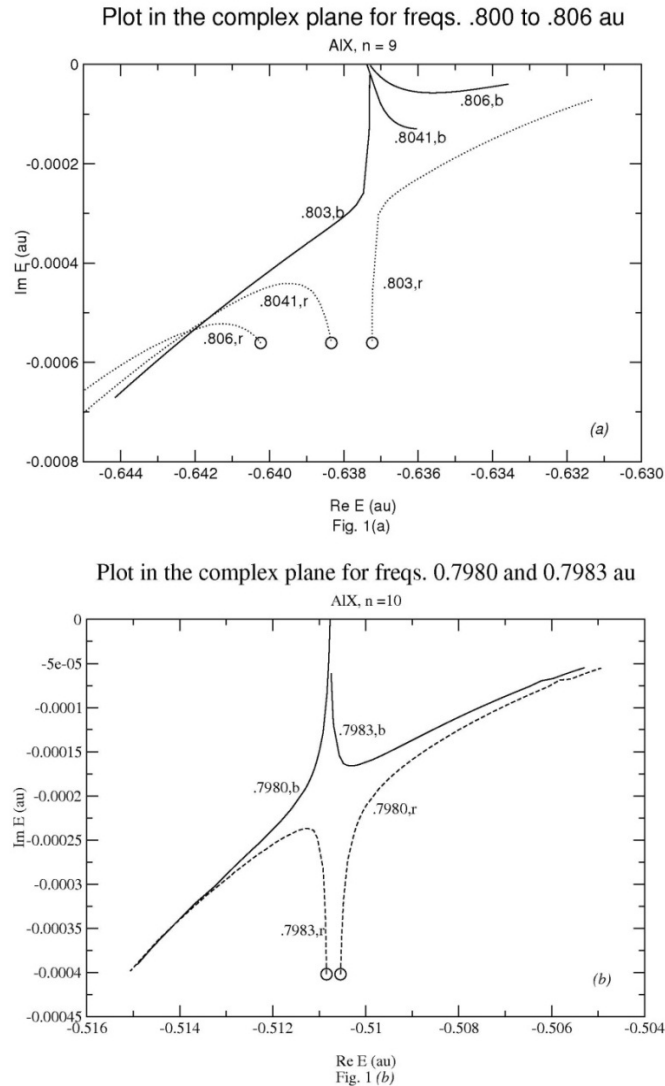


FIG. 1(a) and (b). The motion in the complex plane of trajectories belonging to the ‘bound’ excited and the excited Rydberg states corresponding to  $1s^22s9s(^1S)$  and  $1s^22p9s(^1P^0)$  Rydberg states, and  $1s^22s10s(^1S)$  and  $1s^22p10s(^1P^0)$ , respectively, in  $Al^{10+}$ .

In Figure 1(a, b) we reproduce from Ref. 24. the motion in the complex plane of trajectories belonging to the ‘bound’ excited and the excited Rydberg states corresponding to  $1s^22s9s(^1S)$  and  $1s^22p9s(^1P^0)$  Rydberg states, and  $1s^22s10s(^1S)$  and  $1s^22p10s(^1P^0)$ , respectively, in  $Al^{10+}$ . Fig 1(a) gives the motion in the complex plane of the complex energies belonging to  $1s^22s9s(^1S)$  (denoted by ‘b’) and  $1s^22p9s(^1P^0)$  (denoted by ‘r’), states in Al X as function of frequency and field intensity. Corresponding curves have the same line type (solid or dashed) and are labeled by the frequency from 0.800 to 0.810 in atomic units. Field intensity varied between 0.0 and  $10^{14}$  W/cm<sup>2</sup> and is indicated next to the curves. Zero-field position of the autoionizing state is denoted by big circles. The energy scale is chosen such that  $E_g = 0$ . FIG.1(b) gives the plot in the complex plane for frequencies of 0.7980 and 0.7983 atomic units of the quasi-energies belonging to  $1s^22s10s(^1S^e)$  and  $1s^22p10s(^1P^0)$  in Al X.

The intensity varied from 0.0 to  $7 \cdot 10^{13}$  W/cm<sup>2</sup>. Figure 2(a, b) shows similar results obtained for C<sup>3+</sup>. Fig 2(a) shows trajectories of the complex energies of  $1s^2 2s 5s(^1S^e)$   $1s^2 2p 5s(^1P^0)$  states in C<sup>2+</sup>, for frequencies 0.3085 and 0.3087 atomic units. The field intensity is varied from 0.0 to  $10^{13}$  W/cm<sup>2</sup>. Fig 2(b) gives trajectories of the complex energies of  $1s^2 2s 7s(^1S^e)$  and  $1s^2 2p 7s(^1P^0)$  states in C<sup>2+</sup>, for frequencies 0.2987 and 0.2989 atomic units. The intensity is varied from 0.0 to  $10^{12}$  W/cm<sup>2</sup>.

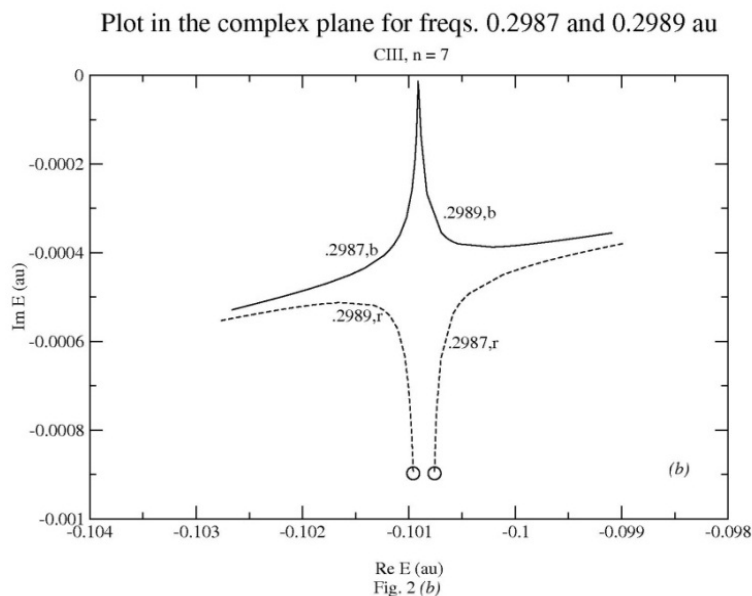
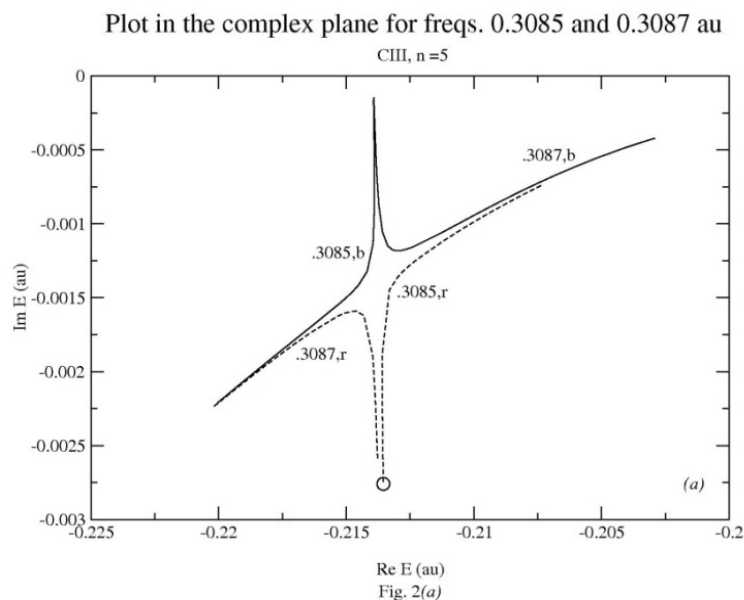


FIG. 2(a) and (b). The trajectories of the complex energies of  $1s^2 2s 5s(^1S^e)$   $1s^2 2p 5s(^1P^0)$  states in C<sup>2+</sup>, for frequencies 0.3085 and 0.3087 atomic units, and the trajectories of the complex energies of  $1s^2 2s 7s(^1S^e)$  and  $1s^2 2p 7s(^1P^0)$  states in C<sup>2+</sup>, for frequencies 0.2987 and 0.2989 atomic units.

The 2-state model has two LIDS points at particular frequencies and intensities. Close to these points, LIDS frequency for fixed intensity can be predicted as complex trajectories with a real part avoided crossing and an imaginary part crossing switch to having a real part crossing and an imaginary part avoided crossing as  $\omega$  passes through LIDS frequency.

In all curves where we are really close to the LIDS position, the imaginary part of the bound state energy, i.e. the width, increased rapidly with intensity while, the real part remained essentially constant. Also, the width of autoionizing state decreased rapidly from its zero field value and its real part of the energy also remained essentially constant. Therefore if the equivalent intensity of the spontaneous emission is less than the LIDS intensity then the two widths are converging towards each other into the region where perturbation theory should not be used.

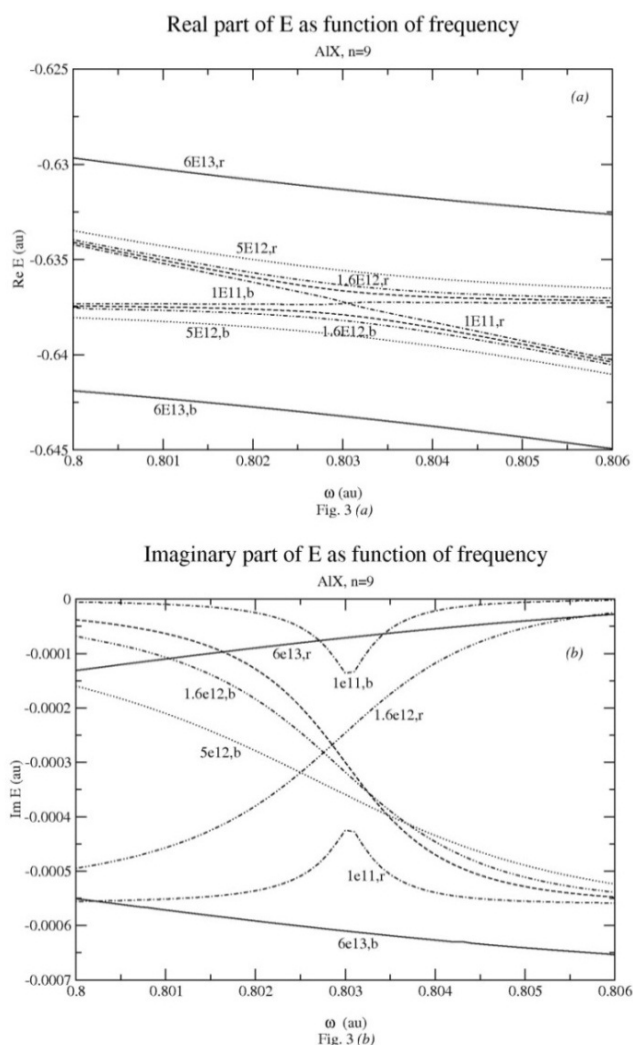


FIG. 3(a) and (b). The behaviour of the real and imaginary of the complex energies at fixed field intensity and as function of the field frequency.

At weak intensity there is a clear evidence of the interference between the two resonant Rydberg states (the first crossing). As the intensity of the field is increased the crossing of the imaginary parts of the quasi-energies which correspond to the 'ground' Rydberg state apparently ceases to exist. In Figure 3(a, b) we reproduce the behavior of the real and imaginary of the complex energies at fixed field intensity and as function of the field frequency. FIG. 3 (a) shows the real parts of  $E$  as function of frequency, in atomic units, for given intensities, corresponding to  $2sns(^1S^e)$  and  $2pns(^1P^0)$  states with  $n = 9$  in Al X. The curves have solid and dashed lines and are labeled as 'b' and 'r', respectively. Corresponding intensities are indicated next to the curves. In Fig 3(b) are given the corresponding imaginary parts of  $E$  as function of frequency, in atomic units, for given intensities.

At lower intensity ( $1.5 \cdot 10^{12} \text{ W/cm}^2$  Al X) the RMF calculations show a dip in the width of the ‘ground’ state at frequency about 0.803 au. These minima become exact zero if the ratio of the squared dipole matrix elements coupling these states to the continua tends to zero. The energies of the Rydberg states are shifted by  $-\omega$ , where  $\omega$  is the laser frequency. Away from the resonances, the curves correspond to the ‘ground’ Rydberg state and the ‘resonant’ Rydberg state, respectively. At low intensity, the avoided crossings are well separated, whereas this is not the case at the higher intensity where we see that the separations of the avoided crossings are comparable to the energy separation of the two Rydberg states [26].

#### 4. INTENSITY DEPENDENCE OF RESONANCE PROFILES IN ULTRA SHORT, HIGH INTENSITY LASER –ATOM INTERACTION

The intensity-dependent behavior of the resonance profiles is closely related to the proximity of LIDS. We have derived a simple model to describe the structure of these degeneracies. From this model one may ascertain the effect of LIDS upon the resonance absorption profile in the photodetachment rate of the ground state of the model ion. We illustrate how the laser field may introduce intensity-dependent multiphoton ionization pathways that compete directly with the intensity-independent autoionization pathway associated with configuration interaction. The description generalizes the non-radiative coupling matrix element of the autoionizing state to the continuum, so as to include an explicit intensity dependence.

The process under investigation is described within the general theory on double poles of the S matrix occurring in laser-assisted electron-scattering by an atom in the neighborhood of an autoionizing resonance with a quasibound state of the composite electron-atom system. For ‘capture-escape’ resonance, the Breit-Wigner expression for corresponding cross section is:

$$\sigma(E, I, \omega) = \frac{2\pi g}{E} \frac{\frac{1}{2}\Gamma_g}{[E - E_g - \omega]^2 + \frac{1}{4}\Gamma_g^2} \quad (2)$$

This quantity becomes zero for a particular value of the electron energy  $E(I, \omega)$  at which the dipole coupling between the ground state and the autoionizing state is zero. Intensity-dependent shifts of the position  $E_g$  are small at frequencies and intensities considered in these calculations and are therefore ignored. A simple model has been developed [27] so as to reinforce the role of Laser Induced Degenerate State phenomenon on resonances obtained by laser.

Considering our very simple 2-state model for  $\text{C}^{2+}$  and  $\text{Al}^{9+}$ , in all these calculations for frequencies near the LIDS frequency the real part of the energy is nearly constant for low intensities up to the LIDS intensity but the imaginary part changes rapidly converging together at LIDS position. Beyond LIDS the real and imaginary parts both diverge from each other. Table 1 gives the calculated widths of the quasienergies at the first LIDS positions. The effect of constant ratio in Table 1 is to produce a resonance profile that becomes narrowed and taller, then wider and lower as laser field intensity increases.

When only a single resonant process occurs, either in the limit that the laser intensity goes to zero so that only the autoionizing resonance remains, or in the limit that the width of the autoionizing state goes to zero, leaving only the ‘capture- escape’ resonance, the ratio of

the scattering cross section to the background cross section reduces to the Fano line shape formula. The Fano resonance formula is algebraically simple. A dimensionless energy  $\varepsilon$  is used to measure energy differences from a resonance energy  $E_r$  in terms of the half-width.

The calculated widths,  $\Gamma$ , in atomic units (*au*), at the first LIDS positions in  $C^{3+}$  are shown in table 1. The principal quantum numbers,  $n$ , describes both, ‘bound’ and ‘excited’ Rydberg states of type  $1s^2 2sns(^1S)$  and  $1s^2 2pns(^1P)$  respectively, embedded by the electric field.

TABLE 1. THE CALCULATED WIDTHS,  $\Gamma$ , IN ATOMIC UNITS (*AU*), AT THE FIRST LIDS POSITIONS IN  $C^{3+}$ .

$n$	$2n^3 \Gamma(au)$
5	0.17
6	0.15
7	0.15
8	0.15
9	0.15
10	0.15
11	0.14
12	0.16

For an *isolated* autoionization state with a resonant width  $\Gamma$  at resonant energy  $E_r$ , the resonant structure can be described in terms of the asymmetry parameter  $q$ . This parameter is a measure of the importance of the direct transition from the ground to the continuum compared to transition via the autoionizing state. High  $q$  means weak direct transition and symmetric line shape since the interference is minimized. Qualitatively, the  $q$  parameter measures the interference between transitions from the initial state to the bound and continuum components of the final-state wave function. If the resonance is dominated by the contributions from the transitions to both bound and continuum components of the final-state wave function, its corresponding  $q$  value is generally large and the resonant feature is approximately symmetric. If the contributions from transitions to bound and continuum components of the final-state wave function are comparable, the resonant structure is asymmetric with an intermediate  $q$  value. If the spectrum is strongly dominated by the transition to the continuum component of the final-state wave function, a *window resonance* with zero cross section is expected either at or near the resonant energy  $E_r$  with  $q \rightarrow 0$ .

In Fig. 4 the ratio  $R = (q+\varepsilon)^2/(1+\varepsilon^2)$  is plotted as function of relative energy parameter and different  $q$  values for the  $1s^2 2pns(^1P^0)$ ,  $n=5$  state in CIV. The relative energy has been determined as  $\varepsilon = [2(E_g + \hbar\omega - E_a)]/(\Gamma_a + \gamma_a - \Gamma_g)$ , where  $E_g$ ,  $\omega$ , and  $E_a$  are, respectively, the field free position of the excited Rydberg state, the tuning frequency and the field-free position of the autoionizing state, as output from the R-matrix Floquet calculation.

Preliminary results on intensity dependence of the line profile have been obtained based on the eigenphase fitting procedure. The method uses R-matrix theory to determine the energy

variation of the eigenphase analytically rather than numerically. Fitting the energy dependent K-matrix directly is difficult because K has a pole in the resonance region. Therefore it is easier to fit the  $\arctan(K)$ . Following this method, the eigenphase derivative is a well behaved function of E near the resonance (FIG. 5).

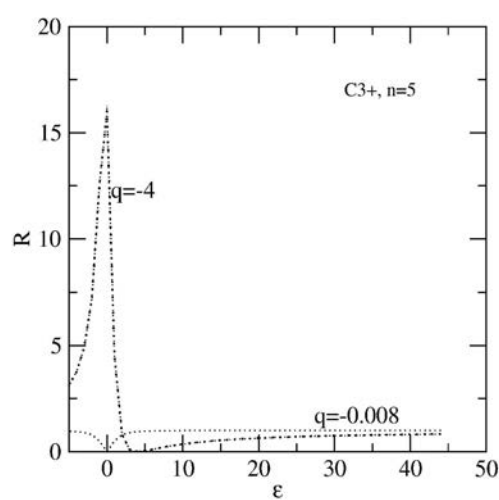


FIG. 4. Line profile ratio for  $1s22p5s$  ( $1P0$ ) resonant state in C IV as function of the relative energy parameter in atomic units(a.u.).

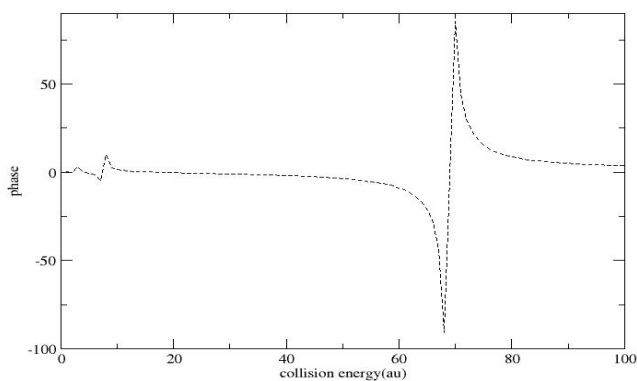


FIG. 5. The phase derivative as function of collision energy for CIV,  $n=4$ .

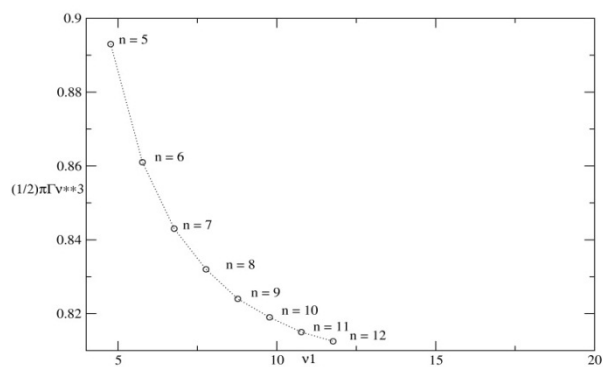


FIG. 6. ‘Scaled’ width dependence of the autoionizing width with the ‘bound’ excited Rydberg state effective quantum number.

This procedure yield to a modified resonance profile that becomes narrower and taller, then wider and lower as  $I$  increases. The procedure allows the generalization of the model so as to include an explicit dependence of the autoionization width upon the laser field and the

coupling matrix element of the autoionizing state to the continuum. The relative energy has been calculated as:  $\varepsilon = 2\omega_{tune} / (\Gamma^a / 2)$ , numerical values for field-free energy difference,  $\omega_{tune}$ . Finally, a scaling relation has been obtained as function of the effective quantum numbers and ionic:  $\varepsilon = 4n^{*3} \omega_{tune} / Z$

Figure 6 shows the ,scaled' width dependence of the autoionizing width with the ,bound' excited Rydberg state effective quantum number( $\nu_1$ ).

Following the second method, based on the eigenphase fitting procedure, but which uses R-matrix theory to determine the energy variation of the eigenphase analytically rather than numerically, in the external region of the R-matrix there are two independent solutions, say  $S(E,r)$  and  $C(E,r)$ , with known asymptotic forms for  $r \rightarrow \infty$ . Quantities such as reactance ( $K$ ) and scattering matrices are obtained on matching the internal radial function  $F$  to  $n \times n_0$  linear combinations of functions  $S$  and  $C$ , for  $n_0$  open channels.

$$F(E,r) = S(E,r) + C(E,r)K(E)$$

Fitting the energy dependent  $K$ -matrix directly is difficult because  $K$  has a pole in the resonance region. Therefore it is easier to fit the  $\arctan(K)$ . Diagonalizing the  $K$ -matrix in the space of the open channels  $n_0$ , i.e. let  $K_{oo}$  have eigenvalues  $\lambda_i$ , then  $K_{oo} X = \lambda_i X$ . The eigenphase in each channel is defined as  $\delta_i = \tan^{-1} \lambda_i$ . We now show that the eigenphase derivative  $\delta'(E)$  is a well behaved function of  $E$  near the resonance. In our case of two state model (one open channel):  $\lambda = K = \tan \delta \cong (\Gamma/2)/(E_r - E) \rightarrow \delta'(E) = (1 + (E_r - E)/(\Gamma/2))^2)^{-1} * 1/(\Gamma/2)$ . Therefore  $\delta'(E)$  has approximately quadratic form near resonance. Denoting  $\Gamma^{r,n}$  radiative width in the channel  $n$ , with  $\Gamma^{r,n} = I / \omega_n$ ,  $\omega_n$  being LIDS frequency, we have obtained usual scaling relation  $\Gamma^{r,n(CIII)} / \Gamma^{r,n(ALX)} = 11/4$ . Corresponding relation for autoionization widths is  $\Gamma^{a,n(CIII)} / \Gamma^{a,n(ALX)} = 1.4 = (11/4)^{1/3}$ . Finally, the branching ratio  $B^{n,CIII} = \Gamma^{r,n(CIII)} / \Gamma^{n,LIDS} = 0.986/n^3$  and  $B^{n,ALX} = \Gamma^{r,n(ALX)} / \Gamma^{n,LIDS} = 0.306/n^3$ , which corresponds to a scaled relation on  $Z$  as  $B^{n,CIII} / B^{n,ALX} = 1/3$ .

## 5. ATOMIC DATA FOR OPACITY CALCULATION

Experimental and theoretical determinations of the radiative opacity have long been of interest. Many physical effects which have been treated approximately or ignored in theoretical models may affect the accuracy of opacity. Some discrepancies are supposed to be a consequence of line saturation effect. We have derived atomic data for opacity model including the contribution of the bound-free and bound-bound transitions. The model is based on escape factor approximation [28].

The Balmer series lies in the near ultra-violet and visible part of the spectrum – between the wavelengths 3646 Å and 6563 Å. It is the spectrum, which needs the largest amount of modeling, as it contains more spectral contributors than the Pachen spectrum. The usually treated situation is that of a fully ionized nucleus in the core plasma receiving an electron from a neutral deuterium atom in the beam. The recombined ion in the plasma then radiates a hydrogen-like spectrum which includes transitions between highly excited states in the visible spectral range. The latter lines are those typically observed and analyzed in charge exchange spectroscopy. Then are two useful quantities needed from theoretical atomic models. The first is the effective emission coefficient for a particular transition made by the recombined hydrogen-like ion in the plasma after receiving an electron from a neutral beam donor. If the

number densities of donor atoms and receiver nuclei are known at points in the plasma, the theoretical emissivity coefficient allows the photon intensity in a ‘charge exchange’ spectrum line along an observational line of sight to be calculated.

Alternatively, from the observed intensity the number density of receiver nuclei may be deduced provided the line of sight through the beam is sufficiently short and the number density of beam donors is known. Thus the second useful quantity is theoretical beam stopping coefficient which allows to calculate the number of donors at any point along the beam path. In this work we refer to the plasma which is basically hydrogen (deuterium) plasma with all its non – negligible contributors. Briefly, the electron density,  $n_e$ , is considered in the range of  $0.5-1.5 \cdot 10^{19} \text{ m}^{-3}$ , the electron,  $T_e$ , and ion temperature,  $T_i$ , are between  $100 - 200 \text{ eV}$  and  $50 - 300 \text{ eV}$  respectively, and main impurities concentrations referring to oxygen and carbon were considered to output a value between 1,5 and 3,0 of the average electric charge,  $Z_{eff}$ . Modeling of the plasma, requiring collisional and radiative processes to perform calculation on population densities, ion abundances, line radiation or radiated power has basically been performed with the aid of Atomic Data and Analysis Structure (ADAS) package which is an interconnected set of computer codes and data collections for assisting in the analysis and interpretation of spectral measurements. Its structure has both interactive and non – interactive capabilities. The interactive part provides immediate display of important fundamental and derived quantities used in analysis together with a substantial capability for exploring parameter dependencies and diagnostic predictions of atomic population and plasma models. The second part is non – interactive but provides a set of subroutines which can be accessed from the user’s own codes to draw in necessary data from the derived ADAS database. Atomic data are calculated via the R-matrix method [29,30].

Based on a collisional-radiative (CR) model for hydrogen, we investigate the relationship of the photon emission rate of Balmer  $\alpha$  and Lyman  $\beta$  lines to the ionization flux or to the recombination flux. Separate account is taken of the total radiated power contributions from these atoms which are dominant constituents of fusion plasmas and play important roles in the edge plasma. To calculate relations between photon emission rate and ionization or recombination flux, the quasi-steady state population density of an excited level,  $n(p)$ , is expressed in terms of population coefficients,  $R_0(p)$  and  $R(I)$ :

$$n(p)=R_0(p)n_e n_i +R_I(p)n_e n(I) \quad (3)$$

with  $n_e$  and  $n_i$ , the electron density and the proton density, respectively, and  $R_0(p)$  and  $R(I)$  are functions of  $n_e$  and  $T_e$ . The time derivatives of  $n(I)$  and  $n_i$  have been expressed in terms of effective ionization,  $S_{CR}$ , and recombination rate coefficients,  $\alpha_{CR}$ . The ionization flux,  $S_{CR} n_e n(I)$ , and the recombination flux,  $\alpha_{CR} n_e n_i$ , have the same dimension as the photon emission rate,  $A(p,q)n_0(p)$  or  $A(p,q)n_I(p)$ , all of them being proportional to  $n_i$ . The model calculation gives numerous values of various excitation, recombination and ionization rate coefficients, and finally values for the populations of levels. The set of differential equations that must be solved to yield collisional - radiative ionization, recombination and level population coefficients has been described on the basis of atomic data and program package ADAS . The  $n_e$  dependences of  $S_{CR}$  and  $A(3,2)R_I(3)$  for  $T_e = 10 \text{ eV}$  (case of ionizing plasma) show no  $n_e$  dependences, because the ionization flux is dominated by direct ionization from the ground and the Balmer  $\alpha$  line is expressed by the coronal equilibrium.

We have obtained  $T_e$  dependences of the ionization and recombination fluxes and the

$$P_{line} = \sum_{p,q} n(p)A(p,q)E(p,q)ergcm^3 sec^{-1}$$

photon emission rates of the Balmer  $\alpha$  line under  $n(I) = n_I = 1m^{-3}$  and  $n_e = 10^{14}cm^{-3}$  where the corona equilibrium is no longer acceptable.  $T_e$  dependences of  $n(1)$  and  $n_I$  are plotted under the constraint of  $n(I)+n_I = 1m^{-3}$  and  $n_e = 10^{13}cm^{-3}$ . A secondary result of our calculation is a revision of the values of the radiated power. The power radiated by radiative recombination and bremsstrahlung depends on the electron density, while the line radiation depends on the excited level population densities. We consider the power lost by line radiation in the form: and the power lost by bremsstrahlung as :

$$P_{brem} = \frac{n_e^2}{X} 1.420 * 10^{-27} Z^2 T^{1/2} ergcm^{-3} sec^{-1}$$

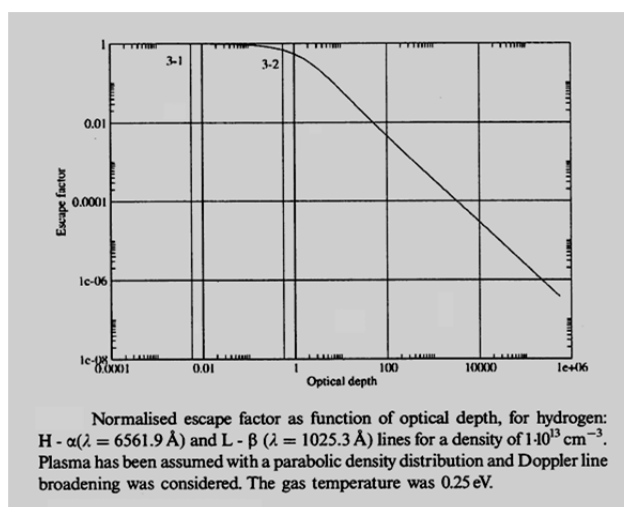


FIG. 7. The dependence of calculated normalized escape factor on plasma depth for studied H- $\alpha$  and L- $\beta$  emission line.

with  $E(p,q)$  the energy difference between levels  $p,q$ , and  $T$  in Kelvin.  $X$  is the ratio of  $n_e$  (the number density of the free electrons) to the number density of bare nuclei of charge  $Z$ . The power lost by radiative recombination has been evaluated. Finally, the model makes use of the previously calculated  $R_o(p)$  and  $R(I)$  and  $n(p)$  to express the total radiated power as:  $P = P_0 + P(1)n(1)$ . FIG. 7 shows the dependence of calculated normalized escape factor on plasma depth for studied H- $\alpha$  and L- $\beta$  emission line.

## 6. CONCLUSION

In this work we investigated the interaction of high intensity laser radiation with atoms and plasmas. Laser-atom interaction has been studied in connection with degeneracy and population trapping. Laser-plasma interaction has been considered from the point of view of relations between photon emission rate and ionization or recombination flux which contribute to the opacity effects.

Our results provide a firm foundation on which larger calculations may be based. From our model one may ascertain the effect of LIDS upon the resonance absorption profile in the photo-detachment rate of the ground state of the model ion. We expect that the autoionization of the lower doubly-excited level will remove the constraint on the size of the probe-pumped

plasma that is imposed by radiation trapping in other photo-pumping schemes. The simulation uses Fano theory combined with the quantum defect method and LIDS model to investigate ‘trapping’ of population at non-zero field intensity and possible population transfer from the excited to auto-ionizing state. The alternative pumping scheme promising possibility to dramatically reduce pump power requirements has important implications for the next generation of plasma lasers. Essentially, it breaks the symmetry between absorption and stimulated emission by using a coherent laser whose frequency closely matches the transition between the upper level and some other auxiliary level. The lasing medium can be coherently prepared in such a way that absorption between the lower and upper levels is reduced or eliminated. The theoretical mechanism for this process is quantum mechanical interference between two different paths leading to the excited state. This scheme involves two close-lying autoionizing (AI) states as upper operating levels. The gain in this scheme can be rather large if the two selected AI states satisfy the following conditions: (a) they decay into the same continuum, (b) one or both AI states have large Fano parameters, and (c) the spacing between these levels is comparable with their autoionizing widths.

Including the effects of statistical plasma microfields is absolutely essential in the modeling of the spectrum. It can shortly be noted, that the Stark broadening of spectral lines serves as an excellent diagnostic for the ion density in the plasma. In atomic hydrogen the Balmer series lies in the visible spectrum, between  $6563 \text{ \AA}$  and  $3646 \text{ \AA}$  at the series limit. The spectrum around the series limit is of special interest. The series limit is located at the wavelength an emitted photon would have if a free ‘zero kinetic energy’ electron recombined with an ion. Under the given plasma parameters of low temperatures ( $\sim 1\text{eV}$ ) and high densities ( $\geq 10^{14} \text{ cm}^{-3}$ ) there is a very marked rise in photo recombination. The spectrally resolved intensity of the photo recombination radiation includes the wavelength dependences via the energy of the emitted photon. The atomic spectra, transition probabilities, population densities, line radiation and photo-recombination were analysed on the basis of atomic data and program package ADAS [4]. The main routine calculates the emission spectrum in a wavelength, electron density and temperature range. This routine calculates the continuum emission (free-free and free bound) as a function of wavelength. The fortran version of the code generates the total emission for hydrogen plus single impurity plasma, which in our case was oxygen. No ionization balance was assumed but the code required all ion stages so a coronal balance has been considered.

## REFERENCES

- [1] STRICKLAND D., and MOUROU, G., “Compression of amplified chirped optical pulses”, *Opt. Commun.* 56, 219 (1985).
- [2] GAVRILA, M., ed., *Atoms in Intense Laser Fields*, *Adv. At. Mol. Opt. Phys. Suppl.* 1 (1992).
- [3] BURNETT, K., REED V.C., and KNIGHT, P.L., *J. Phys. B*: 26,561(1993).
- [4] JOACHAIN, C. J., *Theory of laser-atom interactions*, in: *Laser Interactions with Atoms, Solids and Plasmas*, R.M. More, ed. Plenum Press, New York (1994), p.39.
- [5] DIMAURO L.F., and AGOSTINI, P., *Adv. At. Mol. Opt. Phys.* 35:79(1995).
- [6] PROTOPAPAS, M., KEITEL C.H., and KNIGHT, P.L., *Rep. Progr. Phys.* 60:389(1997).
- [7] MALKA, G., LEFEBRE, E., and MIGUEL, J.L., *Phys. Rev. Lett* 78:3314(1997).
- [8] BAUER, D., MULSER, P., and STEEB, W. H., *Phys. Rev. Lett.* 75:4622(1995).
- [9] MORA P., and ANTONSEN T.M., Jr., *Phys.Rev. E* 53: R2068(1996).

- [10] RYKOVANOV S. G., et al. New J. Phys. 10 (2008)113005 and references herein.
- [11] KNIGHT, P.L., Comments on Atomic and Molecular Physics 15 (1984) 193,
- [12] KYLSTRA, N.J., PASPALAKIS, E., KNIGHT, P.L., J. Phys. B 31(1998)L719.
- [13] SHAO, Y.L., et al., J. Phys. B 28 (1995) 755.
- [14] FURSA D. V., and BRAY I., Phys. Rev. A 52, 1279(1279)].
- [15] CARTWRIGHT D. C., and CSANAK G., Phys. Rev A 38, 2740(1988)
- [16] GRIFFIN, D.C., et al., Phys. Rev. Lett. 72, 3491 -3494(1994).
- [17] BARTSCHAT K., and MADISON D, H., J. Phys. B: At. Mol. Opt. Phys. 21,153(1988).
- [18] BURKE P.G., and BERRINGTON, K.A., Atomic and Molecular Processes: an R-matrix Approach , IOP Publishing, Bristol.1993.
- [19] BARTSCHAT K., et al., M, JPB 29,115(1996), PRA 54 R998(1996), JPB 29,2875(1996).
- [20] BURKE, P.G., et al., , Europhys. Lett. 13: 617(1990).
- [21] BURKE, P.G., FRANCKEN P., and JOACHAIN C J., J.Phys.B 24:761(1991).
- [22] Latinne, O., et al., Terao-Dunsheath, C.J. Joichain, P.G.Burke, C.J.Noble Phys. Rev. Lett.74 (1995) 46.
- [23] Cyr, A., Latinne O., and Burke P.G., J.Phys.B 30: 659(1997).
- [24] STANCALIE, V., Physics of Plasmas 12, 043301 (2005)
- [25] STANCALIE, V., Physics of Plasmas 12, 10075 (2005).
- [26] STANCALIE, V., Laser and Particle Beams, 27 (2009) 345.
- [27] STANCALIE, V., Nuclear Instruments and Methods in Physics Research Section B: Beam Interactions with Materials and Atoms, Volume 267 (2009) 305.
- [28] STANCALIE, V., RACHLEW, E., 2002, Physica Scripta 66(2002)444.
- [29] STANCALIE, V., BURKE, M., SUREAU, A., Phys. Scr. 59 (1999)52.
- [30] STANCALIE, V., Phys. Scr. 61(2000) 459.

# DIRECT DRIVE IGNITION STUDIES FOR LARGE SCALE LASER FACILITIES

V. TIKHONCHUK  
CELIA, University Bordeaux  
Talence cedex, France

## Abstract

This report presents the final part of studies conducted in the framework on the CRP Research Agreement No. 14003 in 2008 – 2010. It concerns the target design studies accomplished by the members of Institut Lasers et Plasmas (ILP) partially under the European collaboration within the HiPER project and the Euratom program "Keep-in-Touch" activities.

## 1. INTEGRATED SIMULATIONS OF IGNITION SCALE FUSION TARGETS FOR THE IFE REACTOR (HIPER) PROJECT

The fast ignition of the compressed fuel with the electrons injected from the tip of the re-entrant cone presents the baseline scheme considered in the framework of the HiPER project. In the present report we discuss the ignition conditions obtained in integrated simulations of fusion targets with a re-entrant cone. Three major parts of this scheme are: the fuel assembly with a nanosecond laser pulse, fast electron acceleration with a high intensity picosecond laser pulse in the cone tip, and the core heating by fast electrons. The fuel assembly is modeled with one- and two-dimensional (2D) radiation hydrodynamic codes. Fast electron acceleration in the cone is simulated with a 2D planar particle-in-cell (PIC) code. The fast electron transport and the fuel ignition are described self-consistently with a 2D cylindrical electron hybrid code coupled to hydrodynamics. It is found that major problem of electron acceleration at laser intensities  $\sim 10^{20} \text{ W cm}^{-2}$  is related to the front rippling at the cone tip. It generates strong magneto-static fields producing a large electron beam divergence. Fuel ignition at acceptable values of the ultra-high intensity (UHI) laser pulse energy requires a substantial reduction of the electron beam divergence, which remains unresolved problem at the moment [1, 2].

The entire modeling is conducted in three steps. First, we design the fuel assembly with special attention to the high value of the areal density and the integrity of cone tip during the compression phase. Simulations are performed with the 1D/2D radiation hydrodynamic code SARA accounting for the cone deformations under the pressure of the collapsing shell. Second, fast electron acceleration by a UHI laser pulse in a cone is studied with 2D PIC simulations without collisions. The pre-plasma generated by the ASE laser pulse was neglected as we are concerned by a reference calculation in the ideal case. The double cone geometry is considered with a thin vacuum slit in the cone walls providing a better electron guiding towards the cone tip. Third, the fast electron transport and energy deposition are studied with a hybrid code coupled to 2D hydrodynamics.

The re-entrant cone can be seriously damaged during the deuterium-tritium (DT) shell implosion and compression due to the shock wave and plasma jet produced when the shell collapses at the center. In order to decrease the jet velocity and the shock pressure at stagnation, we have designed a target with an implosion velocity of  $200 \text{ km s}^{-1}$ , significantly lower than that of the HiPER reference target. The absorbed power pulse is designed such as all shocks are weak and arrive at the inner shell surface equally spaced in time. The 1D hydrodynamic simulation of the spherical shell implosion is carried out until the moment when the peak kinetic energy of the shell is attained. Then, the density, internal energy and velocity profiles are remapped onto a 2D cylindrical mesh with the gold double cone inserted,

and the hydrodynamic simulation was continued with the 2D code until the peak value of the areal density  $\rho R$  is achieved. We suggest an asymmetric fuel implosion to mitigate the cumulative jet formation, to delay the cone tip destruction and to optimize the mass distribution of the compressed core. This is modeled by setting a polar angle dependent implosion velocity at the remapping time. The same effect can be obtained also by a polar variation of the initial shell thickness. Assuming a  $\cos\theta$  (the first Legendre polynomial, P1) asymmetry of the implosion velocity, the most favorable configuration of the compressed core is obtained when the maximum velocity is 10% over the average at the cone walls. Figure 1 (left) demonstrates the density distribution of the compressed fuel at the moment of stagnation, when the hot electrons were injected from the cone tip.

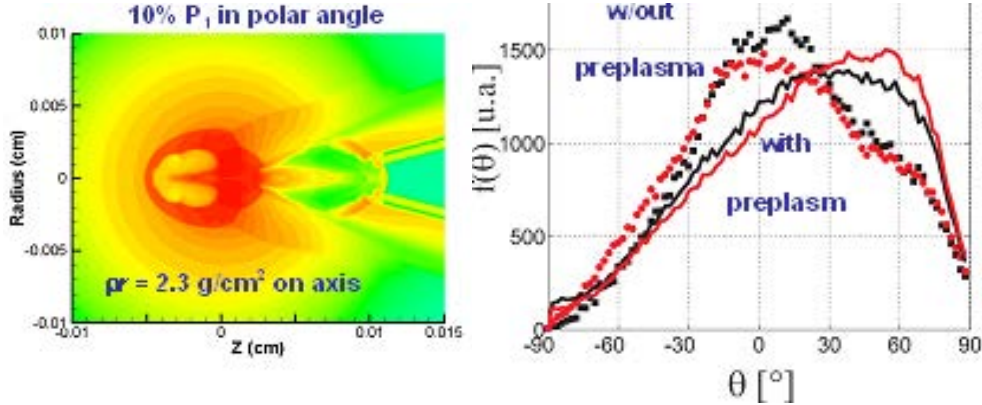


FIG. 1. Left: density distribution in the compressed fuel before launching the electron beam. Right: electron beam angular distribution in the source region.

The characteristics of the electron beam launched inside the double cone at the time of peak  $\rho R$  have been estimated quantitatively by PIC simulations assuming the laser pulse maximum intensity  $2 \times 10^{20} \text{ W cm}^{-2}$ , the wavelength of  $1 \mu\text{m}$ , and the pulse duration of 1 ps. The latter was limited by the performance of the PIC code. Although it is shorter than the pulse duration needed for fuel ignition, it is sufficient for analysis of fast electron characteristics. The distribution on angles of accelerated electrons is characterized by two parameters: the dispersion angle and the radial velocity, see Figure 1 (right). The dispersion of electrons is due to the small-scale magnetic fields self-generated by electron current behind the acceleration zone, while the radial beam velocity induced by the laser ponderomotive force. The total angular width of the electron distribution with respect to the propagation axis is  $55^\circ$ , and we did not succeed to reduce it. The electron energy spectrum in the range between 250 keV and 2.5 MeV is characterized by a Gaussian function with the temperature  $\sim 1 \text{ MeV}$ . The laser-to-electron conversion efficiency is  $\sim 35\%$  if one accounts for the electrons with energies above 100 keV [2].

The fast electron parameters obtained by PIC simulations were then used as the input parameters for ignition simulations with the electron transport code. The damaged cone tip has been artificially removed from the simulation box to avoid the scattering of fast electrons and the magnetic defocusing caused by resistivity gradients. The electron transport is affected by the large scale magnetic field focusing, small scale filamentation and scattering of fast electrons in dense plasmas. The electron initial divergence of  $55^\circ$  suppresses the magnetic field and inhibits the beam collimation. Consequently, the laser pulse energy required for ignition increases above the acceptable level of 100 kJ. Fuel ignition at the electron beam energy level of 40 kJ can be achieved only if the initial beam divergence can be reduced to the

level less than  $35^\circ$  [1]. Possible mechanisms of the beam divergence reduction are under investigation.

## 2. FAST ION IGNITION WITH ULTRA-INTENSE LASER PULSES

The analytical model developed recently [3] and numerical simulations demonstrate that laser pulses with intensities exceeding  $10^{22} \text{ W cm}^{-2}$  may penetrate deeply into the plasma and accelerate efficiently ions in the forward direction. We proposed a new scheme for fast ignition of pre-compressed DT fusion targets with fast ions by using two laser pulses. The first pulse (or a sequence of several pulses) creates a channel with diameter  $\sim 30 \mu\text{m}$  through the plasma corona up to the fuel density  $\sim 1 \text{ g cm}^{-3}$ . The second pulse with a higher intensity accelerates the deuterium and tritium ions at the head of this channel. The overall laser pulse energy required for ignition could be at the level of 100 kJ.

The laser ponderomotive force provides an efficient ion acceleration in bulk dense targets and evacuates a channel enabling further laser beam propagation. A quasi-stationary model of a laser piston predicts the general parameters of the acceleration process in one-dimensional geometry. The particle-in-cell (PIC) simulations confirm the estimated characteristics in a wide range of laser intensities and ion densities and show advantages of circularly polarized laser pulses compared to linear polarization. The characteristics of channel formation and the angular distribution of accelerated ions are found from two-dimensional PIC simulations [3]. This model and integrated numerical simulations are used for design of a new scheme of ion fast ignition [4].

The proposed ignition process proceeds in two stages. Similarly to the scheme of the electron fast ignition, the first laser pulse creates a channel through the plasma corona and the second pulse accelerates the deuterium and tritium ions in the bottom of this channel. The hole boring process itself can be also divided in two steps. For hole boring in an underdense plasma one can utilize a laser pulse of an intensity  $\sim 10^{21} \text{ W cm}^{-2}$ , and our estimates show that a 1 mm deep hole can be produced in 3 ps with the laser power of 3.5 PW. The hole boring in the overdense plasma requires higher intensities, at least  $3 \times 10^{21} \text{ W cm}^{-2}$  and it may take more than 10 ps to create a channel up to densities around  $1 \text{ g cm}^{-3}$  where ions serving for ignition can be accelerated efficiently. The ignition process has been studied by using three different designs of fusion targets. One of them is a relatively small all-DT target designed for the HiPER project, other two targets of a larger size, they are more adapted for a future fusion energy plant. The integrated numerical simulations of the ignition and combustion processes were conducted with the radiation hydrodynamic codes CHIC and DUED combined with the modules of ballistic ion transport.

The baseline HiPER target at the stagnation moment consists with a  $25 \mu\text{m}$  thick shell of the mean density of  $400 \text{ g cm}^{-3}$  at a distance of  $50 \mu\text{m}$  from the center. This target requires 200 kJ of the laser energy for compression. In our simulations, it was ignited with the laser pulse of intensity  $9.3 \times 10^{21} \text{ W cm}^{-2}$  focused in the spot of the radius of  $23 \mu\text{m}$  in the plasma at the density of  $1 \text{ g cm}^{-3}$ . The acceleration zone of a length  $30 \mu\text{m}$  is located at the distance  $60 \mu\text{m}$  from the shell. In the example shown in Figure 2, 20 kJ (73%) of the ion energy is dumped to the dense shell and 23% is deposited along the ion path between the acceleration zone and the dense shell. The laser pulse power is 150 PW and the corresponding laser energy amounts to 350 kJ. The released fusion energy is 8.5 MJ, corresponding to an energy gain of about 15. The ignition process in this example is not optimized because the shell is too thin and consequently too much energy is lost for expansion of the heated region. The fusion

reactions are stagnated at a low level first 20 ps after the ion energy deposition, and the ignition occurs when the exploded part of the shell collides with the opposite, cold part.

The use of thicker shells imploded at a lower velocity may significantly increase the shell areal density at stagnation and improve the ignition performance. These targets could be ignited with laser energy of 100 kJ and a power of 30 PW. These estimates were confirmed by considering the ignition of heavier targets with a higher areal density [4].

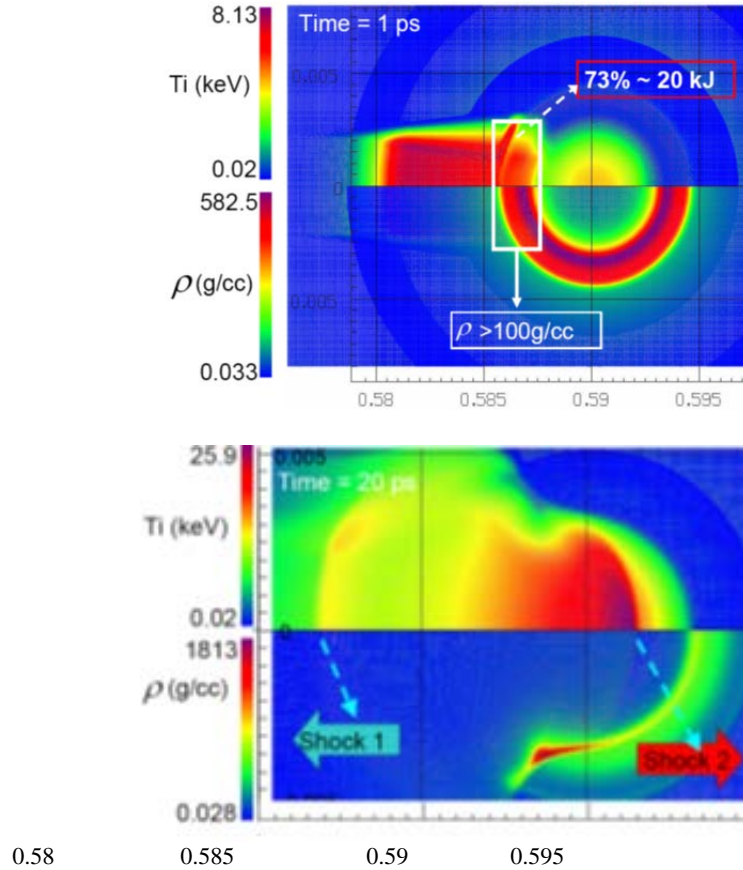


FIG. 2. Temperature (upper part) and density (lower part) distributions in the HiPER target at the time of 1 ps, when ions deposited their energy (left) and at the time of 20 ps, when the ignition occurs (right).

### 3. THEORETICAL STUDIES FOR SHOCK IGNITION

#### 3.1. Gain curves and hydrodynamic modeling for shock ignition

Shock ignition is a highly attractive path to the ignition of DT pellets at a low implosion velocity [5]. That scheme reduces risks of the shell breakup during acceleration and allows compressing larger masses for the same laser energy. Ignition is triggered by a strong shock launched at the end of the coasting phase of the implosion. The shock is obtained by means of a laser pulse of the intensity  $\sim 10^{16} \text{ Wcm}^{-2}$  applied just before the moment of stagnation. Shock ignition produces a non isobaric fuel assembly, where the central hot spot is driven to a significantly higher pressure than the surrounding cold fuel. We revisited the conditions for non isobaric ignition by using the Rosen-Lindl gain model [6]. The gain curves are shown in Figure 3 for the values of the parameter  $\varepsilon = P_{\text{iso}}/P_{\text{shock}}$  that characterizes the pressure in the hot spot  $P_{\text{shock}}$  compared to the pressure  $P_{\text{iso}}$  achieved at isobaric compression. The ignition threshold may be lowered significantly when the non-isobaric parameter  $\varepsilon$  decreases. Gains of 150 are expected at 1 MJ of laser energy and gains of 75 are achievable at the level of 200 kJ.

These estimates provide a strong incentive for the inertial fusion energy demonstrators such as considered in the HiPER project.

A high central pressure in the shock ignition scheme is due to the radial convergence and the collision of the second shock with the rebound shock propagating outward. The shock matching conditions are depending on the shell implosion velocity, which in turn depends on the laser intensity and the target mass. Figure 4 shows the required intensity in the laser spike as a function of the shell implosion velocity, for different values of the target mass and laser energies. These curves define an operating domain for the shock ignition scheme, limited by the hydrodynamic instabilities at high implosion velocities, and parametric instabilities at high laser intensities.

The conceptual design of shock ignition has to be confronted to experiments. A first series of implosions was performed at the Omega laser facility in 2009. They involved implosions of microspheres with and without a final shock. The numerical simulations of the experimental data using the radiative hydrodynamic code CHIC succeeded in restituting the absorbed energy, shock timing, areal mass and burn temperature. The absolute neutron yield was not restituted yet, in the absence of the fuel mix modeling in the CHIC. An international joint application is submitted to the LLNL with the goal of fielding shock ignition experiments on the NIF facility in a 4-5 years future.

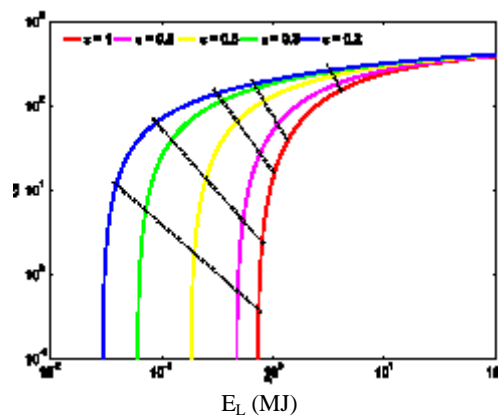


FIG. 3. Gain curves obtained from the model for different values of the non isobaric parameter. Conventional ignition corresponds to  $\epsilon = 1$ .

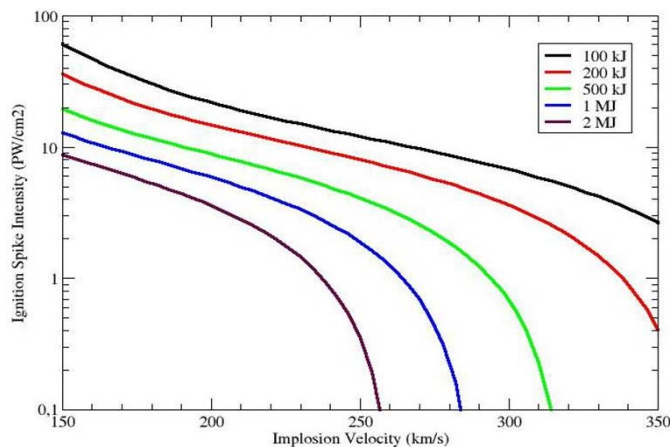


FIG. 4. Intensity of the ignition spike (in units of  $PW\ cm^{-2}$ ) as a function of the implosion velocity (km/s) for the laser compression energies from 0.1 to 2 MJ.

### 3.2. Particle-in-cell simulations of laser–plasma interaction for the shock ignition scenario

The hydrodynamic simulations discussed above demonstrate that the shock ignition is a relatively robust scenario with regard to hydrodynamic instabilities and time synchronization. However, the intensity of the ignition pulse is above  $10^{16}$  W cm<sup>-2</sup>, which is significantly higher than the intensity of compression pulses for directly driven fusion, and nonlinear phenomena in the laser–plasma interaction cannot be avoided. The most important nonlinear processes in this context are three-wave parametric instabilities: stimulated Raman (SRS) or Brillouin (SBS) scattering, two plasmon decay (TPD) and filamentation instability. They can undermine the laser pulse absorption in several ways: the scattered laser light from a low density plasma due to the SBS increases the total reflectivity; the generation of plasma waves associated with the SRS may result in the transformation of a large amount of energy into electron beams with energy much higher than the thermal energy of the surrounding plasma; finally, the absorption may take place in the underdense plasma far from the critical surface, and the transport of energy to the denser plasma may be suppressed. Fortunately, the preheat of a precompressed fuel by fast electrons is a less important issue in the shock ignition context, because the ignition pulse is applied at the end of the implosion phase and the shell areal density is sufficiently high to ensure stopping and absorption of most of the hot electrons. Nevertheless, it is important to understand the nonlinear processes involved in the interaction of the ignition laser pulse with the large scale coronal plasma and the interplay between these processes under the particular conditions of shock ignition characterized by a large density scale length and plasma temperatures of several kiloelectronvolts in the corona.

In order to quantitatively characterize the laser energy absorption, we run fully kinetic simulations of the laser pulse interaction with an inhomogeneous, large size, high temperature plasma. The laser pulse intensity,  $10^{16}$  W cm<sup>-2</sup>, plasma temperature, 5 keV, and the density scale length of  $300 \mu\text{m}$  correspond to the conditions of the shock ignition scenario. The simulations were performed with the 1D3V PIC code on the time scale up to 100 ps. The energy conservation was assured with a high precision. It was demonstrated that after a short initial burst of backscattering, a significant part of the incident laser radiation is absorbed in the underdense plasma and the energy is transported to the dense plasma by electrons with energies 20–40 keV. The absorption mechanism is associated with a self-organized wave resonator and cavitation of large-amplitude plasma waves in the density range below the quarter critical density.

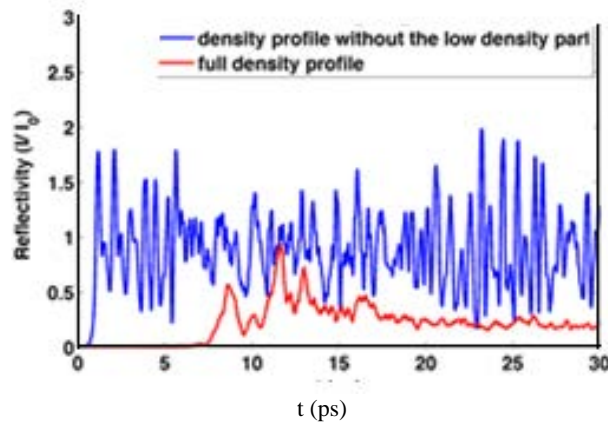


FIG. 5. The reflectivity in relative units with respect to the maximum incident laser pulse intensity resulting from the SBS and SBS+SRS simulations plotted vs time.

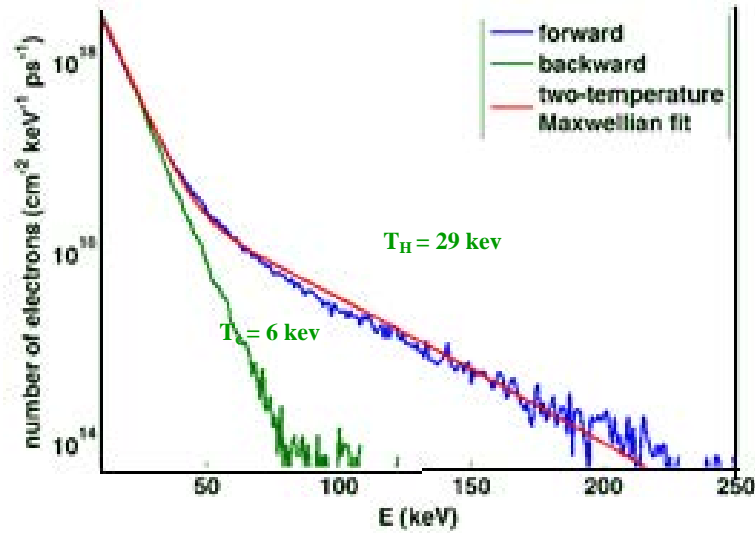


FIG. 6. Temporally averaged energy distribution of the forward and the backward propagating electrons crossing the reference point at the rear boundary.

According to the gain analysis, the SRS should be the dominant process under the conditions of our simulations, while the SRS can take place only in the vicinity of the quarter critical density. For this reason, we first considered a dense plasma layer with the density varying from 0.3 to 1.1 of the critical density. Then the SRS signal dominates the frequency spectrum and it contains about 80% of the entire backscattered energy. The temporal evolution of reflectivity resulting in our simulations is plotted in Figure 5 (blue curve). The reflected signal is integrated over the whole frequency domain. It shows an irregular series of relatively short (less than a picosecond long) bunches with intensity often exceeding the laser intensity.

The results obtained with the full density profile are substantially different, which is clearly seen in Figure 5, where they are plotted in red. Only about 30% of the energy of the reflected light is now contained in the SRS peak, whereas the energy content in the spectral range of SRS ( $0.5-0.8 \omega_0$ ) is about 46%. Our results demonstrate that a high temperature, large scale plasma could provide an efficient collisionless absorption of high intensity laser radiation. A detailed examination of the interaction process reveals that the laser energy is absorbed in narrow, deep density cavities that are created and maintained by two coupled SRS processes forming a self-organized resonator between the zones of  $1/4$ th and  $1/16$ th of the critical density, which are the resonance points for the primary and secondary absolute SRS instabilities. This particular form of plasma response was not seen before, because such specific plasma conditions were not sufficiently explored. The high initial plasma temperature suppresses the SRS development everywhere in plasma with the exception of the resonant point where SRS grows as an absolute parametric instability. A particular combination of strong Landau damping of plasma waves and their localization provokes the plasma cavitation and an efficient laser energy conversion in the flux of moderately energetic electrons shown in Figure 6.

These results indicate rather favourable conditions of the shock ignition scenario. A large absorption coefficient exceeding 70% and a Maxwellian spectrum of hot electrons with a temperature less than 30 KeV are expected to create a high amplitude shock wave near the

ablation surface in the fusion target. The detailed studies of the energy transport by energetic electrons and the ablation pressure formation are under way.

#### 4. CONCLUSIONS.

In a more general sense, our simulations demonstrate an importance and a large innovative potential of large scale kinetic modeling. The first experiments on the shock ignition that were conducted on the Omega laser facility in 2009 demonstrated a laser absorption coefficient that is in agreement with our simulations. Such a specific regime of interaction cannot be seen in smaller plasmas or in short time simulations. The zone of  $1/16$ th of the critical density needs to be described in detail as well and the zone of  $n_c/4$  and some space need to be reserved in order to make the wave propagation and adjustment of phase resonance conditions possible. Moreover, the synergy between two SRS processes is accompanied by their destructive effect on the SBS performance.

#### REFERENCES

- [1] DEBAYLE, A., et al., J. Integrated simulations of ignition scale fusion targets for the HiPER project, Journ. Phys.: Conf. Series (2010).
- [2] DEBAYLE, A., et al., A new interpretation of the divergence of laser-driven relativistic electron beams, submitted to Phys. Rev. Lett. (2010).
- [3] NAUMOVA, N., et al., Hole boring in a DT pellet and fast-ion ignition with ultraintense laser pulses, Phys. Rev. Lett. 102, 025002 (2009).
- [4] TIKHONCHUK, V.T., et al., Fast ion ignition with ultra-intense laser pulses, Nucl. Fusion 50, 045003 (2010).
- [5] RIBEYRE, X., et al., Shock ignition: an alternative scheme for HiPER, Plasma Phys. Control Fusion 51, 015013 (2009).
- [6] SCHURTZ, G., RIBEYRE, X., and LAFON, M., Target design for shock ignition, Journ. Phys.: Conf. Series (2010).
- [7] KLIMO, O., et al., Particle-in-cell simulations of laser-plasma interaction for the shock ignition scenario, Plasma Phys. Control. Fusion, 52 (2010).
- [8] M. LAFON, X. RIBEYRE, and G. SCHURTZ, Gain curves and hydrodynamic modelling for shock ignition, Phys. Plasmas 17, No.5 (2010).

# TARGET AND CHAMBER TECHNOLOGIES FOR DIRECT DRIVE LASER INERTIAL FUSION ENERGY (IFE)

M.S. TILLACK, A.R. RAFFRAY, F. NAJMABADI, L.C. CARLSON  
University of California San Diego  
La Jolla, USA

## Abstract

We report our progress on bench top target “engagement”, which includes tracking, beam steering and verification of accurate illumination. Using room-temperature capsules with prototypical size and mass, we made several system improvements to reduce the total engagement errors to approximately 40  $\mu\text{m}$  rms. We also report on our recent efforts to develop design solutions for dry-wall chambers using direct drive targets, which must somehow manage the intense ion bursts while simultaneously protecting the delicate targets. Several concepts for magnetic diversion of ions in low-pressure chambers have been explored.

## 1. INTRODUCTION

The University of California at San Diego maintained an active program of research on inertial fusion energy (IFE) technology for the duration of the IAEA Coordinated Research Program. Progress was made in two principal research areas:

- Target engagement. We developed and demonstrated systems to track direct-drive targets in flight and to steer simulated driver beams onto the targets with the precision required for target ignition. Bench-top experiments were performed in order to demonstrate the feasibility of these systems and to characterize their performance.
- Chamber design studies. We developed chamber design concepts that integrate armor and structural material choices with a blanket concept providing attractive features of design simplicity, fabrication, maintainability, safety and performance (when coupled to a power cycle). Advanced concepts (including magnetic intervention) that could result in smaller less costly chambers, better armor survival and lower cost of electricity also were investigated.

## 2. TARGET ENGAGEMENT

A significant challenge for the successful implosion of direct-drive inertial fusion energy targets is the repeated alignment of multiple laser beams on moving targets with accuracy on the order of 20  $\mu\text{m}$ . Adding to the difficulty, targets will be traveling up to 100 m/s through a chamber environment that may disturb their trajectories. As part of the High Average Power Laser (HAPL) program, we developed a target tracking and engagement system that is capable of meeting the goals for an inertial fusion power plant. The system consists of separate axial and transverse target detection techniques and a final correction technique using a short pulse laser to interrogate the target’s position 1–2 ms before a chamber center. Steering mirrors are then directed to engage the target at the chamber center.

The three main subsystems are shown in Figure 1 and described in more in detail in [1]. First, a laser-based continuous tracking system sights along the target’s flight path and uses position information from the target’s Poisson spot to determine the target’s transverse position. Second, a system using discrete crossing sensors provides the necessary timing to trigger a glint laser, driver beam laser, coincidence camera, and a verification camera. Finally, a short pulse glint laser illuminates the target a few milliseconds before it reaches chamber center, thus using the glint return from the target itself as the final reference point for aligning the driver beams immediately before engagement. In the pre-steering scenario described

in [2], information from the Poisson spot pre-steers the mirror to take up any gross position errors, while the glint system makes the final, small steering correction.

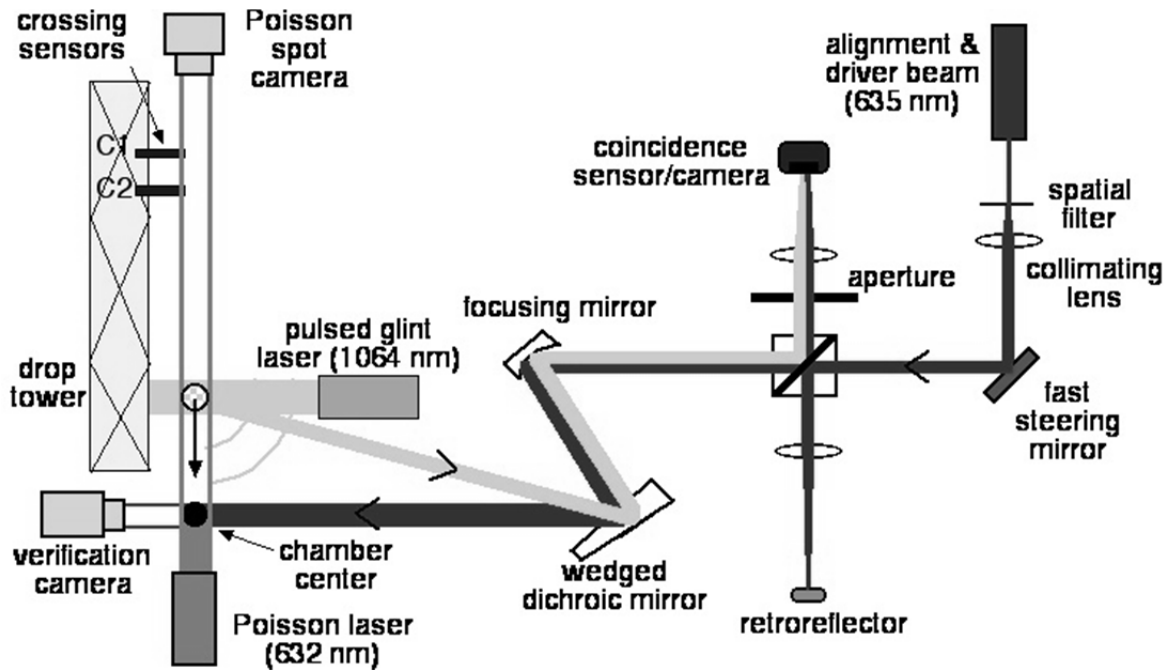


FIG. 1. Schematic of integrated target tracking and engagement demonstration. Focusing mirror to chamber center is 2 m, drop tower is ~2 m tall. (Figure not to scale).

Over the past several years, we constructed and improved upon an integrated tabletop demonstration operating at reduced speeds and path lengths. In August 2007, initial engagement accuracy of moving targets in air using a simulated driver beam was 150- $\mu\text{m}$  rms. Since then, we have taken an encompassing look at all error sources that contribute to the overall engagement error. By focusing on those individual component errors that have the most influence and improving their accuracy, we have substantially reduced the overall engagement error. Table 1 shows the major contributors to error and their individual improvements from 2008 to 2009, resulting in the current aggregate rms error of 34  $\mu\text{m}$ . Figure 2 depicts the stepwise improvement in engagement accuracy as a result of various changes and improvements made to the apparatus and experimental techniques. Future effort will focus on understanding the effect of thermal fluctuations on the experiment and the drifting of the calibration. The engagement of lightweight targets is the next highest priority.

A question that arises concerning the promising engagement precision achieved on the tabletop demonstration is the applicability and scalability to that of a full-scale IFE system. As noted, most of our remaining errors identified in Table 1 arise from sources that are expected to scale well to the increased distances required for an IFE power plant. Engagement still must be demonstrated at prototypic, full-scale chamber distances (17 m rather than 1.5 m). Scaling the injection velocity from 5 m/s to 50-100 m/s will require an injector with a clear sight down the trajectory, faster target positioning measurements, and faster steering mirror positioning. Faster cameras and real-time processing are feasible with current technology, at a higher cost than the demo. However, positioning full-scale steering mirrors in the available time will be more difficult and must be demonstrated. The effect of possibly

turbulent high-speed chamber gas on target trajectory must also be anticipated and better understood. The path forward looks promising and attainable but is not without challenges.

TABLE 1. ERROR CONTRIBUTION LIST

Subsystem	Oct. 2008 Errors ( $1\sigma$ )			April 2009 ( $1\sigma$ )		
	X ( $\mu\text{m}$ )	Y ( $\mu\text{m}$ )	Z ( $\mu\text{m}$ )	X( $\mu\text{m}$ )	Y( $\mu\text{m}$ )	Z( $\mu\text{m}$ )
Poisson spot centroiding	(18)	(15)	6	(2)	(3)	1
Glint return	2	-	3	4	-	4
Verification algorithm	5	-	4	(4)	-	(4)
Mirror pointing	12	-	12	3	-	5
Timing prediction	-	-	35	-	-	(20)
Transverse target motion	24	(24)	10	5	(7)	5
Target diameter variation	3	(3)	3	4	(4)	4
Dynamic steering mirror	-	-	-	5	-	5
Calibration drift/error	-	-	-	12	-	12
Target eng. error (rms, compiled)	27	-	38	15	-	16
Target eng. error (rms, observed)	30	-	29	24	-	24
Total eng. error (total rms, observed)	42 $\mu\text{m}$			34 $\mu\text{m}$		

All errors converted to *target space*, errors in () do not contribute to the compiled error, Z-axis is axial to the target's trajectory, X and Y axis are transverse.

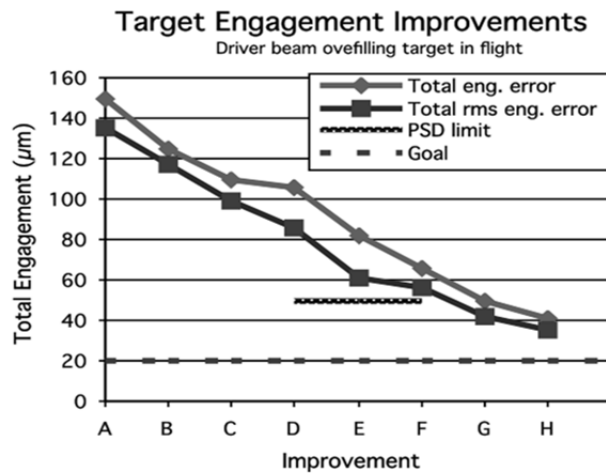


FIG. 2. Step-wise improvement graph with effect on overall target engagement results.

- A. initial setup, 4:1 magnification, defocused glint return
- B. focused glint return
- C. focused glint return, small aperture
- D. 1:1 magnification
- E. 1:1 mag., improved steering calibration, glint camera replaces PSD
- F. stable beamsplitter, small steering
- G. vacuum chamber installed
- H. thermal drift eliminated with on-the-fly calibration, vacuum chamber
- I. electrical noise reduced
- J. target surfaces scrutinized for imperfections

### 3. CHAMBER DESIGN STUDIES

The High Average Power Laser (HAPL) program is focused on the development of laser IFE power plants based on lasers, direct-drive targets and dry wall chambers [3]. As part of this program, we looked at the key issue of survival of the chamber wall under the ion threat spectra (representing ~25% of the yield energy and shown in Figure 3 for a 350 MJ direct drive target [4]). The ions would deposit their energy in the dry wall, which must accommodate the high cyclic temperature levels and gradients. Use of refractory metals such as tungsten as armor can provide the possibility to accommodate the thermal effects of the high-energy deposition with a large enough chamber size [5]. However, a major concern is the possible accumulation of helium from ion implantation. Helium migration in tungsten is slow and the concern is that a build-up of helium could result in local armor failure. For that reason, an engineered armor making use of nano-structured W with low porosity was investigated [5]. It provides a short pathway for the implanted He to diffuse to the interconnected porosity and be released back to the chamber. Initial results on the He release are encouraging (when compared to the release from sintered W with larger microstructure). A parallel R&D effort was launched to assess the He behavior as well as the thermo-mechanical behavior of such an armor under representative laser IFE conditions.

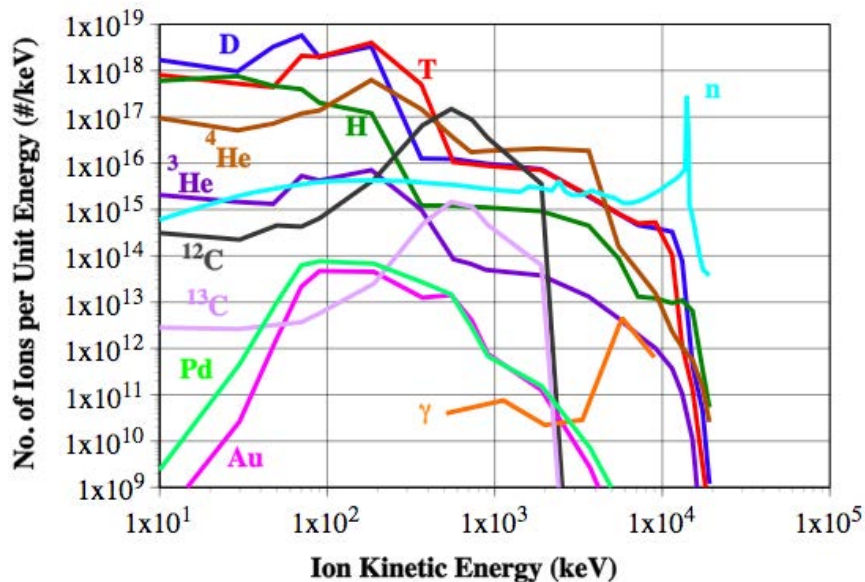


FIG. 3. Ion spectra for HAPL 350 MJ direct drive reference target [4].

In parallel, an effort was launched to investigate the possibility of steering the ions away from the chamber to specially designed dump chambers using magnetic intervention [6]. Options include a simple cusp configuration as well as a bell cusp configuration [7]. In the simple cusp configuration, the ions are contained within the magnetic bottle for, typically, 10-20 bounces after which they leak out of the chamber through a toroidal slot and holes at the poles, where they are directed to specially-designed large-area collectors, as shown in Fig. 4. A biconical chamber configuration was developed to match the shape taken by the expanding plasma in the cusp field, as illustrated in Figure 5. Ion dump plates are shown schematically within the chamber at the equator, through which most of the ions escape, and at the poles.

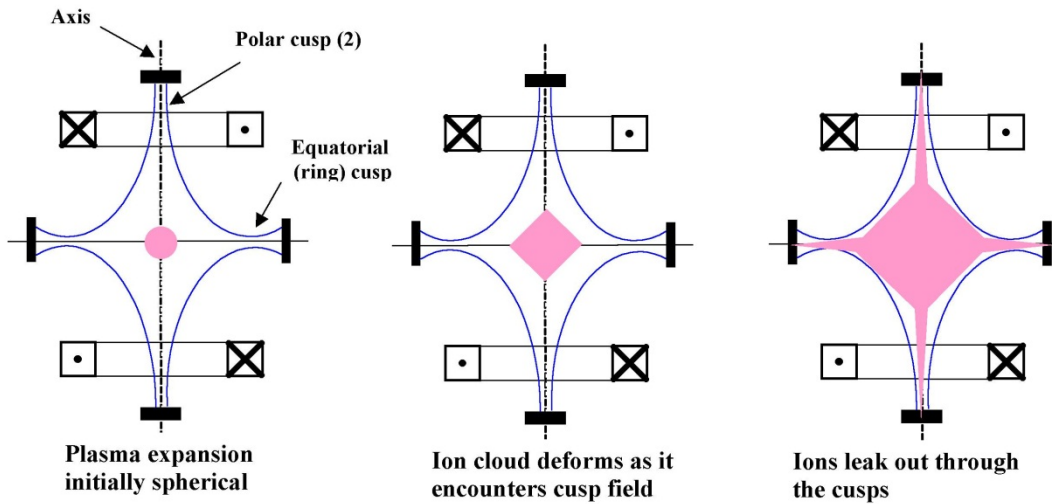


FIG. 4. Simple cusp magnetic configuration.

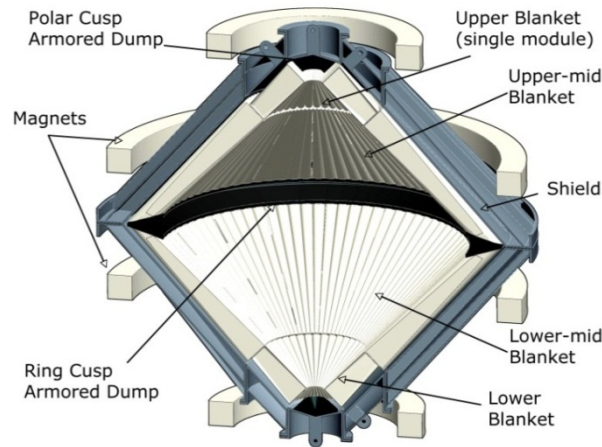


FIG. 5. Biconical chamber for simple cusp configuration [8].

In addition, to reduce the ion flux on the dumps the possibility of using magnetic dissipation in a resistive blanket was explored. A self-cooled liquid breeder blanket concept was developed for this configuration consisting of a number of  $\text{SiC}_f/\text{SiC}$  submodules arranged poloidally in the chamber. Both Pb-17Li and Flibe were considered as candidate liquid breeder. The concept allows for high outlet liquid breeder temperature (1000 C or higher) and, thus, high power cycle efficiency (50-60%) depending on chamber size and  $\text{SiC}_f/\text{SiC}$  properties and temperature limits). The study also included a preliminary integration of the chamber within a reactor including all key systems such as the shield, magnet, vacuum pumping and supports [8]. Although resistive dissipation of >50% of the ion energy seemed possible, there were concerns about the high voltages generated between the blanket modules.

As long as the ions are deposited on solid materials, problems of ion damage and in particular helium retention remain, although now transferred from the chamber wall to an external location where they might be better accommodated. This led to the consideration of liquid dumps in subsequent concepts.

Steering the ions away to a separate dump chamber brings up the intriguing possibility of utilizing a liquid wall to accommodate the ion fluxes provided the right measures are taken to prevent the liquid from contaminating the main chamber. Such measures would include a curved duct geometry to prevent line-of-sight vapor transmission from the dump chamber to the main chamber as well as a condensation trap towards the port junction to the main chamber.

For example, use of a bell cusp was considered, whereby the field in the polar cusps is made as large as practicable so as to direct almost all the ions out of the equatorial cusp. By suitably shaping the field these ions can be directed through a curved duct into an external dump chamber. This configuration is particularly suited to a liquid wall, such as in the case of an oozing dump target. Under the ion energy deposition, the liquid surface would evaporate and then condense on the interior walls of the dump chamber. By avoiding line of sight between the dump surface and the main chamber, the amount of vapor entering the main chamber is negligible and transmission of droplets completely eliminated. Such a bell cusp arrangement, approximately to scale, is shown in Figure 6.

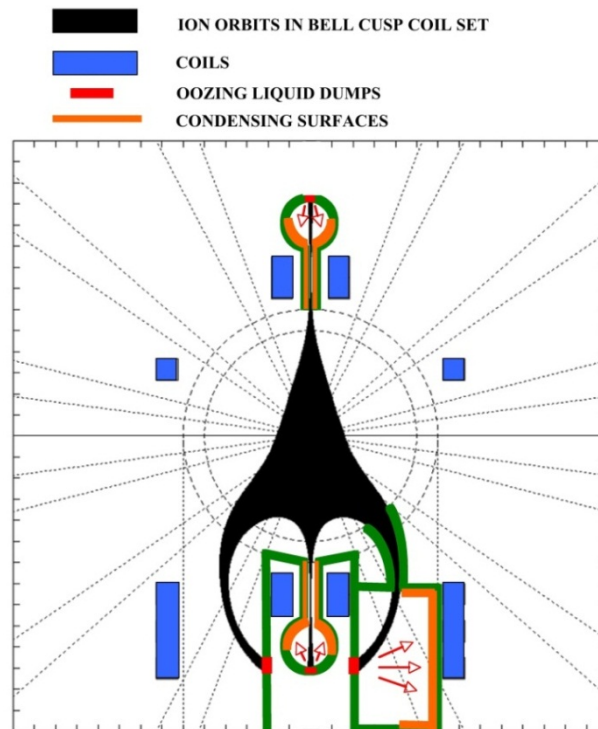


FIG. 6. Schematic of bell or tulip cusp showing the ion trajectory through the port, the evaporation from the liquid dump and the condensation surfaces (the scale is in m with a main chamber radius of 5 m) [7].

Evaporation and condensation studies of the working fluid in the condensation chamber were performed [7]. Different fluids were assessed, including Pb, Sn and Ga. However, other factors including material compatibility would need to be considered before finalizing the design choice. Based on the analysis, condensation was found to be fast with the vapor pressure of Sn (for a 1100 C vapor temperature case) decreasing to 0.076 Pa (0.57 mTorr) after 0.2 s, close to the vapor pressure of Sn at 1010 C, ~0.04 Pa (0.3 mTorr). Similar results were obtained for Ga and Pb also. However, they are based on a simple, albeit conservative, model and would need to be confirmed through more detailed R&D.

#### 4. CONCLUSIONS

Preliminary chamber layout consideration indicated the possibility of blanket coverage meeting the key nuclear requirements [8,9]. Although this initial assessment is encouraging, a more detailed study is required to obtain a better picture, including details of the liquid wall configuration in the dump chamber and of the mass transfer processes, of material compatibility under the operating conditions, of the design of the small polar condensation chambers, and a better assessment of possible contamination of the main chamber through both the dump and laser ports.

#### REFERENCES

- [1] CARLSON, L. C., *et al.*, “Target tracking and engagement for Inertial Fusion Energy – a tabletop demonstration,” *Fusion Sci. Tech.* **52** No. 3 (Oct. 2007) 478-482.
- [2] CARLSON, L. C., *et al.*, “Improving the accuracy of a target engagement demonstration,” *Fusion Science and Technology* **56** (1) July 2009, 409-416.
- [3] SETHIAN, J., *et al.*, “An Overview of the Development of the First Wall and Other Principal Components of a Laser Fusion Power Plant,” *Journal of Nuclear Materials* 347 (December 2005) 161.
- [4] Available at: <http://aries.ucsd.edu/HAPL/DOCS/reftarget.html>.
- [5] RAFFRAY, A. R., BLANCHARD, J., LATKOWSKI, J., NAJMABADI, F., RENK, T., SETHIAN, J., SHARAFAT, S., SNEAD L., and the HAPL Team, “Progress Towards Realization of a Laser IFE Solid Wall Chamber,” *Fusion Engineering & Design* 81 (2006) 1627.
- [6] RAFFRAY, R., *et al.*, “Impact of Magnetic Diversion on Laser IFE Reactor Design and Performance,” Proceedings, 4th International Conference on Inertial Fusion Science and Applications, Biarritz, France, September 2005, *Journal de Physique IV*, 133, 845-848, June 2006.
- [7] RAFFRAY, A. R., *et al.*, and the HAPL Team, “Laser IFE Direct Drive Chamber Concepts with Magnetic Intervention,” *Fusion Science and Technology* 56 (1), 333-340, July 2009.
- [8] RAFFRAY, A. R., *et al.*, “Conceptual Study of Integrated Chamber Core for Laser Fusion with Magnetic Intervention,” Proceedings of the 22nd IEE Symposium on Fusion Engineering, 2007.
- [9] SAWAN, M. E., *et al.*, “Neutronics Analysis of a Molten Salt Blanket for the HAPL Laser Fusion Power Plant with Magnetic Intervention,” Proceedings of the 22nd IEEE/NPSS Symposium on Fusion Engineering, Albuquerque, NM, June 18-21, 2007 (CD-ROM).



# PROGRESS REPORT — PATHWAYS TO ENERGY FROM INERTIAL FUSION — AN INTEGRATED APPROACH

J. WOŁOWSKI, J. BADZIAK, T. PISARCZYK  
Institute of Plasma Physics and Laser Microfusion  
Warsaw, Poland

## Abstract

In the period August 2009 – May 2010 the team of Institute of Plasma Physics and Laser Microfusion in Warsaw have performed the following works within the IAEA Coordinated Research Project: 1) Simulations of proton generation driven by an intense laser pulse, 2) Investigations of mechanisms responsible for plasma jets formation by laser pulse, 3) Study of the new indirect method for two-step laser acceleration of the thin foil. The main objective of the works performed by the team of IPPLM in last period of IAEA\_CRP project, similarly like in previous periods, was to study the process of laser-driven proton beams, especially those produced by skin-layer ponderomotive acceleration (SLPA). Such protons can attain parameters relevant to fast ignition of a fusion target. This report presents the exemplary results of PIC simulations of this process. In the mentioned period the works connected with the laser-produced plasma jet formation and the laser driven macro-particles acceleration for ICF applications have been also realized in IPPLM.

## 1. SIMULATIONS OF PROTON GENERATION DRIVEN BY AN INTENSE LASER PULSE

### 1.1. Introduction

The proton fast ignition (FI) approach to ICF requires picosecond proton beams of intensity  $\sim 10^{20}$  W/cm<sup>2</sup> and current density  $\geq 10^{13}$  A/cm<sup>2</sup> [1,2, 3]. A very promising method of producing the ultraintense ion beams seems to be the method referred to as skin-layer ponderomotive acceleration (SLPA) [4]. In this method, the ponderomotive (radiation) pressure created by a short laser pulse near the critical plasma surface drives forward the plasma (ion) bunch of the ion density higher than the plasma critical density, thus of the density by a thousand times (or more) higher than in the case of target normal sheet acceleration (TNSA) [5], also proposed for proton FI.

In this report it is shown, by means of particle-in-cell (PIC) simulations, that an effective way to increase the SLPA contribution to the ion acceleration process is using short-wavelength ( $\lambda \leq 0.5$   $\mu\text{m}$ ) ps/subps laser pulses of even moderate values of  $I_L \lambda^2 \leq 10^{20}$  Wcm<sup>-2</sup>  $\mu\text{m}^2$ . It enables production of ultrashort ( $\leq 100$  fs), multi-MeV, SLPA-driven proton bunches of extremely high intensities ( $> 10^{21}$  W/cm<sup>2</sup>) and current densities ( $> 10^{14}$  A/cm<sup>2</sup>) probably not attainable by other ion acceleration methods known so far. The laser pulses required for this can be produced using existing or just developed high-power laser facilities.

### 1.2. Results and discussion

For the simulations, a fully electromagnetic, relativistic one-dimensional (1D) PIC code very similar to the well-known LPIC++ code [6] was used. Like in most PIC simulations of laser-driven ion acceleration [7] the collisional effects was neglected in the code, as at relativistic laser intensities and low-Z plasmas, the electron collision time is much longer than the laser pulse duration and non-collisional absorption dominates even for UV laser wavelength. Moreover, both for electrons of  $T_e \geq 100$  keV and protons of energy  $> 1$  MeV (our case) the collisional range in hydrocarbons like CH, CH<sub>2</sub> (realistic proton targets) is much longer than the target thickness. A linearly polarized laser pulse of quasi-Gaussian pulse shape interacted with an inhomogeneous, fully ionized hydrogen plasma layer of the density profile defined by the exponential front part (the preplasma layer) and the constant part of the maximum density and the thickness  $L_T$ . were considered in the simulations. Various target

thicknesses in the range 0.1 – 8 $\mu\text{m}$  and two values of  $n_{\text{max}}$  were also assumed for the simulation. The simulations were performed for laser pulses of the wavelengths corresponding to the first ( $1\omega$ ), second ( $2\omega$ ) and third ( $3\omega$ ) harmonic of Nd:glass laser, of duration from 0.35ps to 2ps and intensities up to about  $10^{21}\text{ W/cm}^2$ .

Fig.1 presents peak values of various parameters of proton beams, as a function of the  $I_L\lambda^2$ . Excluding the laser-protons energy conversion efficiency,  $\eta$ , the parameters of proton beams driven by the  $2\omega$  and  $3\omega$  laser beams are significantly higher than those for the  $1\omega$  beam and the highest values of these parameters are attained for the shortest laser wavelength. One of the reasons for such extreme values of these parameters is the high value of the plasma critical density at  $3\omega$  enabling ponderomotive acceleration of a very dense proton (plasma) bunch. However, at relativistic laser intensities the critical density depends on the laser field amplitude and the critical density for the  $3\omega$  beam approaches the target density and part of the beam is transmitted through a target and lost. It is the reason for a decrease in the conversion efficiency with an increase in  $I_L\lambda^2$  seen for the  $3\omega$  plot in Fig. 1a. This effect is not visible for the target of higher density equal to  $10^{23}\text{ cm}^{-3}$ . In this case, the conversion efficiency for  $3\omega$  increases with an increase in  $I_L\lambda^2$  and reaches the value even twice as high as that for  $1\omega$ . Like in the low-density-target case, the remaining proton beam parameters for  $3\omega$  are significantly higher than those for  $1\omega$ .

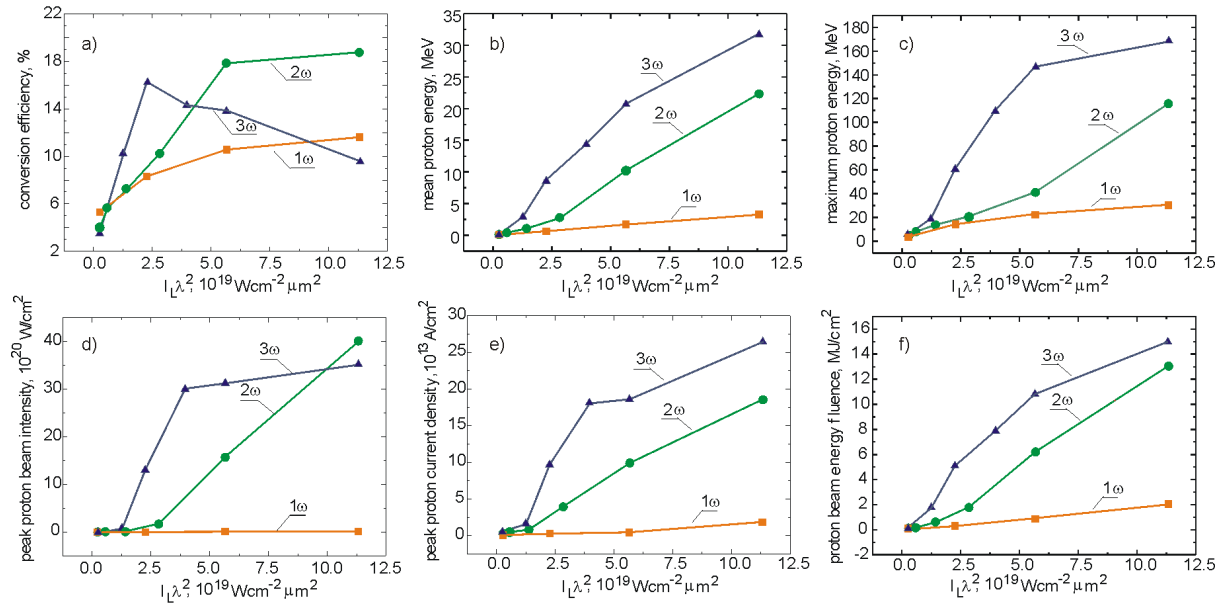


FIG. 1. Parameters of proton beams driven by laser pulses of different wavelengths (corresponding to the  $1\omega$ ,  $2\omega$  and  $3\omega$  beams of Nd:glass laser) as a function of  $I_L\lambda^2$ .  $L_T = 1\mu\text{m}$ ,  $L_n = 0.25\mu\text{m}$ ,  $\tau_L = 0.35\text{ ps}$ ,  $n_{\text{max}} = 4 \times 10^{22}\text{ cm}^{-3}$ .

The effect of the target thickness on the parameters of proton beams driven by laser pulses of different wavelengths but fixed values of the pulse duration (equal 1 ps) and the dimensionless laser amplitude ( $I_L\lambda^2 = 5 \times 10^{19}\text{ Wcm}^{-2}\mu\text{m}^2$ ) is shown in Figs 2 and 3. For the optimum target thicknesses, the conversion efficiencies are similar for  $1\omega$ ,  $2\omega$  and  $3\omega$  for both target densities, but the remaining parameters are considerably higher for the shorter wavelengths. Using short-wavelength ps laser pulses of  $I_L\lambda^2 \sim (0.5 - 1) \times 10^{20}\text{ Wcm}^{-2}\mu\text{m}^2$  makes it possible to produce ultraintense proton beams with high conversion efficiency from the targets of the thickness of a few tens of  $\mu\text{m}$ .

It is an important practical advantage of a short-wavelength driver from the point of view of a possible application of the accelerated proton beam in FI-related laser experiments. The shortening of laser wavelength at  $I_L \lambda^2 = \text{const}$  results in rather rapid diminishing of the TNSA efficiency while the SLPA efficiency remains fixed. As a consequence, when  $\lambda$  is sufficiently small (or  $I_L$  is sufficiently high) the contribution of TNSA to the ion acceleration process can be smaller than that of SLPA.

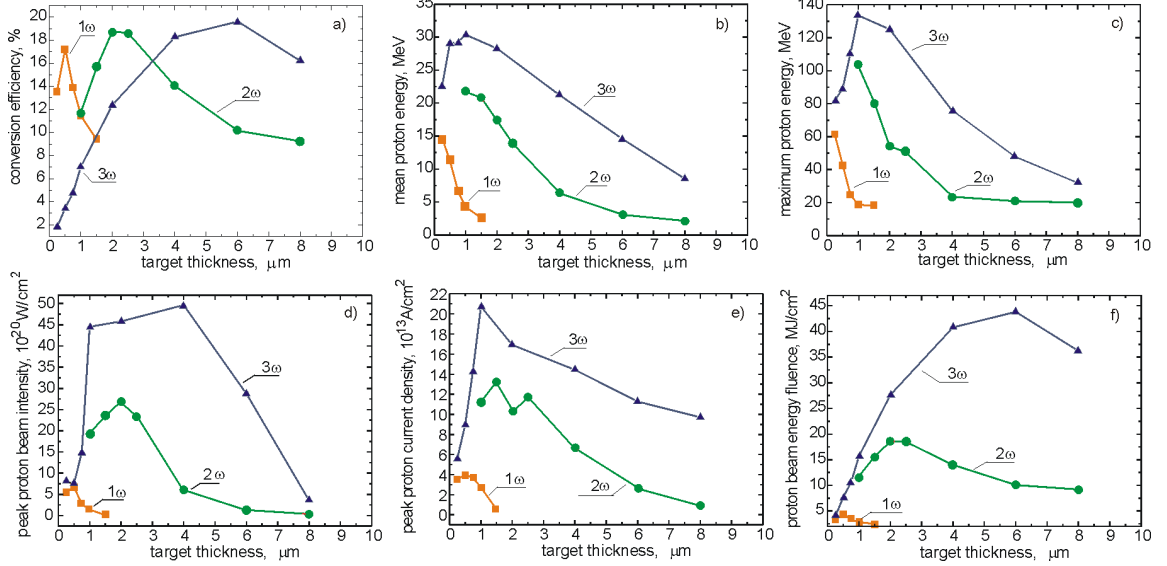


FIG. 2. Parameters of proton beams driven by laser pulses of different wavelengths as a function of the target thickness.  $I_L \lambda^2 = 5 \times 10^{19} \text{Wcm}^{-2} \mu\text{m}^2$ ,  $\tau_L = 1 \text{ ps}$ ,  $L_n = 0.25 \mu\text{m}$ ,  $n_{\text{max}} = 4 \times 10^{22} \text{cm}^{-3}$ .

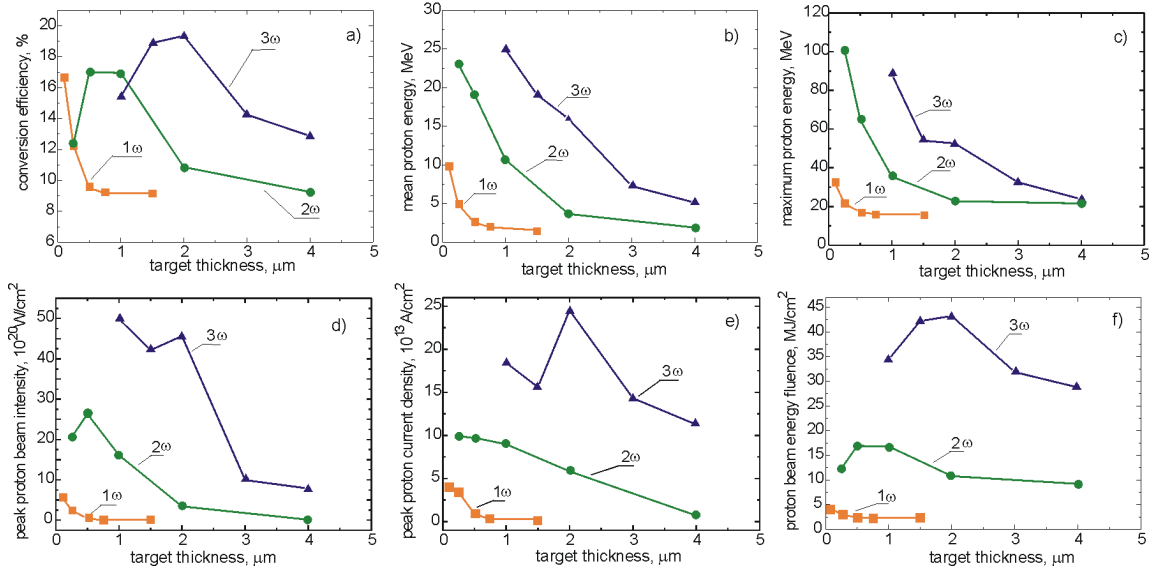


FIG. 3. As for Fig.1 but  $n_{\text{max}} = 10^{23} \text{cm}^{-3}$ .

A formation of high-intensity proton bunches driven by the 1ω and 3ω laser beams of  $I_L \lambda^2 = 5 \times 10^{19} \text{Wcm}^{-2} \mu\text{m}^2$  is illustrated in Fig. 4, which presents spatial (along the z direction) distributions of the electron density, the ion density, the beam intensity, and the ion current density for two different instants of the acceleration process.

In the case of the  $1\omega$  driver, where the TNSA contribution to the acceleration process is significant, in the late phase of acceleration, most of ions (and electrons) are spread in space and only a small part of the ions driven (indirectly) by the ponderomotive pressure forms relatively dense and intense ion spikes. In the case of the short-wavelength driver, a remarkable part of the target plasma is strongly compressed by the ponderomotive pressure and accelerated in the form of well localized in space, very dense and very intense plasma bunch. Both for  $1\omega$  and  $3\omega$ , the quasi-monoenergetic peaks in the spectrum are the result of an action of the ponderomotive pressure (not by TNSA mechanism) and that by a further decrease of the TNSA contribution the “monoenergeticity” of the spectrum can be improved.

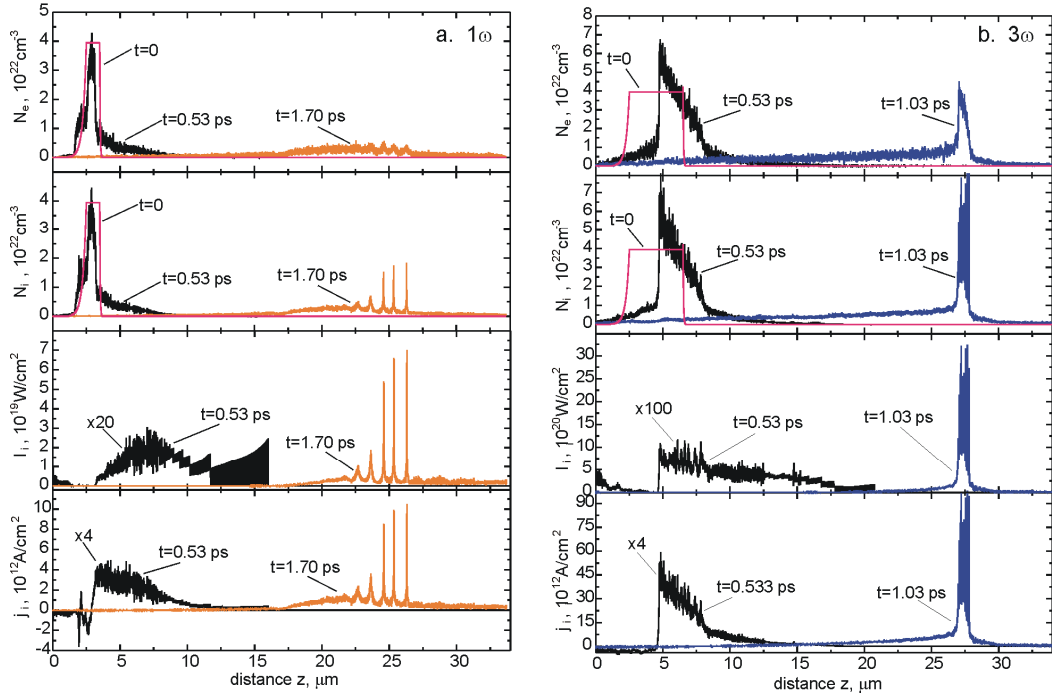


FIG. 4. Spatial distributions of the electron ( $N_e$ ) and proton ( $N_i$ ) density as well as the proton beam intensity ( $I_i$ ) and current density ( $j_i$ ) at different instants  $t$  for the case of  $1\omega$  (a) and  $3\omega$  (b) driver.  $IL\lambda^2 = 5 \times 10^{19} \text{ Wcm}^{-2} \mu\text{m}^2$ ,  $\tau L = 1 \text{ ps}$ ,  $L_n = 0.25 \mu\text{m}$ ,  $n_{\text{max}} = 4 \times 10^{22} \text{ cm}^{-3}$ .

The results of PIC simulations presented above are in a qualitative agreement with the experiment (for details see [8]) performed on the LULI 100TW laser facility. Table I presents a comparison of parameters of a proton beam produced from 1- $\mu\text{m}$  CH target by  $1\omega$  or  $2\omega$  laser pulse of duration 350 fs and  $I_L\lambda^2 = (2.1 \pm 0.2) \times 10^{18} \text{ Wcm}^{-2} \mu\text{m}^2$ . The most important feature of the presented results is a significant difference in the values of both intensity and current density of protons produced by the  $1\omega$  and the  $2\omega$  beam. Both the measurements and simulations show that these values for the  $2\omega$  case are several ( $\sim 4 - 6$ ) times higher than those for the  $1\omega$  case.

TABLE 1. COMPARISON OF PARAMETERS OF A PROTON BEAM PRODUCED FROM 1- $\mu\text{m}$  CH TARGET BY  $1\omega$  OR  $2\omega$  LASER PULSE

	Experiment		PIC simulation	
	$1\omega$	$2\omega$	$1\omega$	$2\omega$
Conversion efficiency [%]	$4 \pm 0.5$	$4.7 \pm 0.6$	4.7 - 4.4	3.8 - 5.8
Proton beam intensity, $10^{17} \text{ W/cm}^2$	$0.9 \pm 0.4$	$5.3 \pm 2.1$	$5.3 \pm 2.1$	1.8 - 2.9
Proton beam intensity, $10^{17} \text{ W/cm}^2$	$0.9 \pm 0.3$	$0.9 \pm 0.3$	2.7 - 1.7	10.6 - 12.1

## 2. INVESTIGATIONS OF MECHANISMS RESPONSIBLE FOR PLASMA JETS FORMATION BY LASER PULSE

### 2.1. Introduction

Collimated plasma outflows (jets) are a subject of great interest in the study of astrophysical phenomena and are of interest also for a new fast ignition concept. The experimental data, such as a strong gradient of electron density on the axis and a great plasma concentration in the centre, indicate that the plasma jet is produced by collision of a convergent plasma on the axis [9]. However, if the target is made of light materials like plastic or Al, no plasma jet configuration is observed, in spite of the same initial laser intensity distribution for both kinds of target material. Our experimental investigations and numerical simulations were aimed at to answer the question concerning differences in an interaction of laser beam with plasma with reference to light and heavy target materials.

### 2.2. Experimental results and interpretation

The experiment was carried out with the use of the PALS iodine laser facility. The plastic and Cu planar targets were irradiated by the laser beam under the following conditions: laser energy of 30 J, wavelength  $\lambda=0.438 \mu\text{m}$  focal spot radius of 400  $\mu\text{m}$  (whereas the focal point was located inside the targets), and the pulse duration of 250 ps (FWHM). In this case the average laser intensity is  $0.24 \cdot 10^{14} \text{ W/cm}^2$ . To study the plasma expansion a 3-frame interferometric system with automatic image processing was used. The delay between subsequent frames was set to 3 ns. The interferometric measurements corresponding to the high-Z (Cu) and low-Z (plastic) target materials are presented in Fig.5 in a form of sequences of interferograms and electron isodensitograms corresponding to them.

In all the diagrams the plasma stream boundary is represented by the electron density contour  $n_e=10^{18} \text{ cm}^{-3}$ . The step of the adjacent equidensity lines is  $\Delta n_e=2 \cdot 10^{18} \text{ cm}^{-3}$ . On the first frame ( $\Delta t=2 \text{ ns}$ ) the plasma configurations corresponding to both the materials are similar. The only difference concerns the plasma volume resulting from the difference in plasma velocities ( $6 \cdot 10^7 \text{ cm/s}$  for plastic and  $4 \cdot 10^7 \text{ cm/s}$  for Cu). One can see that in both the cases plasmas have tendency toward the plasma jet creation. The great difference in the plasma structure appears on the second frame ( $\Delta t=5 \text{ ns}$ ). In the case of Cu target the jet creation is continued, whereas the plastic plasma expansion changes essentially and assumes a divergent character. This character of plasma outflow is also conserved at later time.

The diagnostic system included an X ray streak camera placed in a side view. The streak camera registered radial distribution changes of the plasma radiation in the vicinity of the target surface. The temporal and spatial resolutions of X ray images were 30 ps and 50  $\mu\text{m}$ , respectively. To get radial X ray radiation intensity distributions the registered streak images were transformed by means of the Abel inversion. For both the targets (plastic and Cu) the annular form of the X ray radiation seems to be dominant. However, in the case of the plastic target at a certain instant of the laser action the additional radiation in the center appears. This radiation lasts even long time after the laser pulse end. The change of the annular configuration of the plastic plasma radiation source to a central one corresponds to the change of the initially convergent plasma outflow to a divergent one. At the moment of the central plasma radiation appearance the ablative plasma reaches only a distance of about 100  $\mu\text{m}$  thus making strong deflection of the laser radiation to the axis rather unlikely. Therefore, another phenomenon must be responsible for this process.

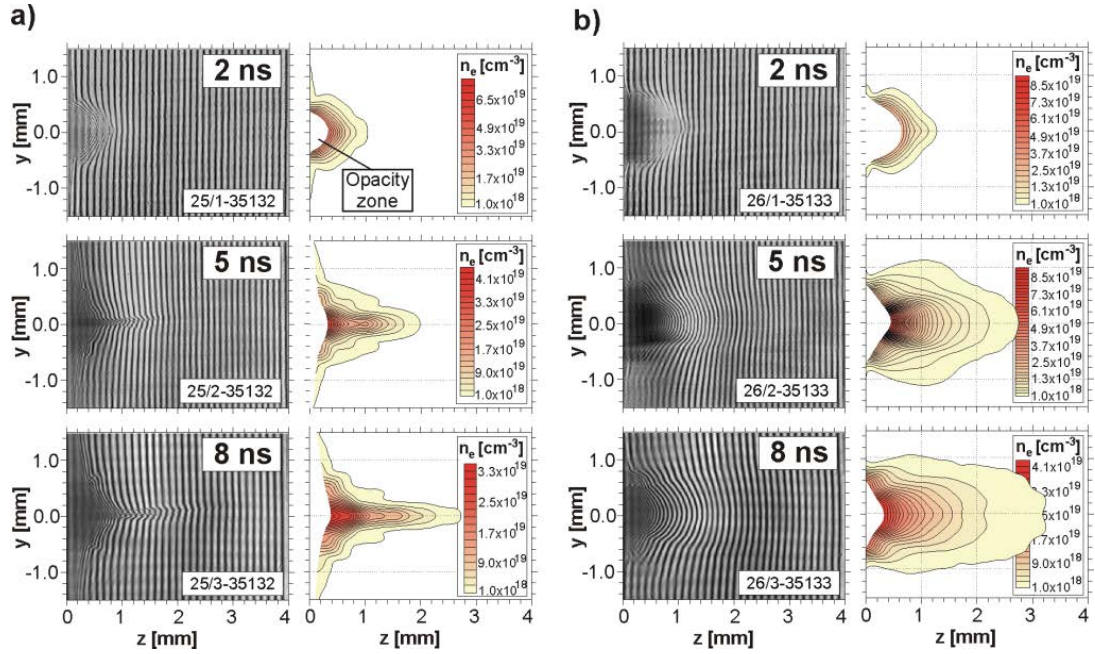


FIG. 5. Sequences of interferograms and electron equidensitograms showing evolution of plasma structure. in the case of: a) Cu and b) plastic target.

An attempt of explanation of it was taken by means of numerical simulations of the laser beam interaction emission and radiation transfer in plasma were not considered. In calculated distributions the essential differences in the plasma expansion features between the plastic and Cu targets are clearly visible. Due to much lower plasma expansion velocity in the case of the Cu target the longitudinal size of the expanded plasma (along the  $z$  axis) at the moment of the laser pulse end is about one half of its transverse dimension. In this case the plasma expansion has a planar geometry. On the contrary, in the case of the plastic target the longitudinal size of the plasma plume is larger than its transverse one and the expansion exhibits the spherical symmetry. The lower velocity of the plasma expansion for Cu target is a result of larger ablation of the mass of this target in comparison to the plastic one. Increase of the evaporated mass of the Cu target in comparison with the plastic target ( $\Delta m_{\text{Cu}}/\Delta m_{\text{CH}} = 5.21$ ) is a consequence of a deeper heating of the target by electron heat conductivity wave in the case of Cu target compared to the case of the plastic target.

### 3. STUDY OF THE NEW INDIRECT METHOD FOR TWO-STEP LASER ACCELERATION OF THE THIN FOIL

#### 3.1. Introduction

In the “classic” scheme of the ablative acceleration of thin foil targets the thrust of plasma blow off on the laser side of the target is utilized to accelerate the remaining portion of the target to high speed (as in a rocket). This process is known as the laser ablative acceleration of thin-foil targets. Thin foil acceleration experiments were conducted as a part of laser fusion research program and they help to understand better the physics of laser-plasma interaction and ablative acceleration processes. Foil and disk targets have the advantage that one can diagnose both sides of the target.

Another important feature is that in a real experiment with flyer target the accelerated foil fragment or disk can be regarded as a superfast macroparticle (projectile) [10]. The most

desirable result of such experiment was to obtain high hydrodynamic efficiency of the conversion process of the absorbed laser light into the flyer kinetic energy should also be high. It is a real problem to fulfil this condition. In most experiments on ablation acceleration of thin foils the hydrodynamic efficiency was lower than 20 %, corresponding to the ablation of 40% of the initial target mass. From the theoretical point of view the hydrodynamic efficiency of the acceleration process of a thin foil can reach the maximum value of 65% (“cold rocket” model) but it means that 80% of the foil mass should be evaporated by laser light. The residual part (20%) of the foil with low density (because of its fast expansion) would achieve high velocity. In a real experiment of ablatively accelerated thin foil target, “cold rocket” model is not realised and the hydrodynamic efficiency is much lower because the significant part of the absorbed laser pulse energy heats the expanding plasma and is not available to drive a thin foil (the “rocket”) directly.

In the last several years experiments with flyer targets grew popular because of the concept of so-called impact fast ignition (IFI) [11], where the ablatively accelerated macroparticle containing DT plays role of an ignitor in a collision process with the compressed DT main fuel. In our previous paper [12] the reversed scheme of thin foil acceleration (RAS) was proposed. Thin foils were accelerated by action of freely expanding ablative plasma. That method appeared to be much more effective than the usually applied conventional method of acceleration. In this report the “Cavity Pressure Acceleration Scheme” (CPAS) is proposed and tested. Pressure induced by laser action inside the target cavity constitutes here the most important factor of foil acceleration. It was expected that such target construction could improve absorption of the laser radiation and to rise efficiency of foil acceleration process. It was demonstrated in the PALS experiment the possibility of both to accelerate a thin-foil target to the higher velocity than that attainable in the “classic” way (in the comparable experimental conditions) and simultaneously to avoid a problem of diminishing of the foil mass during the process of acceleration. The special attention is paid to the problem of acceleration of very thick (300 or 500  $\mu\text{m}$ ) foils.

### 3.2. Experimental set up and results

The following PALS laser parameters for targets irradiation have been chosen:  $\lambda=1.315$   $\mu\text{m}$ , pulse energy in the range of 120-500 J, pulse duration of 250 ps and focal spot diameters at the target surface 100 – 200  $\mu\text{m}$ . The “cavity type” target, shown in Fig. 6, constituted a closed cavity. To study the foil dynamics and deformation a 3-frame shadowgraphic / interferometric system was employed. The delay between frames was set at 3 ns.

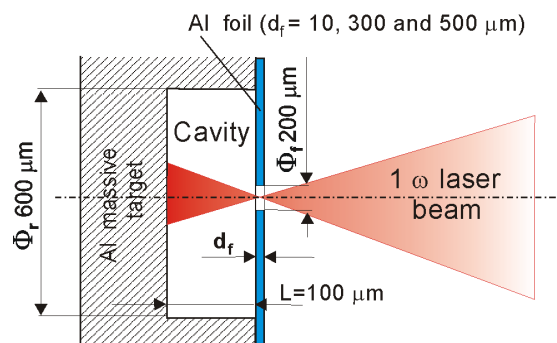


FIG. 6. Construction of the “cavity type” targets used in the experiment.

Investigations of the 10  $\mu\text{m}$  thick Al foil acceleration were carried out for the three laser energies mentioned above. The foil reached velocities in the range of  $(2-3) \cdot 10^7$  cm/s. As our

attention was mainly devoted to the thick foils so the results concerning these foils are presented here in greater detail. In Fig. 6 sequences of shadowgrams for the 300  $\mu\text{m}$  and 500  $\mu\text{m}$  thick foils are presented.

On the basis of these shadowgrams the velocities of the 300  $\mu\text{m}$  thick foil for the laser energies of 120, 300 and 500 J were determined to be equal to  $0.7 \cdot 10^7$  cm/s,  $1.0 \cdot 10^7$  cm/s and  $1.4 \cdot 10^7$  cm/s, respectively. On the other hand, from the simple theoretical analyze it can be found the following relationship between two velocities for two different laser energies:  $v_1/v_2 = (E_1/E_2)^{1/2}$ . The measured experimental points correspond to the theoretical graph calculated using this dependence. Hence we can suppose that in the case of thick foils the same proportionally part of plasma energy is transferred into the foil kinetic energy.

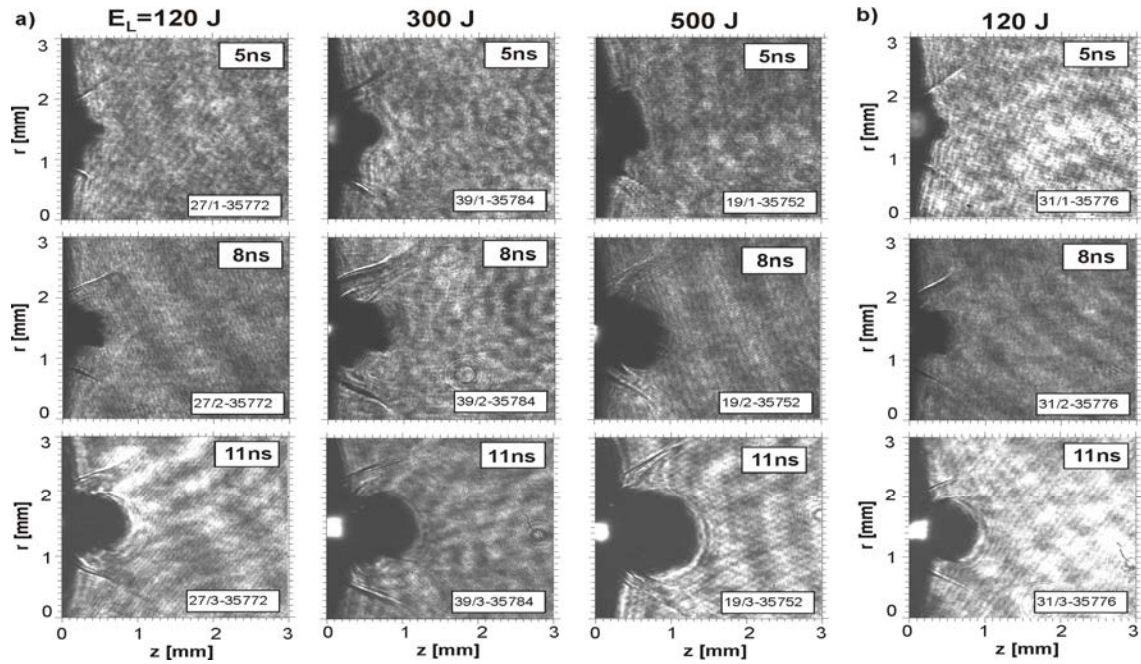


Fig.7. Sequences of shadowgrams for the 300  $\mu\text{m}$  thick foil at different laser energies (a) and for the 500  $\mu\text{m}$  thick foil at energy of 120 J (b).

In Fig. 7 the first and last sequences correspond to the same laser energy (120 J) but represent different foil thicknesses (300 and 500  $\mu\text{m}$ ). The velocities corresponding to both thicknesses differ slightly (in both cases the velocities are roughly on the level of  $0.7 \cdot 10^7$  cm/s). The maximum velocity is reached for a (relatively) thin 10  $\mu\text{m}$  Al foil much faster (for times  $t < 5$  ns) than for thick (100 – 500)  $\mu\text{m}$  foils. The optical shadow boundary movement observed in shadowgrams gives in fact an information about velocity of the determined density layer but not the foil as a whole. It means that the average foil velocity (integrated over all foil mass) is in fact much lower than the velocity estimated from the motion of target optical shadow. For thin foils it also causes that the low density (i.e. invisible part of the accelerated foil) grows fast what gives an effect of slower movement of the rest (visible) foil. This is why there is impression that the thin foil velocity decreases at later times.

#### 4. CONCLUSIONS

In this work we have shown that shortening the laser wavelength causes a growth of the contribution of the SLPA mechanism to the ion acceleration process and at the fixed value of

$I_L \lambda^2$  it results in an increase in almost all ion beam parameters (intensity, current density, energy fluence, mean and maximum ion energy) and in the shifting of the optimum target thickness towards greater values. Even at moderate values of  $I_L \lambda^2 \leq 10^{20} \text{Wcm}^{-2} \mu\text{m}^2$ , a short-wavelength ( $\lambda \leq 0.5 \mu\text{m}$ ) ps/subps laser driver makes it possible to produce ultrashort ( $\leq 100\text{fs}$ ), multi-MeV proton bunches of intensity and current density in excess of  $10^{21} \text{W/cm}^2$  and  $10^{14} \text{A/cm}^2$ , respectively. In particular, using a multi-ps short-wavelength laser driver (e.g.  $2\omega$  or  $3\omega$  beam of Nd:glass laser), possibly with circular light polarization, seems to be a promising way towards highly efficient ( $\eta \geq 15\%$ ) generation of proton (ion) beams of parameters required for ICF fast ignition.

The most important achievement of this paper is finding one additional mechanism taking part in the plasma jet forming toward the two such mechanisms considered so far, namely the annular irradiation and the plasma radiative cooling. Based on numerical simulations, the influence of the plasma expansion regime was identified: in the case of Cu, the planar expansion regime is taking place and in the case of plastic, it is the spherical one. All these three mechanisms play their respective roles in the plasma jet forming. However, the contribution of these mechanisms toward the plasma jet production seems to depend on the target irradiation conditions. This paper also answers the question why no plasma jet is produced in the case of the low atomic number target material, represented here by plastic. Obtained scientific material, both experimental as and theoretical, is inspiring for formulating of new ideas, concerning both improvements of the plasma stream parameters as and the creation of more composite configurations of plasma jet, useful to plasma researches, connected with the realization of ICF as and the simulation of astrophysics processes .

In IPPLM was proposed a new, very effective scheme, which can be applied to accelerate macroparticles to high velocities with efficiency not observed in classic ablative experiments. This mechanism can be named as a “Cavity Pressure Acceleration Scheme” (CPAS). The CPAS allows to use almost all absorbed laser energy (neglecting the energy of the shock wave propagating into the solid target). Also the hydrodynamic efficiency of the energy transfer to the flyer foil is much higher than in conventional ablative acceleration. CPAS enables acceleration by laser of very heavy macroparticles ( $\sim 10^{-1} \text{g/cm}^2$ ) to velocities of  $\sim 10^7 \text{cm/s}$  (authors do not know similar results in the literature) whereas conventional ablative acceleration of that foil was completely unsuccessful (the foil has even not started).

Another advantage of CPAS method is that conversion of laser radiation to higher harmonics it is not necessary. The acceleration of macroparticles to high (thermonuclear) velocity, at a very high hydrodynamic efficiency, “not forgetting” about its density, is general and essential problem from the point of view of their possible applications in the IFE area. One of the possible ways of improvement of this situation is acceleration of macroparticles in cylindrical or conical channels.

## REFERENCES

- [1] BADZIAK, J., JABŁOŃSKI, S., WOŁOWSKI, J., Progress and prospect of fast ignition of ICF targets, *Plasma Phys. Control. Fusion* **49** (2007) B651-B666.
- [2] FERNÁNDEZ, J.C., HONRUBIA, J.J., ALBRIGHT, B.J., FLIPPO, K.A., GAUTIER, D.C., HEGELICH, B.M., SCHMITT, M.J., TEMPORAL, M., AND YIN, L., Progress and prospects of ion-driven fast ignition, *Nucl. Fus.* **49** (2009) 065004.

- [3] TEMPORAL, M., HONRUBIA, J.J., AND ATZENI, S., Numerical study of fast ignition of ablatively imploded deuterium–tritium fusion capsules by ultra-intense proton beams, *Phys. Plasmas* **9** (2002) 3098.
- [4] BADZIAK, J., GŁOWACZ, S., JABŁOŃSKI, S., PARYS, P., WOŁOWSKI, J., HORA, H., Generation of picosecond high-density ion fluxes by skin-layer laser-plasma interaction, *Las. Part. Beams* **23** (2005) 143-147.
- [5] BORGHESI, M., FUCHS, J., BULANOV, S.V., MACKINNON, A.J., PATEL, P.K., ROTH, M., Fast ion generation by high-intensity laser irradiation of solid targets and applications, *Fus. Sci. Techn* **49**(3) (2006) 412-439.
- [6] HOLKUNDKAR, A.R., and GUPTA, N.K., Effect of initial plasma density on laser induced ion acceleration, *Phys. Plasmas* **15** (2008) 123104.
- [7] ESIRKEPOV, T., BORGHESI, M., BULANOV, S.V., MOUROU, G., AND TAJIMA, T., Highly Efficient Relativistic-Ion Generation in the Laser-Piston Regime, *Phys. Rev. Lett.* **92** (2004) 175003.
- [8] BADZIAK, J., JABŁOŃSKI, S., PARYS, P., ROSIŃSKI, M., WOŁOWSKI, J., SZYDŁOWSKI, A., ANTICI, P., FUCHS, J., MANCIC, A., Ultraintense proton beams from laser-induced skin-layer ponderomotive acceleration, *Journ. App. Physics* **104** (2008) 063310-1 6, 2008.
- [9] KASPERCZUK, A., PISARCZYK, T., BORODZIUK, S., ULLSCHMIED, J., KROUSKY, E., MASEK, K., ROHLENA, K., SKALA, J., HORA, H., Stable dense plasma jets produced at laser power densities around  $10^{14}$  W/cm<sup>2</sup>, *Phys. Plasmas* **13** (2006) 062704-1-8.
- [10] BORODZIUK, S., KOSTECKI, J.L., Studies of hypervelocity impact problem by means of laser-target experiments – a new approach, *Las. Part. Beams* **8**(1–2) (1990) 241–5.
- [11] MURAKAMI, M., NAGATOMO, H., A new twist for inertial fusion energy: Impact ignition, *Nucl. Instr. and Meth. A* **54** (2005) 67.
- [12] BORODZIUK, S., KASPERCZUK, A., PISARCZYK, T., ULLSCHMIED, J., KROUSKY, E., MASEK, K., PFEIFER, M., ROHLENA, K., SKALA, J., AND PISARCZYK, P., Reversed scheme of thin foil acceleration, *Appl. Phys. Lett.* **93** (2008) 101502.

## LIST OF PUBLICATIONS BY THE CRP PARTICIPANTS DURING THE CRP

I.B. Földes, E. Rácz, T. Suta and S. Szatmári: Spectroscopical investigations in the VUV of laser plasmas generated by a short pulse KrF laser; Proc. XXIX ECLIM, Eds. O. Cabellos, J. Sanz, G. Velarde, J.M. Perlado, Madrid, 2006, ISBN: 84-690-2624-0, p. 413-418.

J. Badziak, A. Kasperczuk, P. Parys, T. Pisarczyk, L. Ryc, J. Wolowski, S. Jablonski, R. Suchanska, E. Krousky, L. Láska, K. Masek, M. Pfeiffer, J. Ullschmied, L.J. Dareshwar, I. Földes, L. Torrisi, P. Pisarczyk: Production of high-current heavy ion jets at the short-wavelength subnanosecond laser-solid interaction, Appl. Phys. Lett. 91, 081502 (2007).

J. Wolowski, J. Badziak, A. Borrielli, L. Dareshwar, I. B. Foldes, A. Kasperczuk, E. Krousky, L. Laska, K. Masek, A. Mezzasalma, P. Parys, M. Pfeifer, T. Pisarczyk, M. Rosinski, L. Ryc, R. Suchanska, T. Suta, L. Torrisi, J. Ullschmied and P. Pisarczyk: Application of laser-induced double ablation of plasma for enhanced macroparticle acceleration; Journal of Physics: Conference Series 112 (2008) 022072; Proc. IFSA2007, IOP Publishing.

J. Badziak, A. Kasperczuk, P. Parys, T. Pisarczyk, M. Rosiński, L. Ryć, J. Wołowski, R. Suchańska, J. Krása, E. Krousky, L. Láska, K. Mašek, M. Pfeifer, K. Rohlena, J. Skala, J. Ullschmied, L. J. Dharehwar, I. B. Földes, T. Suta, A. Borrielli, A. Mezzasalma, L. Torrisi and P. Pisarczyk: The effect of high-Z dopant on laser-driven acceleration of a thin plastic target; Appl. Phys. Lett. 92, 211502 (2008), Virtual Journal of Ultrafast Science 7, No.6. (June 2008).

I.B. Földes, S. Szatmári: Multiple-beam fast ignition with KrF laser; Proc. 35th EPS Conference on Plasma Phys. Hersonissos, 9 - 13 June 2008 ECA Vol.32, O-2.014 (2008).

I.B. Földes, S. Szatmári: On the use of KrF lasers for fast ignition; Laser and Particle Beams 26, 575-582 (2008).

I.B. Földes, D. Csáti, F.L. Szűcs, S. Szatmári: Plasma mirror and temperature evolution for short pulse KrF lasers; Radiation Effects and Defects in Solids, 165, 429-433 (2010).

I.B. Földes, A. Barna, D. Csáti, F.L. Szűcs, S. Szatmári: Plasma mirror effect with a short pulse KrF laser; Journal of Physics: Conference Series 244, 032004 (2010); Proc. of the Sixth International Conference on Inertial Fusion Sciences and Applications IFSA 2009.

P. Heissler, R. Hörlein, M. Stafe, J.M. Mikhailova, Y. Nomura, D. Herrmann, R. Tautz, S.G. Rykovanov, I.B. Földes, K. Varjú, F. Tavella, A. Marcinkevicius, F. Krausz, L. Veisz, G.D. Tsakiris: Toward single attosecond pulses using harmonic emission from solid-density plasmas; Appl. Phys. B 101, 511-521 (2010).

A. Kasperczuk, T. Pisarczyk, N.N. Demchenko, S.Yu. Gus'kov, M. Kálal, J. Ullschmied, E. Krouský, K. Mašek, M. Pfeifer, K. Rohlena, J. Skála, and P. Pisarczyk: Experimental and theoretical investigations of mechanisms responsible for plasma jets formation at PALS, Laser and Particle Beams. 2009, vol. 27, 415-427.

Ph. Nicolai, C. Stenz, V. Tikhonchuk, X. Ribeyre, A. Kasperczuk, et al.: Studies of supersonic radiative plasma jet interaction with gases at the Prague Asterix Laser System (PALS) facility. Physics of Plasmas. 2008, vol. 15, no. 8, p. 082701-082718.

A. Kasperczuk, T. Pisarczyk, M. Kálal, J. Ullschmied, E. Krouský, K. Mašek, M. Pfeifer, K. Rohlena, J. Skála, and P. Pisarczyk: Influence of target material on structure of the plasma outflow produced by a partly defocused laser beam, *Applied Physics Letters*. 2009, vol. 94, p. 081501-081503.

V.T. Tikhonchuk, Ph. Nicolai, X. Ribeyre, C. Stenz, G. Schurtz, et al.: Laboratory modeling of supersonic radiative jets propagation in plasmas and their scaling to astrophysical conditions. *Plasma Physics and Controlled Fusion*. 2008, vol. 50 (12).

A. Kasperczuk, T. Pisarczyk, Ph. Nicolai, C. Stenz, V. Tikhonchuk, M. Kálal, J. Ullschmied, E. Krouský, K. Mašek, M. Pfeifer, K. Rohlena, J. Skála, D. Klír, J. Kravárik, P. Kubeš, P. Pisarczyk: Investigations of plasma jet interaction with ambient gases by the multi-frame interferometric and X ray pinhole camera systems, *Laser and Particle Beams*. 2009, vol. 27, p. 115–122.

Ph. Nicolai, C. Stenz, V. Tikhonchuk, X. Ribeyre, A. Kasperczuk, T. Pisarczyk, L. Juha, E. Krouský, K. Mašek, M. Pfeifer, K. Rohlena, J. Skála, J. Ullschmied, M. Kálal, D. Klír, J. Kravárik, P. Kubeš, P. Pisarczyk: Supersonic plasma jet interaction with gases and plasmas, *Astrophysics and Space Science*. 2009, vol. 322, p. 11-17.

Ph. Nicolai, C. Stenz, A. Kasperczuk, T. Pisarczyk, E. Krousky, D. Klir, K. Masek, M. Pfeifer, K. Rohlena, J. Skala, J. Ullschmied, M. Kalal, J. Kravarik, E. Tabakhoff, and V. Tikhonchuk: Laboratory studies of multi-material radiative astrophysical jets propagation in plasmas, 6th International Conference on Inertial Fusion Sciences and Applications (IFSA 2009), September 6 – 11, 2009, San Francisco, USA ((accepted for publication in the Conf. Proceedings in the Conference Proceedings: Journal of Physics: Conference Series)

M. Kálal, O. Slezák, M. Martínková, Y.J. Rhee: Compact Design of Nomarski Interferometer and its Application in Diagnostics of Coulomb Explosions of Deuterium Clusters, *Journal of the Korean Physical Society* 2010, vol. 56, No. 1, 287-294.

M. Martínková, M. Kálal, and Y.J. Rhee: Coulomb Explosions of Deuterium Clusters Studied by Compact Design of Nomarski Interferometer, 6th International Conference on Inertial Fusion Sciences and Applications (IFSA 2009), September 6 – 11, 2009, San Francisco, USA (accepted for publication in the Conf. Proceedings: Journal of Physics: Conference Series)

M. Kálal, M. Martínková, Y.J. Rhee: Feasibility Studies of Deuterium Clusters Spatial Density Distribution Measurements by Complex Interferometry (submitted for publication to the Journal of the Korean Physical Society).

M. Kálal, M. Martínková, O. Slezák, H.J. Kong, J.W. Yoon: SBS PCM Technique Applied for Aiming at IFE Pellets: First Tests with Amplifiers and Harmonic Conversion, *Journal of the Korean Physical Society*. 2010, vol. 56, No. 1, 184-189.

M. Kálal, H. J. Kong, E. Koresheva, M. Martínkova, O. Slezák, and S. A. Startsev: Current Status of the SBS PCM Approach to Self-Navigation of Lasers on IFE Targets, 6th International Conference on Inertial Fusion Sciences and Applications (IFSA 2009), September 6 – 11, 2009, San Francisco, USA (accepted for publication in the Conference Proceedings: Journal of Physics: Conference Series).

M. Kálal, H. J. Kong, E. Koresheva, O. Slezák, J.N. Shin, and S. A. Startsev: Recent Progress Made in the SBS PCM Approach to Self-Navigation of Lasers on Direct Drive IFE Targets, Innovative Confinement Concepts Workshop (ICCW 2010), February 16-19, 2010, Princeton, New Jersey, USA (accepted for publication in the Conference Proceedings: Journal of Fusion Energy).

O. Slezák, H.J. Kong, and M. Kálal: Phase Control of SBS Seeding by Optical Interference Pattern Clarified: Direct Applicability for IFE Laser Driver, 6th International Conference on Inertial Fusion Sciences and Applications (IFSA 2009), September 6 – 11, 2009, San Francisco, USA (accepted for publication in the Conference Proceedings: Journal of Physics: Conference Series).

O. Slezák, M. Kálal, and H.J. Kong: Phase-locked stimulated Brillouin scattering seeded by a transient acoustic wave excited through an optical interference field (submitted for publication to the Journal of the Korean Physical Society).

H.J. Kong, S.K. Lee, J.W. Yoon, D.H. Beak, Opt. Rev. 13, 119 (2006).

H.J. Kong, J.W. Yoon, J.S. Shin, D.H. Beak, B.J. Lee, Laser Part. Beams 24, 519 (2006).

H.J. Kong, J.W. Yoon, D.W. Lee, S.K. Lee, M. Nakatsuka, J. Korean, Phys. Soc. 49, S39 (2006).

S. K. Lee, H. J. Kong, J.W. Yoon, M. Nakatsuka, D.K. KO, J. Lee, J. Phys. IV France 133, 621 (2006).

H. J. Kong, Yoon, J. W., D.H. Beak, J.S. Shin, S.K. Lee, D.W. Lee, Laser Part. Beams 25, 225 (2007).

H. J. Kong, J.W. Yoon, J.S. Shin, D.H. Beak, Appl. Phys. Lett. 92, 021120 (2008).

H. J. Kong, J.S. Shin, J.W. Yoon, D.H. Beak, Laser Part. Beams 27, 179 (2009).

H. J. Kong, J.S. Shin, J.W. Yoon, D.H. Beak, Nucl. Fus. 49, 125002 (2009).

J.W. Yoon, J.S. Shin, H. J. Kong, J. Lee, , J. Opt. Soc. Am. B 26, 2167 (2009).

I.V. Aleksandrova, A.A.Belolipetsky, E.R.Koresheva, State of the Problem of Cryogenic Targets in Current Inertial Fusion Program, Vestnik RAEN 7(2), 37-42, 2007 (in Russian).

E.R. Koresheva. Optimizing cryogenic layering for IFE targets for providing target survival during the injection process. Proceed. 1<sup>st</sup> IAEA RCM on Pathways to Energy from Inertial Fusion (Vienna, Austria, 6-10 November 2006).

E.R. Koresheva, Second year progress report on the implementation of the IAEA contract number 13871/RBF“Optimizing cryogenic layering for inertial fusion energy (IFE) targets for providing target survival during the injection process”, Title of the 2<sup>nd</sup> year “Multicriteria optimization for the delivery process of IFE targets with a different fuel structure”, August 15, 2007 – June 15, 2008.

E.R. Koresheva, Third year progress report on the implementation of the IAEA contract number 13871/RBF“Optimizing cryogenic layering for inertial fusion energy (IFE) targets for providing target survival during the injection process”, Title of the 3<sup>rd</sup> year “Elucidation of fundamentals underlying the process of formation of thermo-stable ultra-fine fuel layer”, September 1, 2008 – July 1, 2009.

Fourth year progress report on the implementation of the IAEA contract number 13871/RBF“Optimizing cryogenic layering for inertial fusion energy (IFE) targets for providing target survival during the injection process”, Title of the 2<sup>nd</sup> year “Further elucidation of fundamentals underlying the process of formation of thermo-stable ultra-fine fuel layer”, March 20, 2010.

R. Koresheva et al. A Study on fabrication, manipulation and survival of cryogenic targets required for the experiments at the Facility for Antiproton and Ion Research: FAIR. *Laser Part. Beams* **27**, 255-272, 2009.

E.R. Koresheva. High rep-rate target factory for HiPER: cryogenic target mass production and delivery with a rate of 0.1-to-10 Hz. 3<sup>rd</sup> MWTA, Round table “European project HiPER and international collaboration” (October 18, 2007, Moscow, Russian Federation)

I.V. Aleksandrova, A.A. Belolipetskiy, E.R. Koresheva and S.M. Tolokonnikov “Survivability of fuel layers with a different structure under conditions of the environmental effects: Physical concept and modelling results. *Laser Part. Beams*, 26 (4), 643-648, 2008.

I. Aleksandrova et al. Thermal and mechanical responses of cryogenic targets with a different fuel layer anisotropy during delivery process. *J. Russian Laser Research*, 29 N5, 419-431, 2008.

E.R. Koresheva, I.V. Aleksandrova, A.A. Belolipetskiy. Optimizing cryogenic layering for inertial fusion energy target for lowering fuel layer sensitivity to the external parameters variations arising during target delivery into reactor chamber. Report, XXXIV International conference on Plasma Physics and ICF (Zvenigorod, Moscow sub., Russian Federation, February 12-16, 2007.

E.R. Koresheva. An overview of cryogenic target fabrication and delivery in Russian Federation. Report, 30<sup>th</sup> European Conference on Laser Interaction with Matter (ECLIM-2008, August 31-September 6, 2008, Darmstadt, Germany).

E.R. Koresheva. High rep-rate fabrication, characterization and delivery of free-standing moving cryogenic targets: overview on researches developed at LPI. Report, 2<sup>nd</sup> European Target Fabrication Workshop (2<sup>nd</sup> ETFW), October 27-28, 2008, Abingdon, UK

I.V. Aleksandrova et al. High rep-rate fabrication of free-standing cryogenic targets with isotropic solid fuel layer. Report, 36<sup>th</sup> International Conference on Plasma Physics and ICF (Feb. 9-13, 2009, Zvenigorod, Moscow sub., Russian Federation).

S. Nakai. IFSA Proceeding, *Journal of Physics: Conference Series* 112, 042070(2008).

A. R. Piriz, J. J. López Cela, N. A. Tahir, and D. H. H. Hoffmann: Richtmyer – Meshkov flow in elastic solids, *Phys Rev. E*. 2006, vol.74, 037301.

A.R. Piriz, J. J. López Cela, N. A. Tahir, and D.H.H. Hoffmann: Richtmyer – Meshkov instability in elastic-plastic media, *Phys. Rev. E.* 2008, vol. 78, 056401.

R. Piriz, J.J. López Cela, N.A. Tahir: Rayleigh-Taylor instability in elastic- plastic solids, *J. Appl. Phys.* 2009, vol.105, 116101.

A.R. Piriz, J.J. López Cela, and N.A. Tahir: Linear analysis of incompressible Rayleigh-Taylor instability in solids *Phys. Rev. E.* 2009, vol.80, 046305.

S.A. Piriz, A.R. Piriz, and N.A. Tahir: Rayleigh-Taylor instability in ion beam driven ablation fronts *Phys. Plasmas.* 2009, vol.16, 082706.

M.L. SHMATOV, “Comment on ‘Assessment of potential for ion-driven fast ignition’ ”, *Fusion Sci. Technol.* **52**, 116-117 (2007).

M.L. SHMATOV, “Factors determining the choice of the laser-accelerated ions for fast ignition”, *J. Phys.: Conf. Ser.* **112**, 022061 (2008).

N. NAUMOVA, T. SCHLEGEL, V.T. TIKHONCHUK et al., “Hole boring in a DT pellet and fast-ion ignition with ultraintense laser pulses”, *Phys. Rev. Lett.* **102**, 025002 (2009).

M.L. SHMATOV, “Some thermonuclear power plants as the possible sources of He<sup>3</sup> for space propulsion systems,” *JBIS* **60**, 180-187 (2007).

M.L. SHMATOV, “Advantages of the fast ignition, direct compression targets with two cones from the viewpoint of IFE reactor chamber physics,” *IFSA 2007 Abstracts* (Kobe, Japan, September 9-14, 2007), abstract ThPoIAEA101, p. 209 (2007).

M.L. SHMATOV, “Advantages of fast ignition scenarios with two hot spots for space propulsion systems”, *JBIS* **62**, 219-224 (2009).

S. NAKAI, “Development of integrated IFE system and its industrial application as intense neutron source”, *J. Phys.: Conf. Ser.* **112**, 042070 (2008).

V. Stancalie, *Laser and Particle Beams*, 27 (2009) 345.

V. Stancalie, *Nuclear Instruments and Methods in Physics Research Section B: Beam Interactions with Materials and Atoms*, Volume 267 (2009) 305.

N. Naumova, T. Schlegel, V. T. Tikhonchuk, C. Labaune, I. V. Sokolov and G. Mourou, Hole boring in a DT pellet and fast-ion ignition with ultraintense laser pulses, *Phys. Rev. Lett.* 102, 025002 (2009).

L.C. Carlson, M. S. Tillack, J. Stromsoe, N.B. Alexander, G.W. Flint, D.T. Goodin, R.W. Petzoldt, “Completing the Viability Demonstration of Direct-Drive IFE Target Engagement and Assessing Scalability to a Full-Scale Power Plant,” *Transactions on Plasma Science* 38(3) March 2010, 300-305.

L.C. Carlson, M. S. Tillack, J. Stromsoe, N. A. Alexander, D. T. Goodin and R. W. Petzoldt, “Improving the Accuracy of a Target Engagement Demonstration,” *Fusion Science and Technology* 56 (1) July 2009, 409-416.

L. Carlson, N. Alexander, G. Flint, D. Goodin, T. Lorentz, R. Petzoldt and M. Tillack, "Target Tracking and Engagement for Inertial Fusion Energy: A Tabletop Demonstration," *Fusion Science & Technology* 52(3), Oct. 2007, 478-482.

R. Petzoldt, N. Alexander, L. Carlson, G. Flint, D. Goodin, J. Spalding, M. Tillack, "A Continuous, In-Chamber Target Tracking and Engagement Approach for Laser Fusion," *Fusion Science and Technology* 52(3), October 2007, 454-458.

J.D. Spalding, L. C. Carlson, M. S. Tillack, N. B. Alexander, D. T. Goodin and R. W. Petzoldt, "Longitudinal Tracking of Direct Drive Inertial Fusion Targets," *Fusion Science and Technology* 52(3), October 2007, 435-439.

L. C. Carlson, M.S. Tillack, T. Lorentz, N.B. Alexander, G.W. Flint, D.T. Goodin and R.W. Petzoldt, "Glint system integration into an IFE target tracking and engagement demonstration," *Inertial Fusion Science and Applications 2007, Journal of Physics: Conference Series* 112 (2008) 032039.

R. Raffray, W. Meier, S. Abdel-Khalik, R. Bonazza, P. Calderoni, C. S. Debonnel, Z. Dragojlovic, L. El-Guebaly, D. Haynes, J. Latkowski, C. Olson, P. Peterson, S. Reyes, P. Sharpe, M. S. Tillack and M. Zaghoul, "IFE Thick Liquid Wall Chamber Dynamics: Governing Mechanisms and Modeling and Experimental Capabilities," *Fusion Science and Technology* 49 January 2006.

J. Badziak, S. Jabłoński, P. Parys, M. Rosiński, J. Wołowski, A. Szydłowski, P. Antici, J. Fuchs, A. Mancic, "Generation of Ultraintense Proton Beams Driven by a Short Pulse Multi-TW Laser", *Photonics Letters of Poland*, vol.1, 22 (2009) 22-24.

L. Torrisi, G. Foti, L. Giuffrida, D. Puglisi, J. Wołowski, J. Badziak, P. Parys, M. Rosiński, D. Margarone, J. Krasa, A. Velyhan, U. Ullschmied, "Single crystal silicon carbide detector of emitted ions and soft x rays from power laser-generated plasmas" *Journal of Applied Physics*, 105 (2009) 123304-1-7.

A. Szydłowski, J. Badziak, J. Fuchs, M. Kubkowska, P. Parys, M. Rosiński, R. Suchańska, J. Wołowski, P. Antici, A. Mancic, "Application of solid-state nuclear track detectors of the CR-39/PM-355 type for measurement of energetic protons emitted from plasma produced by an ultra-intense laser" *Radiation Meas.* 44 (2009) 881-884.

## LIST OF PARTICIPANTS

- Batani, D. Dipartimento di fisica “G.Occhialini,  
Università di Milano-Bicocca, Italy
- Desai, T. National Research Institute for Applied  
Mathematics, 497/G, 7<sup>th</sup> Block, Jayanagar,  
Bangalore, India
- Földes, I.B. Department of Plasma Physics, Association  
EURATOM HAS KFKI Research Institute for  
Particle and Nuclear Physics of the Hungarian  
Academy of Sciences, H-1121 Budapest,  
Konkoly-Thege u. 29-33, Hungary
- Hoffmann, D.H.H. Technical University, Darmstadt, Germany
- Kalal, M. Czech Technical University in Prague, Brehova  
7, 115 19 Prague 1, Cz. Republic
- Khaydarov, R. T. Institute of Applied Physics, National  
University of Uzbekistan, Tashkent,  
Uzbekistan
- Kong, H.J. Department of Physics, KAIST, Daejeon,  
Republic of Korea
- Koresheva, E.R. Lebedev Physical Institute of RAS, 53  
Leninskiy Prospect, 119991 Moscow, Russian  
Federation
- Nakai, S. Institute of Laser Engineering, Osaka  
University, Osaka, Japan
- Perlado, J.M. Instituto de Fusión Nuclear (DENIM)  
Universidad Politécnica de Madrid (UPM),  
Madrid, Spain
- Piriz, A. R. E.T.S.I.Industriales, Universidad de Castilla-La  
Mancha, 13071 Ciudad Real, Spain
- Shmatov, M.L. IOFFE physical technical institute  
ST. Petersburg,  
Russian Federation
- Stancalie, V. National Institute for Laser, Plasma and  
Radiation Physics, 409 Atomistilor Str., MG  
36, 077125 Bucharest, Magurele, Romania

Tikhonchuk, V. CELIA, University Bordeaux 1 – CNRS –  
CEA, 351 Cours de la Liberation, 33405  
Talence cedex, France

Tillack, M.S. University of California San Diego, La Jolla,  
CA 92093-0417, USA

Wołowski, J. Institute of Plasma Physics and Laser  
Microfusion, Warsaw, Poland



# Where to order IAEA publications

In the following countries IAEA publications may be purchased from the sources listed below, or from major local booksellers. Payment may be made in local currency or with UNESCO coupons.

## AUSTRALIA

DA Information Services, 648 Whitehorse Road, MITCHAM 3132  
Telephone: +61 3 9210 7777 • Fax: +61 3 9210 7788  
Email: [service@dadirect.com.au](mailto:service@dadirect.com.au) • Web site: <http://www.dadirect.com.au>

## BELGIUM

Jean de Lannoy, avenue du Roi 202, B-1190 Brussels  
Telephone: +32 2 538 43 08 • Fax: +32 2 538 08 41  
Email: [jean.de.lannoy@infoboard.be](mailto:jean.de.lannoy@infoboard.be) • Web site: <http://www.jean-de-lannoy.be>

## CANADA

Bernan Associates, 4501 Forbes Blvd, Suite 200, Lanham, MD 20706-4346, USA  
Telephone: 1-800-865-3457 • Fax: 1-800-865-3450  
Email: [customercare@bernan.com](mailto:customercare@bernan.com) • Web site: <http://www.bernan.com>

Renouf Publishing Company Ltd., 1-5369 Canotek Rd., Ottawa, Ontario, K1J 9J3  
Telephone: +613 745 2665 • Fax: +613 745 7660  
Email: [order.dept@renoufbooks.com](mailto:order.dept@renoufbooks.com) • Web site: <http://www.renoufbooks.com>

## CHINA

IAEA Publications in Chinese: China Nuclear Energy Industry Corporation, Translation Section, P.O. Box 2103, Beijing

## CZECH REPUBLIC

Suweco CZ, S.R.O., Klecakova 347, 180 21 Praha 9  
Telephone: +420 26603 5364 • Fax: +420 28482 1646  
Email: [nakup@suweco.cz](mailto:nakup@suweco.cz) • Web site: <http://www.suweco.cz>

## FINLAND

Akateeminen Kirjakauppa, PO BOX 128 (Keskuskatu 1), FIN-00101 Helsinki  
Telephone: +358 9 121 41 • Fax: +358 9 121 4450  
Email: [akatilaus@akateeminen.com](mailto:akatilaus@akateeminen.com) • Web site: <http://www.akateeminen.com>

## FRANCE

Form-Edit, 5, rue Janssen, P.O. Box 25, F-75921 Paris Cedex 19  
Telephone: +33 1 42 01 49 49 • Fax: +33 1 42 01 90 90  
Email: [formedit@formedit.fr](mailto:formedit@formedit.fr) • Web site: <http://www.formedit.fr>

Lavoisier SAS, 145 rue de Provigny, 94236 Cachan Cedex  
Telephone: + 33 1 47 40 67 02 • Fax +33 1 47 40 67 02  
Email: [romuald.verrier@lavoisier.fr](mailto:romuald.verrier@lavoisier.fr) • Web site: <http://www.lavoisier.fr>

## GERMANY

UNO-Verlag, Vertriebs- und Verlags GmbH, Am Hofgarten 10, D-53113 Bonn  
Telephone: + 49 228 94 90 20 • Fax: +49 228 94 90 20 or +49 228 94 90 222  
Email: [bestellung@uno-verlag.de](mailto:bestellung@uno-verlag.de) • Web site: <http://www.uno-verlag.de>

## HUNGARY

Librotrade Ltd., Book Import, P.O. Box 126, H-1656 Budapest  
Telephone: +36 1 257 7777 • Fax: +36 1 257 7472 • Email: [books@librotrade.hu](mailto:books@librotrade.hu)

## INDIA

Allied Publishers Group, 1st Floor, Dubash House, 15, J. N. Heredia Marg, Ballard Estate, Mumbai 400 001,  
Telephone: +91 22 22617926/27 • Fax: +91 22 22617928  
Email: [alliedpl@vsnl.com](mailto:alliedpl@vsnl.com) • Web site: <http://www.alliedpublishers.com>

Bookwell, 2/72, Nirankari Colony, Delhi 110009  
Telephone: +91 11 23268786, +91 11 23257264 • Fax: +91 11 23281315  
Email: [bookwell@vsnl.net](mailto:bookwell@vsnl.net)

## ITALY

Libreria Scientifica Dott. Lucio di Biasio "AEIOU", Via Coronelli 6, I-20146 Milan  
Telephone: +39 02 48 95 45 52 or 48 95 45 62 • Fax: +39 02 48 95 45 48  
Email: [info@libreriaaeiou.eu](mailto:info@libreriaaeiou.eu) • Website: [www.libreriaaeiou.eu](http://www.libreriaaeiou.eu)

## **JAPAN**

Maruzen Company Ltd, 1-9-18, Kaigan, Minato-ku, Tokyo, 105-0022  
Telephone: +81 3 6367 6079 • Fax: +81 3 6367 6207  
Email: journal@maruzen.co.jp • Web site: <http://www.maruzen.co.jp>

## **REPUBLIC OF KOREA**

KINS Inc., Information Business Dept. Samho Bldg. 2nd Floor, 275-1 Yang Jae-dong SeoCho-G, Seoul 137-130  
Telephone: +02 589 1740 • Fax: +02 589 1746 • Web site: <http://www.kins.re.kr>

## **NETHERLANDS**

De Lindeboom Internationale Publicaties B.V., M.A. de Ruyterstraat 20A, NL-7482 BZ Haaksbergen  
Telephone: +31 (0) 53 5740004 • Fax: +31 (0) 53 5729296  
Email: books@delindeboom.com • Web site: <http://www.delindeboom.com>

Martinus Nijhoff International, Koraalrood 50, P.O. Box 1853, 2700 CZ Zoetermeer  
Telephone: +31 793 684 400 • Fax: +31 793 615 698  
Email: info@nijhoff.nl • Web site: <http://www.nijhoff.nl>

Swets and Zeitlinger b.v., P.O. Box 830, 2160 SZ Lisse  
Telephone: +31 252 435 111 • Fax: +31 252 415 888  
Email: info@swets.nl • Web site: <http://www.swets.nl>

## **NEW ZEALAND**

DA Information Services, 648 Whitehorse Road, MITCHAM 3132, Australia  
Telephone: +61 3 9210 7777 • Fax: +61 3 9210 7788  
Email: service@dadirect.com.au • Web site: <http://www.dadirect.com.au>

## **SLOVENIA**

Cankarjeva Založba d.d., Kopitarjeva 2, SI-1512 Ljubljana  
Telephone: +386 1 432 31 44 • Fax: +386 1 230 14 35  
Email: import.books@cankarjeva-z.si • Web site: <http://www.cankarjeva-z.si/uvoz>

## **SPAIN**

Díaz de Santos, S.A., c/ Juan Bravo, 3A, E-28006 Madrid  
Telephone: +34 91 781 94 80 • Fax: +34 91 575 55 63  
Email: compras@diazdesantos.es, carmela@diazdesantos.es, barcelona@diazdesantos.es, julio@diazdesantos.es  
Web site: <http://www.diazdesantos.es>

## **UNITED KINGDOM**

The Stationery Office Ltd, International Sales Agency, PO Box 29, Norwich, NR3 1 GN  
Telephone (orders): +44 870 600 5552 • (enquiries): +44 207 873 8372 • Fax: +44 207 873 8203  
Email (orders): book.orders@tso.co.uk • (enquiries): book.enquiries@tso.co.uk • Web site: <http://www.tso.co.uk>

### **On-line orders**

DELTA Int. Book Wholesalers Ltd., 39 Alexandra Road, Addlestone, Surrey, KT15 2PQ  
Email: info@profbooks.com • Web site: <http://www.profbooks.com>

### **Books on the Environment**

Earthprint Ltd., P.O. Box 119, Stevenage SG1 4TP  
Telephone: +44 1438748111 • Fax: +44 1438748844  
Email: orders@earthprint.com • Web site: <http://www.earthprint.com>

## **UNITED NATIONS**

Dept. 1004, Room DC2-0853, First Avenue at 46th Street, New York, N.Y. 10017, USA  
(UN) Telephone: +800 253-9646 or +212 963-8302 • Fax: +212 963-3489  
Email: publications@un.org • Web site: <http://www.un.org>

## **UNITED STATES OF AMERICA**

Bernan Associates, 4501 Forbes Blvd., Suite 200, Lanham, MD 20706-4346  
Telephone: 1-800-865-3457 • Fax: 1-800-865-3450  
Email: customercare@bernan.com • Web site: <http://www.bernan.com>

Renouf Publishing Company Ltd., 812 Proctor Ave., Ogdensburg, NY, 13669  
Telephone: +888 551 7470 (toll-free) • Fax: +888 568 8546 (toll-free)  
Email: order.dept@renoufbooks.com • Web site: <http://www.renoufbooks.com>

**Orders and requests for information may also be addressed directly to:**

### **Marketing and Sales Unit, International Atomic Energy Agency**

Vienna International Centre, PO Box 100, 1400 Vienna, Austria  
Telephone: +43 1 2600 22529 (or 22530) • Fax: +43 1 2600 29302  
Email: sales.publications@iaea.org • Web site: <http://www.iaea.org/books>

INTERNATIONAL ATOMIC ENERGY AGENCY  
VIENNA  
ISBN 978-92-0-139710-2  
ISSN 1011-4289